Fall 12-6-2013

Optically-pumped spin-exchange polarized electron source

Munir Pirbhai
University of Nebraska, munirhp@yahoo.com

Pirbhai, Munir, "Optically-pumped spin-exchange polarized electron source" (2013). *Theses, Dissertations, and Student Research: Department of Physics and Astronomy*. 30.
http://digitalcommons.unl.edu/physicsdiss/30

OPTICALLY-PUMPED SPIN-EXCHANGE POLARIZED ELECTRON SOURCE

by

Munir Hussein Pirbhai

A DISSERTATION

Presented to the Faculty of
The Graduate College at the University of Nebraska
In Partial Fulfillment of Requirements
For the Degree of Doctor of Philosophy

Major: Physics and Astronomy
Under the Supervision of Professor Timothy J. Gay

Lincoln, Nebraska
December, 2013

OPTICALLY-PUMPED SPIN-EXCHANGE POLARIZED ELECTRON SOURCE

Munir Hussein Pirbhai, Ph.D.

University of Nebraska, 2013

Advisor: Timothy J. Gay

Polarized electron beams are an indispensable probe of spin-dependent phenomena in fields of atomic and molecular physics, magnetism and biophysics. While their uses have become widespread, the standard source based on negative electron affinity gallium arsenide (GaAs) remains technically complicated. This has hindered progress on many experiments involving spin-polarized electrons, especially those using target gas loads, which tend to adversely affect the performance of GaAs sources. A robust system based on an alternative way to make polarized electron beams has been devised in this study, which builds on previous work done in our lab. It involves spin-exchange collisions between free, unpolarized electrons and oriented rubidium atoms in the presence of a quenching gas.

This system has less stringent vacuum requirements than those of GaAs sources, and is capable of operating in background pressures of ~1mTorr. Beams with ~24% polarization and 4μA of current have been recorded, which is comparable to the performance obtained with the earlier version built in our lab. The present system is however not as unstable as in the previous work, and has the potential to be developed into a "turn-key" source of polarized electron beams. It has also allowed us to undertake a study to find factors which affect the beam polarization in this scheme of producing

polarized electrons. Such knowledge will help us to design better optically-pumped spin-exchange polarized electron sources.

PREFACE

Contents from sections 2.2.6 and 3.6 have been published in *Review of Scientific Instruments* (2013).

Results from sections 4.1, 4.4 and 4.6 have been accepted for publication in *Physical Review A* (2013).

TABLE OF CONTENTS

LIST OF TABLES

LIST OF ILLUSTRATIONS

CHAPTER 1. Introduction

1.1 Electron spin and its polarization

In addition to its mass and negative charge, an electron has an intrinsic spin angular momentum $\vec{S}$ of magnitude

$$\left|\vec{S}\right| = \hbar\sqrt{S(S+1)} = \hbar\sqrt{\frac{1}{2}\left(\frac{1}{2}+1\right)} = \hbar\sqrt{\frac{3}{4}} \tag{1.1}$$

where $S = 1/2$ is the spin quantum number associated with the spin angular momentum, and $\hbar$ is Planck's constant divided by 2π [1]. The electron has a magnetic dipole moment μ_s related to this spin angular momentum, and it is given by

$$\mu_s = -\frac{g_e \mu_B}{\hbar} \cdot S. \tag{1.2}$$

Here, g_e is the electron spin g-factor, and μ_B is the Bohr magneton. Spin can classically be thought of as the angular momentum associated with a small spinning object [2]. But, such a picture has limitations. For example, estimates obtained for the spatial extent of the electron's internal structure using the classical picture range between 10^{-13} and 10^{-11} cm while data from high-energy colliders indicate that the electron is a point-like particle without any structure down to 10^{-18} cm [3]. Measurement of the component of the electron's spin along any given axis yields either $+\frac{\hbar}{2}$ or $-\frac{\hbar}{2}$. The former, corresponding to "spin-up," refers to an electron with its component parallel to the axis (see figure

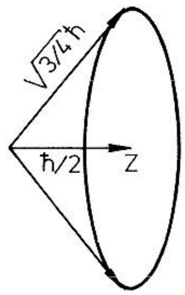

Figure 1.1: A “spin-up” electron. Its spin component of $\frac{\hbar}{2}$ is parallel to the axis of quantization z. (After Kessler [1].)

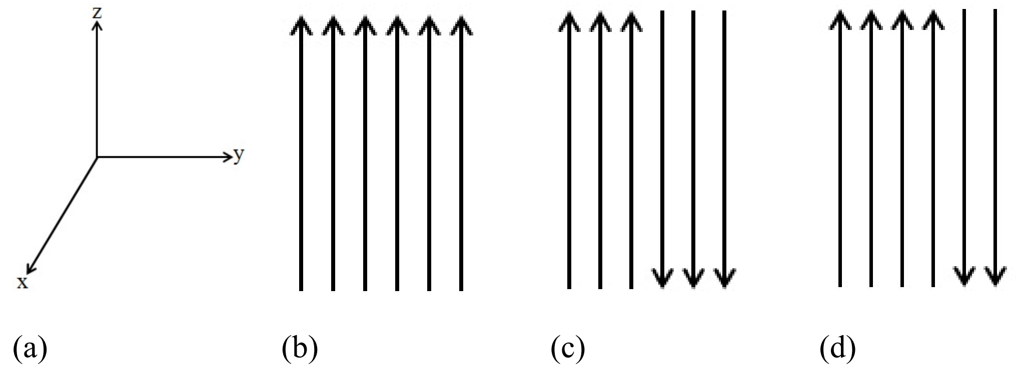

Figure 1.2: With the axis of quantization chosen along the z axis as shown in (a), the electron ensemble in (b) is polarized, in (c) unpolarized, and in (d) partially polarized. (Adapted from [1].)

1.1) while the latter, “spin-down,” describes a particle with its component antiparallel to the axis.

This work deals with spin-polarized electron beams. A group of electrons is said to be spin-polarized if the population of particles in the “spin-up” and “spin-down” states are unevenly distributed [1]. Such an ensemble is characterized by a polarization $\vec{P}$ defined as

$$\vec{P} = \frac{N_\uparrow - N_\downarrow}{N_\uparrow + N_\downarrow}\hat{z}. \tag{1.3}$$

Here, $\hat{z}$ represents the unit vector along the axis of quantization. The number of electrons in the spin-up and spin-down states are denoted by $N_\uparrow$ and $N_\downarrow$. Thus, the electron ensemble in figure 1.2(d) has a polarization of $\frac{4-2}{4+2}=\frac{1}{3}$ in magnitude if the quantization axis is chosen along the z of the coordinate system in 1.2(a). Alternatively, an electron beam with polarization P along the axis of quantization can be thought of as being composed of a totally polarized fraction and an unpolarized fraction, mixed in the ratio P to $(1-P)$. In this case, the density matrix describing such a beam is given by

$$\rho = (1-P)\begin{pmatrix} 1/2 & 0 \\ 0 & 1/2 \end{pmatrix} + P\begin{pmatrix} 1 & 0 \\ 0 & 0 \end{pmatrix}. \tag{1.4}$$

Here, $\begin{pmatrix} 1 & 0 \\ 0 & 0 \end{pmatrix}$ is the density matrix for a beam totally polarized along the axis of quantization while $\begin{pmatrix} 1/2 & 0 \\ 0 & 1/2 \end{pmatrix}$ denotes the density matrix for an unpolarized beam. Electron beams can be either longitudinally or transversely spin-polarized. Longitudinally spin-polarized electron ensembles have their polarization vectors along the beam axis whereas transversely spin-polarized particles have theirs perpendicular to the beam axis.

1.2 Applications of spin-polarized electrons

Polarized electron beams are important to many branches of physics. They offer unique information about the dynamics of matter. Several examples of how they are used are given below.

1.2.1 Atomic and molecular physics

Experiments involving polarized electron beams allow atomic physicists to obtain much more information about the most basic elastic scattering processes than would be available if unpolarized electrons were used [1]. If only the Coulomb and spin-orbit interactions are considered, elastic scattering of electrons from spinless, structureless targets is described by two scattering amplitudes [4]:

$$f = |f| e^{i\Upsilon_1} \text{ and} \tag{1.5}$$

$$g = |g| e^{i\Upsilon_2}. \tag{1.6}$$

In the case of "direct" scattering, where the incident and scattered electrons have the same spin, the differential cross section is

$$\frac{d\sigma}{d\Omega} = |f|^2. \tag{1.7}$$

When an incident electron results in a scattered electron of the opposite spin, the "exchange" differential cross section is given by

$$\frac{d\sigma}{d\Omega} = |g|^2. \tag{1.8}$$

If the electron beam is initially unpolarized, the differential cross section is [4]

$$\left[\frac{d\sigma}{d\Omega}\right]_{unpolarized} = \frac{1}{2}\left(|f|^2 + |g|^2 + |f - g|^2\right). \tag{1.9}$$

Hence, the information due to direct and spin-flip scattering cannot be separated with incident unpolarized electron beams. To be able to measure the amplitudes f and g, polarized electrons have to be scattered from the atoms. Additionally, we can monitor the spin polarization vector $\vec{P}_e^{\,0}$ of the scattered electrons which will take the form [4]

$$\vec{P}_e^{\,0} = S\vec{n} + T\vec{P}_e + U\left(\vec{n} \times \vec{P}_e\right) \tag{1.10}$$

where

$$S = -\frac{2|f||g|\sin(\gamma_1 - \gamma_2)}{|f|^2 + |g|^2}, \tag{1.11}$$

$$T = \frac{|f|^2 - |g|^2}{|f|^2 + |g|^2}, \text{ and} \tag{1.12}$$

$$U = \frac{2|f||g|\cos(\gamma_1 - \gamma_2)}{|f|^2 + |g|^2}. \tag{1.13}$$

Here, $\vec{P_e}$ is parallel to the scattering plane and refers to the spin polarization vector of the incident electrons (see figure 1.3). The spin polarization vector $\vec{P}_e^{\,0}$ of the scattered electrons consists of three components: $S\vec{n}$, which is normal to the scattering plane, $T\vec{P_e}$, a component parallel or antiparallel to $\vec{P}_e^{\,0}$, and $U\left(\vec{n} \times \vec{P}_e\right)$, which is in the scattering plane but perpendicular to $\vec{P_e}$. By measuring the spin polarization of the scattered electrons in these three directions, we obtain the data necessary to determine the moduli $|g|$, $|f|$ and their phase difference $\left(\gamma_1 - \gamma_2\right)$. Hence, scattering experiments with polarized electrons can yield the maximum possible information about the elastic scattering process, assuming that the collision kinetics is well-defined. Such studies have been performed with many atoms including mercury, xenon, rubidium and cesium among others [1, 5]. Inelastic scattering of polarized electrons has, on the other hand, helped us better understand the mechanisms involved in spin-orbit coupling and exchange interactions among the incident and target electrons as well as the Coulomb field of the screened nucleus.

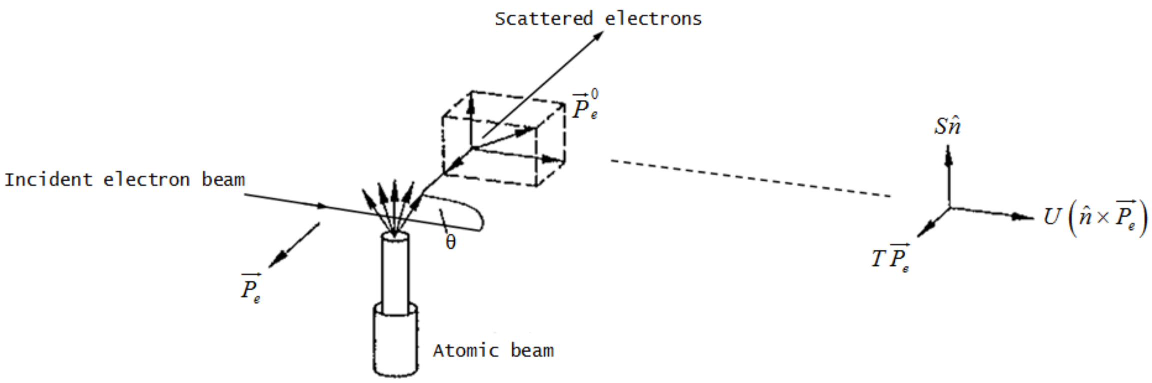

Figure 1.3: Schematic diagram showing how the polarization components of the incident and scattered electron beams are defined. The polarization vector $\vec{P}_e$ of the incident electrons is parallel to the scattering plane. (Adapted from [5].)

Scattering of polarized electrons from chiral molecules has also been investigated [1, 6]. These molecules must be made of at least four different atoms in a non-coplanar arrangement [7]. In order for the molecule to exhibit chirality, the four atoms or groups of atoms must be different from one another. In essence, a chiral molecule is a particle with no superposable mirror image. The two non-superposable mirror images of chiral molecules are labeled D- and L-enantiomers. In nature, one finds, for example, that natural proteins are made of L-amino acids only while carbohydrates and nucleic acids consist solely of D-sugars [1]. The origin of this dissymmetry is a mystery. It has been speculated that it originates from the preferential interaction of longitudinally polarized electrons emitted from β radiation with one enantiomer compared to the other, leading to more substantial degradation of one over the other. Bonner *et al.* [8] tested this hypothesis by irradiating a mixture of D- and L-leucine with longitudinally polarized electrons. They found that D-leucine was degraded to a larger extent. However, subsequent studies [9] failed to reproduce their results.

1.2.2 Nuclear physics

In high-energy physics, polarized electrons can be used to reveal details about the nuclear structure [1]. Researchers have, for instance, investigated how the deep inelastic scattering of longitudinally polarized electrons by polarized protons depends on spin [10]. Various models of the nuclear structure predicted an asymmetry in the differential inelastic cross-sections for parallel and anti-parallel mutual orientations of the electron and proton spins. However, estimates of this asymmetry varied among the models. Experimental determination of this asymmetry using polarized electron beams helped high-energy physicists find out which model is valid and should thus be used to extract accurate information about the spin distribution of quark constituents inside protons.

Polarized electrons can also be used in experiments to test the Weinberg-Salam theory, which unifies two fundamental interactions in physics [11, 12]. This theory predicts that the cross-section for inelastic scattering of electrons from unpolarized nuclei depends on both the weak and electromagnetic interactions; it comprises an interference term between the weak and electromagnetic amplitudes. One would therefore expect different scattering intensities for beams with polarization parallel and anti-parallel to the direction of propagation. Such dependence of the scattering cross section from an unpolarized target on the electron helicity violates parity conservation, which is characteristic of weak interactions.

1.2.3 Surface physics

Applications of polarized electron beams are not limited to studies of the dynamics of particle collisions. The electron with its intrinsic spin angular momentum $\vec{S}$ has a magnetic moment associated with it which can interact with and be affected by the magnetization of surfaces. Information obtained from this interaction helps researchers to study the electron spin configurations of these surfaces [13]. Electrons possess other properties which make them suitable probes for such studies. For instance, the strong Coulomb interaction prevents electrons from embedding themselves deeply in a solid [14]. The resulting short mean free path and probing depths allow information to be readily obtained about surface-specific properties. Electron-based techniques are therefore ideal for investigating magnetic properties of surfaces and thin films. Such magnetic properties are important for data storage devices and future electronics such as spin valves, magnetic memories, spin injectors and magnetic sensors [15]. Among the spin-sensitive methods devised for these studies are spin-polarized photoemission spectroscopy [16], spin-polarized inverse photoemission spectroscopy (SPIPES) [17, 18], spin-polarized electron energy loss spectroscopy (SPEELS) [19], and spin-polarized low energy electron microscopy (SPLEEM) [20].

Transmission of spin-polarized free electrons through ferromagnetic structures offers another means of investigating the properties of thin foils [21, 22]. In these experiments, the spin polarization $\overrightarrow{P_e}$ of the incident electron beam is oriented either parallel or anti-parallel to the magnetization of the material. The energy distribution of the transmitted electron beam may exhibit different behaviors for the two polarizations of the incident beam as can be seen in figure 1.4. This information is important to understand how the transport of low energy electrons in metals depends on spin.

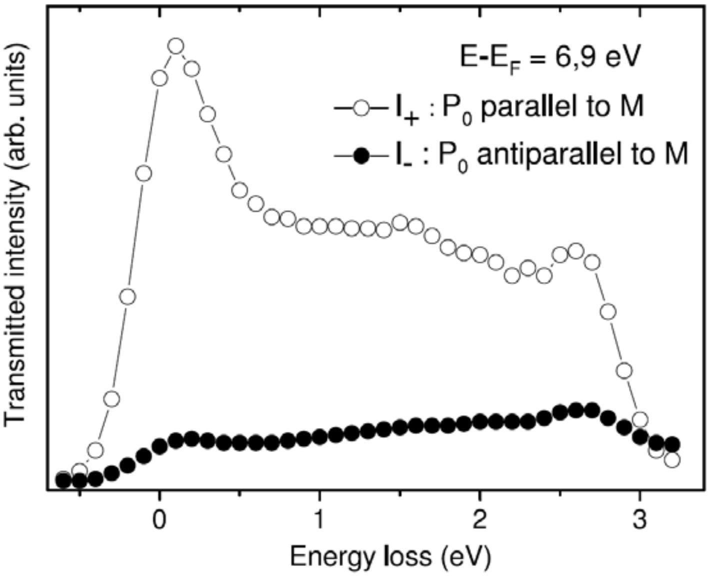

Figure 1.4: Intensity spectra $I_+(E)$ and $I_-(E)$ of an Au/4 nm Co/Au trilayer as a function of the electron energy loss. Here, $I_+(E)$ refers to the energy loss distribution for an incident electron beam with its spin polarization $\overrightarrow{P_0}$ parallel to the magnetization M of the sample while $I_-(E)$ refers to the energy loss distribution for an incident electron beam with its spin polarization $\overrightarrow{P_0}$ anti-parallel to the magnetization M of the sample. The energy of the incident electrons is 6.9eV. (After Dey *et al.* [21].)

Spin-polarized electron energy loss spectroscopy (SPEELS) is another valuable probe of surface physics [23]. With the help of an analyzer, the energy and momentum transfer of the scattered electrons to the sample are recorded to obtain information about its magnetization. Magnetization dynamics of surfaces is governed by spin waves. The latter are disturbances that propagate in magnetic materials, thus affecting their ordering. Spin waves can be excited when spin-polarized electrons scatter from a magnetic material along its magnetization direction. The projectiles will lose energy in the process, and the energy difference equals the energy of the excited spin wave. Researchers can then use this information to determine the ordering in magnetic materials and their magnetization.

1.3 Sources of polarized electrons

Polarized electrons are produced from processes such as photoionization, photoemission, autoionization, secondary emission, impact ionization and diffraction [1]. The most successful sources based on some of these processes are reviewed in the following subsections. They are characterized by their beam current I, their degree of polarization P, the direction of polarization of the electrons, their emittance, which describes the electron beam quality (it is the product of the width of the beam and its transverse velocity spread), and their figure-of-merit $\mathrm{FOM}\,(=P^2 I)$, which is inversely proportional to the statistical error obtained in an experiment with an electron beam of polarization P and current I [24].

1.3.1 Photoemission from gallium arsenide (GaAs)

The GaAs photocathode source enjoys the widest application in polarized electron physics. It is the state-of-the-art in polarized electron sources, yielding high current and polarization, greater than 80% with strained GaAs layers [25]. The polarization of the electron beam can be reversed optically, which is highly desirable for the elimination of instrumental uncertainties. Typically, a photocurrent of ~20μA can be produced with just 1mW of incident light [24]. The quantum efficiency for such sources, defined as the number of electrons emitted per incident photon, for such sources is ~1%. The energy distribution of its electron beam is narrow. At 300 K, its full width at half-maximum of the energy distribution is about 0.15 eV [24]. It is thus ideal for experiments requiring "monochromatic" beams.

Photoemission from the gallium arsenide crystal proceeds in three steps [26]. First, a photon is absorbed by the crystal. This process creates an electron-hole pair with the electron transitioning from the valence band maximum to the conduction band minimum. The electron then diffuses to the surface of the crystal, which has had its work function reduced by applying cesium and oxygen to produce negative electron affinity (NEA) conditions. Finally, the particle escapes into vacuum.

By examining the band structure of GaAs near the center of the Brillouin zone (Γ point) [24], one can understand why the photoelectrons are spin-polarized. The band structure and its corresponding states are illustrated in figure 1.5. If the electrons in the crystal are excited with circularly polarized $(\sigma^{\pm})$ light, Δm_j must be equal to +1 (for σ^{+} light) or -1 (for σ^{-} light) according to the selection rules. Excitation from the fourfold degenerate $P_{3/2}$ level by, say, σ^{-} light would yield three times more electrons in the $m_j = m_s = +1/2$ state than in the $m_j = m_s = -1/2$ state of the $S_{1/2}$ level. Such a situation would result in photoelectrons with a maximum polarization of 50%. This number is actually closer to

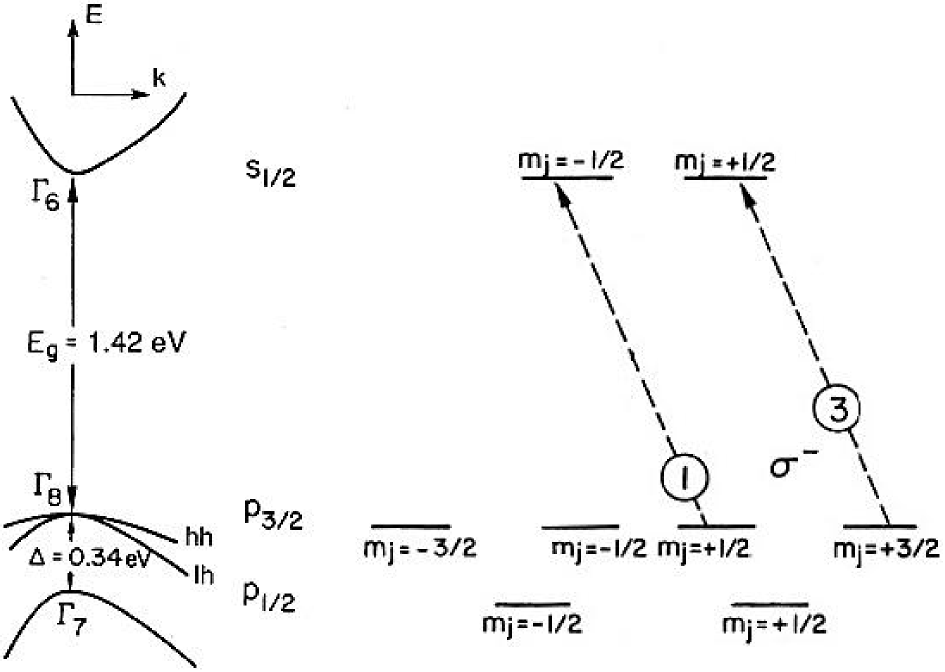

Figure 1.5: The GaAs energy bands at the center of the Brillouin zone are shown on the left. Here, E_g represents the band gap energy, and Δ the spin-orbit splitting of the valence band. On the right, the allowed transitions between the $P_{3/2}$ and $S_{1/2}$ levels for σ^- circularly polarized light are depicted. The circled numbers denote the relative transition probabilities. (After Celotta *et al.* [24].)

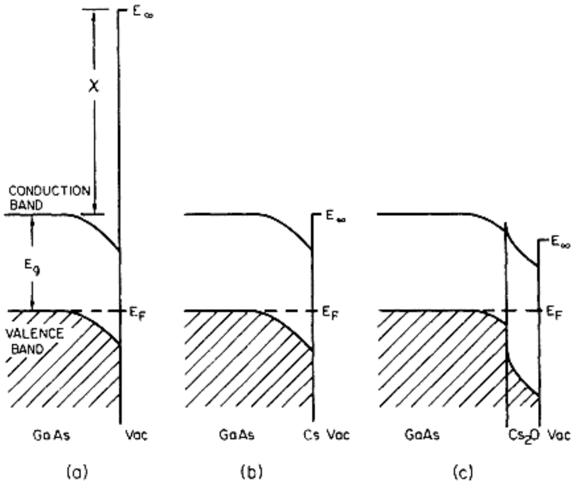

Figure 1.6: Effects of different surface treatments on the energy bands near the surface in p-type GaAs: (a) a high electron affinity clean GaAs crystal; (b) an approximately zero electron affinity GaAs crystal with a layer of Cs, and (c) a negative electron affinity GaAs crystal with Cs-O treatment. (After Pierce *et al.* [27].)

35% for bulk GaAs at room temperature due to depolarizing effects [24] as the electrons diffuse to the surface and are emitted into the vacuum from the bulk.

Unfortunately, the GaAs polarized electron source is difficult to operate [28, 29, 30], especially with regard to the production of negative electron affinity (NEA) conditions at the surface. Ordinarily, electrons excited to the conduction band minimum would be approximately 3eV below the vacuum level and could not escape from the GaAs (please refer to figure 1.6). By treating the surface with cesium and oxygen successively in a process called activation, it is possible to lower the vacuum level at the surface below the energy of the conduction band minimum in the bulk to achieve the NEA condition. The electrons can thus escape into vacuum after excitation to the conduction band. These complex procedures generally present a steep learning curve to graduate students in university laboratories, who may spend many months learning how to prepare useable GaAs photocathodes. Unlike accelerators such as CEBAF and MAMI, university laboratories cannot afford teams of technicians to continuously maintain and run these sources. Furthermore, GaAs electron emitters require stringent vacuum systems. In pressures greater than $\sim 5\times10^{-11}$ Torr, the bare GaAs is highly susceptible to contamination, and the activation process will generally fail [31]. This vacuum requirement proves challenging for experiments involving target gas loads, for example in the search for electron circular dichroism [6] or in the investigation of fluorescence polarization from spin-polarized electron impact on atoms and molecules [32]. In such an environment, the GaAs photocathode must be activated regularly; its quantum efficiency lifetime rarely exceeds 8 hours. Moreover, electron beam transmission and focusing conditions become unstable. There exists a definite need for a user-friendly, turn-key source of polarized electrons.

1.3.2 Photoionization of polarized atoms by unpolarized light

Polarized electrons can also be generated by photoionizing a beam of polarized alkali atoms. A source relying on this principle was built by Alguard et al. [33], and was used at the Stanford Linear Accelerator. In such a source, an alkali atomic beam from an oven was polarized by passing it through a six-pole magnet. The polarized atomic beam then entered another region with a high magnetic field, which decoupled the electronic and nuclear spins of the atoms. This process minimized depolarization due to the hyperfine interaction. The atoms were then photoionized with unpolarized ultraviolet light to produce polarized photoelectrons.

This scheme created pulsed electron beams with a repetition rate of ~180 Hz and ~85% longitudinal polarization. However, the current, at $\sim 10^9$ electrons/pulse, was low. Moreover, reversing the electron polarization was a relatively slow process because it involved switching the orientation of the magnetic field in the photoionization region.

1.3.3 Photoionization of unpolarized atoms by circularly polarized light (Fano effect)

In 1969, Fano determined that polarized electrons can be produced by ionizing an unpolarized atomic beam with circularly polarized light [34]. The Fano effect relies on the spin-orbit interaction of photoemitted electrons in the continuum of high Z alkalis such as rubidium and cesium. An alkali atom has one valence electron, which can be in either the $m_j = +1/2$ or $m_j = -1/2$ of the $n^2S_{1/2}$ level. When the atom is ionized using σ^+ circularly polarized light, the electron can transition to one of the following continuum states: ${}^2P_{3/2}(m_j = 3/2)$, ${}^2P_{3/2}(m_j = 1/2)$, or ${}^2P_{1/2}(m_j = 1/2)$. The relative intensities of these three possible transitions will fix the magnitude of the electron polarization *P*. These transition probabilities depend solely on their radial ionization matrix elements R_1, R_2 and R_3 [4]:

$$P = \frac{2(R_3 - R_1)(2R_3 + R_1) + (R_3 - R_1)^2}{(2R_3 + R_1)^2 + 2(R_3 - R_1)^2}. \tag{1.14}$$

In the absence of the spin-orbit coupling, $R_1 = R_3$, and the electron polarization vanishes.

Electrons from Fano sources are longitudinally polarized. Their polarization can be reversed optically. The Fano mechanism has been employed to create both pulsed and continuous polarized electron beams. The maximum polarization produced by a pulsed source [35] was 90% with $\sim 10^9$ electrons/pulse and a repetition rate of 0.05 Hz. The continuous source [36] generated beams with 63% polarization. However, its electron current was on the order of nanoamperes. The electron energy distribution was ~3 eV, too large for many applications.

1.3.4 Field emission from ferromagnetic europium sulfide (EuS) on tungsten

In 1972, Mueller *et al.* [37] found that electrons with a polarization of 89% were produced by field emission from a tungsten tip coated with a thin film of ferromagnetic europium sulfide. The EuS acts as a spin filter for electrons tunneling into its empty conduction band from the tungsten. The simplified band model in figure 1.7 can explain the observation of Mueller *et al.*. Below the Curie temperature, europium sulfide becomes a ferromagnetic insulator with its 4f states above the valence band. These states are totally polarized because the europium atom has 7 valence electrons, all with the same spin, localized in these states. The exchange interaction of the conduction electrons with those of the polarized 4f states causes a shift in the energy of particles with opposite spins in the conduction band. Electrons in the conduction band with spins parallel to those in the 4f state lie lower in energy than those with spin antiparallel. Consequently, the internal barrier ϕ_i experienced by electrons trying to tunnel from W into EuS will be spin-dependent; the ferromagnetic splitting of the EuS conduction band causes the barrier to be of different heights for the two spin states. Kisker *et al.* [38] have argued that the effect of the external barrier at the EuS-vacuum interface can be neglected when explaining why polarized electrons are emitted from ferromagnetic europium sulfide on tungsten in an applied electric field; only the internal barrier ϕ_i need to be considered. If an electric field $\vec{E}$ is applied near the surface of the emitter, it causes the EuS energy bands to decrease in energy with distance x from the W surface. For a large enough $\vec{E}$, the conduction band of the EuS can be lower than the Fermi level, corresponding to energy E_F, of the W. Electrons of one spin can then tunnel from the tungsten through the barrier height ϕ_i to the lower conduction band before proceeding into the vacuum.

Electron current of ~10^{-8} A has been produced with this technique. Owing to their small emitting areas (~100 nm), field emitters act essentially as point sources of polarized

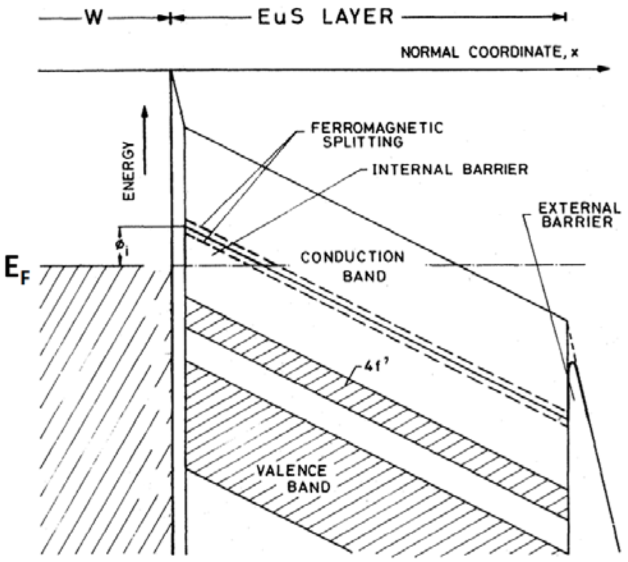

Figure 1.7: Simplified band model for the W-EuS emitter. The internal barrier ϕ_i determines the emission current. It is different for spin-up and spin-down electrons due to the ferromagnetic splitting of the EuS conduction band. (After Celotta *et al* [24].)

electrons, and are therefore very bright. The polarization is transverse to the electron beam axis. Reversing it is a complex process which involves raising the temperature of the field emitter above the Curie temperature and cooling it in an applied magnetic field of the appropriate direction. This source is also operated under stringent conditions: ultrahigh vacuum pressures of $\leq 10^{-10}$ Torr and temperatures of $\leq 10\,\mathrm{K}$.

1.3.5 Chemi-ionization of optically-oriented metastable helium

This technique was devised at Rice University in the mid-1970s, and has been significantly upgraded since then [39, 40, 41]. In such a source, a microwave discharge first produces metastable helium atoms in the $2\,^3S_1$ state, which lies 19.8eV above the

1^1S_0 ground state as shown in figure 1.8. These atoms are then optically pumped using circularly polarized 1.08 μm light from a neodymium-doped lanthanum magnesium hexaluminate (LNA) laser. Through repeated absorption and emission of photons, the helium atoms eventually populate the $m_j = +1$ or $m_j = -1$ magnetic sublevels of the $2\,^3S_1$ state, depending on the helicity of the pump light used. The polarized helium atoms are finally chemi-ionized by collisions with carbon dioxide gas. In this reaction, spin angular momentum is conserved. It implies that optical orientation of the helium triplet metastables will lead to polarized free electrons. The resulting spin-polarized electrons are extracted and are formed into a beam electrostatically.

Figure 1.9 illustrates the performance of the helium flowing afterglow source. Polarized electrons of ~90% at currents of 100 nA can be obtained with such a scheme. The polarization can be reversed optically. Moreover, the FWHM (full width at half maximum) of the polarized electrons energy spectrum is ~150 meV, which is comparable to that of GaAs sources. This source is stable. It has the potential to compete with conventional GaAs sources because it does not require ultrahigh vacuum (operating pressure: ~0.05 to 1 Torr). Also, it does not involve complicated activation procedures. However, this source needs large, high speed mechanical pumps to handle the flow rate of helium gas, which may make it cumbersome. Attempts to use this source at the Orsay linac failed because of repeated laser and vacuum problems [42].

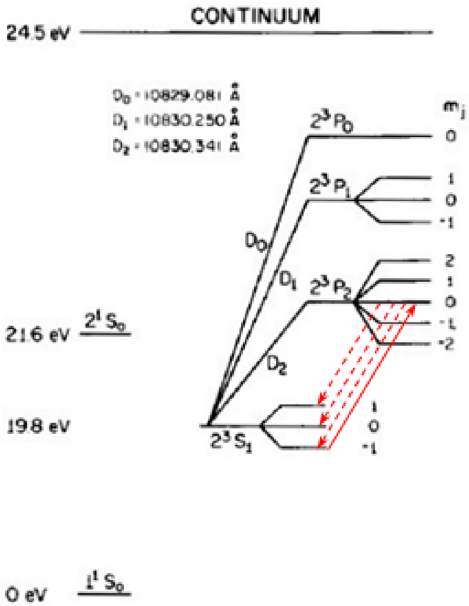

Figure 1.8: Relevant energy levels of helium. The optical pumping cycle increases the population of the $m_j = +1$ sublevel of the 2^3S_1 state for right-circularly-polarized (RCP) light whereas for left-circularly-polarized light, the $m_j = -1$ sublevel is preferentially populated. For example, the red solid line shows atoms in the metastable 2^3S_1 $m_j = -1$ state absorbing RCP light. The dashed lines denote their subsequent decay pathways. Repeated absorption and emission of photons transfer the population to the 2^3S_1 $m_j = +1$ state. (After McCusker *et al.* [43].)

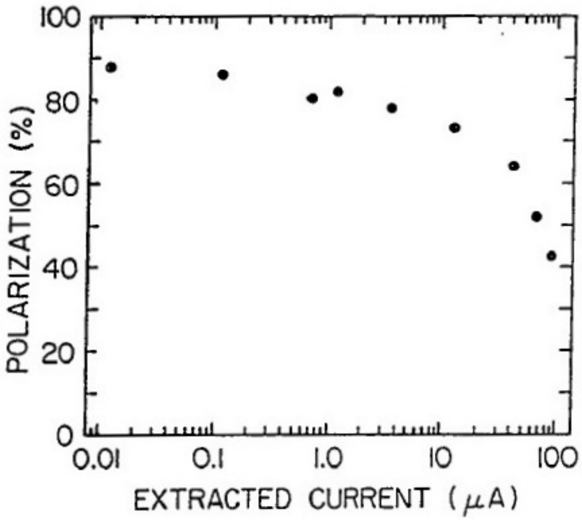

Figure 1.9: Performance of the helium flowing afterglow source. (After Rutherford *et al.* [41].)

1.3.6 Spin-exchange collisions with oriented atoms

Sources based on this principle can offer another viable alternative to the GaAs photocathodes. This thesis focuses on this method of polarizing electrons. Burke and Shey were the first to suggest that spin-exchange scattering of unpolarized electrons from oriented one-valence-electron atoms could produce beams of polarized electrons [44, 45]:

$$e(\uparrow) + A(\downarrow) \rightarrow e(\downarrow) + A(\uparrow) \tag{1.15}$$

In such a scattering process, an electron with, say, spin-up, $e(\uparrow)$, collides with a spin-down atom, $A(\downarrow)$, resulting in a spin-down electron and a spin-up atom.

Using the principle of spin-exchange collisions, Farago *et al.* created a pulsed source of polarized electrons in 1966 [46, 47]. In their experimental setup, a beam of potassium atoms emerges from an oven, and is oriented by a six-pole magnet. Free electrons emitted by a thermionic cathode are injected and are trapped using a combination of electric and magnetic fields in a Penning trap. Besides confining the motion of the electrons in the radial direction, the magnetic field defines the quantization direction relative to which the polarization vector of the atomic beam is oriented. Thus, it also describes the direction of polarization of the output electrons. In the Penning trap, the electrons undergo direct and spin-exchange collisions with the alkali beam. At the end of the prescribed trapping time, the electrons are released, and they emerge longitudinally polarized. Polarizations of 45% with a pulse repetition rate of 50 times per second were obtained. However, less than 10^5 electrons could be generated per pulse.

After extensive theoretical calculations [48], R. J. Krisciokaitis-Krisst *et al.* designed and built a system with improved performance [49]. A two-element electron gun with an indirectly heated cathode provided the free unpolarized electrons. The particles were trapped, and underwent spin-exchange scattering with polarized atomic hydrogen. The atomic target was obtained by dissociating molecular hydrogen in a microwave cavity. The atomic hydrogen was then polarized by passage through an axially-tapered six-pole magnet. This source produced pulses of electrons with 60% polarization. The repetition rate was about 50Hz. Among the factors contributing to the increased electron polarization were the longer interaction length between the electrons and the target atoms (~30cm), and the higher degree of orientation of the hydrogen atoms (~70%). Each pulse also contained two orders of magnitude more electrons than the source of Farago *et al.* [46]. However, this electron current is still insignificant compared to that of the GaAs photocathode.

In 1998, Batelaan *et al.* [29] finally achieved performances comparable to first-generation GaAs photocathodes [50] with their electron spin filter. Their source was based on the spin-exchange collisions of free unpolarized electrons with rubidium atoms oriented using the technique of optical pumping [51]. Optically-pumped alkali atoms were polarized with resonant circularly polarized light. The polarization of the atoms and hence that of the electrons can be reversed by flipping the helicity of the light. In low magnetic fields, less than 0.3T for rubidium [52, 53, 54], a quenching gas must be added to the alkali vapor for it to be effectively polarized [55, 56]. The quenching gas causes the excited rubidium atoms to decay non-radiatively. Radiative decay would create photons with random propagation directions that might be absorbed by the oriented atoms, thus leading to their depolarization.

A schematic representation of the apparatus built by Batelaan *et al.* is shown in figure 1.10. A rubidium ampoule was placed in a 2.75” Conflat nipple, and was heated to form an alkali vapor of the desired density (~10^{12} atoms/cm^3). The free unpolarized electrons were produced by ionizing, with a cold-cathode discharge, the quenching gas (~1Torr) that filled the vacuum chamber. Under the influence of longitudinal electric and magnetic fields, the free electrons drifted through the gas mixture. The 600G magnetic field defined the quantization axis as well as constrained the radial diffusion of the electrons. While drifting, the electrons scattered multiple times, predominantly from the quenching gas. In addition to causing the electrons to lose energy (the electron-rubidium spin-exchange cross section is largest for thermal electrons [57]), this process increased the path length of the electrons, and hence, their likelihood of making a spin-exchange collision with polarized rubidium atoms. This scheme eliminated the use of an electron trap, thus paving the way for a continuous source of polarized electron beams. The performance of the source developed by Batelaan *et al.* is shown in figure 1.11. Two different quenching gases were tried: nitrogen and helium. Electrons with 26% polarization and 2μA of current were generated. The FWHM of the energy spread was estimated to be 1eV. These numbers show that the optically-pumped electron spin filter has the potential to be a turn-key source of polarized electron beams, operating at reasonable pressures of 10^{-4}-10^{-3} Torr.

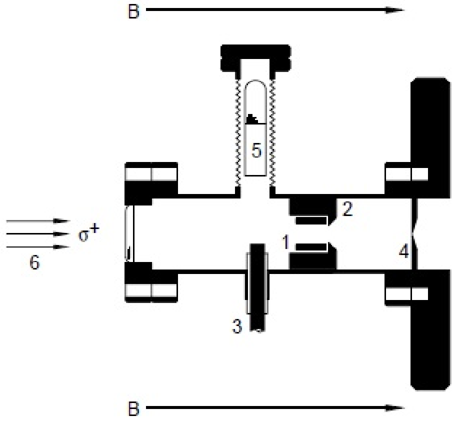

Figure 1.10: Diagram of spin filter showing: (1) dc-discharge cold cathode; (2) discharge anode; (3) discharge high-voltage feedthrough; (4) electrically isolated field plate and exit aperture; (5) Rb ampoule; (6) optical pumping radiation. A magnetic field is applied to the entire apparatus. (After Batelaan *et al.* [29].)

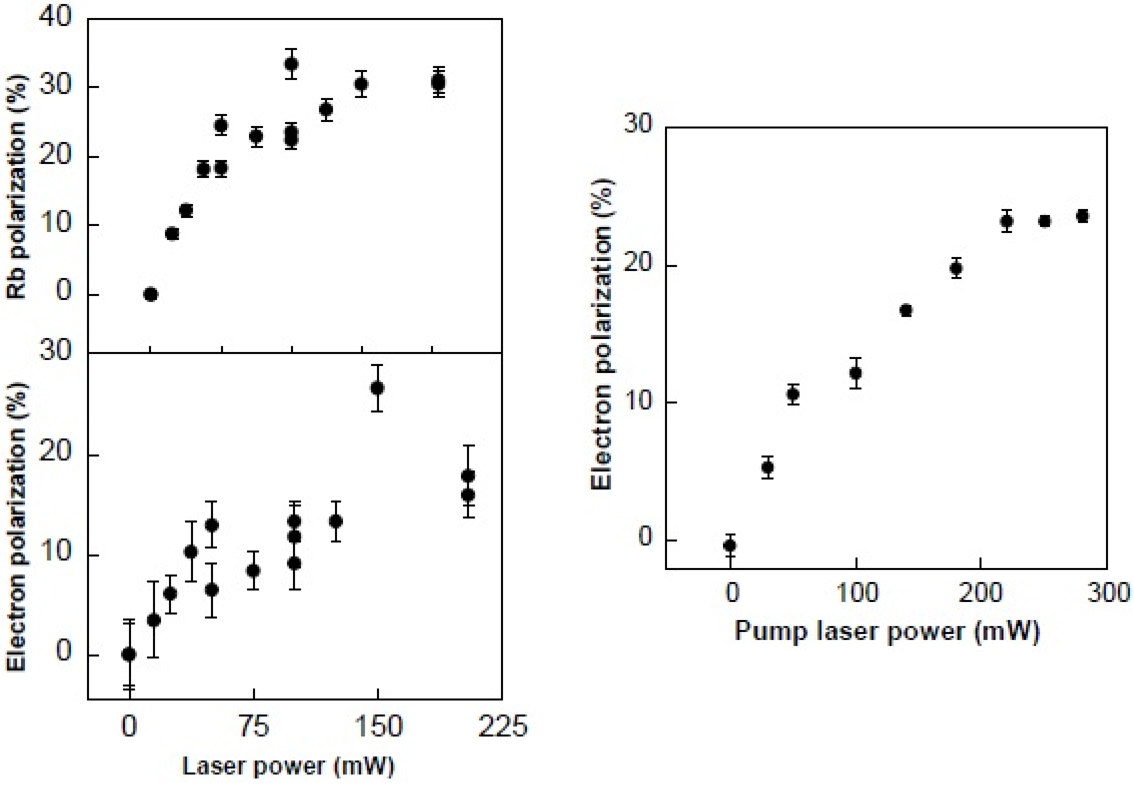

(a) (b)

Figure 1.11: Performance of the optically pumped electron spin filter with two different buffer gases: (a) nitrogen at 0.4 Torr, and (b) helium at 2 Torr. The rubidium densities were 7x10^{11} atoms/cm^3 and 3x10^{12} atoms/cm^3. (After Batelaan *et al.* [29].)

1.4 Motivation for current research

This work builds on that of Batelaan *et al.* [29]. In their setup, Batelaan *et al.* were ionizing the nitrogen, or helium buffer gas, to produce the free, unpolarized electrons. These gases also served to quench and thus, to better orient the rubidium vapor. In essence, the two mechanisms were coupled. This feature made systematic studies to understand the factors affecting the generation of polarized electrons very difficult, if not impossible. For example, the spin-exchange cross section between electrons and rubidium atoms is largest for very slow particles (see figure 1.12). Batelaan *et al.* could not readily investigate how the energy of the incident electrons would influence their final polarization. An ideal system for such studies would therefore separate the production of free, unpolarized electrons from the optical pumping of the alkali vapor.

Subsequent studies [30] based on the scheme developed by Batelaan *et al.* [29] also highlighted the inherent instability of the cold-cathode discharge. They made the need to identify a simpler mechanism to generate the free, unpolarized electrons more pressing. But above all, these same studies could produce electron beams with no more than 2% polarization. This thesis work was primarily aimed at ensuring that the scheme developed by Batelaan *et al.* [29] can generate polarized electrons reliably, and can thus be developed into a viable turnkey source in the future.

Moreover, as discussed in the previous section, the buffer gas serves many key roles in the operation of the optically-pumped spin-exchange polarized electron system. It is important to find buffer gases which help the apparatus to yield high electron

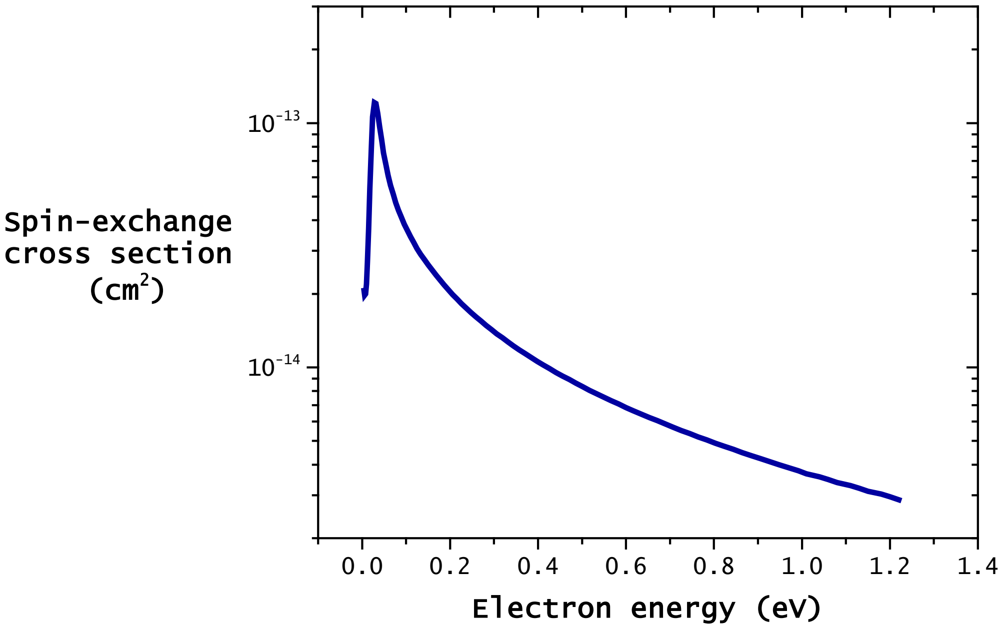

Figure 1.12: Electron-rubidium spin-exchange cross-section as a function of incident electron energy. (Adapted from [57].)

polarization as well as current. Batelaan *et al.* [29] tried nitrogen and helium as buffer gases. In this work, we expanded the list to include hydrogen and ethylene. We observed how the system performed with nitrogen, helium, hydrogen and ethylene, all at approximately 200mTorr. We tried hydrogen as buffer gas because W. Happer, whose group at Princeton has worked extensively on the production of spin-polarized atomic hydrogen by spin-exchange optical pumping, suggested it [42]. Hrycyshyn *et al.* have, on the other hand, shown that ethylene is the most effective at orienting rubidium atoms compared to the other gases mentioned above [58]. We also wanted to investigate whether the pump laser's wavelength, the electric field across the spin-exchange cell, and the energy of the incident electrons have any influence on the polarization of the electron beam. Knowing which factors affect the performance of the optically-pumped electron spin filter will be critical to the realization of a viable, turnkey source of polarized electrons.

CHAPTER 2. Experimental setup

2.1 Evolution of the experimental setup

Initially, L. Neukirch and E. B. Norrgard were assigned to this project. A schematic diagram of the prototype they originally built is shown in figure 2.1. In their final design, the bends at the ends of the apparatus were eliminated, and an inline thermionic electron gun was installed, which supplied free, unpolarized electrons. The electron beam was guided along the apparatus with longitudinal magnetic fields produced by four electromagnets. It was collimated by a first differential-pumping aperture, upstream of the collision region. There, the electron beam would have encountered a mixture of rubidium and quenching gas. The alkali vapor would have been optically pumped by an off-axis laser beam. The circularly-polarized laser light would have been reflected off the downstream exit aperture and back into the collision chamber to give it two chances to pump the rubidium vapor. This aperture was electrically isolated from the rest of the chamber. It provided an electric field inside the interaction region. Thus, the electrons could drift through the gases and eventually exit the chamber. A hole was drilled through the ceramic base of the commercially-available filament of their electron gun to let the probe beam through. The hairpin-style thermionic filament wire, being 0.13mm in diameter, allowed the 2mm in diameter probe beam to pass through, and travel to the collision region where it interacted with the rubidium vapor. By monitoring changes in

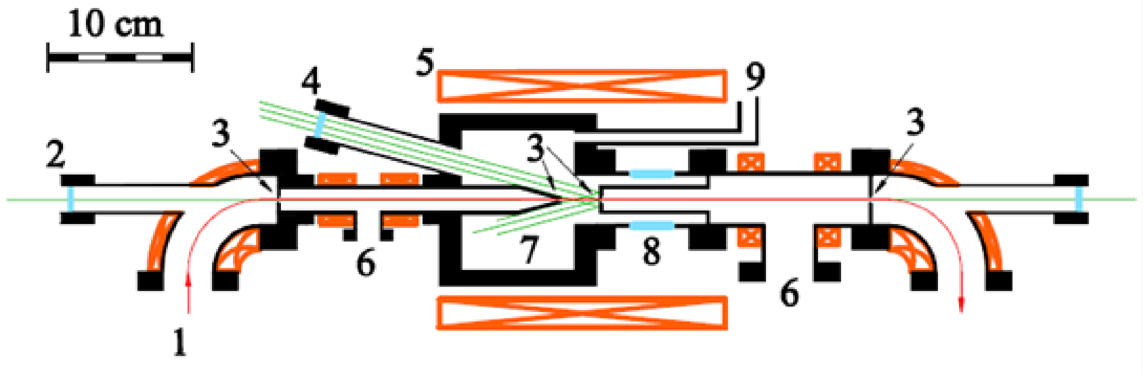

Figure 2.1: L. Neukirch's and E. B. Norrgard's spin filter apparatus showing (1) incident electron beam, (2) probe laser, (3) differential pumping and beam-defining apertures, (4) pump beam, (5) solenoidal magnet, (6) differential pumping port, (7) spin-exchange chamber, (8) insulating break, (9) buffer gas inlet.

the plane of polarization of the portion of the probe beam emerging from the vacuum system, one could determine the alkali vapor's density and degree of orientation using the diamagnetic and paramagnetic Faraday effects [59, 60, 61]. These techniques to monitor the properties of the rubidium vapor target are described in detail in section 2.2.2 and 3.5.

Initial tests of this system showed that it was flawed. Only small currents of electrons could be transported to the Faraday cup intermittently. The causes of this problem were never resolved. When the particles did make it through the apparatus, energies of at least 150eV were required. Even at these high energies, less than 1nA of current was registered on the Faraday cup when the nitrogen pressure in the collision region reached ~0.2 Torr. Ultimately, this system was abandoned, and a simpler design was sought. Dr. D. Tupa, for instance, suggested that the pump light should be counter-propagating with the electron beam. Electrons have a better chance of being polarized using such an experimental setup for a couple of reasons. As the particles penetrate deeper into the collision cell, they will slow down as a result of losing energy through multiple collisions with the buffer gas. They will thus experience larger electron-rubidium spin-exchange collisions deeper inside the interaction region. With the proposed experimental geometry, the rubidium vapor is likely to have its highest degree of orientation at the downstream end where the pump light enters the collision cell and electrons exit the interaction region. Indeed, the pump light will be absorbed by the alkali atoms, and will be attenuated as it travels through the cell [62]. Thus this setup favors interaction between the most highly-polarized rubidium atoms, and those electrons which have slowed down the most and so have the greatest probability of undergoing spin-exchange collisions.

Dr. Tupa also recommended placing a 6” six-way Conflat chamber between the electron gun and the electron optical polarimeter. A smaller collision cell attached to a Conflat flange would be inserted from the top port of the six-way chamber. A reservoir loaded with rubidium would sit at the bottom of the collision cell. The entrance and exit apertures of the interaction volume would be collinear with the electron beam. It was suggested that a xyz-manipulator could facilitate alignment of the system.

Further discussions with Mr. Les Marquart and Dr. P. D. Burrow yielded key ideas for the final design. They suggested simplifying the alignment procedure by building the electron gun immediately upstream of the interaction volume instead of having the former in a separate vacuum chamber. Dr. Burrow advocated using a collision cell similar to those used in electron swarm experiments [63]. Such a cell would be broken into many different electrodes with each biased at a slightly more positive potential than the previous one. Such a feature, he argued, would provide a more uniform electric field inside the interaction region. These ideas gave the impetus for the current prototype.

2.2 Overview of the apparatus

The new source design used to acquire the data presented in this study is shown in figures 2.2 through 2.7. In the following sections, the main aspects of the apparatus will be described. More figures will be provided to supplement the discussion. It consists of five segments: the source, a differential pumping chamber, the optical electron polarimeter, and the probe and pump optics.

I will start by discussing the optical layout. It should be noted that we are dealing with 795 nm pumping light, corresponding to the rubidium D1 transition. All mirrors (BB1-E03) and beam samplers (BSF10-B) in this study were bought from Thorlabs. They are 1” in diameter, and they are rated for wavelengths ranging from 750 nm to 1050 nm.

2.2.1 Pump optics

The pump optics allows us to polarize the alkali vapor parallel or antiparallel to the apparatus’s longitudinal magnetic field. For this purpose, I used a 60mW diode laser (Sacher Lasertechnik 795nm TEC-050 Cheetah series) fiber-coupled to a tapered amplifier (Sacher Lasertechnik 795nm TEC-400 Cheetah series). When the fiber-coupler is properly aligned, the laser system produces up to 1W of laser power. I would typically use about 850mW during experimental runs. The pump wavelength can be set at any

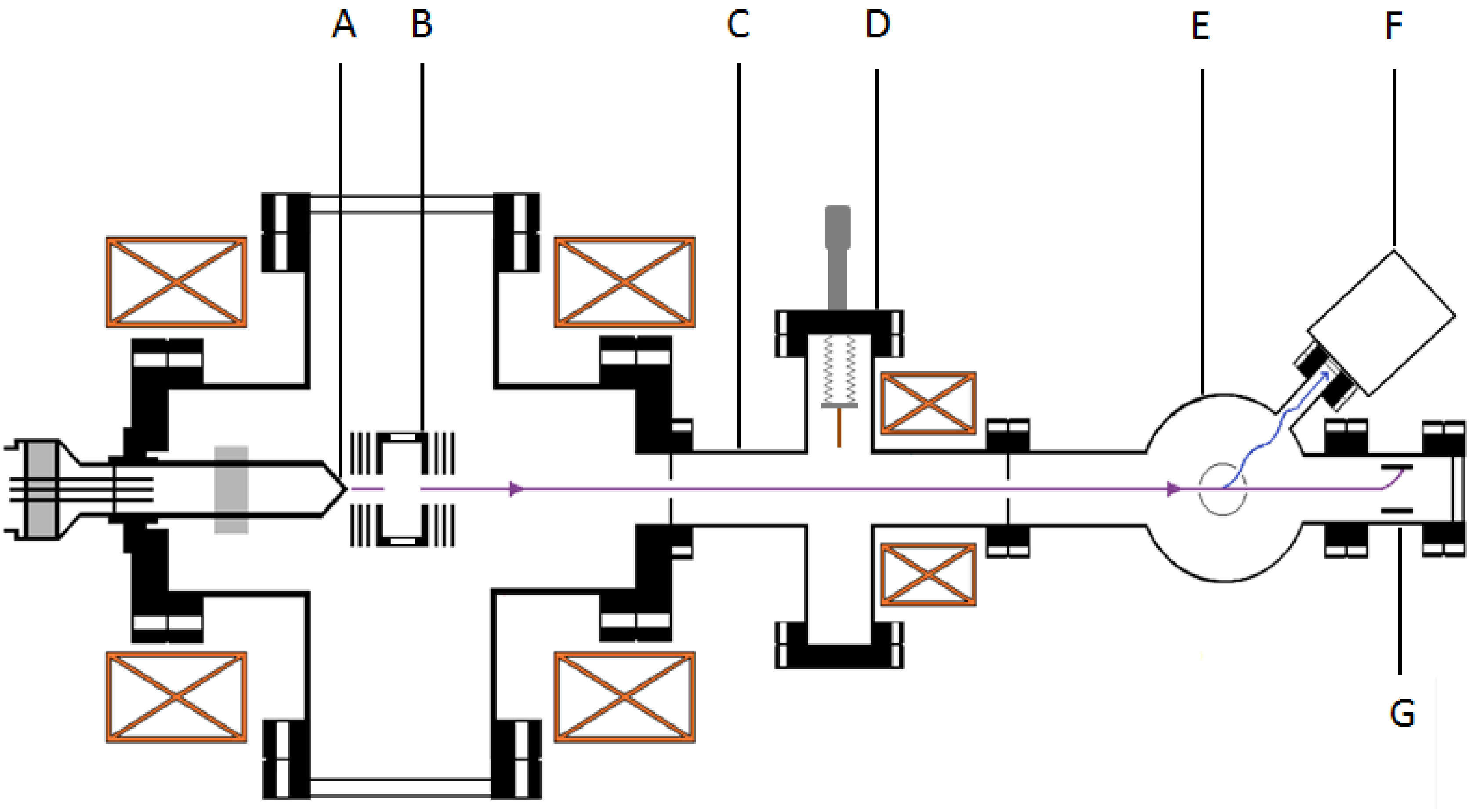

Figure 2.2: Schematic of the entire apparatus. Here, A represents the tungsten filament, B the collision cell, C the differential pumping chamber, D the retractable electron collector, E the electron polarimeter, F the optical polarimeter, and G the Faraday cup.

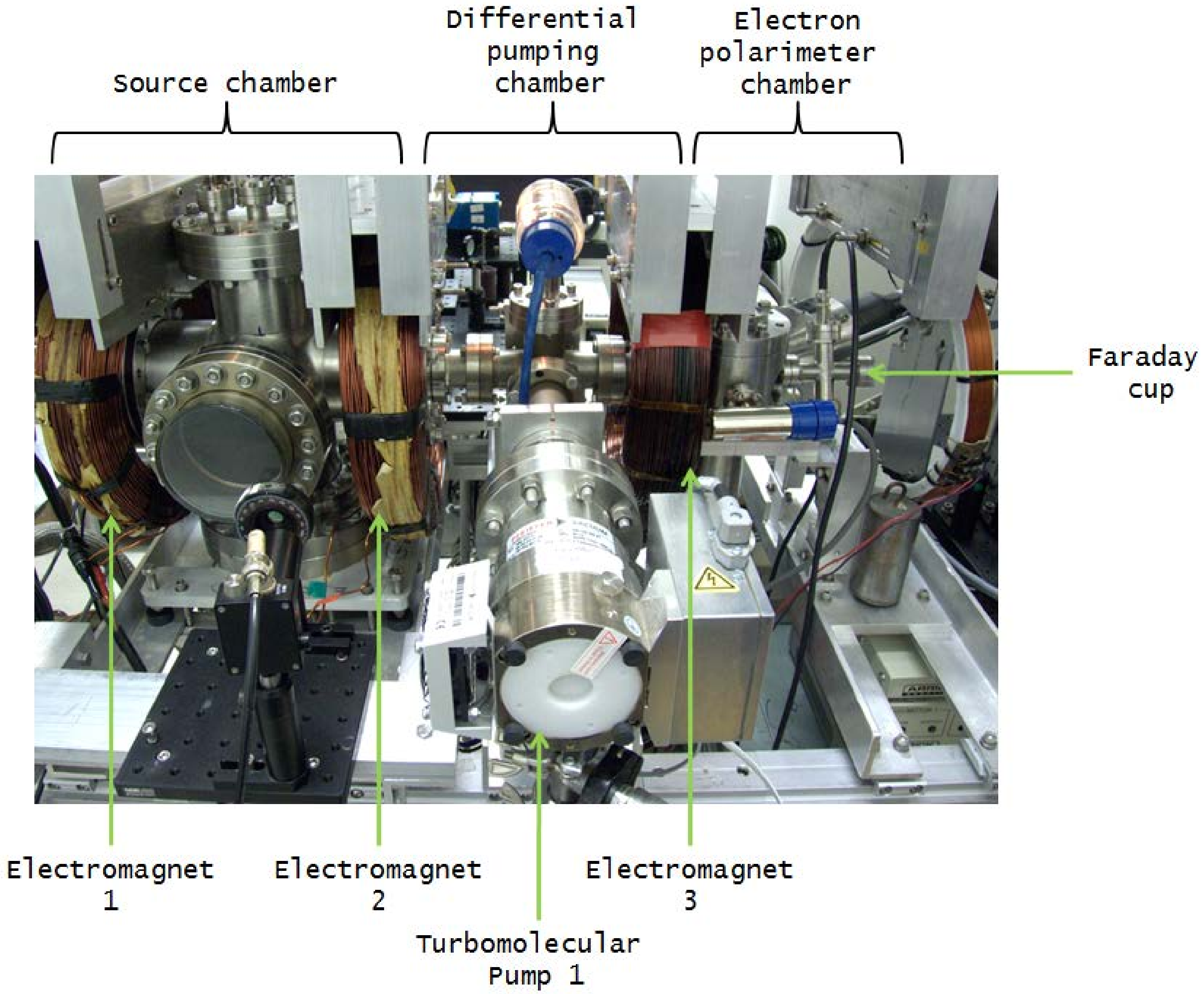

Figure 2.3: Photograph of the apparatus shown in figure 2.2. Shown are the 3 main electromagnets providing the longitudinal field guiding the electron beam, the chamber housing the source, the differential pumping chamber, the electron optical polarimeter, and the chamber in which the Faraday cup is located. (See text for more details.)

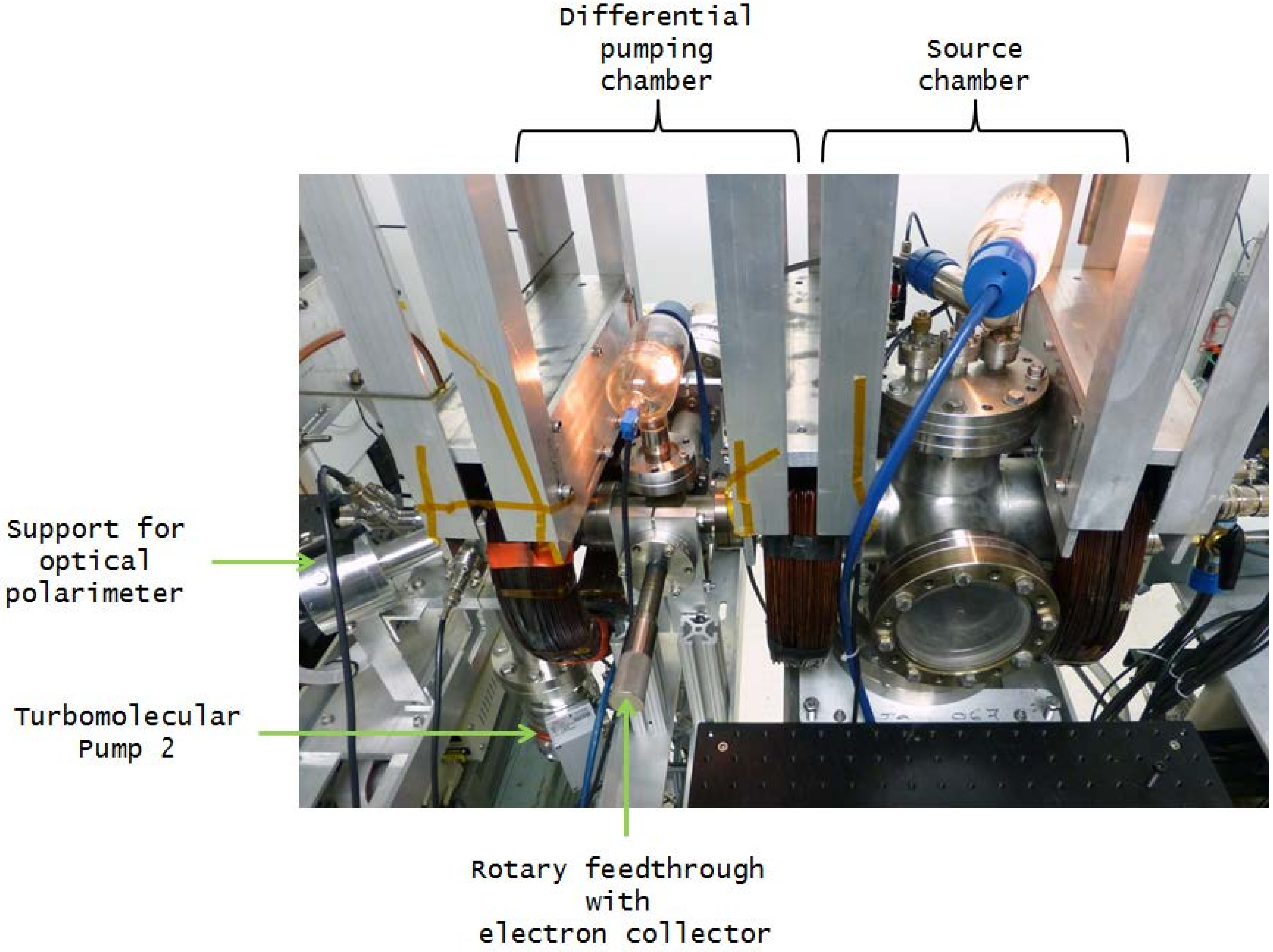

Figure 2.4: Photograph of the apparatus shown in figure 2.2 (continued). This view shows the other side of the apparatus. From this angle, one can see the Conflat flange with the rotary feedthrough used to move the electron collector in the differentially-pumped chamber in and out of the beam's path.

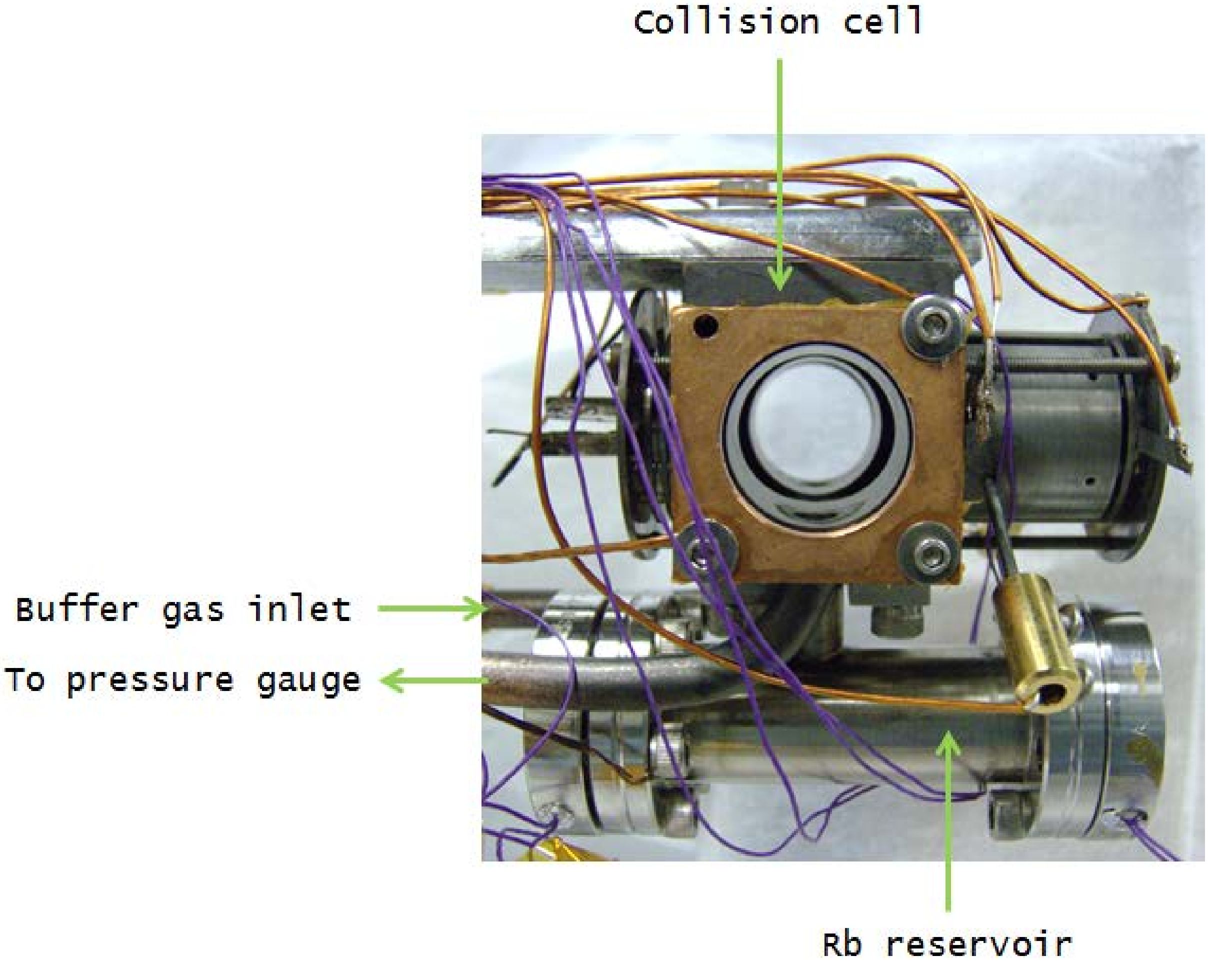

Figure 2.5: The collision cell, rubidium reservoir and electron gun are built as one unit. The tubes connected to the former serve to introduce buffer gas into the system and to monitor its pressure. The electrical connections for the thermionic electron filament are visible at the left.

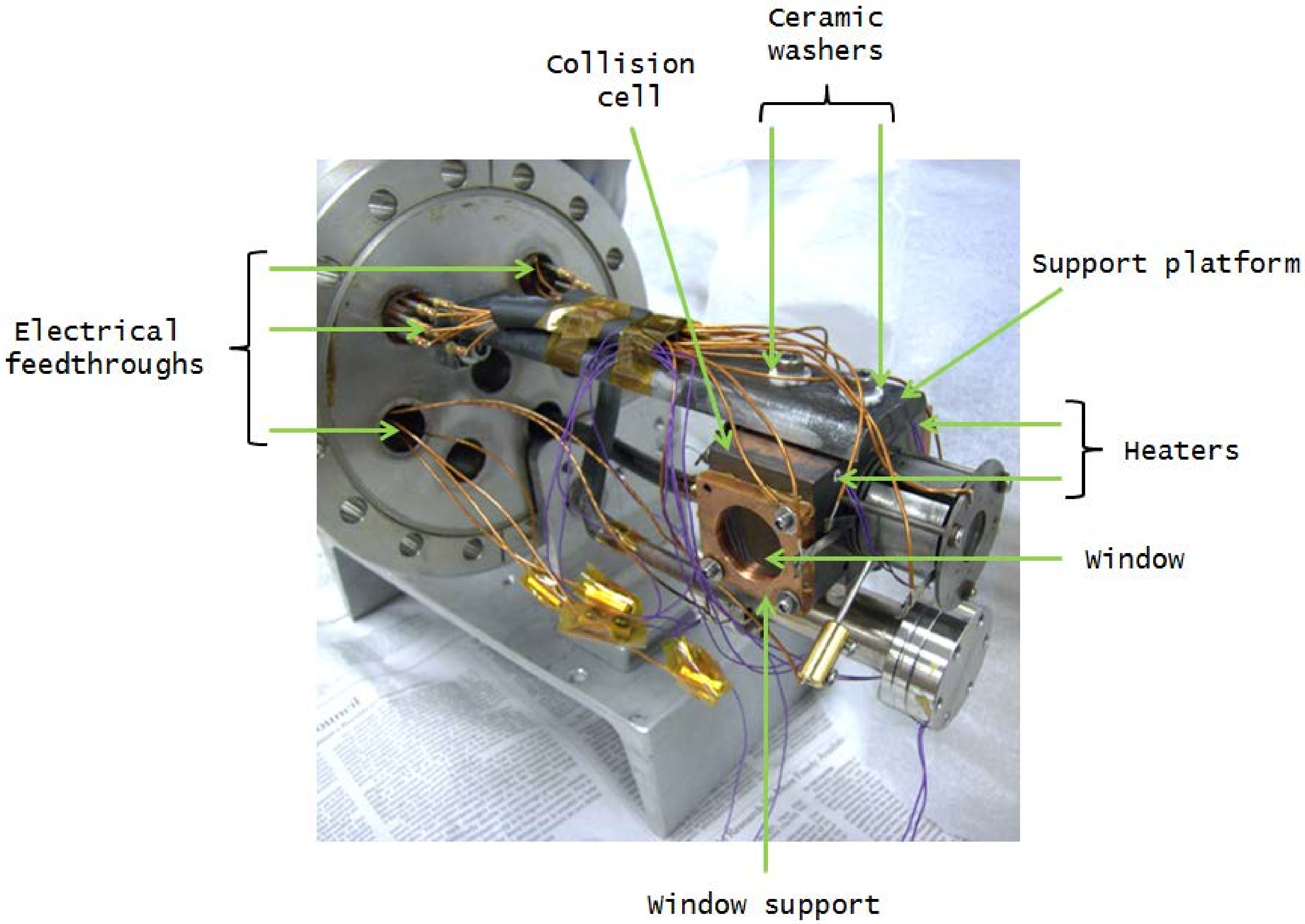

Figure 2.6: The collision cell/ electron gun unit is supported from above by an aluminum platform, which is attached to the 6” Conflat flange. Heaters are embedded in the collision cell. Kapton-insulated wires provide electrical contact between the electrodes and the feedthroughs. Also shown is the window through which the probe beam exits the collision cell. It is kept in place by a copper support bolted to the collision cell. (See text for more details.)

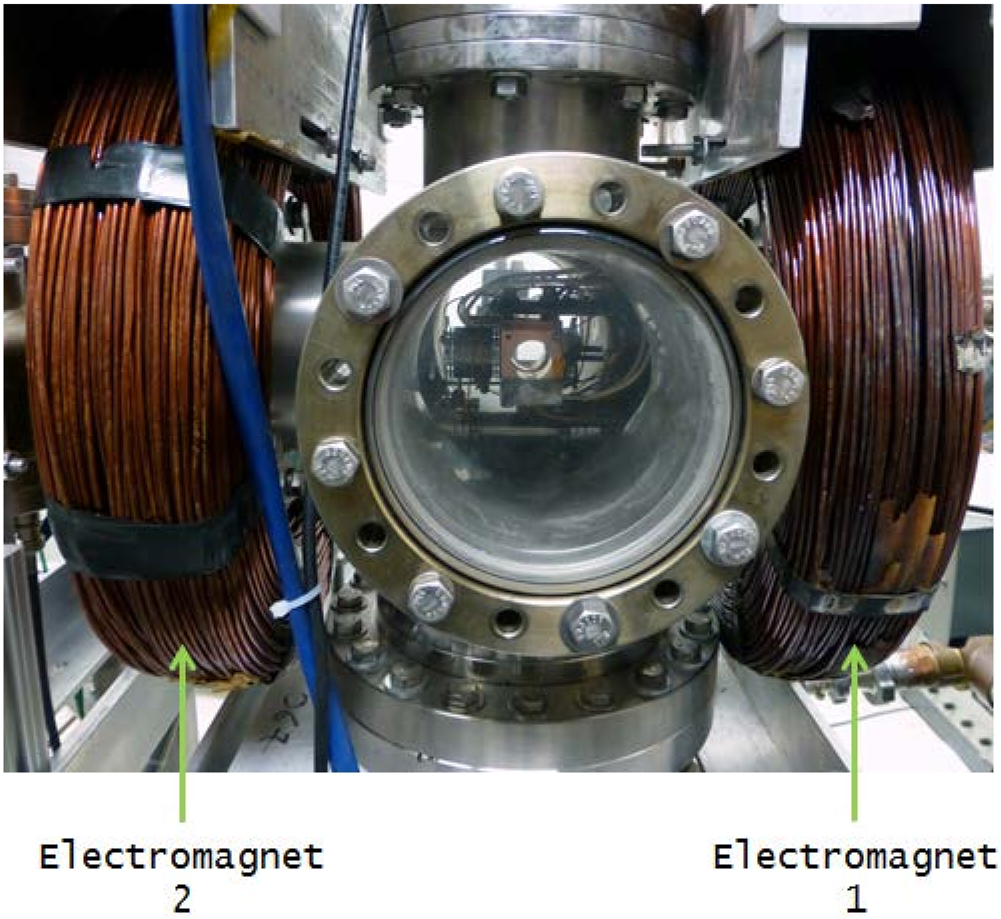

Figure 2.7: The collision cell/electron gun system under vacuum in the Conflat 6” six-way cross.

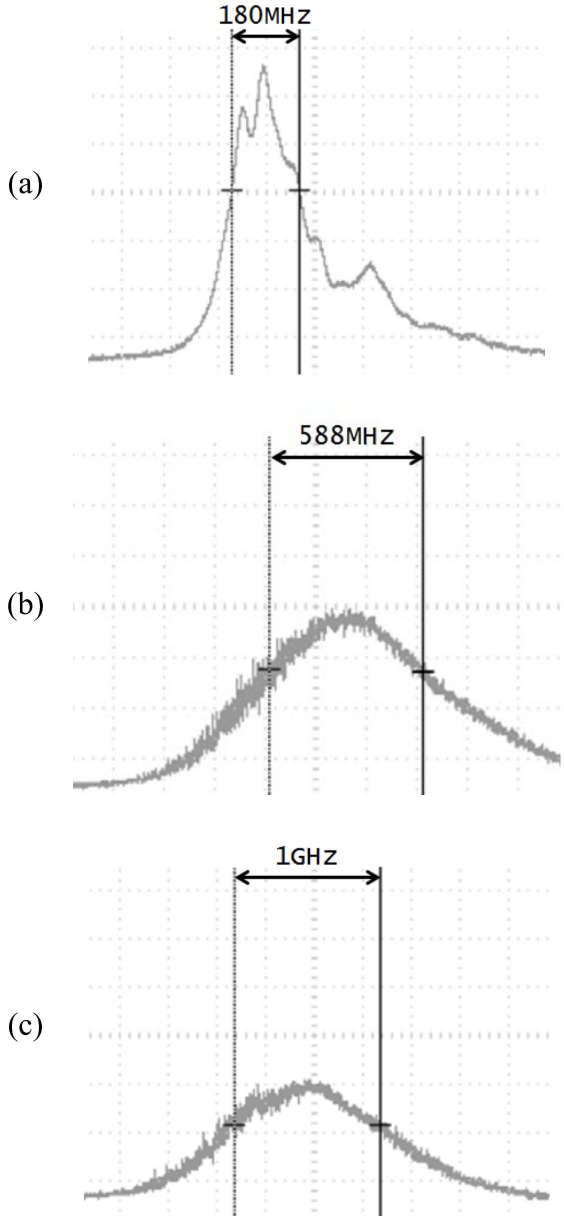

Figure 2.8: Spectral profile of pump beam: (a) unbroadened, (b) broadened with a FWHM of 588 MHz, and (c) broadened with a FWHM of 1 GHz.

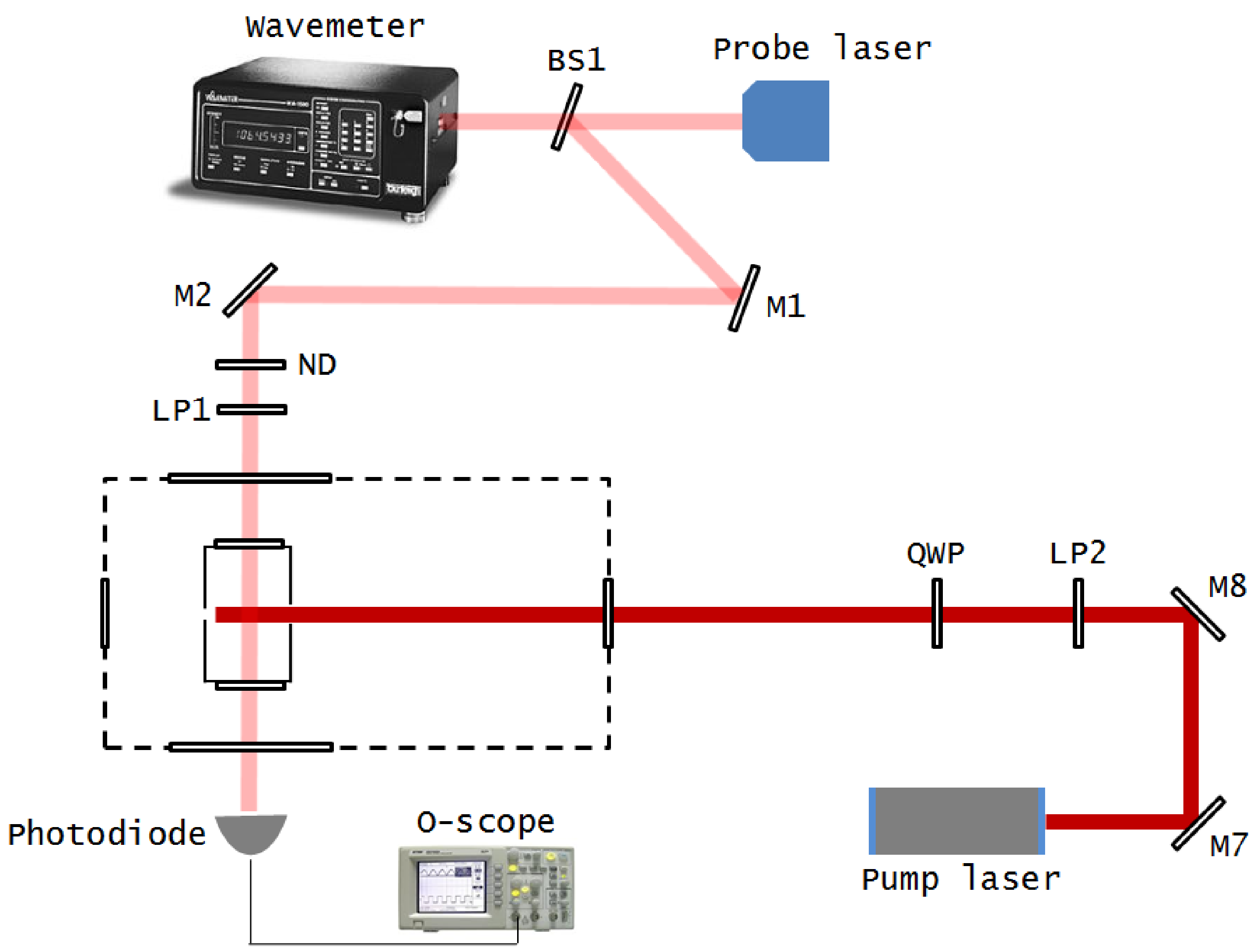

Figure 2.9: Optical layout showing pump laser and probe laser optics when monitoring the thickness of the rubidium vapor. The black dashed-line rectangle represents the vacuum system with its four viewports. The inner chamber is the collision cell. Here, ND refers to a neutral density filter, M1-M8 to mirrors, BS1 to a beam sampler, LP1-LP2 to linear polarizers, and QWP to a quarter-wave plate.

point along the rubidium D1 absorption line by changing the temperature on the laser controller. By applying white noise of different amplitudes (V_{noise}) from a function generator (Stanford Research Systems DS345) to the laser head, the Gaussian profile of the pump beam can also be broadened (see figure 2.8).

As seen in figure 2.9, the pump beam is guided into the vacuum system using a pair of mirrors (M7 and M8). Before entering the first vacuum chamber, it passes through a linear polarizer and a quarter-wave plate to be circularly polarized. This combination of optical elements causes the laser power to drop to ~650 mW. The circularly polarized, 2 mm pump beam passes through a mini-Conflat viewport, and travels along the axis of the vacuum system to the rubidium vapor in the collision cell. This viewport was obtained from one of the cabinets in the laboratory; its manufacturer is unknown. During this study it was found that the glass affects right- and left-circularly polarized 795nm light differently. The viewport reflects a portion of the pump light, which retraces its path to the laser housing and splashes next to its output aperture. Visual inspection of this reflected beam spot reveals that its intensity is different for right- and left-circularly polarized light. Moreover, if linearly-polarized pump light is sent through the vapor, the rubidium atoms are expected to align with the quantization axis instead of undergoing orientation as in the case with circularly polarized pump light. Both the rubidium and electron polarizations, P_{Rb} and P_e, would be zero under such circumstances. The opposite was actually observed. Linearly polarized pump light still yielded nonzero P_e. As can be seen in figure 2.10, these effects cause the polarization of the electron beam obtained with our source to have different magnitudes for the two circular polarizations of the pump beam.

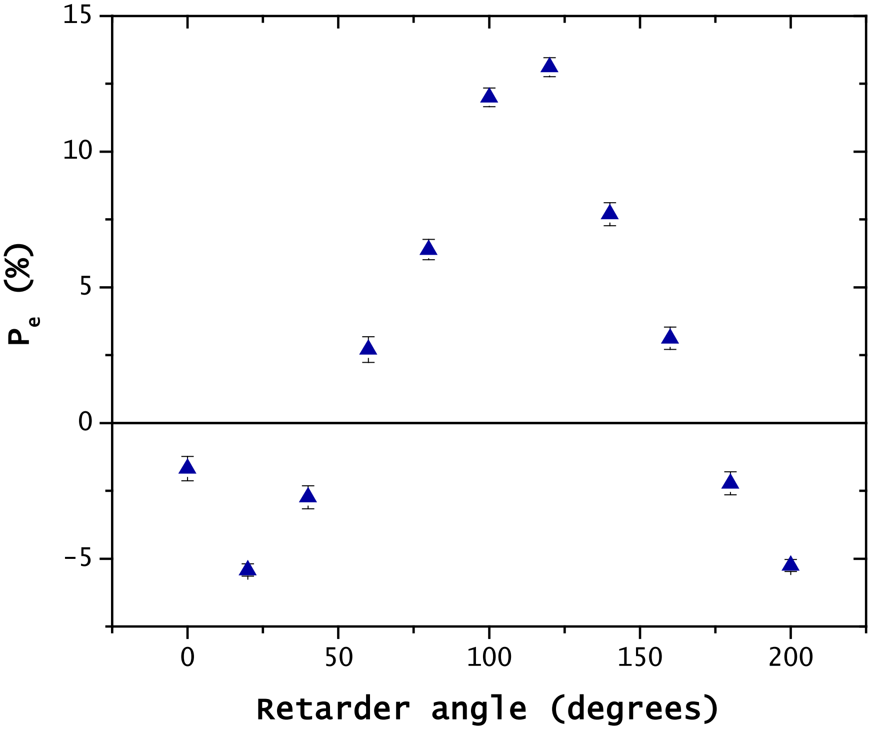

Figure 2.10: The viewport has adverse effects on the performance of the system, causing the electron polarization to have different magnitudes for the two circular polarizations of the pump light. Under the current experimental conditions, the pump light is polarized circularly by setting the retarder at 20^o and 110^o.

A flip mount holding a mirror (see figure 2.11) has been placed after the laser. When the bandwidth and wavelength are to be measured, the mirror is flipped up to sendthe pump beam to a spectrum analyzer (Coherent model 240) and to a wavemeter (Angstrom WS-6). The flip mount is retracted to let the beam through to the collision cell.

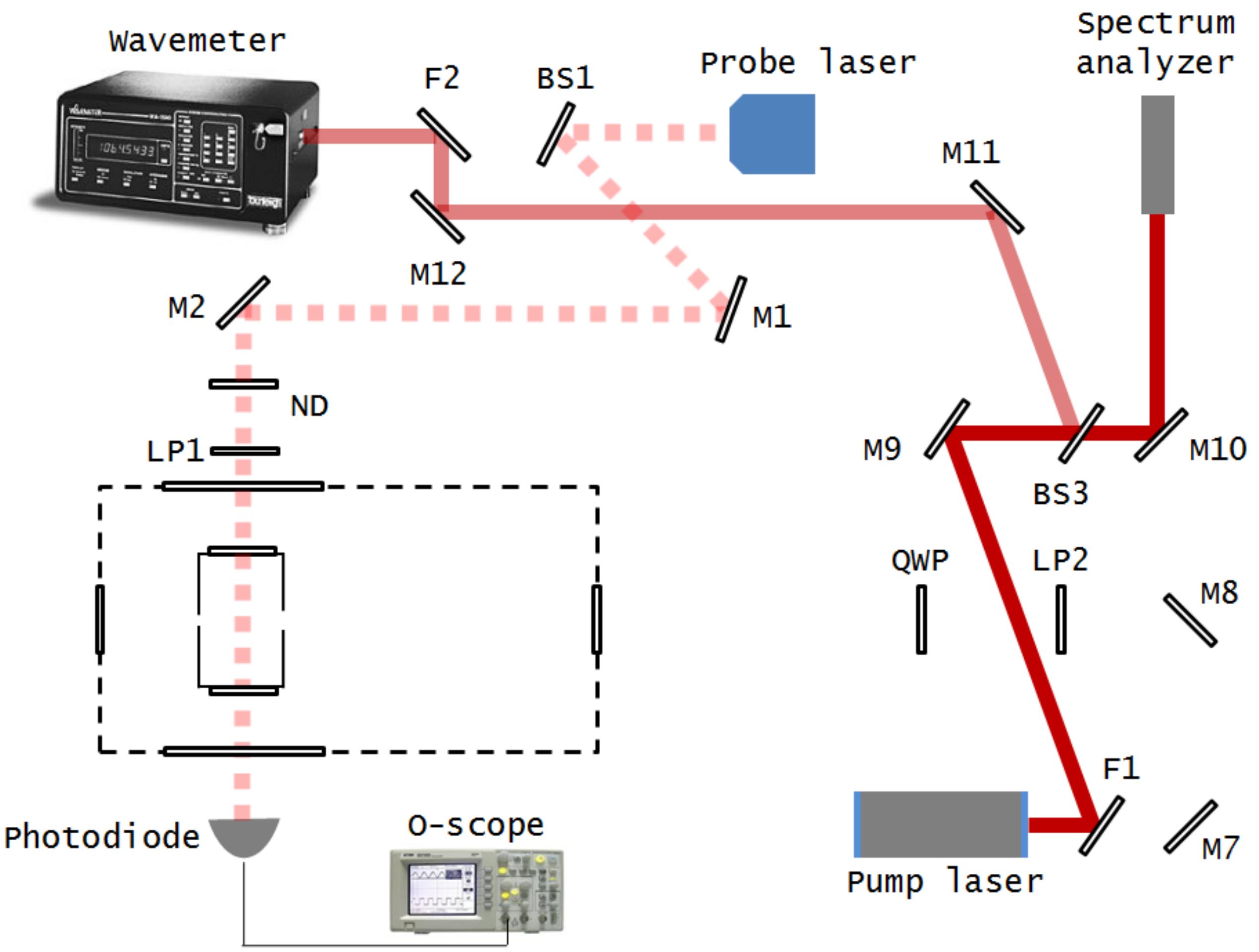

Figure 2.11: Optical layout when monitoring the wavelength and spectral broadening of the pump light. To this end, flip mirrors F1 and F2 are positioned in the path of the pump beam. The beam sampler BS3 allows a weaker portion of the pump light to travel to the wavemeter while the main part makes its way to the spectrum analyzer. The red dashed-line represents the probe beam. When flip mirror F2 is up, the portion of the probe beam which usually travels to the wavemeter (see figure 2.9) is blocked.

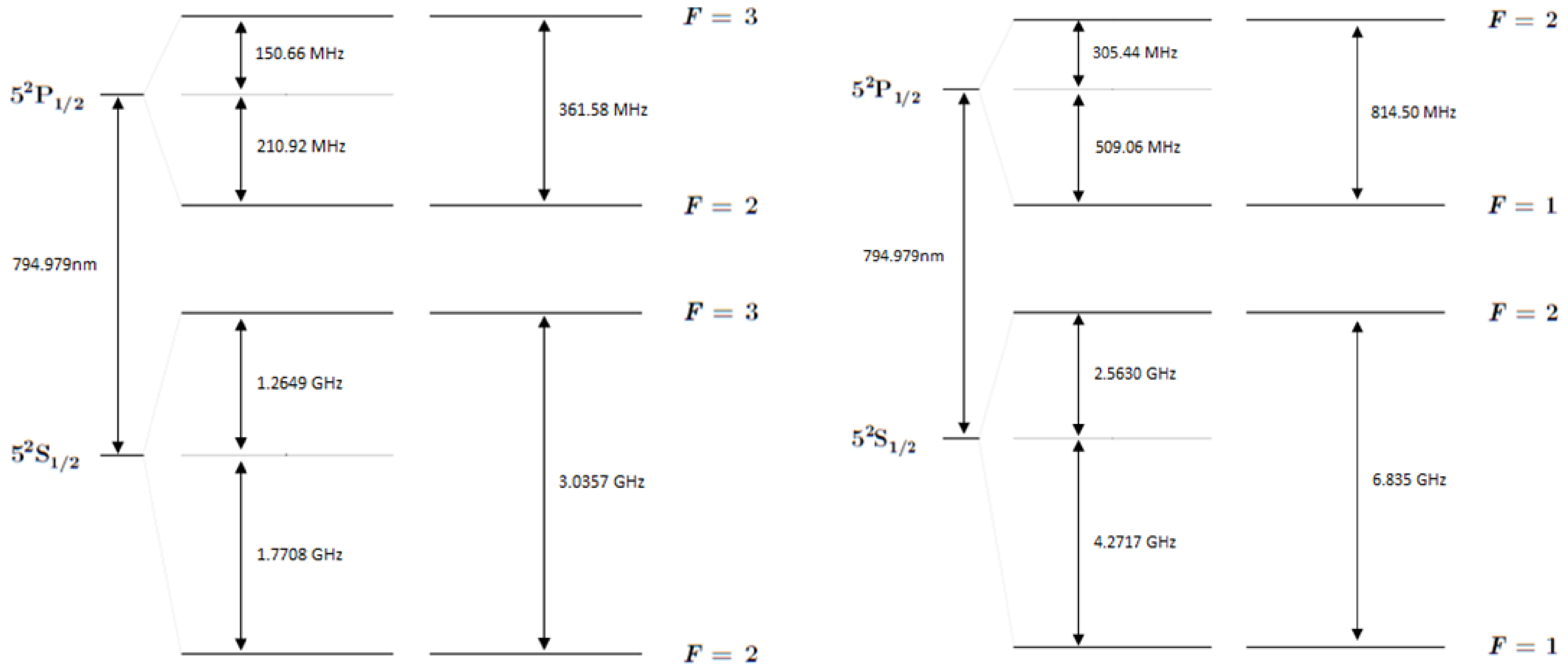

(a) (b)

Figure 2.12: (a) Rubidium-85 D1 transition hyperfine structure with frequency splitting between the hyperfine energy levels, and (b) rubidium-87 D1 transition hyperfine structure with frequency splitting between the hyperfine energy levels (reproduced from references [133] and [107]). (Not drawn to scale.)

2.2.2 Probe optics

The probe optics help us to monitor the rubidium vapor thickness, and when possible, its polarization. In the majority of experimental runs, I used the optical configuration in figure 2.9 to estimate the alkali density. The probe laser (New Focus Vortex 6000) outputs ~7mW of power. Its bandwidth is about 200kHz. Its wavelength can be modulated from 794.9122nm to 795.0995nm by applying a periodic sawtooth signal from a function generator (HP 3311A) to the laser controller. Absorption profiles related to the D1 transition of the rubidium vapor can be gathered in such a way.

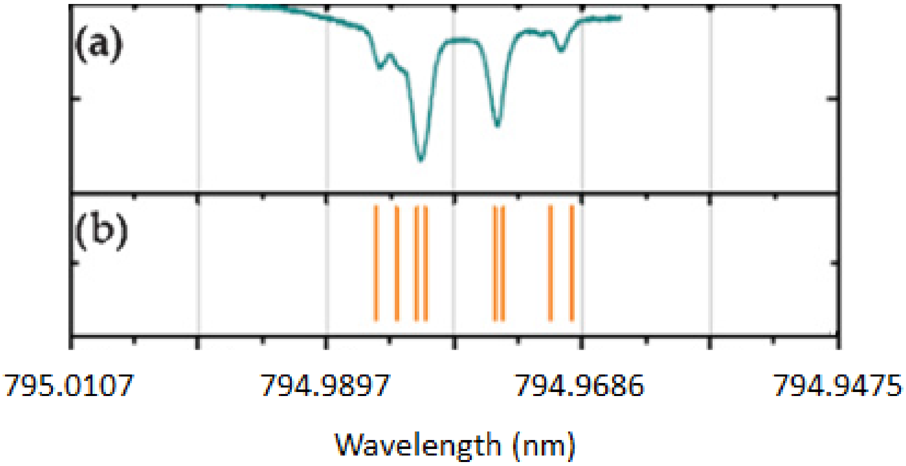

Figure 2.13: (a) Absorption profile of rubidium from a reference cell. (b) The positions of the hyperfine ground (g) to excited (e) level transitions of Rb; from left to right: 87Rb $F_g = 2 \rightarrow F_e = 1$, 87Rb 2 → 2, 85Rb 3 → 2, 85Rb 3 → 3, 85Rb 2 → 2, 85Rb 2 → 3, 87Rb 1 → 1, 87Rb 1 → 2. See figure 2.12 for additional details on the rubidium energy levels. (adapted from [64])

The probe beam first interacts with a beam sampler (BS1) (see figure 2.9). The transmitted part of the beam is sent to the wavemeter. The reflected portion is directed into the collision cell by two mirrors (M1 and M2). Before going into the vacuum system, the beam passes through a neutral density filter followed by a linear polarizer. This arrangement attenuates its power to ~20 μW. The probe intensity is kept low so that it does not affect the polarization of the vapor. Both the vacuum chamber and the collision cell have viewports on their sides through which the beam can enter and exit. After interacting with the rubidium vapor, the probe beam emerges from the vacuum system. Its intensity is recorded by a photodiode (Thorlabs DET 36A) whose signal is captured on an oscilloscope (Tektronix TDS 2014B). Figure 2.14 shows an example of an absorption profile recorded using such a setup.

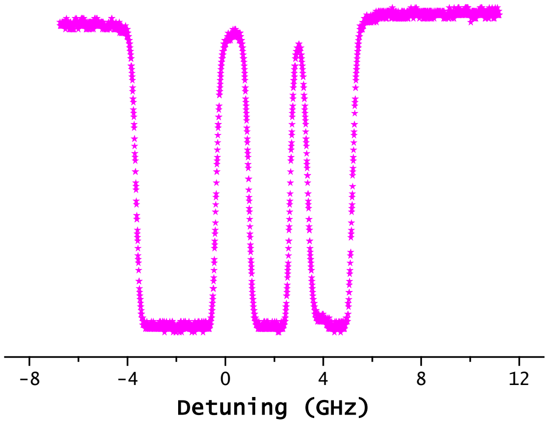

Figure 2.14: Oscilloscope signal showing the D1 absorption profile of rubidium vapor in the collision cell. Detuning is with respect to the Rb D1 line center. The rubidium density was about (4×10^{12}) atoms/cm^3.

When the probe beam is used to measure the rubidium density and polarization by the diamagnetic and paramagnetic Faraday effects [59, 60, 61], the optical components are configured as shown in figure 2.15. The beam is guided along the axis of the vacuum chambers, antiparallel to the pump beam, by a set of six mirrors. Along the way, it passes through an optical chopper (Thorlabs MC1000A) and a linear polarizer. It enters the

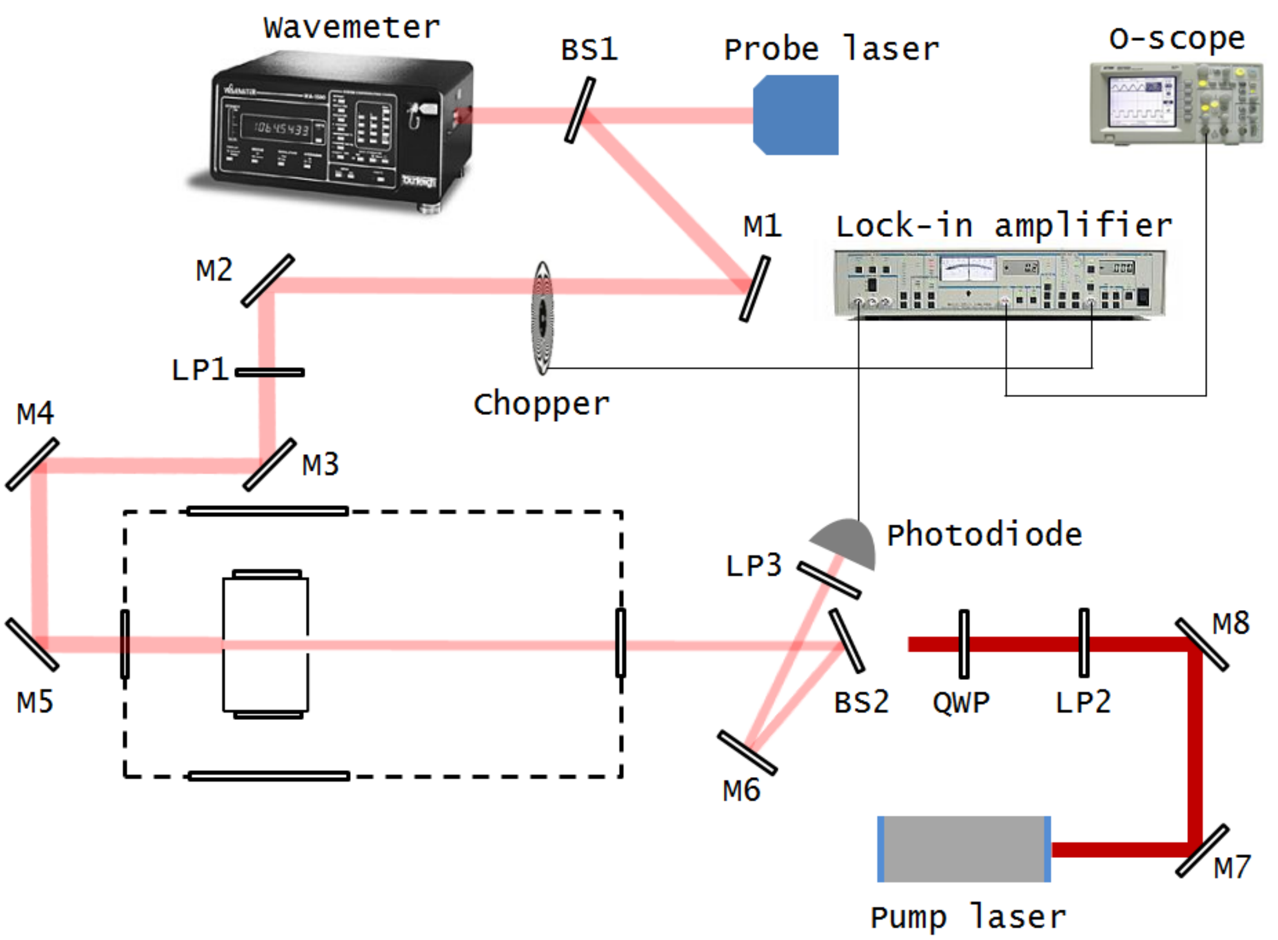

Figure 2.15: Optical layout when measuring the density of the rubidium vapor and its polarization by the Faraday effect. Here, M1-M8 refer to mirrors, BS1-BS2 to beam samplers, LP1-LP3 to linear polarizers, and QWP to a quarter-wave plate.

collision cell, interacts with the rubidium vapor, and emerges from the vacuum system. It then encounters a beam sampler. The reflected part of the beam is directed to a linear polarizer and a photodiode by a mirror. By using the combination of linear polarizer and photodiode, I can determine the angle of rotation of the plane of polarization of the probe beam after it has interacted with the rubidium vapor. To this end, the signals from the photodetector and the optical chopper are fed into a lock-in amplifier (Stanford Research Systems SR510). The output of the latter is read on an oscilloscope (Tektronix TDS 2024B).

2.2.3 Vacuum system

Vacuum schematics of the apparatus are shown in figures 2.16, 2.17 and 2.18. The source chamber is a 6” Conflat six-way cross. Conflat viewports (zero profile 7056 glass, nominal flange diameter: 6”) are located on the sides of the chamber so that the probe laser can access the collision cell. An Edwards “Diffstack” diffusion pump (MK2 series, 700 L/s pumping speed) is attached at the bottom of the six-way cross. Convectron and ion pressure gauges are fitted at the top. These elements are critical in monitoring the pressure inside the cross when buffer gas is admitted into the collision cell during experimental runs. In order to prevent excessive backstreaming of diffusion pump oil into the chamber, the chamber pressure must be maintained below 10^{-3}Torr (and, preferably, below 10^{-4} Torr). A differentially pumped 2.75” Conflat six-way cross is attached to the final port. The two chambers are separated by a copper disk with a 5 mm aperture to allow the electron beam through.

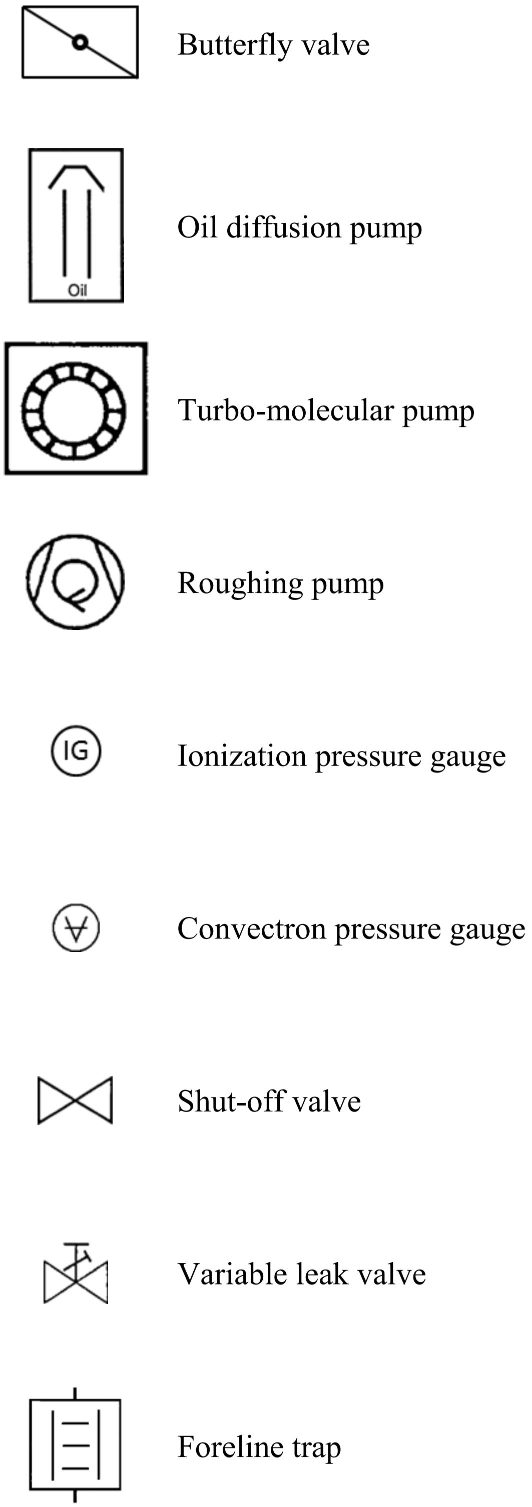

Figure 2.16: Symbols used in the following two figures, which are vacuum schematics of the apparatus.

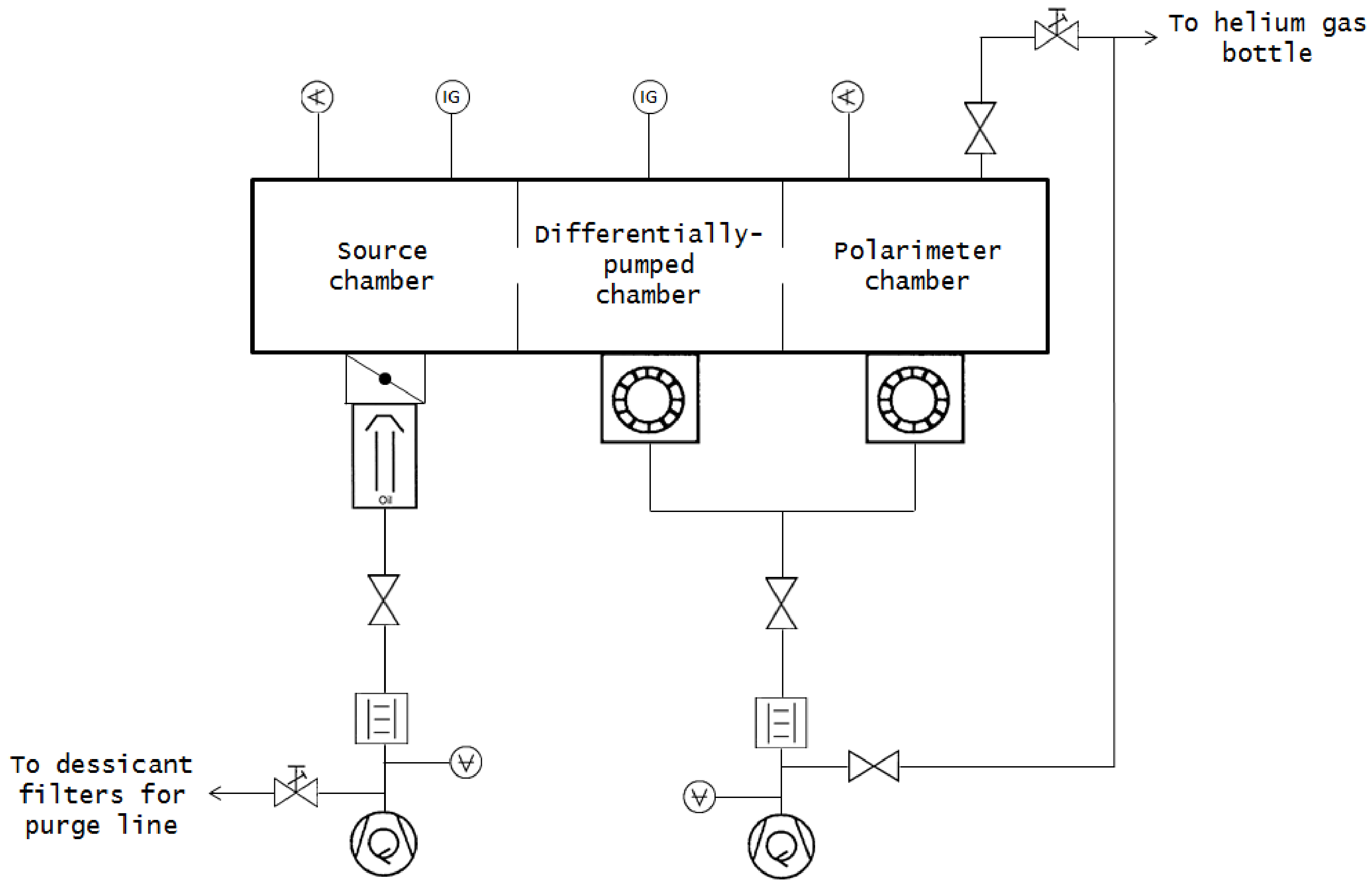

Figure 2.17: Vacuum schematic of the main apparatus. The purge line was based on reference [79].

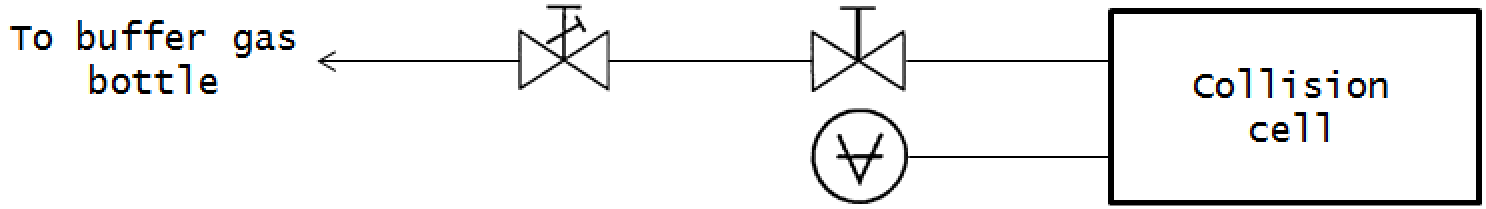

Figure 2.18: Vacuum schematic of the collision cell. The cell accommodates two gas lines. A Convectron gauge is attached to one, and buffer gas is introduced into the interaction region via the other.

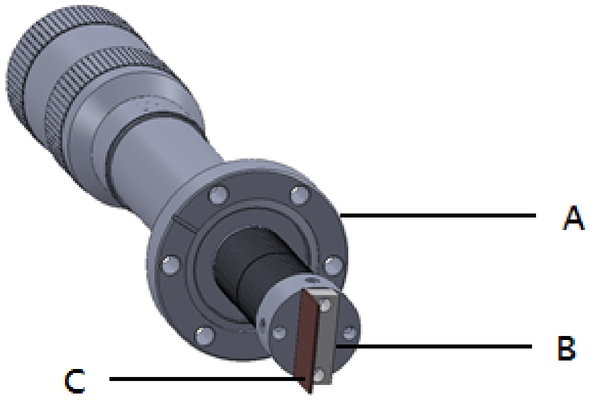

Figure 2.19: Electron collector in the differentially-pumped chamber. Shown are the Conflat flange A with its rotary feedthrough, the rectangular macor cuboid B, and the copper electrode C.

Besides an ion pressure gauge, the differentially-pumped chamber contains an electron collector on a Conflat rotary motion feedthrough (See figures 2.2, 2.4 and 2.19). The collector consists of a copper electrode, ~4 x 2 x 0.1 cm. The latter is electrically isolated from the rotary motion feedthrough, which is at ground. This isolation is achieved by fastening the copper electrode to a rectangular cuboid made of Macor, ~4 x 2 x 0.8 cm. The electrode is connected to a single-ended, grounded shield coaxial feedthrough on a 2.75” Conflat flange at the bottom of the six-way cross. Thus, the copper electrode can be linked to an ammeter from the outside. It is used to monitor the electron beam current reaching the differentially-pumped chamber while the positions of the source’s electromagnets are being optimized for electron transport. Once alignment of the electromagnets is complete, the collector can be retracted to let the beam through to the optical electron polarimeter.

The polarimeter is attached to the differentially-pumped chamber. It contains the elements to determine the polarization of the electron beams as well as the electron current. The vacuum in the differentially pumped chamber and the polarimeter is maintained by turmolecular pumps (Pfeiffer Vacuum HiPace 80). It must be noted that these pumps cannot handle a magnetic field greater than 50G. Since the field caused by the solenoidal guiding magnets in the vicinity of the apparatus exceeds this value, the pumps were positioned at least 40 cm away from the longitudinal axis of the vacuum system (See location of pumps in figures 2.3 and 2.4), in a region where they experienced a field of ~20 G.

Two Welch 1397 (pumping speed: 500 liters per minute) are used as backing pumps for the diffusion and turbomolecular pumps. The latter employ the same backing pump. The base pressure of the apparatus is ~5 x 10^{-7} Torr. When the collision cell is filled with 200 mTorr of gas, the pressure above the diffusion pump can be as high as 10^{-3} Torr.

2.2.4 Electromagnets

Three main electromagnets provide an axial magnetic field along the apparatus (see figures 2.3 and 2.7). From here on, I will designate those before and after the source as 1 and 2, and the one after the differentially-pumped chamber as 3. They were built by Levi Neukirch and Eric Norrgard for the earlier prototype discussed above, and were adapted to the present setup. Owing to lack of proper documentation on their part, work had to be undertaken to determine the physical characteristics of these electromagnets, especially with regard to their dimensions and number of turns per unit length. To this end, the longitudinal magnetic field produced by each electromagnet due to different applied currents was recorded with a Hall probe placed on axis at a distance x_1 from the coil (see figure 2.20 and Table 2.1). Figure 2.21 shows the results of this investigation. Using the slopes of the lines of best fit of these graphs as well as the equation describing the axial magnetic field B of a finite, air-core solenoid [65], the number of turns per unit length, n, of the electromagnets could be determined:

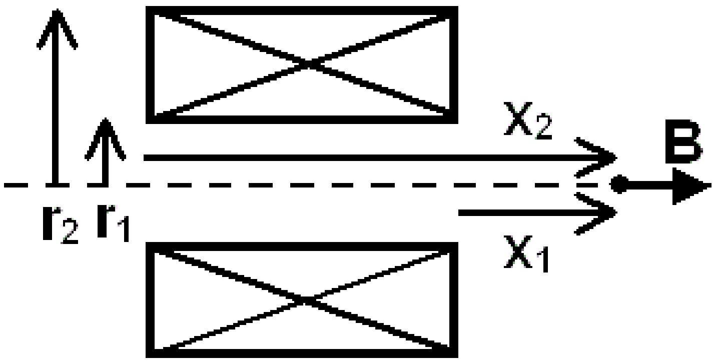

Figure 2.20: Definition of the parameters r_1, r_2, x_1 and x_2 used in the text.

Table 2.1: Physical properties of the electromagnets. (See figure 2.20 for more details.)

Electromagnet	**r1 (cm)**	**r2 (cm)**	**x1 (cm)**	**x2 (cm)**	**n (turns/cm)**
1	11.0	15.3	0	6.5	45
2	11.0	15.3	0	6.5	42
3	11.0	15.3	10.0	16.5	52

$$B = \frac{\mu_o in}{2(r_2 - r_1)} \left\{ x_2 \ln\left(\frac{\sqrt{r_2^2 + x_2^2} + r_2}{\sqrt{r_1^2 + x_2^2} + r_1} \right) - x_1 \ln\left(\frac{\sqrt{r_2^2 + x_1^2} + r_2}{\sqrt{r_1^2 + x_1^2} + r_1} \right) \right\}. \tag{2.1}$$

Here, μ_o is the permeability constant and i the current supplied to the electromagnet. The other parameters in equation (2.1) are defined in figure 2.20. The physical characteristics obtained for the three electromagnets are tabulated in Table 2.1. Using these numbers, equation (2.1) and the superposition principle [66], we can determine how the axial magnetic field varies along the apparatus. For example, figure 2.22 shows how

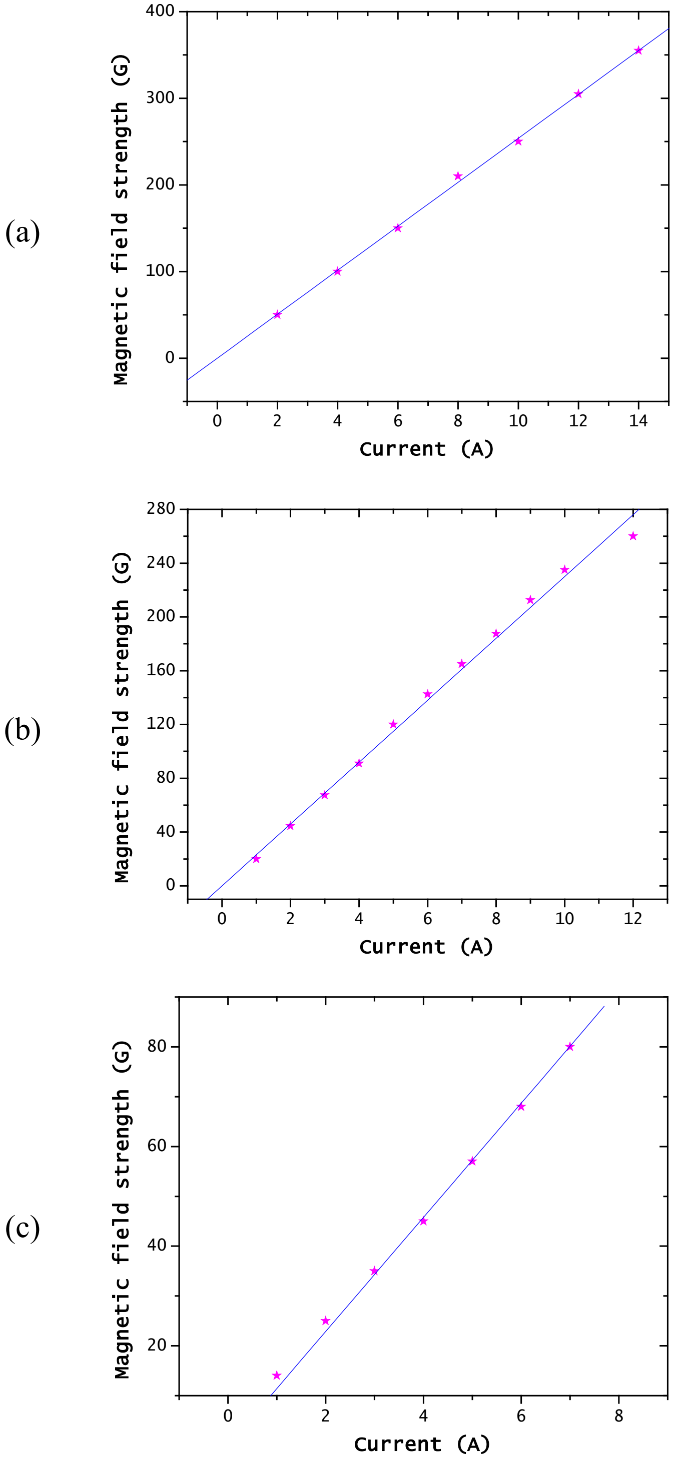

Figure 2.21: Magnetic field strength recorded for different applied currents through (a) electromagnet 1, (b) electromagnet 2, and (c) electromagnet 3. The equations describing the lines of best fit are (a) $B = (25.4 \pm 0.1) \cdot I$, (b) $B = (23.0 \pm 0.3) \cdot I$, and (c) $B = (11.4 \pm 0.1) \cdot I$. (See text for details.)

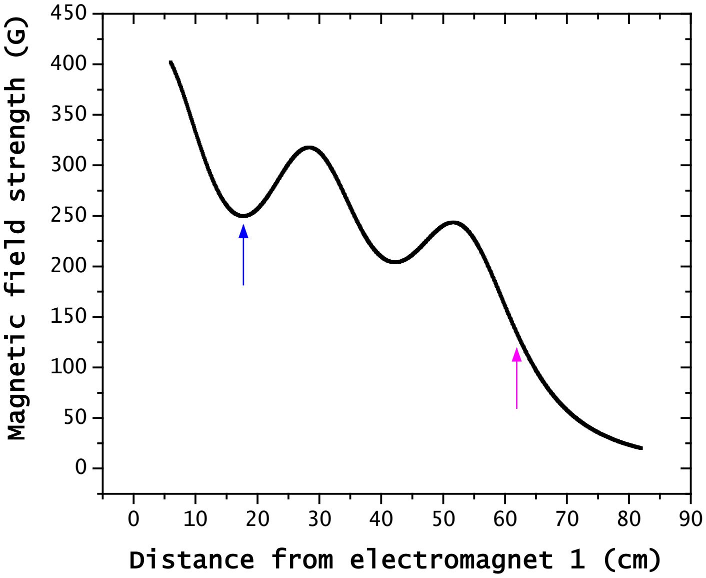

Figure 2.22: Variation of magnetic field strength along the apparatus. Electromagnet 1 refers to the one before the source. The blue and magenta arrows indicate the approximate positions of the collision cell and of the target cylinder in the optical electron polarimeter, respectively.

the magnetic field changes as a function of distance from electromagnet 1 for a typical set of currents employed during experimental runs corresponding to 15A through 1 and 2, and 6A through 3. These are provided by a HP 62698 DC power supply, a Sorensen Nobatron DCR40-20A, and a Sorensen Nobatron DCR80-5A.

The electromagnets need to be aligned to maximize the electron current reaching the Faraday cup. The positions of electromagnets 1 and 2 are adjusted first. They provide the longitudinal magnetic field guiding the free electrons along the axis of the source chamber and into the differentially-pumped region. Before tuning these electromagnets, the electron collector on the Conflat rotary motion feedthrough in the latter chamber is placed in the path of the electron beam, and the current reaching it is monitored. The ammeter is likely to read zero with the magnets misaligned. The supports holding the electromagnets are on rails, which allow the former to slide along the axis of the apparatus up until they run into a vacuum chamber. The positions of electromagnets 1 and 2 can thus be adjusted by shifting them backward and forward while watching for electrons to make it to the collector, and the ammeter reading is non-zero. The supports have also been designed to let the electromagnets to be lifted slightly, perpendicular to the axis of the apparatus. The final step in alignment involves raising the electromagnets slowly to see if this increases the current reaching the electron collector. Once this is accomplished, the electron collector is retracted, and the current on the Faraday cup is monitored next. The position of electromagnet 3 is now fine-tuned to get the most electrons onto the Faraday cup. Finally, slight adjustments are made to electromagnets 1 and 2 to see whether they increase the Faraday cup current further. If this step only affects the electron beam adversely, the magnets are brought back to their optimal position. The magnetic field along the system is now properly aligned.

2.2.5 Source

The electron gun and the collision cell for the prototype of the polarized electron source are built as one unit. I will first focus on the collision cell (see figure 2.23). It is made of oxygen- free copper. Its dimensions are ~2 x 1.1 x 1.26”. Along the path of the probe laser, as shown in figure 2.23, it is 2” long, and it has a hole ~0.73” in diameter drilled transversely through it. Uncoated sapphire windows, 1” in diameter, are located on either side (see figures 2.6, 2.24 and 2.28). They allow the probe beam to enter and exit the collision cell from the side. The windows are pressed against silicone O-rings

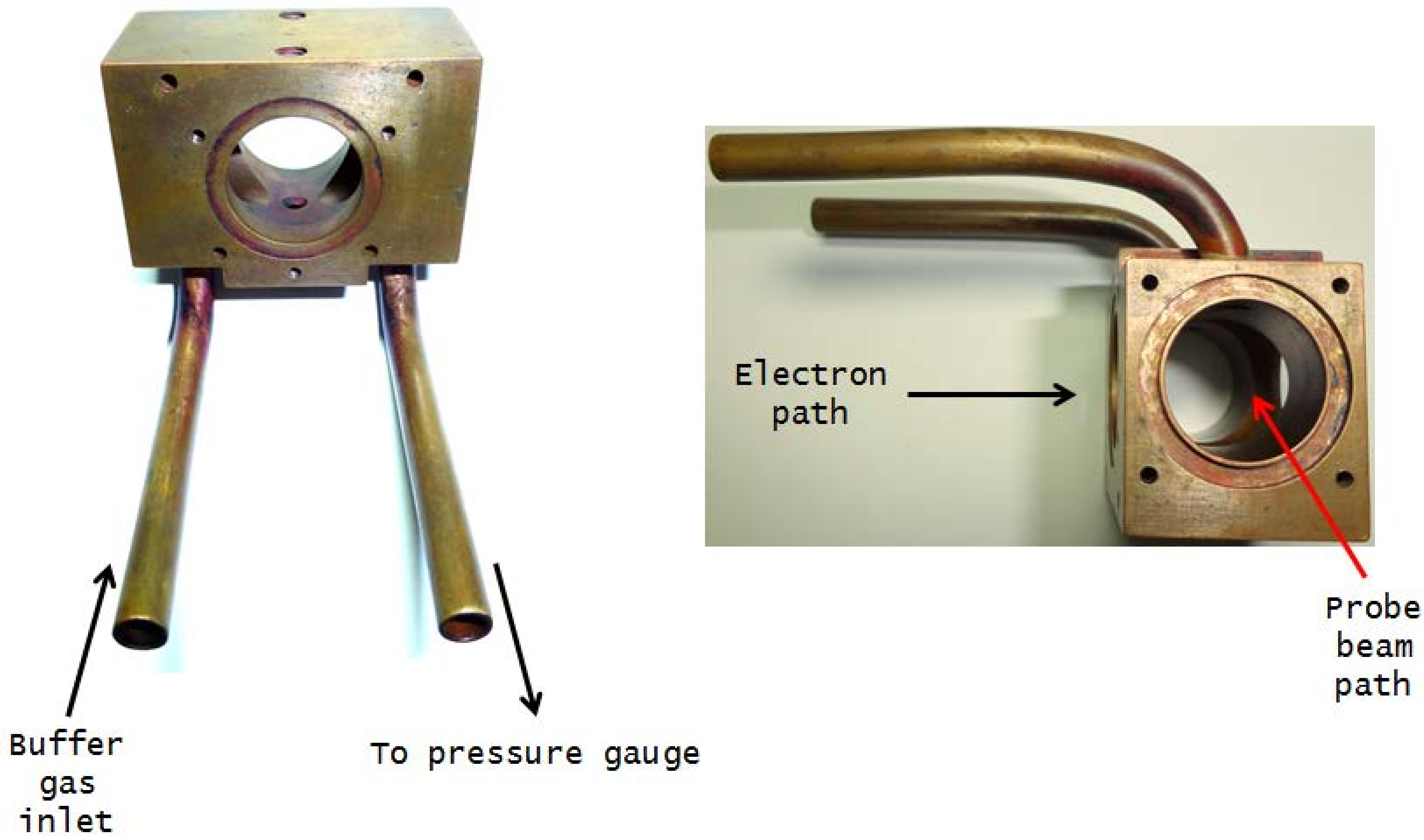

Figure 2.23: The main chamber of the collision cell. Shown are the openings along the electrons’ and probe beam’s paths. (See text for more details.)

(Mcmaster-Carr AS568A Dash number 019). This arrangement is held in place by a square copper support bracket with 1.1” sides. It has a ~0.72” hole drilled through the middle to expose the sapphire window but also four holes, ~0.2” in diameter, in its corners. The support can thus be bolted to the collision cell.

Along the path of the electrons (see figure 2.23), the collision cell is 1.1” long, and it has a hole, ~0.8” in diameter, drilled through it. There are two tubular extensions from the copper rectangular cuboid. One of these allows the collision cell to be filled with buffer gases of interest during experimental runs. The other is connected to a Convectron pressure gauge that monitors the pressure inside the collision cell. At a temperature of $(25 \pm 5)\,^{o}\mathrm{C}$, pressure readings have an uncertainty of ±3% [67].

A Conflat nipple (nominal flange O.D 1.33”) is attached at the bottom of the collision cell by a 6mm ID aluminum tube. The former acts as the rubidium reservoir. A broken 1g alkali ampoule (Strem Chemicals, 1g, 99+% purity, pre-scored ampoule, product number: 93-3736) is stored in it during experimental runs. The collision cell and the reservoir are heated by a total of six cartridge heaters (Mcmaster-Carr, OD: 0.125”, length: 1.25”, 50W, 0.42A, product number: 8376T22). The heaters fit snugly into holes drilled through the collision cell and in the flanges sealing the Conflat nipple (see figure 2.24). The tight fit allows heat to be dissipated rapidly to the surroundings. The rubidium reservoir and the collision cell contain two and four heaters respectively. The unit is also fitted with two type-K thermocouples (Accu-Glass, product number: 100850). The locations of the thermocouples are also shown in figure 2.24. The temperature of the collision cell and of the reservoir can thus be monitored during experimental runs.

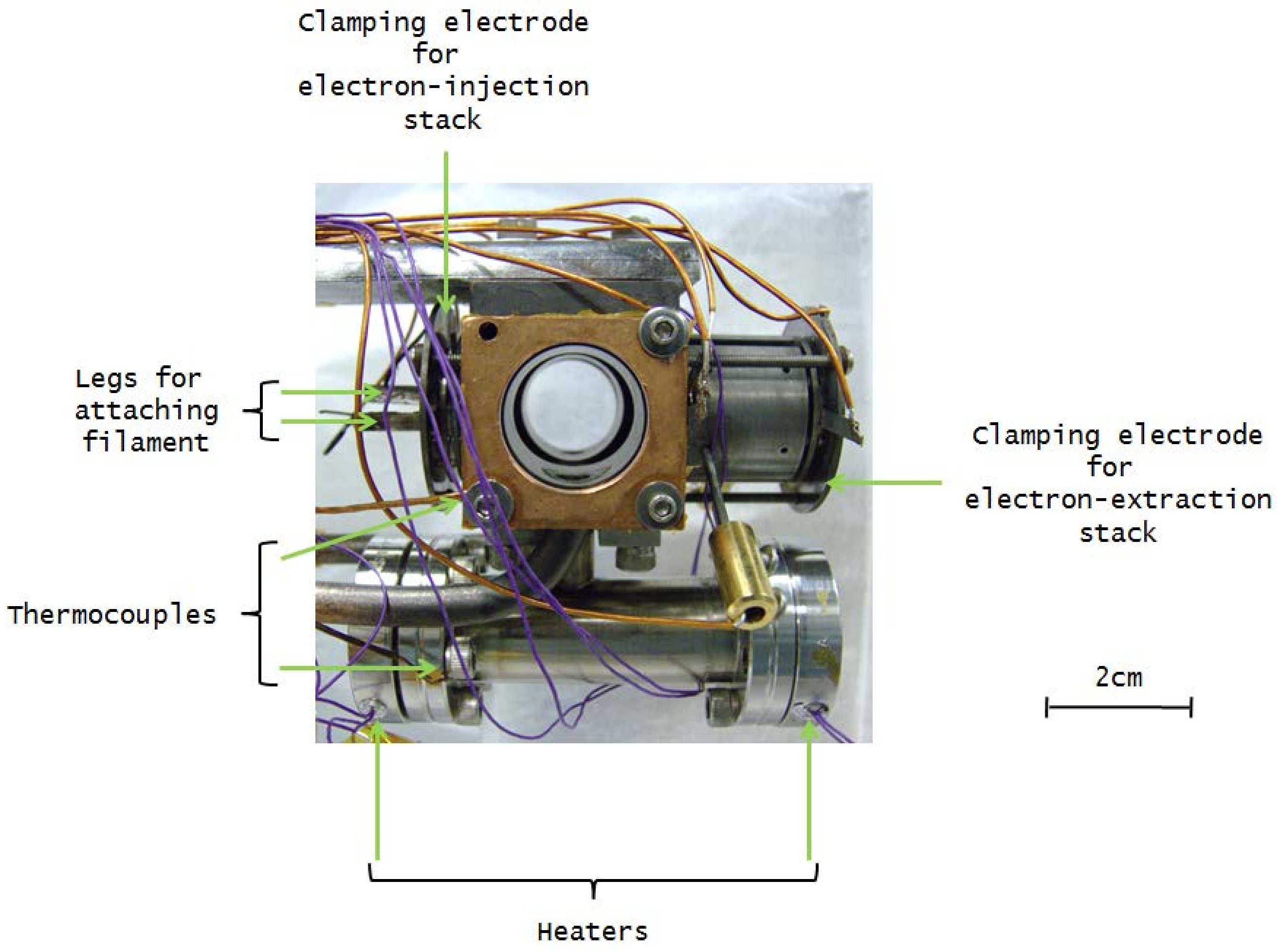

Figure 2.24: Location of thermocouples, reservoir heaters, and legs to which the tungsten filament is spot-welded are shown on the collision cell/electron gun unit.

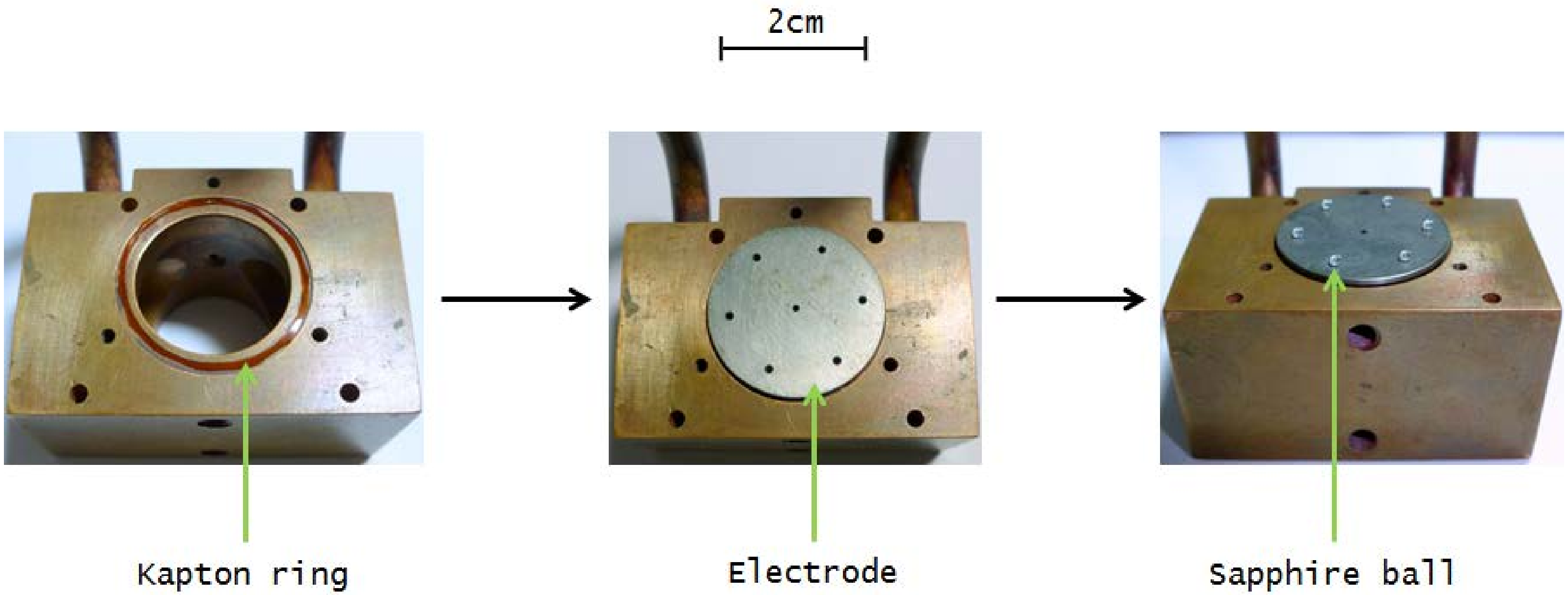

Figure 2.25: Electron gun assembly. The Kapton ring prevents the electrode from being in electrical contact with the collision cell. After the sapphire balls have been put in place, another electrode can be positioned on top. This arrangement allows electrodes making up the electron gun to be stacked.

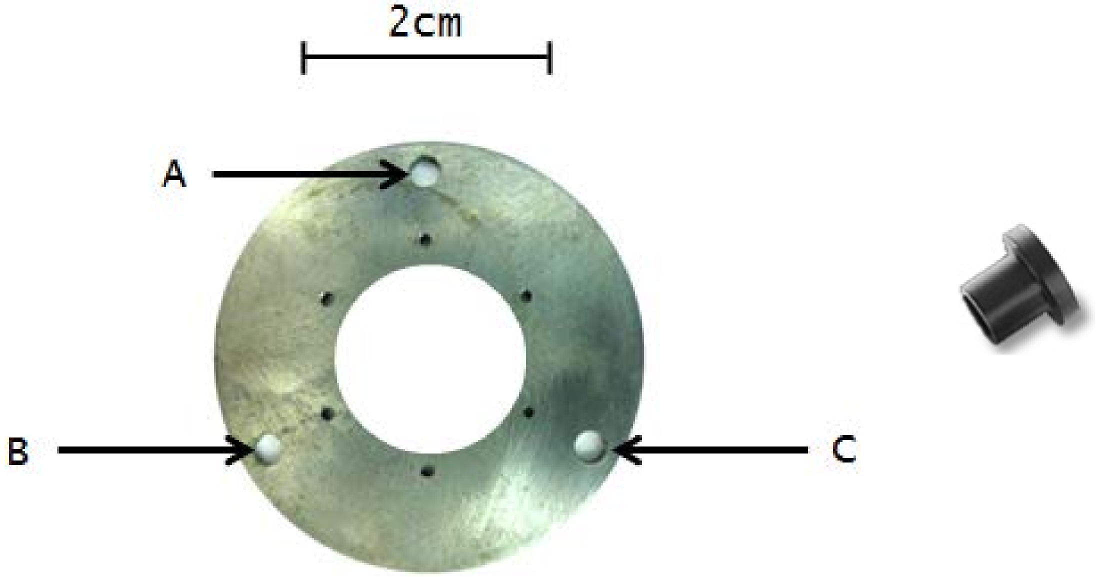

(a) (b)

Figure 2.26: The clamping electrode (a) used to fasten the stacks of electrodes to the collision cell chamber, as shown in figure 2.23. Vespel sleeves such as the one in (b) are inserted in the openings at A, B and C. This arrangement allows the clamping electrode to be electrically isolated from the collision cell as discussed in the text.

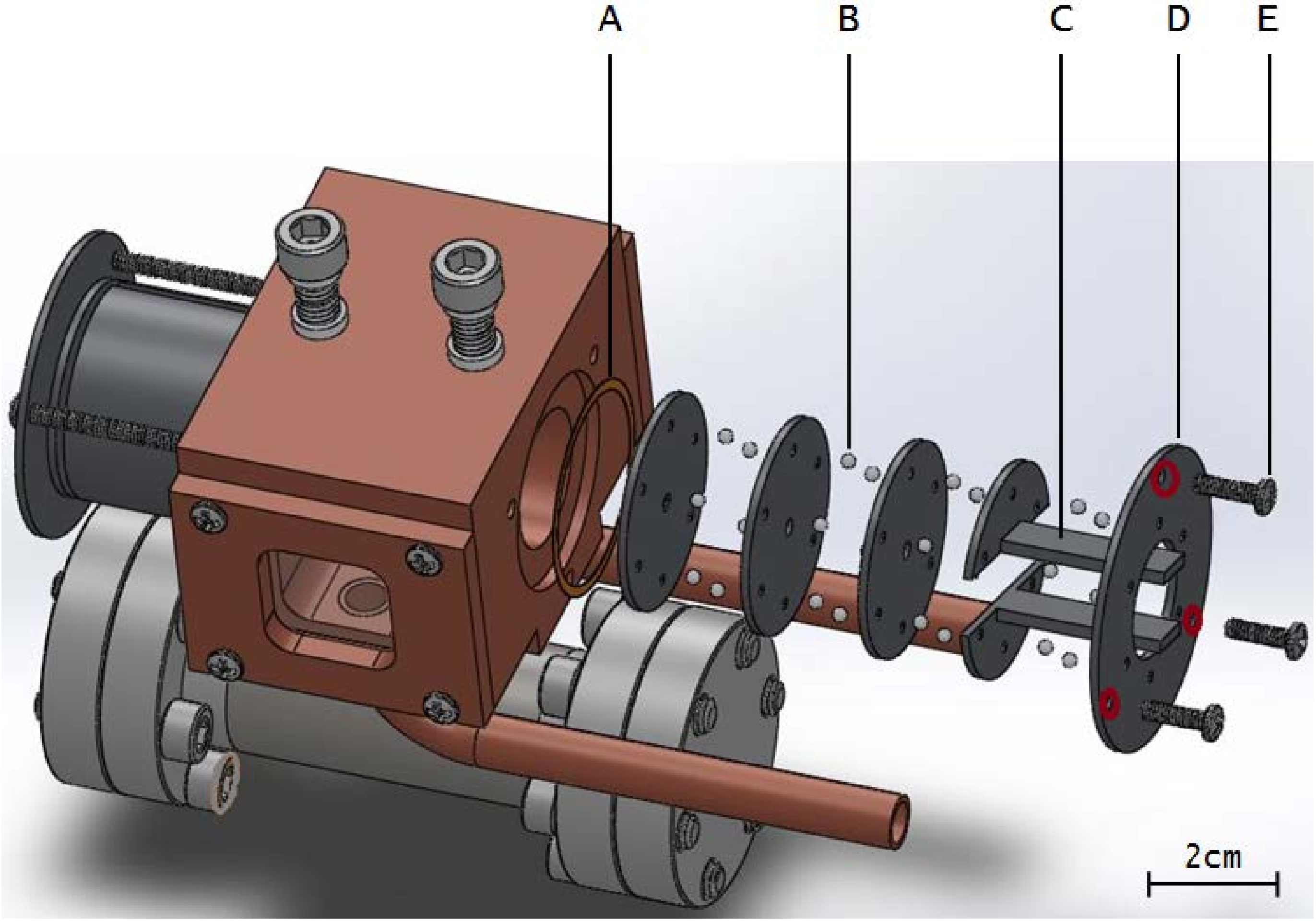

Figure 2.27: Scale assembly drawing of the electron-injection electrode stack. Shown are the Kapton ring A, a sapphire ball B, and the leg of one of the electrodes to which the tungsten filament is spot-welded C. The electrode D (for a more detailed view, see figure 2.25) presses the stack of electrodes against the collision cell while the “clamping” screw E holds the stack into place.

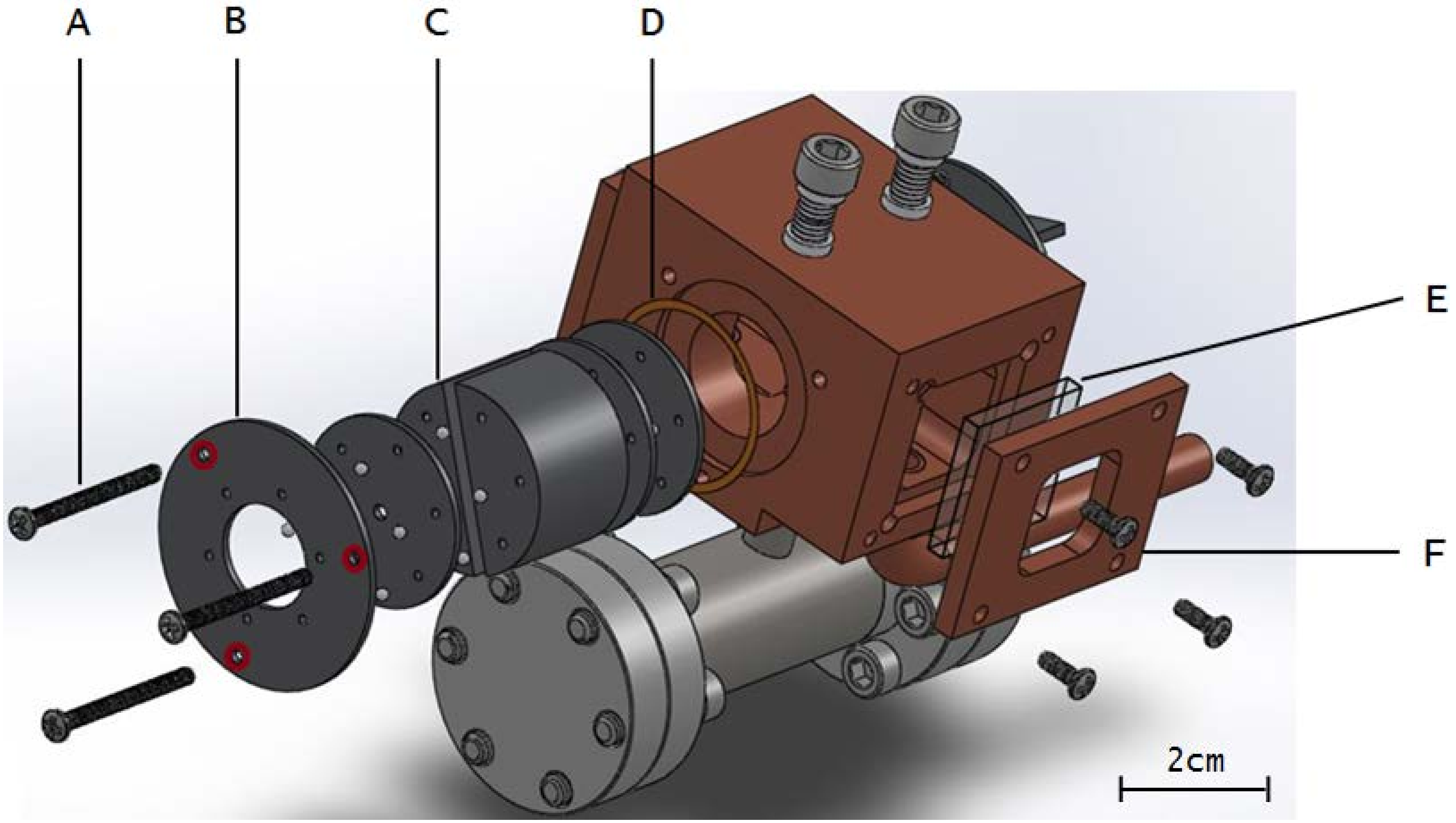

Figure 2.28: Assembly of electron-extraction electrode stack, and side window of the collision cell. Here, A represents the “clamping” screw holding the stack into place, B the electrode pressing the stack against the collision cell, C one of the deflector electrodes, and D the Kapton ring. The window E is held into position by the support F, which is fastened to the collision cell using four screws.

The electron gun is built into the upstream end of the collision cell. Both ends of the latter contain stacks of electrodes to transport electrons to and from the interaction region. The upstream electron injection stack comprises five electrodes, including the filament, while the downstream electron extraction stack holds six electrodes, including a pair of deflectors. Both stacks are electrically isolated from the collision cell by Kapton polyimide rings (thickness: 0.005”, OD: 0.970”, ID: 0.912”). A Kapton ring is laid on the face of the collision cell (see figure 2.25). An electrode is then placed on top of it. The electrode is made of molybdenum. It is 1” in diameter. It has six holes equally spaced around its edge. The holes are ~0.03” wide, and they are diametrically opposite to each other on a ~0.8” diameter. A sapphire ball, 0.0625” in diameter, is placed in each hole. Using this technique, electrodes can be stacked on top of each other, separated by the insulating balls. The last electrode to be stacked, called the clamping electrode (see figure 2.24 and 2.26), is a molybdenum ring (OD: 1.4”, ID: 0.6”). Besides the six regular holes which fit on the sapphire balls, this clamping electrode has three extra outermost ones. Screws (2-56 thread) are inserted through them. The collision cell has three corresponding tapped holes. By tightening these screws, the clamping electrode presses the whole stack against the collision cell, thus holding it in place. The clamping electrodes would be at the same potential as the collision cell if it was not for Vespel sleeves (See figure 2.26b) inserted in their outermost apertures. These sleeves prevent the screws from being in electrical contact with the clamping electrode. Hence, the clamping electrodes can be biased at potentials independent of that of the collision cell. Apart from the electrode at the entrance of the collision cell, which has a 1mm aperture, all other electrodes responsible for the forward transport of electrons have 2mm holes drilled on their centers. In this prototype, the free, unpolarized electrons are produced by thermionic emission from a pure tungsten filament (thickness: 0.01mm, width: 0.9mm). The filament is spot-welded to the legs of the electrode pictured in figures 2.24, 2.27 and 2.29.

The unit hangs from an aluminum support attached to a 6” Conflat flange (see figure 2.6). The prototype is held on the support by two bolts which are electrically insulated from the latter by ceramic inserts and washers. This arrangement prevents the collision cell from being in electrical contact with the handle, and from being grounded. In summary, the prototype has been designed to allow each electrode to be biased at a potential independent of the rest of the chamber.

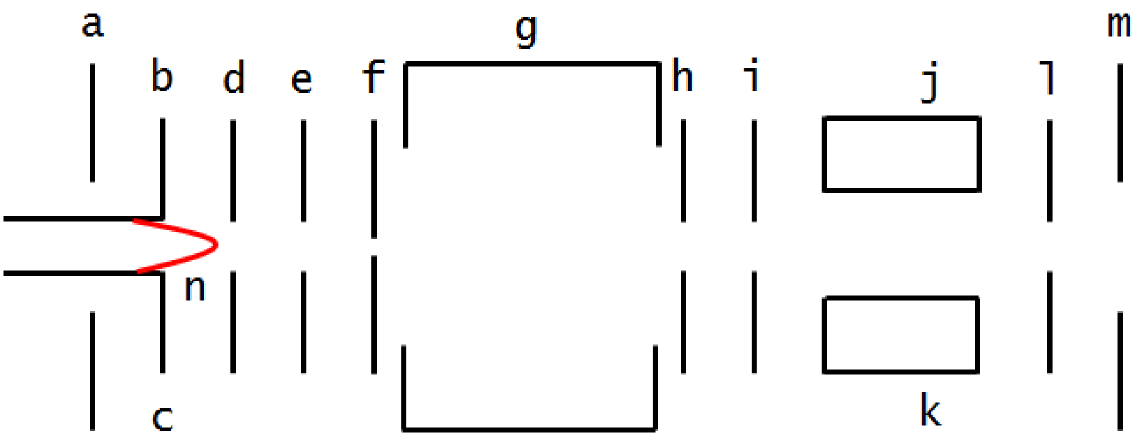

Figure 2.29: Schematic of the collision cell/electron gun electrode system. The filament n is spot-welded to the legs of electrodes b and c. The electron-injection stack consists of an additional four electrodes: a, d, e, f and c. The electron-extraction stack contains six electrodes: h, i, j, k, l and m.

The Conflat flange holding the prototype has three multipin electrical feedthroughs (see figure 2.6). The electron injection electrodes are connected to one feedthrough, the electron extraction ones to another, and the cartridge heaters as well as the thermocouples to the last one. The connections from the electrodes to the feedthroughs are made with Kapton insulated wire (Accu-Glass, 22 AWG, product number: 100680). The thermocouple leads are attached to a pair of multimeters capable of gathering temperature readings. The potentials to the electrodes and to the reservoir's heaters are provided by Agilent E3612A power supplies. The collision cell's heaters are connected in parallel. They are powered by a DC regulated supply from Circuit Specialists (CS112001X).

2.2.6 Electron optical polarimeter

The electron polarimeter is shown in figures 2.30, 2.31 and 2.32. Unlike the rest of the vacuum system, the main polarimeter chamber is constructed of aluminum. If stray electrons strike the nonconductive oxide on an unprepared aluminum surface, they will charge the walls [68]. To prevent this effect, the inside of this chamber was coated with a thin, uniform layer of aqueous colloidal graphite (Aerodag). The polarimeter main chamber contains eight Conflat ports. The electron beam enters the chamber through the opening at A. The electron collector is located at the opposite end E. The latter consists of the halves of a longitudinally split, hollow cylindrical electrode. The halves are biased with potentials to deflect and collect the primary electron beam. The pump laser enters the system through the anterior viewport of the electron collector, counter propagating with the electron beam. A Convectron pressure gauge is mounted on one of the ports. A 60 L/s turbomolecular pump (Pfeiffer Vacuum HiPace 80), attached at the bottom of the chamber, maintains the vacuum at a base pressure of 10^{-7}Torr, which rises to 10^{-3}Torr when gas is introduced.

The helium injection assembly is fitted to the top of the polarimeter chamber. Target gas flows through a feedthrough, with an outer diameter of 0.25″, welded on a 2.75″ Conflat flange before passing into a copper capillary with 0.125″ outer and 0.061″ inner diameters. The end of the capillary is approximately 5 mm above the electron beam. Trantham et al. [69] have shown that the fluorescence intensity is close to a maximum at this height while Fischer et al. [70] have demonstrated that the Stokes parameters are independent of height above this value. A stainless steel cylinder of outer diameter 25.5mm and wall thickness 1mm encloses the helium injection assembly. The former is electrically isolated from the rest of the chamber. It is used as an electrode to define the nominal electrical potential of the collision volume, and also serves to direct the effusive flow of gas from the target capillary into the turbo pump.

The metallic inner energy-defining cylinder has two collinear apertures (see figure 2.30), each 6mm in diameter, through which the electron beam enters and exits the collision region. Photons emitted from the excited helium pass through a 40mm focal-length collection lens, and travel to the optical train via an opening at 36.5° from the electron beam axis. For maximum efficiency in measuring longitudinal polarization, the axis of the optical polarimeter should make the smallest possible angle with the electron beam axis. However, room was left for the chamber housing the Faraday cup, and more importantly, for the window through which the laser used in the rubidium optical pumping process enters the apparatus. Therefore, the minimum possible angle between the optical polarimeter axis and the electron beam direction was 36.5°.

For a given P_e, the relative Stokes parameters P_1 and P_3 are functions of electron energy. Therefore, to obtain P_e accurately, the energy spread of the beam, and hence, the electric potential must vary minimally in the region yielding detectable fluorescence from the excitation of the target gas by the electrons. To provide an electric potential as uniform as possible in this region, the capillary should be at the same voltage as the stainless steel cylinder. Therefore, it cannot be welded to the feedthrough, which is grounded. It is instead fitted through a cylindrical Delrin® retainer which is surrounded by a copper mounting sleeve. The sleeve is in electrical contact with the outer metallic cylinder as well as with the copper capillary. For the optically-pumped electron spin-filter experiments, a -6V potential is applied to the cylinder when the relative Stokes parameters are measured at electron energies corresponding to the peak of the helium $2^3S \rightarrow 3^3P$ optical excitation function. The outer vacuum chamber is held at ground. While the electric potential may vary spatially in the collision volume due to contact potential differences between the cylinder and the capillary, a SIMION® simulation, shown in figure 2.33, revealed that the electric potential changes by less than 0.3% within this region. Here, we assumed a contact potential of -0.5V for the capillary relative to the inner cylinder, corresponding to a typical voltage observed between two different metals which are in contact in electron optics systems.

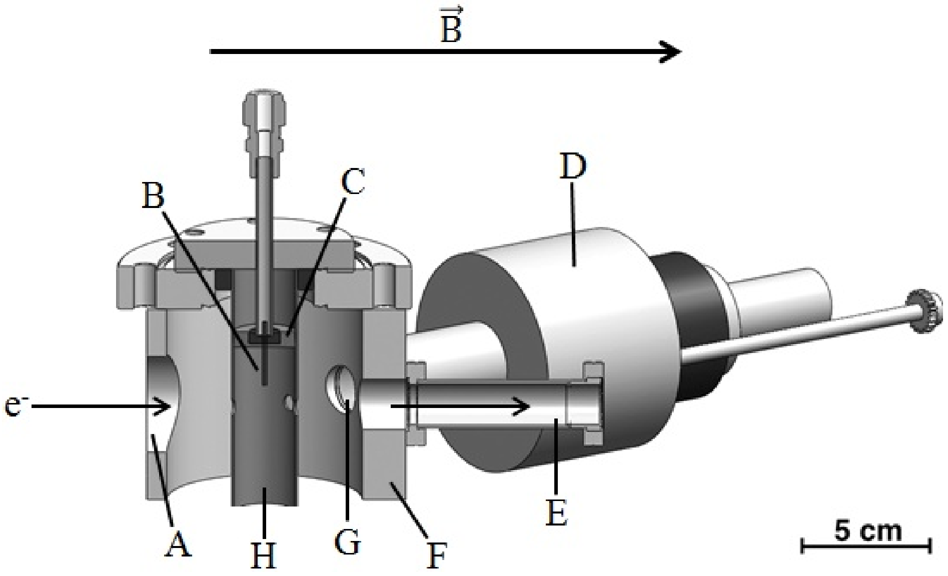

Figure 2.30: Vertical cut-away view of the electron polarimeter. The incident electrons enter the chamber through A traveling from left-to-right, guided by a longitudinal 10 mT magnetic field. Shown also are the target-gas-feed copper capillary B, its mounting sleeve C, the optical polarimeter D, the chamber housing the electron collector and viewport E, the main vacuum chamber F, the fluorescence collection lens G, and the stainless steel inner energy-defining cylinder H.

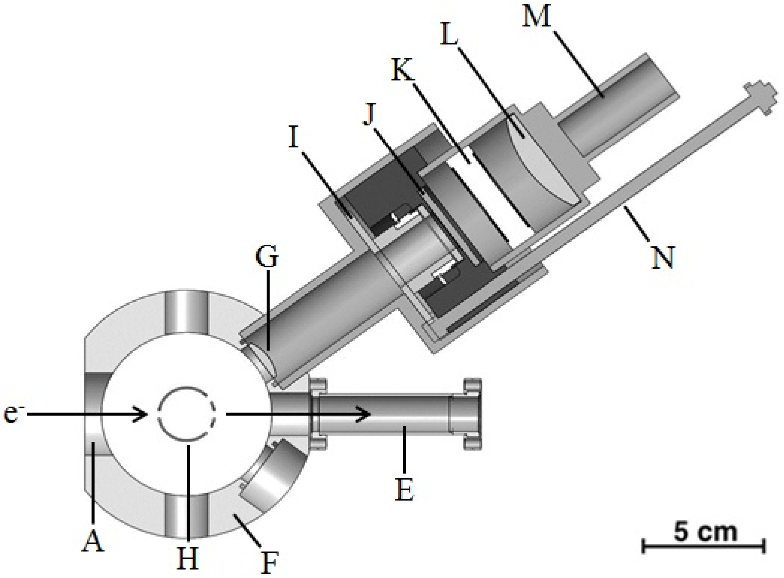

Figure 2.31: Horizontal cross-sectional view of the optical polarimeter. Letter designations for the collision chamber are the same as those in Fig. 2. Shown also are the hollow gear in which the retarder is mounted I, the linear polarizer J, the interference filter K, the focusing lens L and the photon counting module M. The rod N has step-down gears at either end and connects the retarder to a stepper motor.

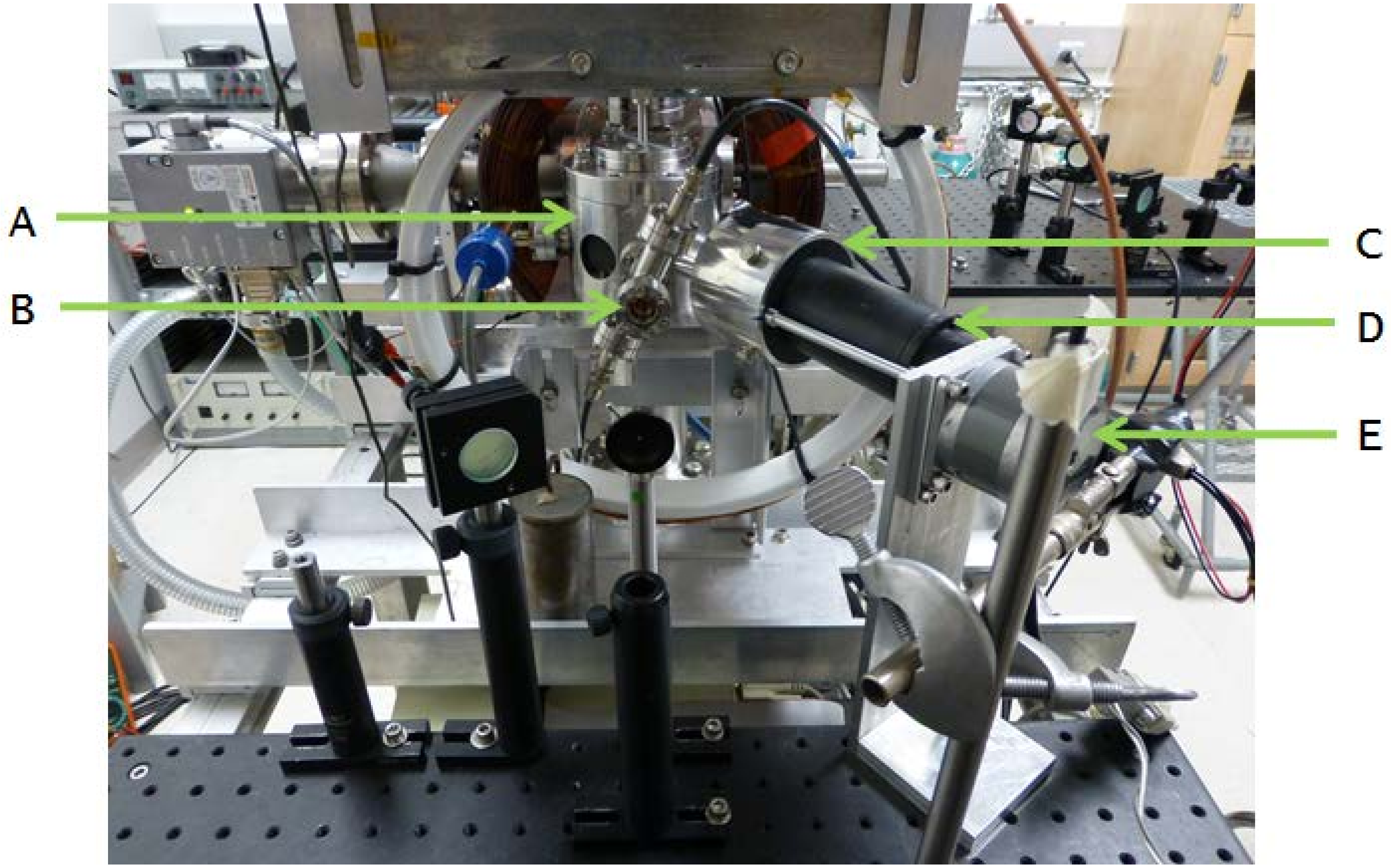

Figure 2.32: Photograph of the downstream end of the apparatus. Shown are the optical electron polarimeter chamber A, the vacuum chamber B containing the Faraday cup and the viewport through which the pump beam enters the system, the support C housing the optical part of the polarimeter, the photomultiplier tube D, and the stepper motor E.

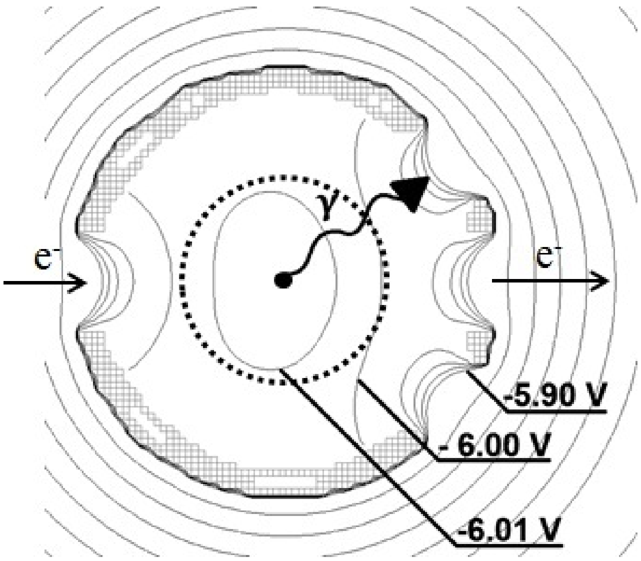

Figure 2.33: SIMION 8.0 simulation of the contour lines inside the stainless steel inner energy-defining cylinder. A horizontal slice through the center is shown. The potential varies by less than 0.3% along the path of the electron beam in the region where the helium atoms are excited. Here, the focal point of the fluorescence collection lens is indicated (●) while the region within the dashed circle represents the "sensitive volume" [71] of the optical polarimeter. A contact potential offset of -0.5V for the capillary needle (which ends 5mm, in scale, above the plane of this diagram) is assumed in this simulation.

The optical polarimeter, shown in detail in figure 2.31, uses a rotating retarder and a fixed linear polarizer downstream to determine the relative Stokes parameters P_1, P_2 and P_3. Measurements of P_e are therefore unaffected by polarization sensitivity of the photon detector because it observes a single polarization of light. The optical train comprises a collimating lens, the retarder, linear polarizer, an interference filter, a focusing lens, and a photon counting module. The retarder and linear polarizer are cut from plastic sheets (International Polarizer Inc. No. IP104WR-P and Rolyn No. 65.5305 respectively) commonly available in student laboratories. The retarder is mounted in a gear with a circular hole cut in its center for the transmission of light along its axis. The latter is connected to a stepper motor via a rod with step-down gears at either end. The stepper motor can thus rotate the retarder in increments of 7.5^o. The photodetector is a Hamamatsu photon counting head (H6180-01), which includes a bialkali photomultiplier tube, a high-voltage DC/DC power supply, and a high-speed photon counting circuit integrated into a compact unit.

Labview® 7.0 software fully automates operation of the polarimeter controlling the rotation of the stepper motor, the application of voltages to the inner cylinder, and the acquisition of data related to photon count rate, Faraday cup current and pressure in the chamber. The software was installed on a personal computer outfitted with a National Instruments (NI) PCI-6024E hardware card, a NI PCI-GPIB hardware card, parallel printer ports, and USB ports. The PCI-6024E card contains two counters. While one counts pulses, the other determines the actual time interval during the counting process. The Faraday cup current was read with a Keithley 6485 GPIB picoammeter.

CHAPTER 3. Operation

The different components comprising the system were described in the previous chapter. Here, we explain how they are operated, especially with regard to the transport of electrons along the apparatus, working with rubidium and its vapor, and measuring the polarization of the beam. We begin this discussion with the electron gun, which is responsible for producing free, unpolarized electron beams.

3.1 Electron gun

Table 3.1: Typical potentials applied to the different electrodes during operation of the system. Electrodes are biased with respect to the elements denoted in the third column.

Electrode	Approximate potential (V)	Biased with respect to
g	28.5	f
h	41.1	f
i	-35	ground
j	-33	ground
k	-30	ground
l	40	k
m	0	ground
n	9	ground
o	0	ground
p	0	ground

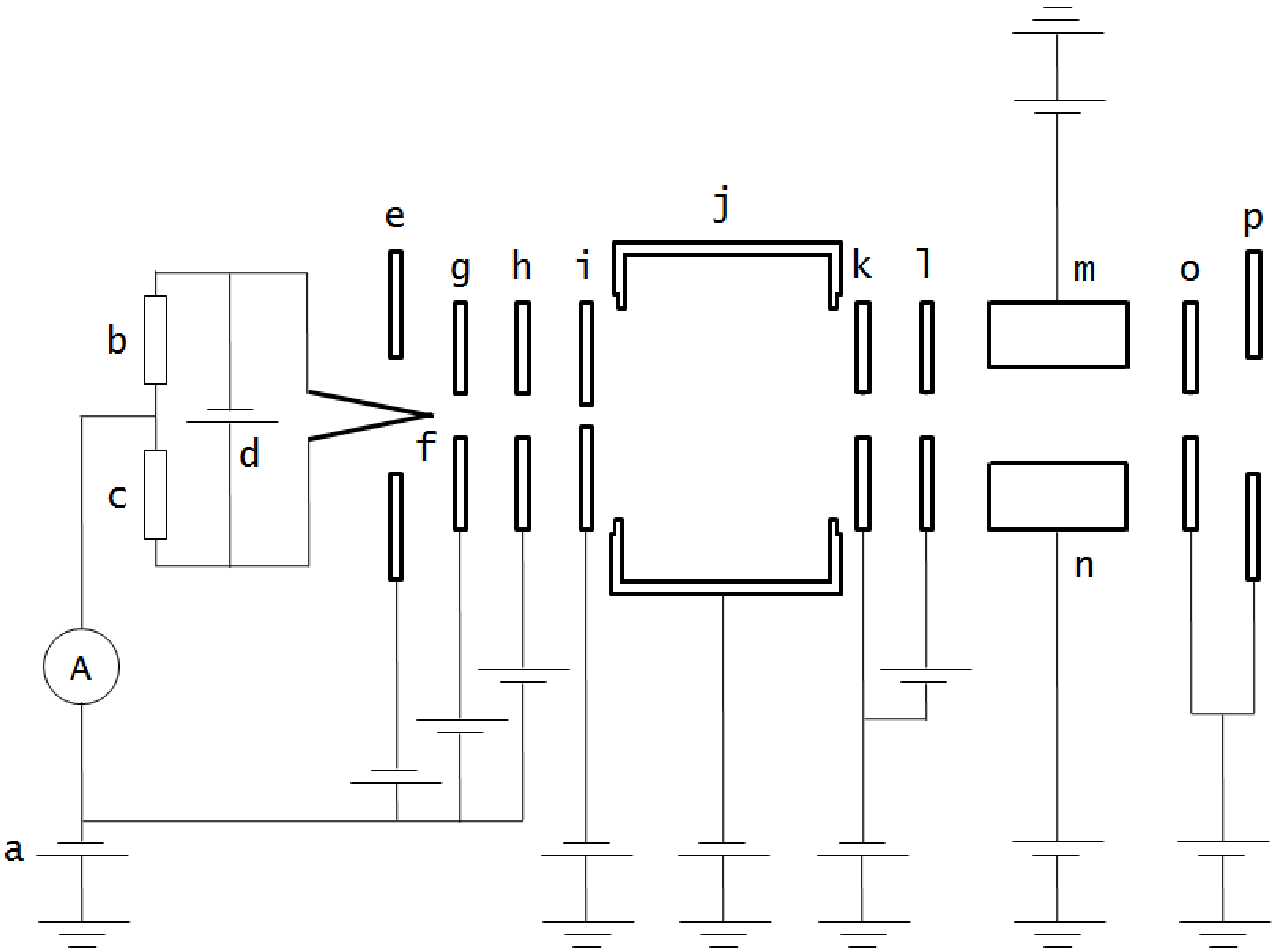

Figure 3.1: Circuit diagram for the electron gun/spin exchange target electrode biasing. Here, “i” and “k” are the entrance and exit electrodes while “j” is the collision cell. The resistors b and c have ~$10^8\Omega$ of resistance each. The filament “f” can be biased at different potentials using the power supply “a.” Its emission current can be read with the ammeter.

Figure 3.1 shows a circuit diagram of how the different electrodes of the source are electrically biased. The potentials listed in Table 3.1 are typically applied to the electrodes during experimental runs. The tungsten filament “f” is biased using the power supply “a.” The electron-injection-clamping electrode “e” is at the same potential as that of “a,” referred to as the filament bias from now on. The optimal bias for deflector “n” to maximize current recorded on the Faraday cup changes every time the source is taken apart and re-assembled. During operation, the current through the filament is set with the help of power supply “d” (HP 6286A). With no gas in the collision cell, the following emission currents $I_{emission}$ are typically obtained as the current I_{fila} passing through the tungsten filament is varied:

Table 3.2. Typical filament emission current with no gas in the collision cell.

$I_{fila}\ (A)$	$I_{emission}\ (\mu A)$
2.5	1
3.0	16
3.5	55

We are effectively changing the temperature at which the filament is operating by varying I_{fila} [72], which according to Richardson’s law [73], affects the number of electrons emitted thermionically:

$$J = AT^2\,\mathrm{e}^{-\frac{W}{kT}}, \tag{3.1}$$

where J represents the density of emitted current, A the Richardson constant, W the work function of the metal, and T its temperature. When buffer gas is introduced into the collision cell and exits through the apertures at the ends, it comes into contact with the hot tungsten filament, cooling it in the process. This decreases the emission current. For instance, while $I_{fila} = 2.5$ A generates an emission current of 1μA with no gas in the collision cell, only 0.2μA is observed with ~200mTorr of nitrogen in the system. More current has to be supplied to the tungsten filament to obtain similar emission currents as those with an empty collision cell. I usually apply ~4.5A when the gas load is 200mTorr in the collision cell, which causes the ammeter reading the emission current from the filament to register about 300μA. This value also depends on which buffer gas is used in the collision cell. For example, with ethylene, the emission current can jump as high as 3mA, a phenomenon observed by Dr. P. D. Burrow during electron transmission spectroscopy experiments [74]. The ethylene molecules decompose on contact with the hot filament, coating the latter with carbon. Baker *et al.* [75] have observed that such a process can lower the work function of pure tungsten, thus leading to increased electron emission.

The present design of the source is not devoid of problems. First, the rubidium vapor tends to cool down on the inner surface of the collision cell fairly quickly. Eventually, the latter, especially the windows, are coated with a thick layer of alkali metal (see figure 3.2). The rubidium deposit also causes the entrance, exit and copper electrodes to conduct electrically, thus, affecting electron transport (see figure 3.3). The proximity of the reservoir, the collision cell and the tungsten filament proves problematic.

(a) (b)

Figure 3.2: (a) Front and (b) back view of one of the windows on the collision cell. The alkali vapor cools down on and coats these components with rubidium and its oxide (white residue) fairly quickly, affecting passage of the probe beam in the process. (See text for more details.)

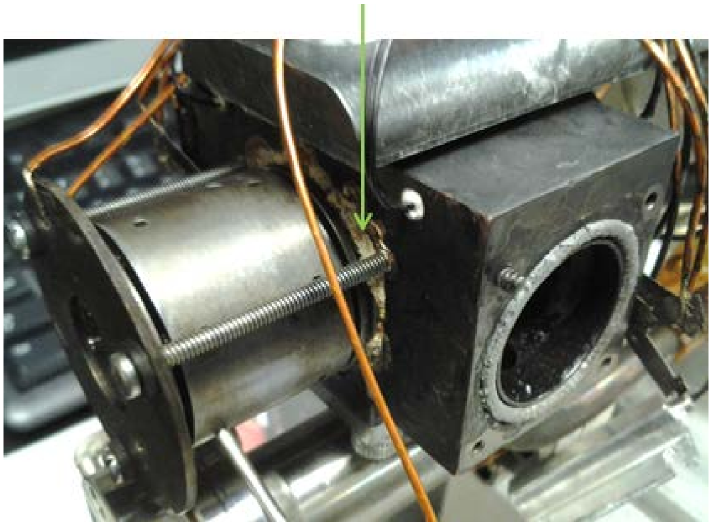

Figure 3.3: During operation of the source, rubidium and its oxide accumulate on and around the exit electrode (green arrow), eventually causing it to short out with the collision cell.

Currently, the heat from the collision cell dissipates rapidly to the reservoir so that the two are at almost the same temperature. The collision cell should actually be much hotter than the reservoir (by at least 40^{o}C according to Dr. P. D. Burrow who has worked extensively with alkali vapors under vacuum conditions) to prevent the rubidium vapor from cooling down in the former. Attaching more heaters to the cell does not improve the situation; it simply causes more heat to dissipate to the reservoir. I have had limited success in getting the cell hotter than the reservoir by attaching a heat-sink at the junction connecting the two components. The heat-sink consists of an approximately 40cm long Kapton-insulated wire (the same kind used to connect the electrodes to the electrical feedthroughs; see chapter 2) which has been wrapped around the junction of the reservoir and the collision cell. The ends of the wire have been tied to the wall of the 6” Conflat flange supporting the source. This helps to dissipate heat from the cell to the latter, thus keeping the reservoir cooler than the collision cell by ~15^{o}C. Alternatively, the system could be modified by placing the reservoir further from both the collision cell and the tungsten filament. Such a setup combined with a heat-sink would mitigate the effects of thermal conduction and radiation to the reservoir. This would allow us to heat the collision cell to even higher temperatures without affecting the reservoir, and would prevent rubidium vapor from cooling down on the walls of the former.

Moreover, the hot tungsten filament radiates enough heat to warm the collision cell. Rubidium which has coated the cell from previous use is vaporized whenever the filament is turned on. Additionally, since the electron-injection and electron-extraction optics stacks possess no direct source of heat, rubidium exiting the collision cell builds up on them. Over time, the sapphire balls become conductive, and the whole unit shorts out. If the rubidium density is kept below 10^{12} atoms/cm^{3}, the system can run for a month with minimal wear and tear. With densities close to 10^{14} atoms/cm^3 and above, several electrodes will short out among each other after a single use. The electrodes will experience increased leakage currents after each run with densities of $\sim 10^{13}$ atoms/cm^3. One can run for a couple of weeks at such densities before the system has to be cleaned.

Another problem along the same line concerns the tungsten filament. With the latter operating at such high temperature, sublimated tungsten will deposit on neighboring sapphire balls. The filament will eventually short out with its neighboring electrodes (parts “e” and “g” in figure 3.1). The procedure to clean deposits from these balls (described in the following section) is very complex, involving the use of corrosive chemicals such as hydrofluoric acid and nitric acid [76]. It is best to discard the sapphire balls every time the system is cleaned, and replace them with new ones.

3.2 Cleaning the source

Here, I describe the key steps in cleaning the apparatus. The system is first brought to atmospheric pressure. The 6” flange supporting the gun system is then unbolted from the vacuum chamber and attached to a support stand. The assembly consisting of the collision cell, the electrodes and the reservoir are typically coated with rubidium. In order to minimize the risk of ignition of the alkali metal during the cleaning process, I leave the gun assembly open to air overnight. Most of the rubidium will have turned into oxide the following morning. The Kapton-insulated wires, which provide electrical contact to the feedthroughs attached to the 6” flange, are disconnected from the electrodes. The assembly consisting of the collision cell, the electrodes and the reservoir, all of which form a single unit, is detached from the aluminum handle (see figure 2.6) it is fastened to. It is taken to the fume hood where it is disassembled. Each part is carefully sprayed with methanol until all residual rubidium has reacted. The different components, except for the windows and clamping electrodes (described in section 2.2.5), are immersed in a beaker of methanol and are sonicated. Windows are cleaned by hand to avoid scratching them. The clamping electrodes are subjected to the same treatment to prevent the Vespel sleeves (see figure 2.25) embedded in them from reacting with the methanol. Sapphire balls can be cleaned [76] by immersing them in a solution composed of equal parts hydrofluoric acid and nitric acid (12 molar in concentration). After standing for approximately 2 hours, they are carefully retrieved from the solution, and are thoroughly rinsed with distilled water.

The parts are then dried. The electrodes and the collision cell will be coated with an insulating layer. The molybdenum metal making up the electrodes will contain patches of a white and light brown residue. The deposit inside the collision cell, on the other hand, will consist of a white powder and a black liquid of some sort. The nature of this residue is unknown, but its removal is vital for effective electron transport, otherwise electrons striking it will charge up the walls and affect the beam. Removal of the residue is achieved by sanding down the electrodes and the collision cell with fine sandpaper (grit: 320). In the process, care must be taken not to damage the Vespel sleeves. Once the non-conducting residue has been removed, the electrodes, with the exception of the clamping ones, and the collision cell are sonicated in methanol again. The parts are then dried. The inside of the collision cell is coated with a thin, uniform layer of aqueous colloidal graphite (Aerodag®). The source is now ready to be assembled.

After the stacks of electrodes have been clamped to the collision cell, the tungsten filament is spot-welded in position. For me, this is the most frustrating step. It can take a whole day to align the filament with the apertures in the electrodes. Moreover, if the tip of the filament is placed too close to the next electrode (electrode "g" in figure 3.1), it will come in electrical contact with the latter when the hot filament expands or droops. The tip of the filament should be positioned at least 1mm away from electrode "g". The current setup could be modified to accommodate commercially-available electron emitters on ceramic bases. They would be easier to replace. However, given the large gauge of wire they use, I doubt they can last as long as the present filament, particularly at the pressures we are operating, or even match the high electron current produced by the latter. For instance, tungsten filaments typically employed in electron guns in our lab and bought from Kimball Physics are rated to have a maximum emission current of 50μA; we need 300μA or more.

The unit is now bolted to its support on the 6" Conflat flange. The Viton tubing connecting the collision cell to the gas line and to the pressure gauge is replaced. Rubidium tends to diffuse and accumulate on the inner walls of the tubing. This process eventually results in the collision cell shorting to ground via the now conductive Viton tubing. The Kapton-insulated wires from the electrical feedthroughs are connected to the electrodes. The heaters as well as the thermocouples are mounted on the unit, and the system is finally ready to be loaded with a rubidium ampoule.

3.3 Loading the rubidium

Once it is under vacuum, the system does not have the capability to be loaded with rubidium nor is it configured to allow us to break a sealed alkali ampoule placed in its reservoir. Therefore, the rubidium ampoule has to be loaded in the reservoir before it is positioned inside the vacuum chamber. If the ampoule is broken in air, a layer of rubidium oxide will form on the metal's surface. It will take temperatures greater than 200°C to break it down before the rubidium can be released in vapor form [77]. Several times when we needed to resort to such high temperatures to break the oxide crust, the rubidium was released rapidly and violently, coating much of the gun system and on one spectacular occasion, producing a Rb fire in the vacuum system! The Kapton polyimide rings (described in section 2.2.5) insulating the entrance and exit electrodes from the collision cell do not withstand such high temperatures for very long. The heat seems to cause the rings to become thinner. Consequently, the entrance and exit electrodes (parts labeled "i" and "k" in figure 3.1) eventually short out to the collision cell. Therefore, the ampoule is broken under liquid hexane, which prevents the rubidium from reacting with oxygen. In the following paragraphs, I describe this procedure.

The base holding the Conflat flange with the collision cell and electron gun assembly is tipped so that the axis of the reservoir is now at an angle of ~45° to the horizontal (see figure 3.5). It is filled with liquid hexane (C_6H_{14}). Care must be taken to prevent the fluid from spilling over into the collision cell. Otherwise the Aerodag$^{®}$ coating may wash onto the entrance and exit electrodes, and may short out the various

Figure 3.4: Pre-scored rubidium ampoule used in the system.

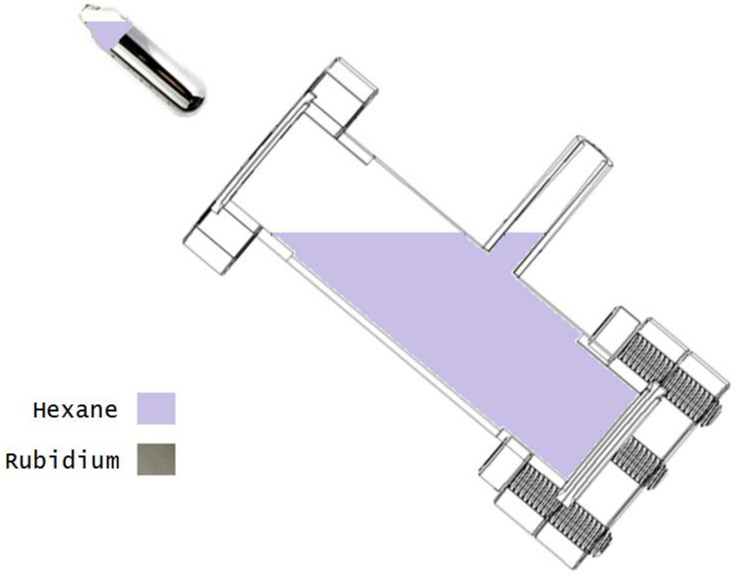

Figure 3.5: Shown in this cross-sectional view of the reservoir is the level to which the chamber is filled with liquid hexane before a new rubidium ampoule is loaded inside. (See text for more details)

elements. A beaker is next filled with liquid hexane. The pre-scored rubidium ampoule is immersed in the beaker and broken. To do this, I usually immerse my gloved hands into the beaker, grab the ampoule, snap it, and let the parts sink back to the bottom. I then lift the ampoule out of the beaker with tweezers. The empty portion of the rubidium ampoule should be filled with liquid hexane as it is taken out of the beaker (see figure 3.5). I advise against dropping the ampoule at this stage; it will catch on fire. Finally, the ampoule is inserted into the reservoir. The latter is again filled with liquid hexane. The mini-Conflat blank at the downstream end of the reservoir (see for example figure 2.28) is now attached and sealed using an oxygen-free, high-conductivity (OFHC) copper gasket. The cartridge heater is positioned back on the sealing blank. The 6” Conflat flange supporting the electron gun assembly is now ready to be introduced into the vacuum chamber. As the liquid hexane evaporates quickly, the source chamber should be pumped down to roughvacuum (~10 mTorr) as soon as possible. Any leftover liquid hexane should be poured back into its container, and should be stored in the chemical cabinet. This substance is toxic [78]. Long-term exposure will damage the nervous system. Short exposures cause minor headaches.

3.4 Buffer gas pumping issues

Unlike the apparatus described in Batelaan *et al.* [29], our system cannot handle more than 200mTorr of quenching gas in the collision cell. If this value is exceeded, the pressure above the 700Ls^{-1} diffusion pump reaches the critical 1mTorr regime, which results in significant backstreaming of diffusion pump oil into the six-way cross housing the collision cell [79]. Part of the problem lies at the junction connecting the vacuum chamber with the diffusion pump. The latter has a ~10” OD and ~6.3” ID while the former has a 6” OD and a 3.8” ID. To bridge this gap, a 10” OD to 8” OD straight tube nipple reducer was installed on the diffusion pump. This arrangement was followed by an

8” OD and 4” ID zero length reducer and finally, the six-way cross was attached on top. This scheme reduces the pumping speed of the diffusion pump in the vacuum chamber to ~500Ls^{-1}. Gas emanates from two apertures in the collision cell, 1mm (upstream) and 2mm (downstream) in diameter. Calculations show that such a system can handle ~200mTorr of buffer gas in the collision cell before the pressure above the diffusion pump surpasses 1mTorr, in agreement with our observations. These estimates were obtained with the help of reference [80].

3.5 Measuring rubidium density and polarization

Before any density and polarization measurements can be performed, rubidium vapor has to be introduced into the collision cell. The heaters are therefore switched on, and the collision cell is heated slowly. During this process, the probe beam, whose wavelength is being modulated from ~794.960nm to ~795.010nm, is made to go transversely through the collision cell. The arrangement described in figure 2.9 is used to monitor the intensity of the light. When alkali vapor eventually starts to fill the collision cell, an absorption profile corresponding to the rubidium D1 transitions, such as the one shown in figure 2.14, will be observed on the oscilloscope screen. If no absorption profile is recorded by the time the temperature of the collision cell reaches ~110°C, the reservoir heaters are turned on. The reservoir is heated slowly until rubidium vapor starts to build up in the collision cell. The latter’s temperature is adjusted constantly to try to keep it hotter than the former by at least a couple of degrees. A rubidium D1 absorption profile can usually be observed when the temperature of the reservoir reaches about 75°C.

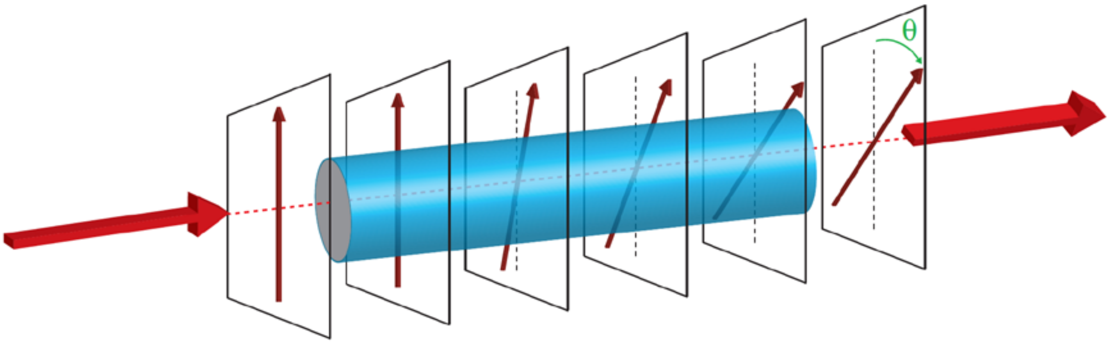

Figure 3.6: Propagation through a birefringent vapor causes rotation of the plane of polarization of linearly polarized light by an angle proportional to θ. (See text for details.) (Adapted from [81].)

Once the rubidium vapor has built up in the collision cell and the absorption profile has stabilized, implying that the vapor thickness is not changing anymore, the density of the rubidium vapor N_{Rb} and its polarization P_{Rb} are usually inferred from the Faraday diamagnetic and paramagnetic effects [82]. In essence, the alkali vapor becomes birefringent as a result of a population difference induced by optical pumping in the ground state and/or the application of a longitudinal magnetic field. Therefore, in measuring the quantities of interest, the probe beam is sent through the rubidium vapor, parallel to the magnetic field, and the rotation of its plane of polarization is monitored (see figure 3.6). Determining N_{Rb} and P_{Rb} has proved no trivial matter with this system. The filament tends to block the probe light. Given that the former's width is comparable to the aperture size of the entrance electrode, ~1mm, it is extremely challenging to get the probe beam into the collision cell. When the probe beam does go through, light with less than 0.3μW of power emerges from the vacuum system (out of 1mW of incident light). Interaction with the beam sampler "BS2" (please refer to figure 2.15) causes the probe's power to drop further. Consequently, it becomes challenging to locate the position of the beam, and guide it to the detector responsible for measuring Faraday rotation angles.

Moreover, the window through which the pump light enters and the probe beam emerges from the vacuum system reflects part of the beam. The reflected portion of the pump beam travels back to the pump laser. On the way, it encounters the same beam sampler “BS2” as the probe beam. Part of this pump light scatters, and follows a similar path as the probe laser all the way to the photodiode. Care must be taken to prevent the scattered pump light from saturating the photodetector. This situation also requires the use of phase-sensitive-detection techniques involving an optical chopper and a lock-in amplifier to extract the signal corresponding to the probe light.

The steps in measuring N_{Rb} and P_{Rb} by the Faraday effects with a probe beam traveling through an alkali vapor parallel to a magnetic field have been documented in references [29, 61, 83]. I will briefly go through them. I will first focus on determining the number density. With the electromagnets off and no pump light, I locate the angle θ_o at which the transmission axis of the linear polarizer “LP3” (refer to figure 2.15) is perpendicular to the plane of polarization of the probe beam. In other words, I minimize the photodiode signal by rotating the transmission axis of the linear polarizer “LP3.” This procedure is repeated for several different wavelengths of the probe beam, detuned from the line center of the rubidium D1 transition. The electromagnets are now turned on. The magnetic field will cause the alkali vapor to become birefringent. Consequently, the plane of polarization of the probe beam will rotate as the light travels through the gas. The photodiode reading will not be minimal anymore. This situation is remedied by rotating the transmission axis of the linear polarizer "LP3" again. The angle θ_B at which the new minimum occurs is recorded. This step is duplicated for all the detunings measured with no magnetic field. The rubidium density can then be found from the following equation [83, 60]:

$$N_{Rb} = \frac{6\pi h\delta^2(\theta_B - \theta_o)}{\mu_B L\Gamma\lambda_{D1}^2 B}. \tag{3.2}$$

Here, μ_B is the Bohr magneton, L the distance travelled by the probe beam through the vapor, B the magnetic field strength, δ the detuning from line center, h Planck's constant, Γ the natural linewidth, and λ_{D1} the wavelength of the D1 transition. The choice of detuning is crucial. If one probes too close to the rubidium D1 line center, one may face rotations of the plane of polarization of over 360°. With the present experimental setup, it is impossible to distinguish a rotation angle of $(\theta_B - \theta_o)^o$ from $(\theta_B - \theta_o + n\cdot 180)^o$ where n is an integer. It is imperative to be able to tell these angles apart because according to equation (3.2), they correspond to different rubidium densities. Therefore, I recommend starting at large detunings where the rotation angles are barely noticeable. For example, as can be seen in table 3.3, with rubidium densities of ~10^{13} atoms/cm^3 in the system, the rotation angle is relatively small, 4°, for a detuning of ~10GHz from the D1 line center, and rises to 11° for a detuning of ~6GHz. These data were taken with the probe beam traveling along the collision cell parallel to the magnetic field.

When the rubidium vapor is polarized by letting the pump light through the

Table 3.3. Typical rotation angles recorded when determining [Rb] by the Faraday effect.

Probe wavelength (nm)	Probe detuning from Rb D1 line center (GHz)	θ_o (degrees)	θ_B (degrees)	$(\theta_B$-$\theta_o)$ (degrees)	[Rb] (x10^{12} atoms/cm^3)
794.9992	9.653	4	0	-4	4.0
794.9967	8.467	3	355	-8	6.2
794.9924	6.427	4	353	-11	4.9

collision cell, the oriented alkali vapor will cause the plane of polarization of the probe beam to rotate further. The photodiode signal is minimized again by rotating the transmission axis of the linear polarizer "LP3" through angle θ_p. The rotation angle of the probe light's polarization due to the oriented alkali vapor is then given by $(\theta_p - \theta_B)$ [84]. The degree of polarization of the rubidium vapor is obtained from [83]

$$P_{Rb} = \frac{16\pi\delta(\theta_P - \theta_B)}{N_{Rb} L \Gamma \lambda_{D1}^2}. \tag{3.3}$$

During this whole process, the electromagnets are left on in order not to affect the electron beam.

In principle, this technique to measure N_{Rb} and P_{Rb} can be applied when the probe beam is incident on the birefringent alkali vapor at an angle of less than 90° to the magnetic field lines. It would have been convenient to use the viewports on the side of the collision cell for this. However, these become coated with an opaque layer of rubidium quickly (see figure 3.2). The probe beam could only get through the collision cell if sent at the very edge of the viewport, perpendicular to the magnetic field. In such a case, the technique relying on the Faraday effect was not applicable, and another method of estimating the alkali vapor's density had to be sought. A procedure based on absorption spectroscopy [60, 85] was devised to that end. Absorption profiles of the alkali vapor in the collision cell were acquired using the setup described in section 2.2.2, and could be used to estimate its density with the following procedure. The acquired absorption profiles were compared with ones generated with a program written in Mathematica by P. Siddons from the University of Durham [85], who has worked extensively on developing models to describe the interaction of light with rubidium vapors. The computer program is based on the theory of references [85] and [86]. It outputs the absorption profile of rubidium vapor in a cell with a user-defined length and temperature. It first converts the temperature put in by the user into its corresponding alkali density using equations typically employed in the determination of rubidium vapor pressure curves [87]. In essence, the program determines the density corresponding to the input temperature by using available rubidium vapor pressure curves. For a particular thickness of the alkali vapor, it then calculates the refractive indices and absorption coefficients over the range of wavelengths related to the D1 transitions. Finally, it outputs the theoretical absorption profile. For our collision cell length, we generated a library of such profiles, corresponding to different temperatures and hence rubidium densities. To estimate the vapor's thickness, the experimentally-acquired absorption profile was compared to the theoretical ones by superposing them on top of each other until the best match was found. Several examples of such superposition are shown in figure 3.7. In each case, the black dashed curve is the experimentally-acquired absorption profile while the blue and magenta curves have been generated with the software. These provide an

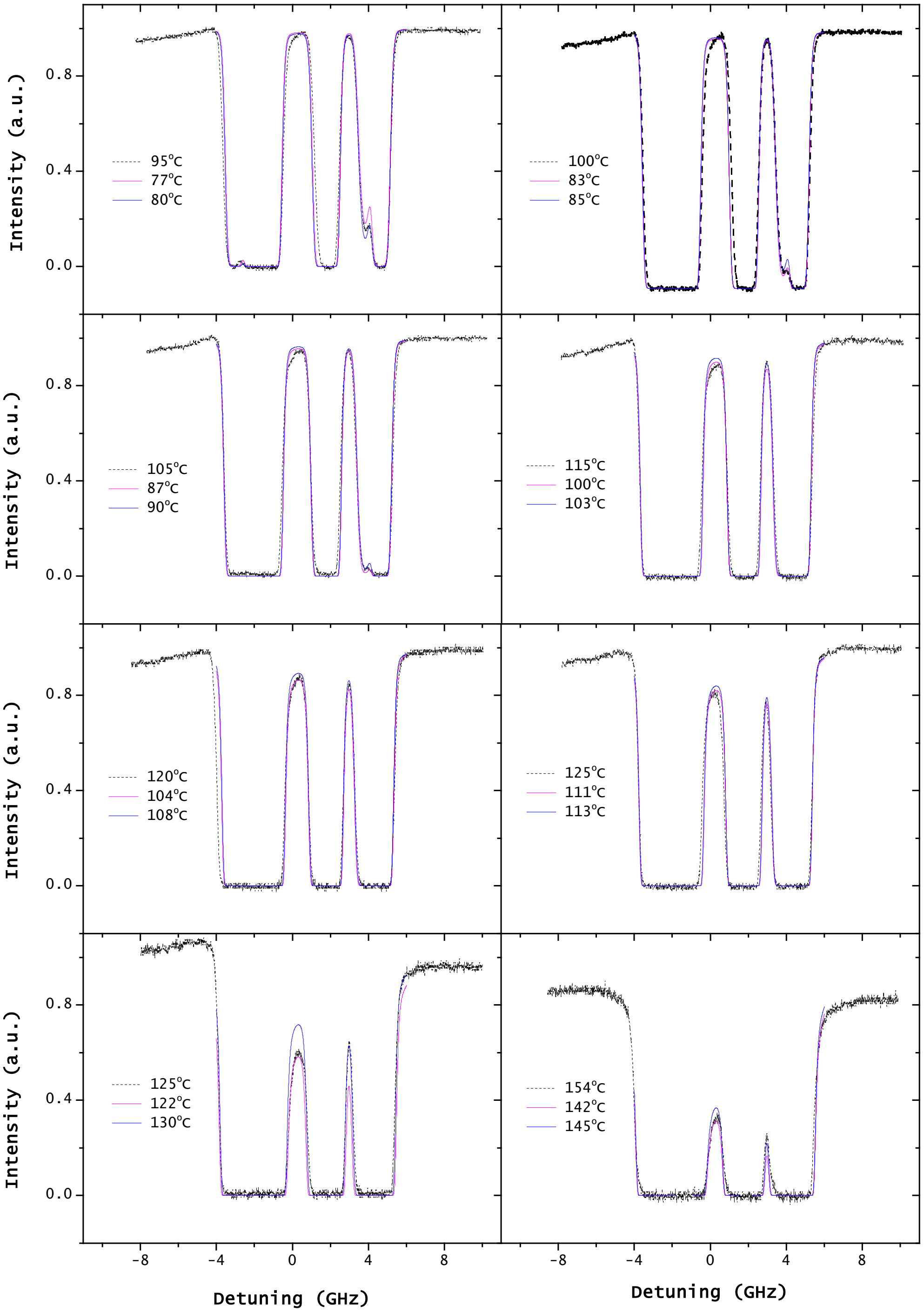

Figure 3.7: Estimating the rubidium density using the method outlined in the text. Starting from the first row and going from left to right, the densities were found to be, in units of atoms/cm^3, $(1.4\pm0.2)\times10^{12}$, $(2.1\pm0.1)\times10^{12}$, $(2.8\pm0.3)\times10^{12}$, $(6.7\pm0.6)\times10^{12}$, $(9\pm1)\times10^{12}$, $(1.27\pm0.08)\times10^{13}$, $(2.9\pm0.6)\times10^{13}$ and $(7.3\pm0.6)\times10^{13}$. (See text for more details.)

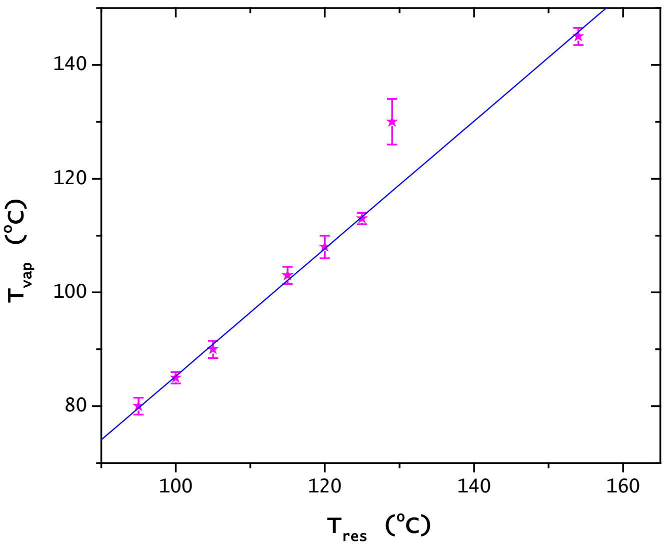

Figure 3.8: Under the current experimental conditions, the following functional relationship exists between the reservoir temperature T_{res} and that obtained from vapor pressure curves, T_{vap} : $T_{vap} = (-27 \pm 4) + (1.12 \pm 0.03) \cdot T_{res}$.

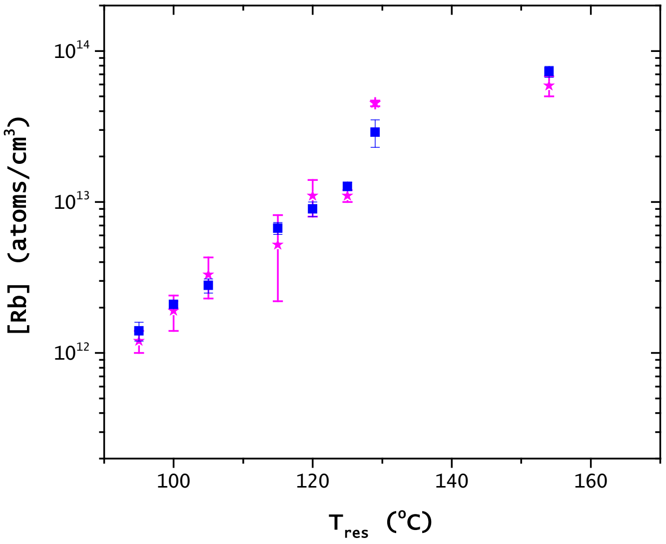

Figure 3.9: Comparison between rubidium densities [Rb] obtained using the method devised from absorption spectroscopy (blue) and those gathered with the Faraday rotation technique (magenta), performed at an angle of ~79° to the magnetic field lines.

upper and a lower bound on the rubidium density. It can also be seen from the legends of figure 3.7 that the temperatures read by the reservoir thermocouple (values related to the black dashed curve) when the experimental absorption profiles were acquired do not match those obtained from the vapor pressure curves (values related to the blue and magenta curves) [87]. This is not surprising considering that the thermocouple was not directly measuring the temperature of the rubidium vapor but was attached outside of the reservoir, at one of the ends housing a heater. However, figure 3.8 shows that a functional relationship may exist between the temperatures read by the thermocouple and those obtained from the vapor pressure curves. In figure 3.9, densities estimated using the method just outlined were compared to those taken with the Faraday rotation technique, performed at an angle of ~79^{o} to the magnetic field lines, and they are in reasonable agreement. It should be noted that the method of estimating rubidium densities using absorption spectroscopy is extremely tedious and time-consuming. There is a pressing need to prevent rubidium from cooling down on the viewports. The suggestions outlined in section 3.1 could be implemented to this end.

3.6 Electron polarimetry data acquisition

The electron optical polarimeter described in section 2.2.6 works on the principle of inelastic exchange collisions of polarized electrons with helium atoms [88]:

$$\begin{aligned} \vec{e} + He\left(1^1S_0\right) &\rightarrow \overset{\rightarrow}{He}{}^*\left(3^3P\right) + e' \\ &\rightarrow He^*\left(2^3S\right) + \left(h\nu\right)_\sigma \left(388.9nm\right). \end{aligned} \tag{3.4}$$

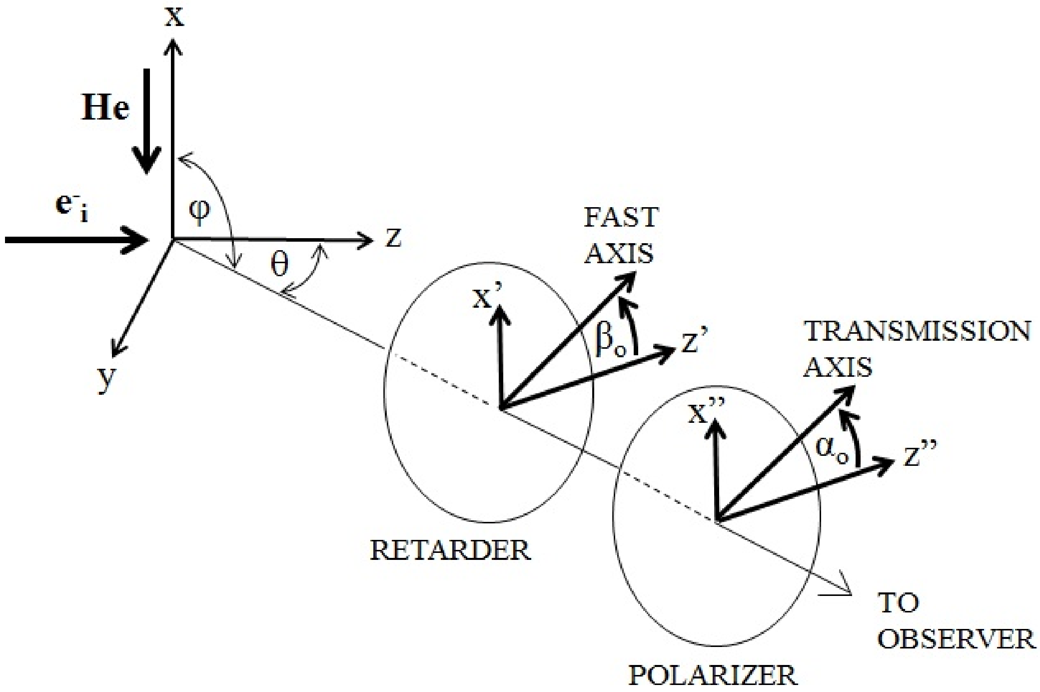

Figure 3.10: Schematic of the helium optical electron polarimeter geometry. In our device, $\varphi = 90^o$ and $\theta = 36.5^o$. The electron beam is incident along z while the helium gas flows towards the –x direction. The initial offset of the retarder's fast axis and the linear polarizer's transmission axis are denoted by β_o and α_o respectively.

The spin angular momentum of the electron is transferred to the helium by exciting the latter from the 1^1S_0 state to the 3^3P state. Eventually, the excited atom decays into the metastable state 2^3S by emitting circularly polarized light. The relative Stokesparameters P_1, P_2 and P_3 of this 388.9nm $3^3\text{P}\rightarrow 2^3\text{P}$ He radiation can be related analytically to the polarization of the electron beam P_e [88]. Here, P_1, P_2 and P_3 describe, respectively, the difference between the amount of horizontal and vertical linear polarization relative to the electron beam axis, of linear +45° or -45° polarization, and of right- or left- circular polarization of the light, all normalized to the total intensity [89]. If we apply the results from [90] to our collision geometry, shown in figure 3.10, we find that [91]

$$P_e = P_3\left(\frac{2.6409}{1.0614 + 0.9386P_1}\right). \tag{3.5}$$

We can deduce the electron polarization by determining P_1 and P_3 experimentally. On the other hand, P_2 vanishes if the spin-orbit interaction in the Hamiltonian describing the electron-atom scattering is negligible, which is a necessary condition for the validity of equation (3.5).

This polarimeter consists of a rotating waveplate in front of a fixed analyzer. It is a well-documented [32, 89, 69, 92] technique for finding the relative Stokes parameters. I will now describe how this device is operated. According to the Mueller calculus, the transmitted intensity $I_i^{'}$, normalized to the vacuum chamber pressure and the Faraday cup current [93], for light incident on such a polarimeter obeys [32]

$$\begin{aligned} I_i^{'} = I\Big\{1 &+ \frac{1}{2}P_1k_{inc}\left\lfloor\cos\left(2\alpha_o\right)\left[\cos\left(4\beta_i+4\beta_o\right)\left(1-\cos\delta\right)+\left(1+\cos\delta\right)\right]+\sin\left(2\alpha_o\right)\sin\left(4\beta_i+4\beta_o\right)\left(1-\cos\delta\right)\right\rfloor \\ &+\frac{1}{2}P_2k_{inc}\left\lfloor\cos\left(2\alpha_o\right)\sin\left(4\beta_i+4\beta_o\right)\left(1-\cos\delta\right)-\sin\left(2\alpha_o\right)\left[\cos\left(4\beta_i+4\beta_o\right)\left(1-\cos\delta\right)-\left(1+\cos\delta\right)\right]\right\rfloor \\ &-P_3k_{inc}\sin\left(2\beta_i+2\beta_o-2\alpha_o\right)\sin\delta\Big\}. \end{aligned} \tag{3.6}$$

Here, δ is the retardance of the waveplate, and k_{inc} is a measure of the efficiency [89] of the linear polarizer. The latter is given by $(k_1-k_2)/(k_1+k_2)$, where k_1 and k_2 are the maximum and minimum transmittances of completely linearly polarized light through the polarizer. The retarder angle β_i is equal to (i−1) × 22.5° where i = 1, 2,…,16. Equation (3.6) describes a truncated Fourier series. The relative Stokes parameters can be obtained in terms of Fourier coefficients [32]:

$$I = f_o - \frac{f_1\cos(4\alpha_o) + f_2\sin(4\alpha_o)}{2(1-\cos\delta)(1+\cos\delta)^{-1}}, \tag{3.7}$$

$$P_1 = \frac{f_1\cos(2\alpha_o) + f_2\sin(2\alpha_o)}{Ik_{inc}(1-\cos\delta)}, \tag{3.8}$$

$$P_2 = \frac{f_2\cos(2\alpha_o) - f_1\sin(2\alpha_o)}{Ik_{inc}(1-\cos\delta)}, \text{and} \tag{3.9}$$

$$P_3 = \frac{-f_3}{Ik_{inc}\sin(\delta)} \tag{3.10}$$

where f_o, f_1, f_2 and f_3 are defined as

$$f_o = \frac{1}{16}\sum_{i=1}^{16} I_i', \tag{3.11}$$

$$f_1 = \frac{1}{16}\sum_{i=1}^{16} I_i'\cos(4\beta_i + 4\beta_o), \tag{3.12}$$

$$f_2 = \frac{1}{16}\sum_{i=1}^{16} I_i'\sin(4\beta_i + 4\beta_o), \text{and} \tag{3.13}$$

$$f_3 = \frac{1}{16}\sum_{i=1}^{16} I_i'\sin(2\beta_i + 2\beta_o - 2\alpha_o). \tag{3.14}$$

A comprehensive account of how to determine δ and k_{inc} can be found in [94]. The value of k_{inc} was determined by using an optical train consisting of an unpolarized light source (white LED), two linear polarizers, a 388.9nm interference filter and a photodetector. The polarizers were cut from the same Rolyn plastic sheet (No. 65.5305) so that their k_{inc} would be identical. The transmission axes of these optical components were first set parallel to each other. The linear polarizer right after the light source was rotated incrementally for one revolution, and the light intensity was recorded at each position. The resulting data was fitted to equation (2.15) of reference [94] to obtain k_{inc}:

$$I_i = I\left[1 + k_{inc}^2 \cos(2\theta_i)\right]. \tag{3.15}$$

Measurement of the retardance δ was accomplished by setting the transmission axes of the linear polarizers parallel to each other again. The waveplate was then inserted in between the linear polarizers. The retarder was rotated incrementally for one revolution, and the light intensity was recorded at each position. The resulting data was fitted to equation (2.16) of reference [94] to obtain δ:

$$I_i = I\left\{1 + k_{inc}^2\left[\cos^2(2\theta_i) + \cos(\delta)\sin^2(2\theta_i)\right]\right\}. \tag{3.16}$$

For our experimental setup, we obtained the following: $\delta = (1.65 \pm 0.01)$ radians, and $k_{inc} = (0.971 \pm 0.001)$, which are within 2% of the manufacturers' specifications.

The procedure to obtain the offset angles, α_o and β_o, of the linear polarizer's transmission axis and the retarder's fast or slow axis has been adapted from reference [94]. I will outline how these quantities are established. First, the transmission axis of the linear polarizer is carefully positioned in the horizontal plane of the apparatus containing the electron beam's axis (refer to figure 3.10). At this stage, $\alpha_o \approx 0$. The optical polarimeter is then removed from its support on the vacuum chamber, and is placed on a laser table without its photomultiplier tube and retarder attached. A photodiode (Thorlabs DET10A) is set behind it. The signal of the former is monitored with an oscilloscope. Light from an incandescent lamp is collimated and is shone through the polarimeter to the

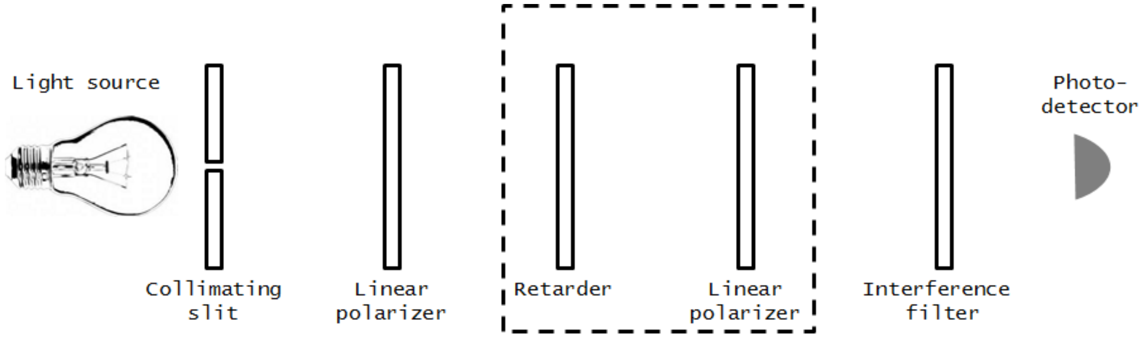

Figure 3.11: Layout for calibrating the offset angles of the polarimeter's linear polarizer and retarder, represented inside the dashed box. (See text for more details.)

photodiode. Another linear polarizer is now positioned in front of the lamp. It is rotated until the signal of the photodetector is maximized. At this point, the transmission axes of the linear polarizers are aligned. Next, the retarder is remounted in the optical polarimeter. At this point, it will be located between the linear polarizers (see figure 3.11). When the fast or slow axis of the waveplate is parallel to the transmission axes of the polarizers, the photodiode signal will be maximized again. This position of the retarder is marked. This situation corresponds to $\phi = (\beta_o - \alpha_o) = 0$. The difference ϕ between the offset angles can be obtained more accurately by rotating the retarder incrementally by 7.5° for several revolutions and measuring the light intensity at each position. The data is then fitted to:

$$I_i' = I\left\{1+\frac{1}{2}P_1 k_{inc}\left[\cos\left(4\beta_i+4\beta_o\right)\left(1-\cos\delta\right)+\left(1+\cos\delta\right)\right]\right\} \tag{3.17}$$

which is equivalent to equation (3.6) with $\alpha_o = P_2 = P_3 = 0$ to account for the fact that the light is linearly polarized along the transmission axes of the linear polarizers. In this case, β_o is actually ϕ. The latter is obtained from the fit.

This value of ϕ and the fact that $P_2 = 0$ when the transmission axis of the polarimeter's linear polarizer is aligned with the electron beam axis [95] are used to determine α_o and β_o accurately. We have previously assumed that $\alpha_o \approx 0$. If α_o is not zero but γ, β_o will be equal to $\phi + \gamma$. We can collide unpolarized electrons with helium atoms, and record the fluorescence intensity from the 388.9nm transition as the retarder is rotated incrementally for several revolutions. Such data, taken at 23.6eV, are shown in figure 3.14. We then repeat this for several electron energies. We use these data to determine P_1 and P_2. To this end, we input the data into equations (3.7) to (3.14), which are rewritten in terms of the known parameter $\phi = (\beta_o - \alpha_o)$ and the free parameter γ. The free parameter is varied and is chosen such that it minimizes P_2 as discussed in reference [94]. This value of γ is then used to evaluate α_o and β_o. Figure 3.15 shows how P_1 and P_2 vary as the energy of the electron beam changes from approximately 23.1eV to 30.1eV.

Before taking these data, an energy scale is established by measuring the optical excitation function for the helium 3^3P state. Due to contact potential differences, the electron energy is not necessarily the electric charge times the applied difference in potential between the target and electron emitter. The potential yielding electrons with energies corresponding to the threshold energy for the helium 3^3P excitation needs to be determined. Such an excitation function is shown in figure 3.12. The intensity signal starts to rise at an electron energy very close to the known value for the threshold of the

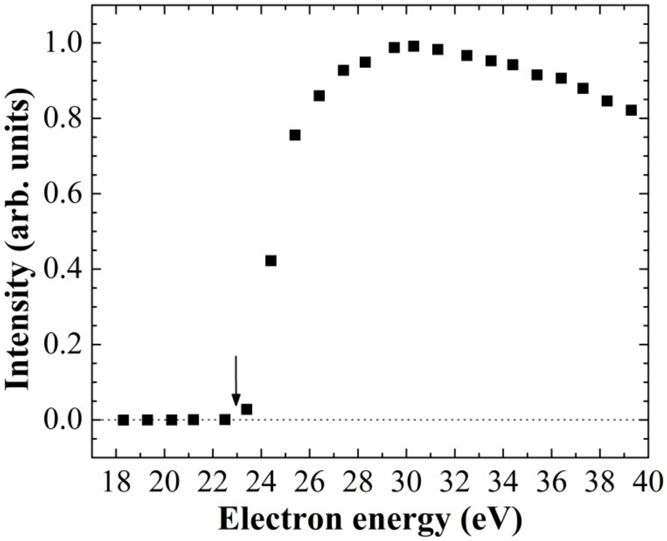

Figure 3.12: The electron impact excitation function for the transition of helium $2^3S \rightarrow 3^3P$, 388.9 nm. Arrow indicates the known threshold energy.

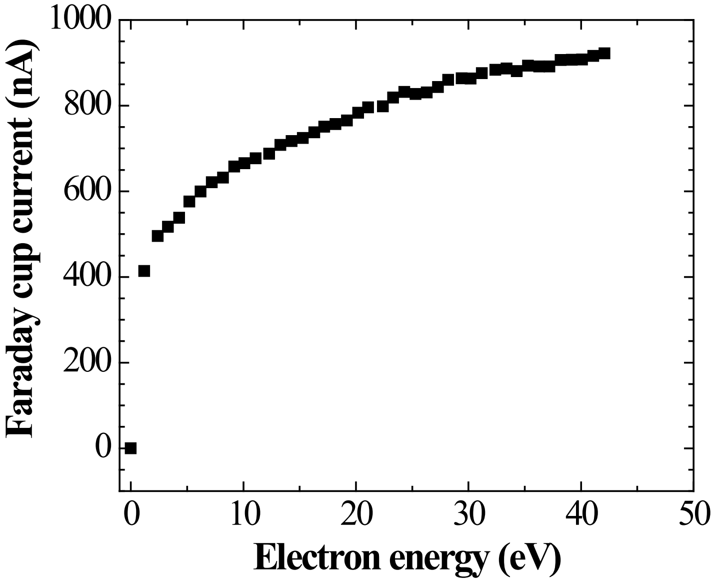

Figure 3.13: Profile of the Faraday cup current as a function of electron energy. The energy spread of the electron beam is determined to be about 1.5 eV. (See text for details.)

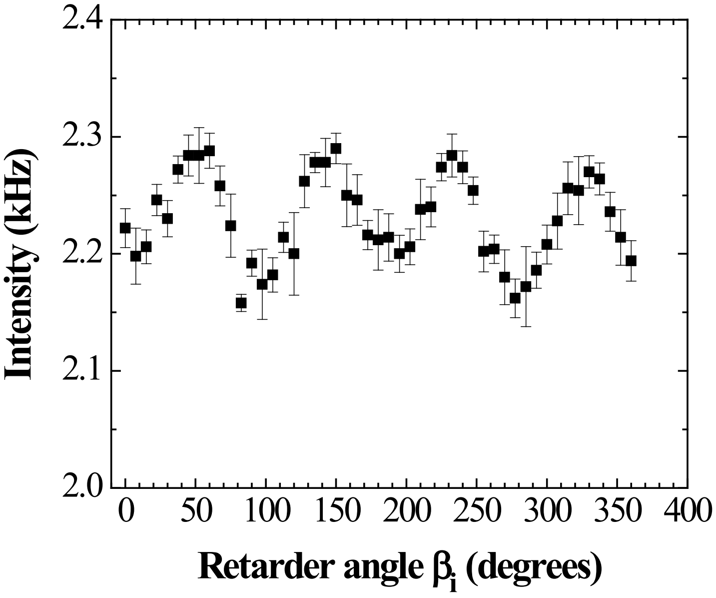

Figure 3.14: Variation in fluorescence intensity as the retarder is rotated. The electron-beam energy was 23.6 eV. At this energy, the efficiency of the polarimeter is about 2.3 Hz/nA for a chamber pressure of 1 mTorr, as read by the Convectron gauge corrected for helium gas. This number rises to ~20 Hz/nA for electron energies corresponding to the peak of the optical excitation function.

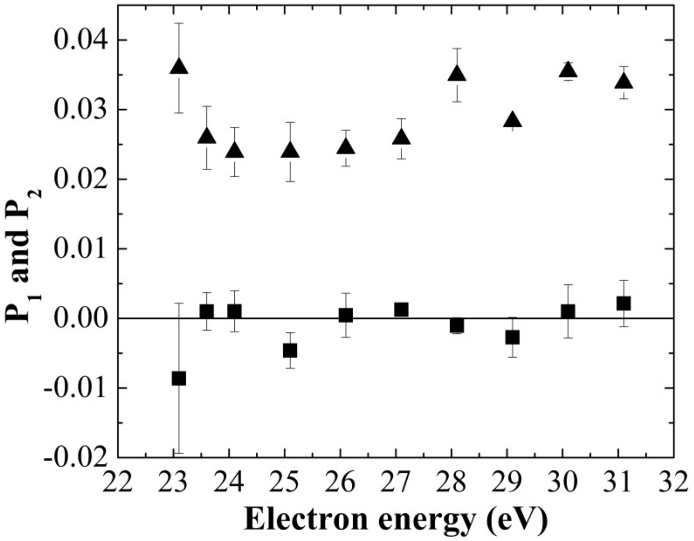

Figure 3.15: Energy dependence of P_1 (▲) and P_2 (■). The error bars denote the standard deviation of the mean of five data sets taken through five complete retarder revolutions Here, $\alpha_o = (0 \pm 1)^o$ and $\beta_o = (37 \pm 1)^o$.

$3^3P \rightarrow 2^3S$ He transition. Therefore, discrepancies in the electron energy due to contact potential differences amount to less than 1eV. Figure 3.13 shows how the current recorded on the Faraday cup varied as a function of electron energy. These data are equivalent to what would be obtained from performing a retarding field analysis on the beam (more information on this technique can be found in section 4.6.1) because the energy of electrons incident on the helium gas in the polarimeter chamber was actually changed by applying retarding potentials on the target cylinder (part "H" in figure 2.30). Hence, figure 3.13 can be used to estimate the energy spread of the electron beam with no gas in the collision cell, and it is found to be ~1.5eV.

Once the polarimeter has been calibrated and the values of P_1 essential to equation (4.5) have been evaluated, the relative Stokes parameter P_3 is obtained by the "2-point method" [92] during the operation of the source:

$$P_3 = \frac{I^{'}(\beta_o = 135^o) - I^{'}(\beta_o = 45^o)}{I^{'}(\beta_o = 135^o) + I^{'}(\beta_o = 45^o)} \tag{3.18}$$

where $I^{'}(\beta_o = 45^o)$ and $I^{'}(\beta_o = 135^o)$ are the normalized fluorescence intensities taken with the retarder's fast (or slow) axis at 45^o and at 135^o to the transmission axis of the optical polarimeter's linear polarizer. By alternating between these two angles, N pairs of measurements are made. At each step, the photomultiplier tube counts the number of photons for ~3s. During this time period, a reading of the polarimeter chamber pressure and the average of 120 samples of the Faraday cup current are also acquired by Labview software.

I will now describe how the data is normalized and is analyzed to find the polarization of the electron beam. Despite turning the ambient light off during data collection, the count rates taken above the threshold of the 388.9nm helium transition are still contaminated by other background sources. This background contribution must be determined and compensated for. It consists of two components: an electron-beam-independent part and an electron-beam-dependent portion. Light from the glowing filament contributes mainly to the electron-beam-independent part while the electron-beam-dependent portion comprises photons from the electron-impact excitation of background gases in the polarimeter chamber and their subsequent de-excitation. The former is evaluated by taking N_1 pairs of measurements with no electron beam reaching the polarimeter chamber. To this end, a large enough retarding potential is applied on the last electrodes of the electron gun to prevent the beam from making its way to the polarimeter chamber. The electron-beam-dependent portion of the background contamination is determined by taking N_2 pairs of measurements below the threshold energy of the helium 3^3P excitation.

Let $(CR)_{nobeam,45}$ be a measured count rate with the retarder's axis at 45^{o} to the linear polarizer's transmission axis and with no electron beam reaching the polarimeter. The average of all N_1 measurements of $(CR)_{nobeam,45}$ is calculated. We label this average $\overline{(CR)_{nobeam,45}}$. This procedure is repeated for the data taken with the retarder's axis at 135^{o} to obtain $\overline{(CR)_{nobeam,135}}$. Let $(CR)_{below,45}$ be a measured count rate corresponding to an electron energy below the threshold of the helium 388.9nm transition, and with the retarder's axis at 45°. The next step involves the subtraction of $\overline{(CR)_{nobeam,45}}$ from each of the N_2 measurements of $(CR)_{below,45}$. This process gets rid of the contribution of the electron-beam-independent background contamination from the count rates taken below the threshold energy. The resulting quantities are normalized to their respective Faraday cup current $I_{below,45}$ and polarimeter chamber pressure $P_{below,45}$:

$$(CR)_{below,45,norm} = \frac{(CR)_{below,45} - \overline{(CR)_{nobeam,45}}}{I_{below,45} \times P_{below,45}}. \tag{3.19}$$

We now have N_2 normalized count rates corresponding to the retarder's axis at 45°, and to the electron energy being below the threshold energy. The average of these N_2 points is determined. We label this quantity $\overline{(CR)_{below,45,norm}}$. These steps are repeated for the data taken with the retarder's axis at 135° to obtain $\overline{(CR)_{below,135,norm}}$.

Afterwards, N_3 pairs of measurements are taken with the electron beam energy above the threshold of the 388.9nm helium transition. The quantities $\overline{(CR)_{nobeam,45}}$, $\overline{(CR)_{nobeam,135}}$, $\overline{(CR)_{below,45,norm}}$, and $\overline{(CR)_{below,135,norm}}$ are used to compensate for background contamination from these measurements. As usual, I will focus on the data taken with the retarder's axis at 45°. First, $\overline{(CR)_{nobeam,45}}$ is subtracted from each of the N_3 data points $(CR)_{above,45}$. The resulting quantity is normalized to its respective Faraday cup current $I_{above,45}$ and polarimeter chamber pressure $P_{above,45}$. Next, the mean normalized count rate obtained below the threshold energy is subtracted from the N_3 normalized count rates collected above the threshold energy:

$$(CR)_{above,45,norm} = \left[\frac{(CR)_{above,45} - \overline{(CR)_{nobeam,45}}}{I_{above,45} \times P_{above,45}} \right] - \overline{(CR)_{below,45,norm}}. \tag{3.20}$$

This procedure is repeated for the data collected with the retarder's axis at 135° to obtain $(CR)_{above,135,norm}$. For each of the N_3 pairs of normalized data points, P_3 is determined:

$$P_3 = \frac{(CR)_{above,135,norm} - (CR)_{above,45,norm}}{(CR)_{above,135,norm} + (CR)_{above,45,norm}}. \tag{3.21}$$

We now have a distribution of P_3 values. The mean and the standard error of this distribution are calculated to find $\overline{P_3}$ and its uncertainty.

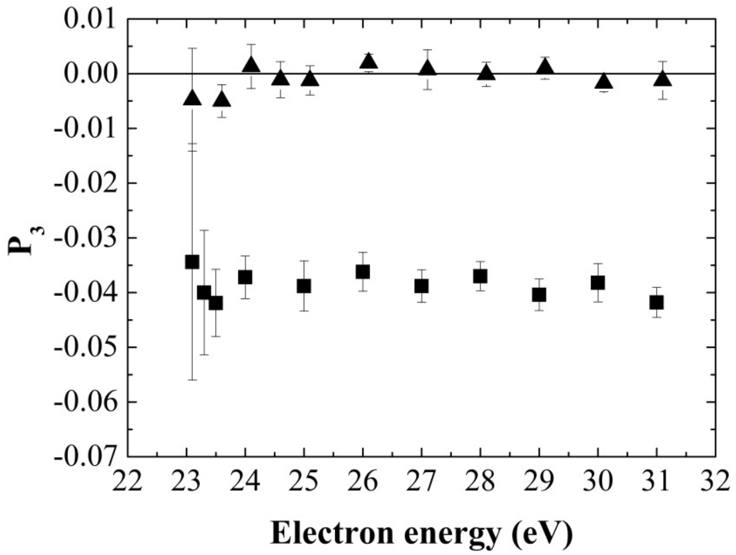

Figure 3.16: Energy dependence of P_3 with unpolarized (▲) and polarized (■) electrons.

During the operation of the source, $\overline{P_3}$ is found both with and without the pump laser going through the collision cell. If there is any residual $\overline{P_3}$ without the pump light, it is subtracted for the one with the pump light. The uncertainty in the resulting quantity is evaluated in quadrature. Using this value of P_3 as well as P_1 for the particular electron energy used in the polarimetric measurements, we can determine the polarization P_e of the electron beam with equation (4.5). The uncertainty in P_e is calculated by propagating those in P_3 and P_1. Overall, the uncertainties in δ, k_{inc}, α_o and β_o contribute negligibly. Figure 3.16 shows the energy dependence of $\overline{P_3}$ with unpolarized and polarized electrons from the optically-pumped electron spin filter.

CHAPTER 4. Results

In this study, I varied certain parameters of the source to see whether they affect the electron polarization. Such knowledge will serve as a guide to build better optically-pumped polarized electron sources. Among the factors investigated are:

1. the pump laser's wavelength (electron-spin reversal phenomenon),
2. the pump laser's power,
3. the pump laser's line-width,
4. the choice of quenching gas,
5. the driving electric field across the collision cell, and
6. the energy of the electrons incident on the gas mixture.

In the following sections, I present our findings.

4.1 Dependence of electron polarization on the pump laser wavelength

In this experiment, I looked at how the electron polarization P_e is affected by the pump laser's wavelength for a given spectral line-width and light polarization. The optical state-preparation of rubidium atoms with the optical pumping technique is sensitive to these pump laser parameters. It is therefore important to find parameters yielding high degrees of orientation of the rubidium vapor's electronic spin, especially since in this system, free, unpolarized electrons undergo spin-exchange collisions with the alkali atoms:

$$e(\uparrow) + Rb(\downarrow) \rightarrow e(\downarrow) + Rb(\uparrow). \qquad (4.1)$$

and P_e follows P_{Rb} closely as was demonstrated by Batelaan *et al.* [29] (see figure 1.11). Not exercising care in choosing the above-mentioned pump light properties can have adverse effects on the polarization of the rubidium vapor as was shown by Norrgard *et al.* [64]. For example, if the pump light is not circularly-polarized but is contaminated with a component of linear polarization, and is simultaneously spectrally-narrow such that only a few of the hyperfine transitions are being effectively pumped, a reversal in the rubidium vapor's electronic spin polarization is observed as the pump wavelength is detuned from the rubidium D1 line center [64] (see figure 4.1). We noted a similar reversal in the polarization of the electron beam when the pump wavelength was varied; it followed the behavior of P_{Rb} closely. In the following sections, I will explain qualitatively why this reversal in P_{Rb}, and hence, in P_e, occurs. I will then briefly go through the experimental setup. Finally, I will present our results.

4.1.1 Origin of the electron-spin reversal phenomenon

In optical pumping experiments to orient a vapor of, say, rubidium-85 parallel (or anti-parallel) to the quantization axis, we want all atoms to transfer to the highest (or lowest) m_F sublelvel of the ground state hyperfine level with the largest quantum number F. Thus, for rubidium-85 (refer to figure 4.1b and 4.2 for the location of the different hyperfine transitions with respect to the D1 line center, and for energy level

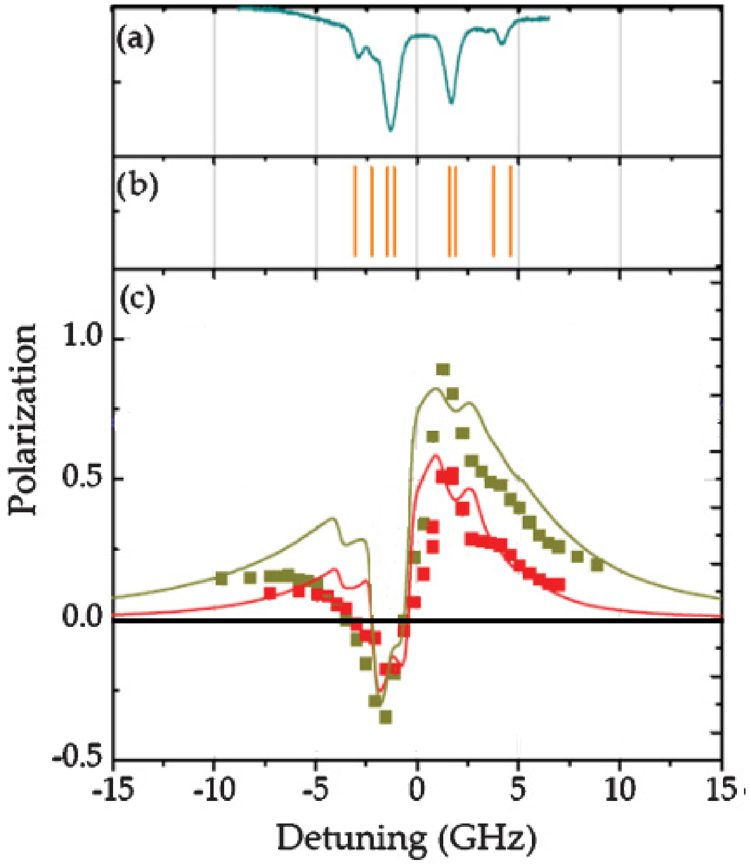

Figure 4.1: (a) Absorption scan of the probe beam from a Rb reference cell. (b) The positions of the hyperfine ground (g) to excited (e) level transitions of Rb; from left to right: ^{87}Rb $F_g = 2 \rightarrow F_e = 1$, ^{87}Rb 2 → 2, ^{85}Rb 3 → 2, ^{85}Rb 3 → 3, ^{85}Rb 2 → 2, ^{85}Rb 2 → 3, ^{87}Rb 1 → 1, ^{87}Rb 1 → 2. (c) Measured (data points) and calculated (curves) polarization of a natural-abundance rubidium vapor as a function of the pump laser frequency. Red data: 0.1 torr nitrogen, 8.4×10^{12} cm^{-3} rubidium density; red curve: 0.1 torr nitrogen, 99.5% σ^+ light polarization. Green data: 1.0 torr nitrogen, 8.8×10^{12} cm^{-3} rubidium density; green curve: 1.0 torr nitrogen, 99.5% σ^+ light polarization. (Adapted from [64].)

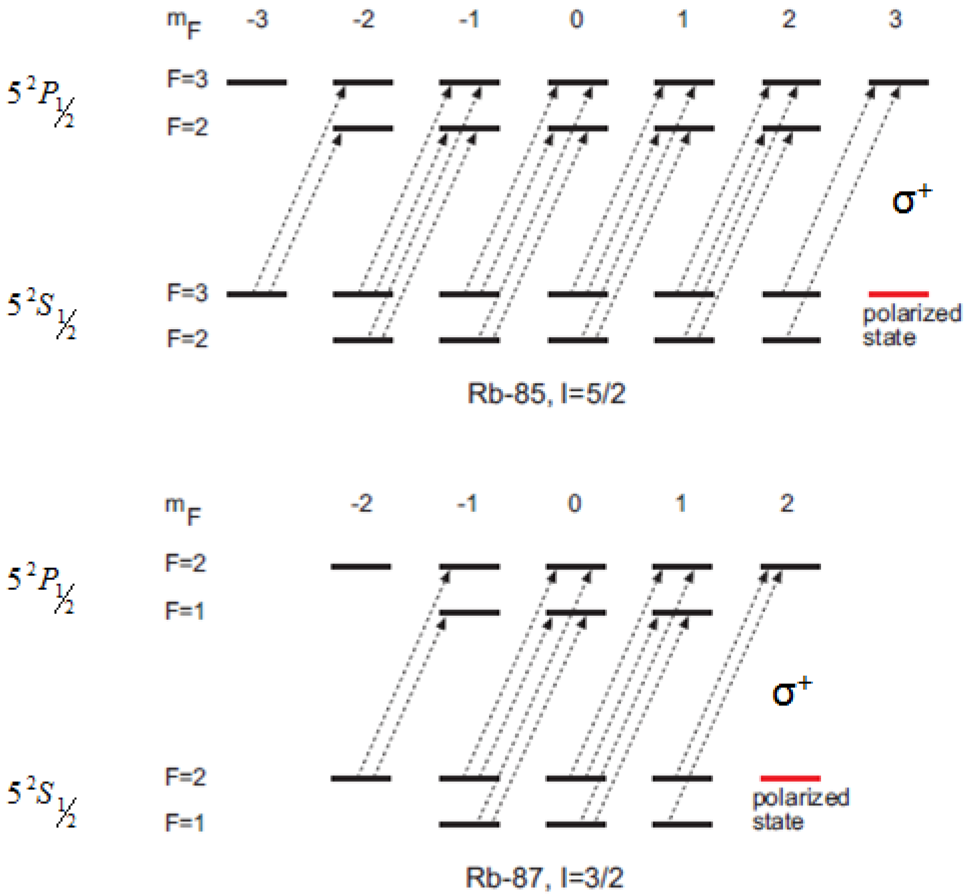

Figure 4.2: Schematic of optical pumping for both rubidium-85 and rubidium-87. The incident light is σ^+ circularly-polarized light. The electric dipole selection rules dictate that Δm_F is +1. (Adapted from [96].)

diagrams of the two Rb isotopes), we want the atoms to be in the $(F_g = 3, m_F = 3)$ sublevel, corresponding to complete orientation of the alkali vapor parallel to the quantization axis (or in the $(F_g = 3, m_F = -3)$ sublevel which corresponds to complete orientation anti-parallel to the quantization axis). Such a situation is desired because in the $(F_g = 3, m_F = 3)$ sublevel, the probability of finding the outer electron of the alkali atom with $m_S = 1/2$ is 1. Hence, the expectation value of the electronic spin of the rubidium vapor will be $1/2$.

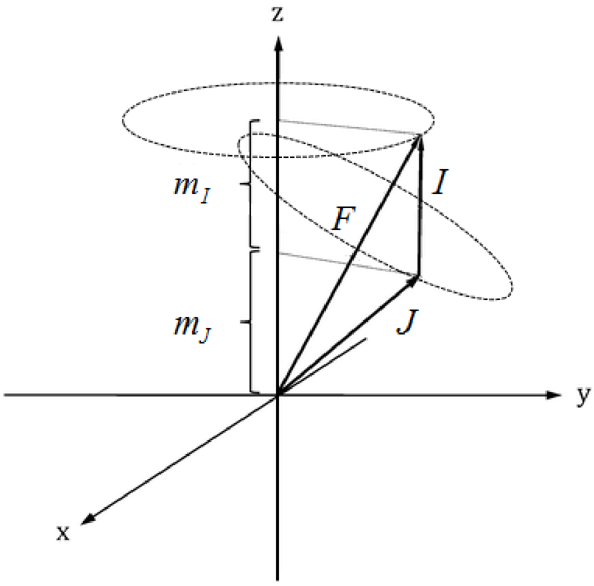

Figure 4.3: Vector coupling of the nuclear (*I*) and electronic (*J*) angular momenta. Here, m_I and m_J are the components of the nuclear and electronic angular momenta along the quantization axis z. (Adapted from [97].)

To understand the previous fact, we should keep in mind that the quantum number $m_F = m_I + m_J$ (see figure 4.3), and $m_J = m_L + m_S$. In the $5\,^2S_{1/2}$ state, $m_L = L = 0$.

Therefore, in the ground state of rubidium-85, $m_J = m_S$. Since the angular momentum J is $1/2$, its component m_J along the quantization axis $\vec{z}$ can be either $1/2$ or $-1/2$. A rubidium-85 atom also has a nuclear spin I of $5/2$, implying that its z-component m_I can be $-5/2$, $-3/2$, $-1/2$, $1/2$, $3/2$ and $5/2$. Now, in the $(F_g = 3, m_F = 3)$ sublevel, the only combination of m_I and $m_J = m_S$ which will yield an m_F of 3 is $(m_I = 5/2, m_J = m_S = 1/2)$, and thus, the rubidium atom is oriented parallel to the quantization axis.

Complete orientation of the vapor is ideally achieved with resonant 100% circularly polarized light. The electric dipole selection rules dictate that with circularly-polarized pump light, Δm_F must be equal to ± 1. With σ^+ light, Δm_F is $+1$. Therefore, the atoms will shuttle to sublevels with higher m_F, and eventually, settle in the “dark” or completely “polarized” state $(F_g = 3, m_F = 3)$ where they cannot absorb any more photons (see figure 4.2).

If the σ^+ pump light is spectrally-narrow such that we are effectively pumping on the $F_g = 3 \rightarrow F_e = 2,3$ transitions, only the population of the sublevels of $F_g = 3$ will be excited, in contrast to the situation described in figure 4.2. Some of these excited atoms will decay to the $F_g = 2$ sublevels. Unless there exists mechanism to excite them again and transfer them to the $F_g = 3$ state, they will stay in the “dark” $F_g = 2$ level because the pump light is not resonant with the $F_g = 2 \rightarrow F_e = 2,3$ transitions. Such a situation will prevent the alkali vapor from achieving complete orientation because unlike the

$(F_g = 3, m_F = 3)$ and $(F_g = 3, m_F = -3)$ levels, the other sublevels of the ground state are linear superpositions of two states from the uncoupled basis $(m_I, m_J = m_S)$. For instance,

$$(F_g = 2, m_F = 2) \rightarrow -\sqrt{\frac{1}{6}}(m_I = \frac{3}{2}, m_J = \frac{1}{2}) + \sqrt{\frac{5}{6}}(m_I = \frac{5}{2}, m_J = -\frac{1}{2}),$$

and a rubidium atom in this sublevel has a higher probability of being measured with $m_S = -1/2$.

A combination of a spectrally-narrow laser, for example with a FWHM of ~500MHz, and circularly-polarized pump light which is contaminated with a linearly-polarized component will affect the orientation of the alkali vapor more acutely. Balykin [98] showed theoretically that circularly-polarized light with 1% linear polarization will cause rapid depletion of the "dark" state population in optical pumping experiments. His study was, however, limited to determining how the population of the "dark" state varied with time. In-depth studies conducted by Norrgard *et al.* [64] revealed startling consequences of pumping with a spectrally-narrow laser and imperfect circularly-polarized light. Their data, shown in figure 4.1 for nitrogen pressures of 0.1Torr and 1Torr, displays a reversal in the electronic spin orientation of the rubidium vapor for a range of pump wavelengths even though the helicity of the light was constant and predominantly circular (~99.5%).

The reversal occurs when the ~500 MHz spectrally-wide pump laser is on resonance with the $F_g = 3 \rightarrow F_e = 2,3$ transitions. Thus, the pump laser cannot effectively pump the $F_g = 2 \rightarrow F_e = 2,3$ transitions. While most rubidium atoms are transferred to the $(F_g = 3, m_F = 3)$ sublevel by absorption of the predominantly σ^+ light,

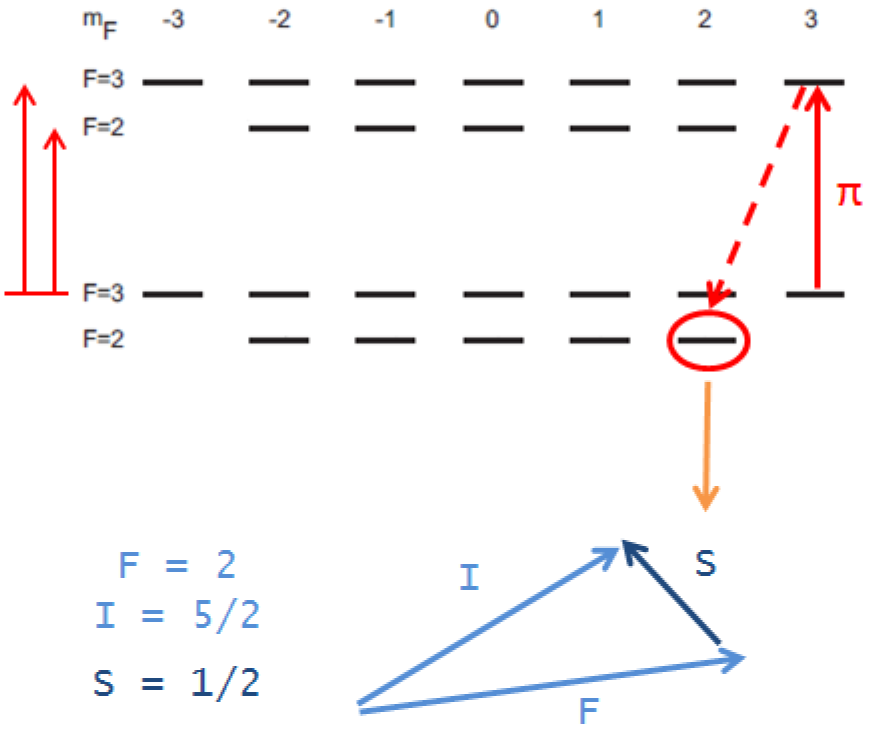

Figure 4.4: Pump light on resonance with the $F_g = 3 \rightarrow F_e = 2,3$ transitions of rubidium-85. The $(F_g = 3, m_F = 3)$ sublevel is not a "dark" state when the pump light is contaminated with a linearly-polarized (π) component. In this case, rubidium atoms accumulate in the $(F_g = 2, m_F = 2)$ state where the expectation value of the electronic spin is negative.

the linearly polarized component drives the population of this sublevel to the $F_g = 2$ state, especially the $(F_g = 2, m_F = 2)$ sublevel (see figure 4.4). In essence, there is no dark state in this case because atoms in the $(F_g = 3, m_F = 3)$ sublevel can still absorb the linear component of the pump light. The pump light cannot depopulate the $F_g = 2$ sublevels effectively because its spectral profile does not overlap significantly with the line-shape of the $F_g = 2 \rightarrow F_e = 2,3$ transitions. The atoms remain stuck in the $F_g = 2$ state. Consequently, the outer electrons of the rubidium atoms have a higher probability of being measured with $m_S = -1/2$ as discussed above, and the alkali vapor's electronic spin polarization is reversed even though the pump light is predominantly σ^+ light.

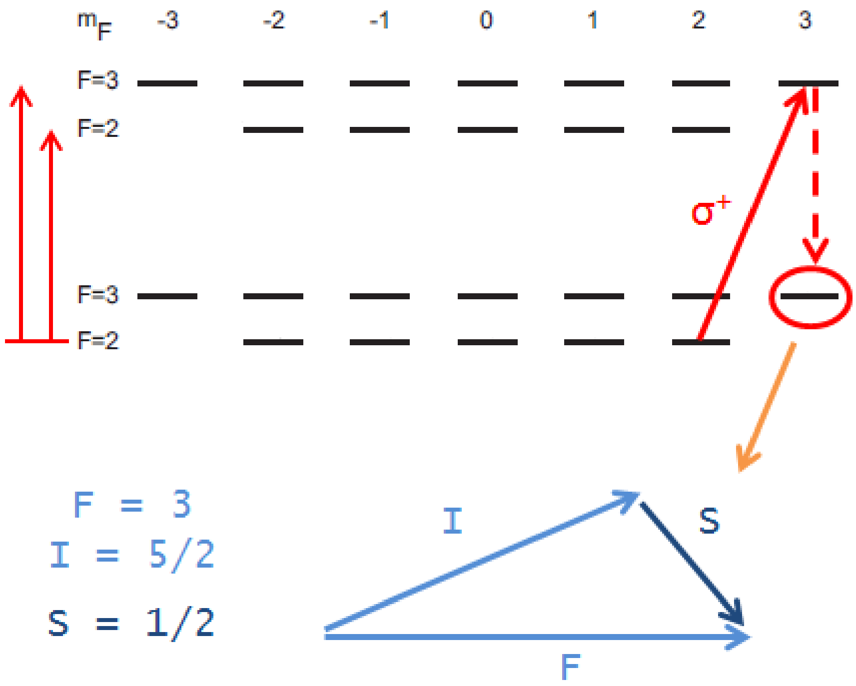

Figure 4.5: Pump light (σ^+) on resonance with the $F_g = 2 \rightarrow F_e = 2,3$ transitions of rubidium-85. Rubidium atoms accumulate in the $F_g = 3$ sublevels with high m_F quantum numbers. Expectation value of the alkali vapor's electronic spin is observed to be positive in this case.

If the pump light is on resonance with the $F_g = 2 \rightarrow F_e = 2,3$ transitions instead, the population of the $F_g = 2$ sublevels will be depleted. In this case, absorption of both the right-circularly-polarized and linearly-polarized components of the pump light transfer atoms to the $F_g = 3$ state. Since the light is predominantly circularly polarized, most of the atoms will move to sublevels with higher m_F quantum numbers. In this case, the majority of rubidium particles have larger probabilities of being measured with

$m_S = 1/2$. The rubidium electronic spin polarization P_{Rb} is observed to be in the opposite direction to that of the previous case (see figure 4.5). This discussion forms the basis of Norrgard *et al*'s [64] explanation of the electronic spin reversal phenomenon in optically-pumped rubidium vapor.

4.1.2 Experimental setup

In this experiment, the polarization of the rubidium vapor and that of the electron beam were measured simultaneously as a function of pump laser wavelength. The pump light's spectral bandwidth was constant throughout the process. As the pump beam's wavelength was swept from 794.9675 nm to 794.9950 nm during the data-taking process, the retardance of the wave-plate (part labeled "QWP" in figure 2.16) responsible for making the light circularly-polarized varied by about 30μrad [99]. According to Mueller calculus [100], this would affect the pump light's helicity negligibly; we can assume it was constant during this study. In this particular experiment, we were able to send the probe beam downstream past the filament, along the axis of the apparatus. The arrangement outlined in figure 2.16 was used to measure the rubidium vapor's density [Rb] and electronic-spin orientation P_{Rb} by the Faraday effects as discussed in chapter 3.

Measurements were taken when the apparatus had reached equilibrium. In other words, I waited several hours for the magnetic field, the electron current, the temperature of the system and [Rb] to stabilize. The rubidium vapor was then polarized by admitting the pump light to the collision cell. The polarization of the alkali vapor was inferred from the rotation of the plane of polarization of the probe beam as outlined in section 3.5.

Afterwards, the probe beam was blocked, and measurements were performed to determine the electron beam's polarization P_e. These steps were repeated at each pump wavelength. Once data related to P_e and P_{Rb} had been gathered, the pump beam was blocked. The rubidium density was then measured. For such a measurement, the magnetic field had to be turned off at some point. The rubidium density is therefore determined at the very end of the experimental run so that we do not have to wait for the system to stabilize again. The electromagnets dissipate large quantities of heat to the vacuum chambers. Turning the former off cools the latter, which may affect the thickness of alkali vapor. Therefore, the relevant steps in measuring the rubidium density were done as soon as the electromagnets are off.

For this experiment, the quenching gas employed was nitrogen, at a pressure of ~200mTorr. The rubidium density was measured to be $(5.0 \pm 0.6) \times 10^{12}$ atoms/cm^3. The free, unpolarized electrons incident on the gaseous mixture had energies of ~1eV. The current reaching the Faraday cup was ~200nA. The potential on electrodes "j" and "k" (see figure 3.1) was -31.5V with respect to ground. The pump light's spectral bandwidth was ~2GHz and its power was ~650mW.

4.1.3 Results

The results of this experiment are shown in figure 4.6. The polarization of the electron beam P_e tracks the rubidium polarization P_{Rb} closely. In order to extract electron beams with the highest polarization, it is therefore important to use parameters delivering the best electronic spin orientation of the alkali vapor. These data also allow us to find the "polarization transfer efficiency" α, the constant of proportionality between P_e and P_{Rb} [101]:

$$P_e = \alpha P_{Rb}. \tag{4.2}$$

By plotting P_e as a function of P_{Rb}, we can evaluate this polarization transfer efficiency. Such plots are shown in figures 4.7 and 4.8 both for this system and for the electron spin filter built by Batelaan *et al.* [29]. A polarization transfer efficiency of ~25% is obtained in the former case while the latter yielded ~46%.

We can find the factors affecting α by solving the rate equation for P_e [62, 102]:

$$\frac{dP_e}{dt} = k_{SE}\left[Rb\right]P_{Rb} - k_{SE}\left[Rb\right]P_e - \Gamma_e P_e. \tag{4.3}$$

The first term describes the transfer of polarization from oriented rubidium atoms to free, unpolarized electrons while the second refers to the opposite process where polarized electrons undergo spin-exchange collisions with unpolarized rubidium particles. Here, k_{SE} is the rubidium-electron spin-exchange rate coefficient, $\left[Rb\right]$ the alkali density, and Γ_e the relaxation rate of the electron polarization through processes other than spin-exchange collisions such as magnetic spin-flip processes occurring either in electron collisions with the chamber walls or with the rubidium atoms or the buffer gas. The spin-exchange rate coefficient k_{SE} is the product of the rubidium-electron relative velocity and its corresponding spin-exchange cross-section, averaged over the distribution of relative velocities. The solution to the rate equation is [62, 102]

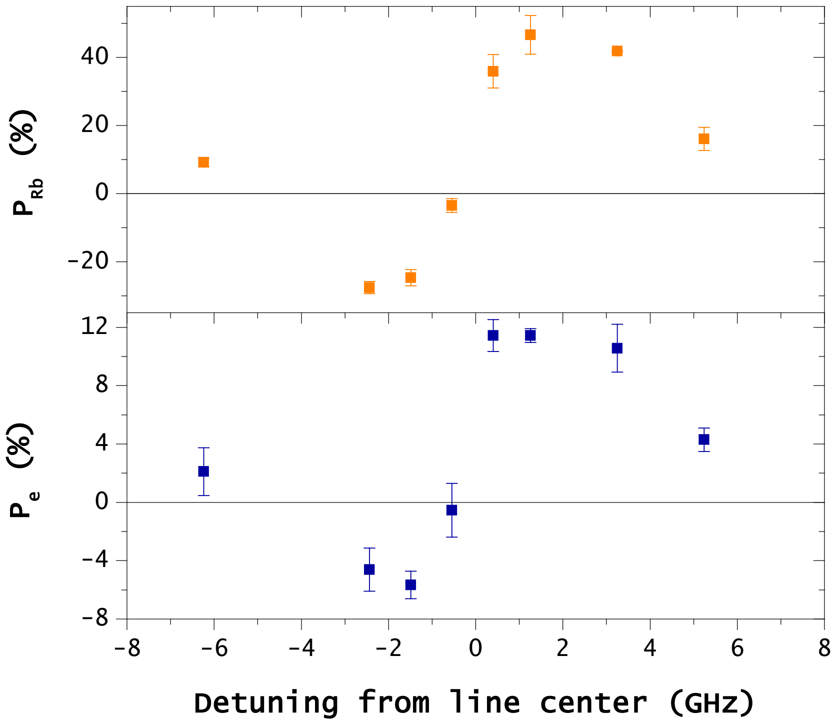

Figure 4.6: Behavior of P_{Rb} and P_e as the pump laser's frequency is varied across the rubidium D1 absorption line. The electron polarization follows that of the rubidium vapor closely, even exhibiting the electron-spin reversal phenomenon. In this experiment, [Rb] was $(5.0 \pm 0.6) \times 10^{12}$ atoms/cm^3, the buffer gas was nitrogen at a pressure of ~200mTorr, the incident electron energy was 1eV, the pump light's spectral bandwidth was ~2GHz, and its power was ~650mW.

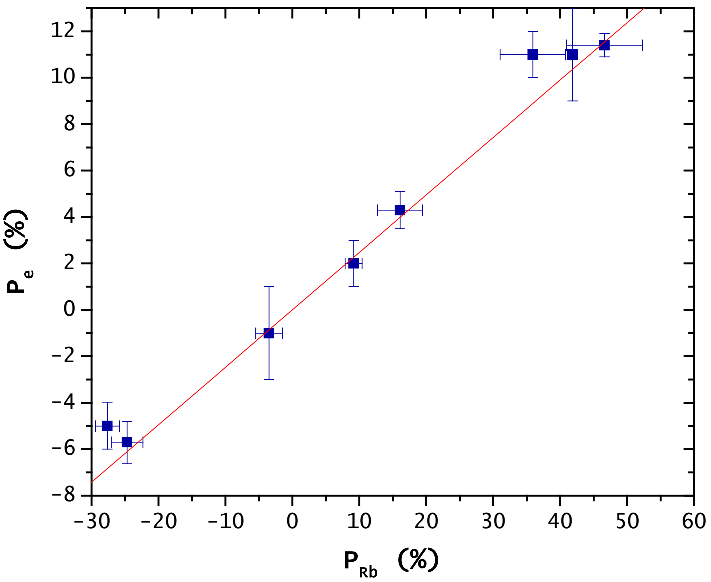

Figure 4.7: Determination of the polarization transfer efficiency (see text on page 91) of our system for the data of figure 4.6. A linear fit to the data yields $P_e = (0.25 \pm 0.01) P_{Rb}$. The polarization transfer efficiency is therefore ~25%.

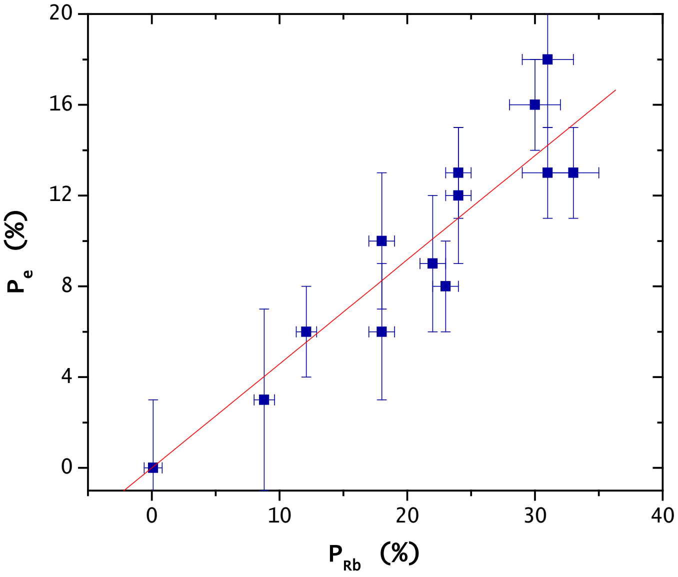

Figure 4.8: Polarization transfer efficiency for the spin filter developed by Batelaan *et al.* [29]. The experimental conditions included an [Rb] of 7×10^{11} atoms/cm^3, the buffer gas was nitrogen at a pressure of 400mTorr, and the pump light's spectral bandwidth was ~40GHz. The outlier with P_e of 27% for a pump laser power of 150mW was not included. A linear fit to the data yields $P_e = (0.46 \pm 0.02) P_{Rb}$. The polarization transfer efficiency was ~46%.

$$
\begin{aligned}
P_e\left(t_c\right) &= \frac{k_{SE}\left[Rb\right]}{k_{SE}\left[Rb\right]+\Gamma_e}\left\{1-\exp\left[-\left(k_{SE}\left[Rb\right]+\Gamma_e\right)t_c\right]\right\}\cdot P_{Rb} \\
&= \alpha\cdot P_{Rb}.
\end{aligned}
\tag{4.4}
$$

Hence, the polarization transfer efficiency depends on several factors, namely the relative velocity between rubidium atoms and free electrons, the spin-exchange cross-section, the rubidium density, and the interaction time t_c between the electron beam and the alkali vapor.

This result may explain the higher polarization transfer efficiency for the older spin filter [29] despite the lower rubidium density used (Batelaan *et al.*: 7×10^{11} atoms/cm^3, current system: 5×10^{12} atoms/cm^3). The cell length in the former case was ~7cm, and they used a nitrogen pressure of 0.4Torr, compared to 0.2Torr and a length of ~3cm for the current setup. A longer cell length causes free electrons to interact with the gaseous mixture, especially the polarized alkali vapor, for a longer time interval. It can be seen from the equation above that a longer interaction time will lead to higher P_e. Indeed, as the interaction time increases, electrons are more likely to undergo spin-exchange collisions with polarized rubidium atoms. The higher nitrogen pressure, on the other hand, causes the frequency of collisions between free electrons and the molecules to be larger. Electrons will lose more energy to the nitrogen. This will increase the spin-exchange cross-section experienced by the free electrons (see figure 1.12), which in turn, will raise the spin-exchange rate coefficient k_{SE}, and hence, P_e. Another consequence of the higher nitrogen pressure and collision frequency is that electrons will undergo longer effective path lengths [29] as they travel through the gas. By scattering multiple times on the nitrogen molecules, the total distance traveled by the particles through the collision cell becomes longer. From the random walk analysis performed by Batelaan *et al.* [29], the effective path length (*EPL*) of electrons in the gas will be approximately

$$EPL = \frac{L^2}{\lambda}, \tag{4.5}$$

where L is the cell length and λ the mean free path. Assuming no energy loss as the particles moved through the nitrogen gas, the effective path length of, for example, 1eV electrons in the system built by Batelaan *et al.* [29] would have been over 10 times longer than in the present apparatus. A longer effective path length would increase the probability of electrons undergoing spin-exchange collisions with the alkali vapor. All these factors may have improved the transfer of polarization from oriented rubidium atoms to electrons in the former case.

The ratio ξ of polarization transfer efficiencies α obtained from figures 4.7 (present system) and 4.8 (apparatus of Batelaan *et al.* [29]) is about 1.8. Using the expression for α in equation 4.4 and that of the effective path length in 4.5, we proceed to make a rough estimate of ξ to see how it compares with the experimentally-determined value of 1.8. To simplify this problem, we assume that all electrons are drifting with a constant energy of 1eV, and that k_{SE} is given by the mean relative velocity between free electrons and rubidium atoms times the average spin-exchange cross-section σ_{SE}. Since $\sigma_{SE} = 3.1\times10^{-15} cm^2$ for 1eV electrons [57], and their drift velocity in nitrogen gas is $\sim 9\times10^5 cm/s$ [103], $k_{SE} \approx 2.8\times10^{-9} cm^3/s$. The times t_c taken by electrons to travel the effective path lengths in the system of Batelaan *et al.* [29] and the current one are approximately $6.8\times10^{-4}s$ and $6.3\times10^{-5}s$, respectively. The relaxation rates Γ_e of the electron polarization are unknown. Since we are only looking for a ballpark figure for ξ, we assume Γ_e is negligible. Given these considerations, we estimate the theoretical ratio of polarization transfer efficiencies to be ~1.4, which is within 20% of the experimental value of 1.8.

4.2 Effect of pump light's bandwidth on the electron polarization

The laser line-width is another important parameter in the optical pumping of rubidium atoms. It can have an impact on how much of the light's spectral profile interacts with the atomic line-shape function of the rubidium D1 transition. In other words, it can affect how much of the spectral profile is on resonance with the rubidium atoms in the vapor. A preliminary study of how the pump light's bandwidth affects the electron polarization was carried out since the present pump laser allows us to broaden the full width at half maximum (FWHM) of its quasi-Gaussian spectral profile. An in-depth investigation of the effects of the pump light's spectral width on the polarization of rubidium vapor in a sealed glass cell is currently being conducted by E. Litaker.

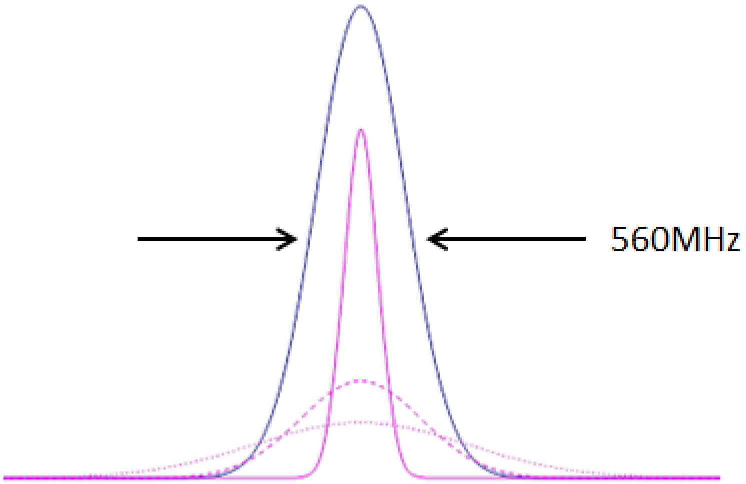

Figure 4.9: Simplified representation of the experiment. The blue curve denotes a Doppler-broadened absorption profile while the magenta curves correspond to different spectral profiles of the pump light. When the pump light has a large bandwidth, a significant portion of its spectral profile is not on resonance with the transition. Thus, more light travels through the vapor unabsorbed. At 100°C, a typical temperature used in this study, the Doppler effect causes the absorption profile due to each rubidium D1 hyperfine transition to be broadened by about 560MHz.

In this experiment, I varied the pump light's spectral bandwidth, and I measured the resulting electron polarization. Figure 4.9 shows the laser's Gaussian spectral profile on resonance with the Doppler-broadened absorption profile of an idealized rubidium hyperfine transition. Initially, the pump light has a small bandwidth, which is gradually increased. Such a procedure affects the mean rate at which an unpolarized rubidium atom absorbs photons. This quantity is given by the integral, with respect to frequency, of the product of the absorption cross-section for light on resonance with the transition, and the photon flux associated with the laser's spectral profile [104, 105].

In this investigation, I used nitrogen as the buffer gas, at a pressure of 110mTorr. The rubidium density was approximately 6×10^{12} atoms/cm^3. The electrons were incident on the collision cell with ~2eV of energy. The Faraday cup collected a steady current of about 350nA. The pump light was tuned to 794.9762nm, which produced the highest P_{Rb} and P_e in the wavelength-dependence study of section 4.1. Its power was measured to be 560mW after the quarter wave-plate "QWP" in figure 2.9.

The results of this investigation are shown in the top panel of figure 4.10. Data were taken for both unbroadened pump light and spectrally-broadened light. The spectrum analyzer used in this study could not resolve line-widths narrower than 160MHz because it contained mirrors with a free spectral range of 30GHz and a finesse of 188. The unbroadened pump light is, however, quoted as having a FWHM of ~10MHz by the laser's manufacturer, Sacher Lasertechnik. The largest broadening studied corresponds to a FWHM of 2.2GHz. The data show that the electron polarization rises steadily as the pump light's line-width is increased until it reaches 1.8GHz. It then decreases for the larger line-width.

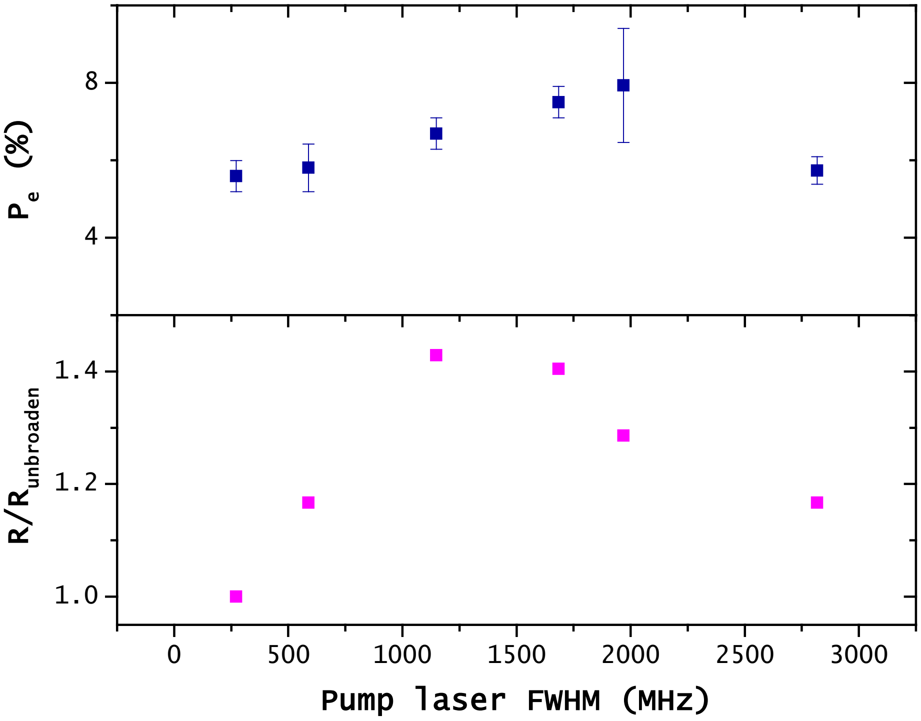

Figure 4.10: Shown in the top panel is the variation of the electron polarization with the bandwidth of the pump light's spectral profile. The bottom panel represents a theoretical determination of the optical pumping rate due to the different laser line-widths studied. The optical pumping rates have been normalized to that corresponding to the unbroadened pump light.

Starting with the assumption that the electron polarization is directly affected by the rubidium polarization, a valid supposition in light of the results of [29] and of section 4.1, we can attempt to explain the trends in the data by looking at the impact of the pump light's spectral bandwidth on the steady-state solution for P_{Rb}, which is given by [59]

$$P_{Rb} = \frac{R}{\Gamma + R}. \tag{4.6}$$

Here, Γ is the spin relaxation rate of the alkali atoms, and R is the mean rate at which an unpolarized rubidium atom absorbs photons [104]:

$$R = \int_0^\infty \Phi(\nu)\sigma(\nu)d\nu, \tag{4.7}$$

where $\Phi(\nu)$ is the photon flux incident on the atom and $\sigma(\nu)$ is the total photon absorption cross-section, both at frequency ν. The photon flux depends on the spectral profile of the pump light. So does the optical pumping rate and the rubidium polarization. The photon flux at frequency ν associated with light with a Gaussian spectral profile can be described by [104]

$$\Phi(\nu) = \Phi(\nu_l) e^{-4(\nu-\nu_l)^2 \bullet \ln(2) \bullet \frac{1}{(\delta\nu_l)^2}}. \tag{4.8}$$

Here, $\nu_l = \frac{c}{\lambda_l}$ is the central frequency of the profile and $\delta\nu_l = c\frac{\delta\lambda_l}{\lambda_l^2}$ is the full width at half maximum. For a laser beam of intensity I_l,

$$\Phi(\nu_l) = \frac{2I_l\sqrt{\pi \ln(2)}}{\pi h\nu_l\delta\nu_l}. \tag{4.9}$$

In order to evaluate the optical pumping rate, we also need the total optical absorption cross-section σ of D1 light. For the sake of making the integral manageable, we use Doppler-broadened line profiles to describe the relevant hyperfine transitions. The total photon absorption cross-section at frequency ν is then given by [106]

$$\sigma(\nu) = \pi r_e cf \sum_{F,F'} A_{F,F'} G\left(\nu - \nu_{F,F'}\right), \tag{4.10}$$

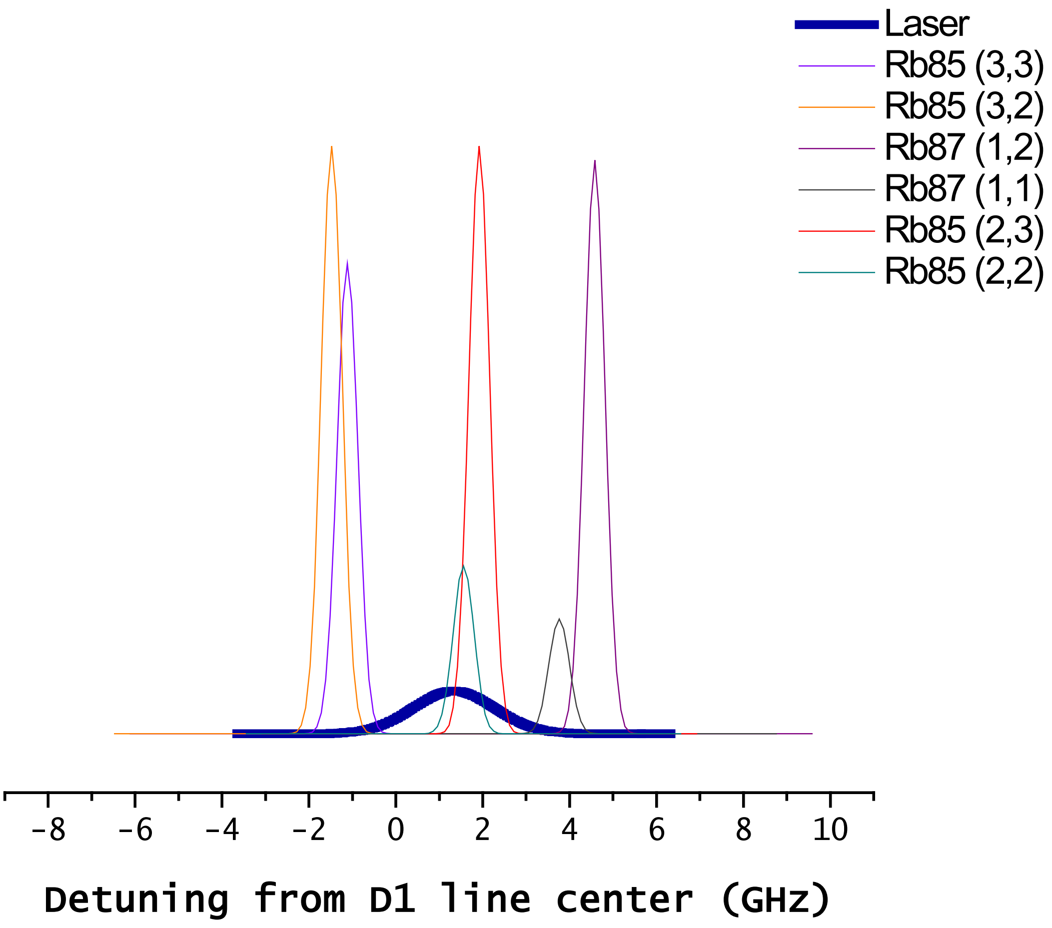

Figure 4.11: When broadened to 2.2 GHz, a significant fraction of the laser's spectral profile is not on resonance with the Rb hyperfine transitions. Only the D1 transitions significantly affected by the pump light are shown on this diagram. The amplitudes of the transitions are representative of the magnitude of their photon absorption cross-sections, which depend on the relative strengths of the transitions $A_{F,F'}$.

where r_e is the classical electron radius, c is the speed of light, f is the oscillator strength for the D1 transition, $\nu_{F,F'}$ is the resonance center frequency of the $F \rightarrow F'$ hyperfine transition, $A_{F,F'}$ is the relative strength of the transition, and $G\left(\nu - \nu_{F,F'}\right)$ is the frequency response of a Doppler-broadened line profile.

The bottom panel of figure 4.10 shows the optical pumping rate obtained, based on the above equations, for the laser line-widths studied under the current experimental conditions. The y-axis actually represents the optical pumping rate normalized to that with the spectrally-unbroadened pump light. We see that the optical pumping rate rises steadily as the pump light's spectral profile is broadened. A greater fraction of the profile is on resonance with the hyperfine transitions. Thus, more rubidium atoms can absorb photons. Eventually, the optical pumping rate reaches a maximum, and starts to decrease for larger line-widths. In this case, a large portion of the spectral profile does not overlap with the absorption cross-section associated with the rubidium hyperfine transitions as can be seen in figure 4.11.

The larger statistical error bar in the electron polarization (top panel of figure 4.10) for a pump laser line-width of 1.97GHz may reflect the fact that the wavelength of the light was fluctuating at this broadening and the one above it. It varied between 794.9760nm and 794.9764nm instead of staying steady at 794.9762nm as at the other line-widths. Such a variation in wavelength causes a fluctuation of about ±7% in our theoretical determination of the optical pumping rate for a line-width of 1.97GHz. As P_{Rb} depends on the optical pumping rate [30], fluctuations in the latter may have caused changes in the former, which in turn, may have affected P_e. The same variation in wavelength produces only a change of approximately ±3% in the optical pumping rate for a 2.82GHz line-width. This may explain the relatively smaller statistical error bar in the electron polarization at such a line-width compared to that at 1.97GHz. The rubidium polarization is more sensitive to fluctuations in pump light's wavelength at this line-width than at 2.82GHz.

These estimates correspond to optical pumping rates at a position along the cell where the laser light first interacts with the rubidium atoms. Due to absorption by the alkali vapor, the pump light will be attenuated as it travels through the cell. The estimates above did not take this into account, and represent an approximation of the actual situation. Nevertheless, they indicate the possible cause of the trend observed in the electron polarization in this study.

4.3 Dependence of electron polarization on pump laser power

In this experiment, we varied the pump laser's power to see how it affected the electron polarization. The intensity of the pump light can alter the fraction of alkali atoms in the different hyperfine sublevels. This can in turn have an impact on the polarization of the vapor, and hence, on that of the electron beam. According to Steck [107], a laser beam of intensity greater than 2mW/cm^2 can saturate a thin ensemble of rubidium atoms. As the vapor becomes optically thick or a quenching gas is added, the exact value of this saturation intensity will depend on the rates of the different photo-physical processes occurring in the vapor as discussed below.

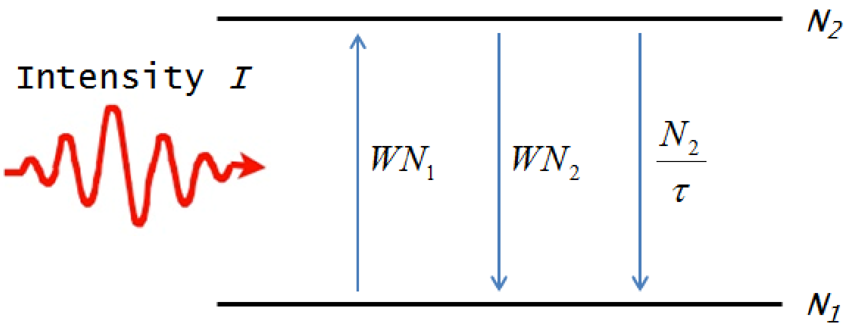

Figure 4.12: Two-level system interacting with resonant light of intensity *I*. (See text for more details) [108]

Let us consider, for instance, a sample of two-level systems (see figure 4.12) with a homogeneously broadened absorption line. If the sample is illuminated with resonant light of intensity *I*, the rate equations describing the populations N_1 and N_2 of the two levels are [108]

$$\frac{dN_1}{dt} = -WN_1 + WN_2 + \frac{N_2}{\tau}, \text{ and} \tag{4.11}$$

$$\frac{dN_2}{dt} = WN_1 - WN_2 - \frac{N_2}{\tau}. \tag{4.12}$$

Here, W is the transition rate due to photon absorption (or stimulated emission) while $1/\tau$ is the decay rate from the excited state via processes other than stimulated emission. In terms of the total population $N_t\left(= N_1 + N_2\right)$ and the population difference $\Delta N\left(= N_1 - N_2\right)$ between the two levels, the rate equation becomes

$$\frac{d}{dt}\Delta N = -\Delta N\left(\frac{1}{\tau} + 2W\right) + \frac{1}{\tau}N_t. \tag{4.13}$$

The steady state solution $\left(\frac{d}{dt}\Delta N = 0\right)$ yields

$$\Delta N = \frac{N_t}{1 + 2W\tau}, \text{ or} \tag{4.14}$$

$$N_2 = N_t \cdot \frac{W\tau}{1 + 2W\tau}. \tag{4.15}$$

At this point, let us define the saturation parameter I_s as $\frac{h\nu}{2\sigma\tau}$ where σ is the absorption cross-section of the transition, and $h\nu$ is the energy of an incident photon. With W given by $\frac{\sigma I}{h\nu}$, the steady state solution can then be rewritten as

$$N_2 = \frac{N_t}{2}\frac{\left(I/I_s\right)}{1+\left(I/I_s\right)}. \tag{4.16}$$

It can be seen that when the intensity I of the pump light is equal to I_s, the steady state population of level 2, N_2, is $N_t/4$. The intensity of the pump light at which such a situation occurs is known as the saturation intensity. If $I \gg I_s$, $N_2 \to N_t/2$. As mentioned above, the saturation intensity depends on the rate $1/\tau$ at which atoms decay from the excited state through processes other than stimulated emission, such as spontaneous emission. The presence of a quenching gas can cause this rate to increase as excited atoms collide with the former and decay to the ground state faster. In such a case, higher laser intensities would be needed to saturate the sample (see figure 4.13).

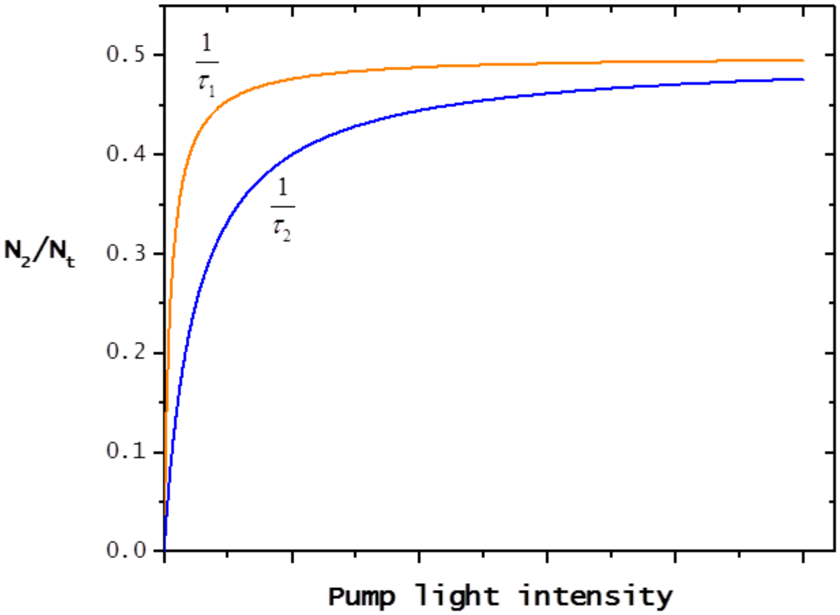

Figure 4.13: Fractional population of the upper state N_2 as a function of incident pump light intensity for two different relaxation rates: $\frac{1}{\tau_1}$ and $\frac{1}{\tau_2}$. Here, $\frac{1}{\tau_2}$ is five times greater than $\frac{1}{\tau_1}$. Higher pump light intensity is needed in the former case to saturate the sample.

In this experiment, we wanted to investigate whether we have enough pump light power to saturate the rubidium vapor and maximize the population of its "dark" state when quenching gas is present in the system. Above a certain laser power, the population of the different sublevels of the rubidium vapor will stop changing, and P_{Rb} will reach a maximum. We can anticipate that the polarization of the electron beam will follow that of the alkali vapor in light of the results of the previous section and of reference [29]. Hence, P_e will plateau when P_{Rb} does. The effects of the pump light power on the rubidium vapor can thus be inferred from the electron polarization.

The optical configuration described in figure 2.9 was used in this study. Only the polarization of the electron beam could be monitored. The buffer gas in the collision cell was nitrogen at a pressure of ~200mTorr. The energy of the incident electron beam was ~2eV. The current reaching the Faraday cup was ~300nA. In this experiment, the rubidium densities were approximately $\left(1\times10^{12}\right)$ atoms/cm^3 and $\left(3\times10^{12}\right)$ atoms/cm^3. The spectral bandwidth of the pump laser was ~2 GHz, and its wavelength was 794.9762nm. The pump power was measured with a Newport® power meter (model: 841-PE), which according to its owner's manual, has an accuracy of ±5%.

The results of this investigation are shown in figure 4.11; polarization of the electron beam reaches a maximum and levels off at about 150mW. Therefore, under the current experimental conditions, pump light intensities of about 5W/cm^2 are needed to saturate the rubidium vapor. This is not surprising considering that Liu *et al.* [109] have determined that the saturation intensity can rise from ~2mW/cm^2 to ~8W/cm^2 for a Doppler-broadened rubidium absorption profile. Compared to the highest power available to us, which corresponds to 650mW right before the beam enters the vacuum system, it takes relatively low power to saturate the rubidium vapor at the largest buffer gas pressures our system can handle. It is unlikely that more laser power will improve the performance of the current apparatus.

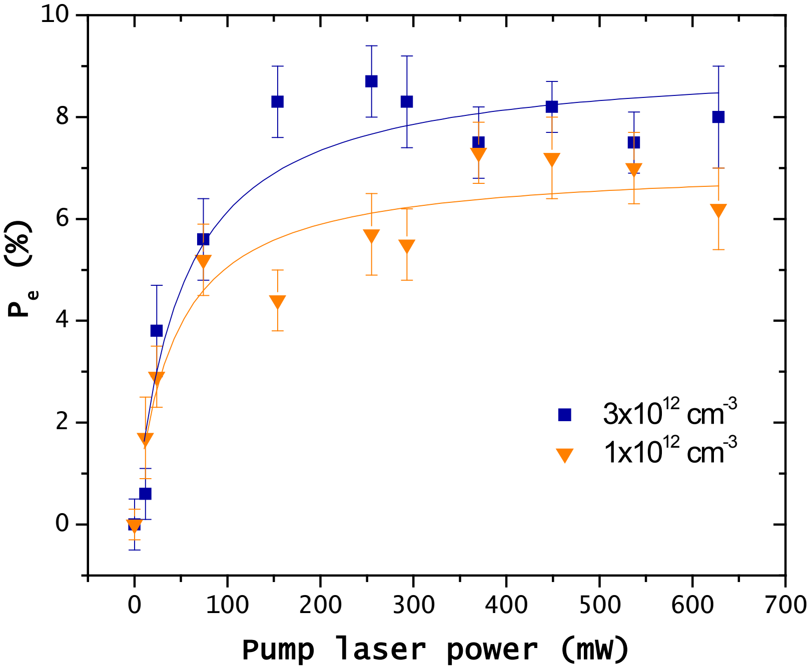

Figure 4.11: Variation of electron polarization with pump laser power for two rubidium vapor thicknesses: $\left(1\times10^{12}\right)\text{cm}^{-3}$ and $\left(3\times10^{12}\right)\text{cm}^{-3}$. (See text for details.)

The asymptotic value of the electron polarization was determined in each case by fitting the datasets to a function of the following form:

$$P_e = \frac{A \cdot P_l}{1 + B \cdot P_l}, \tag{4.17}$$

where P_l is the pump laser power, and A and B are free parameters. These free parameters were obtained from the curve-fitting software, Originlab, and they are shown in table 4.1. It is thus found that under the current experimental conditions, the electron polarizations tend to about 9.5% and 8% when [Rb] is 3×10^{12} atoms/cm^3 and 1×10^{12} atoms/cm^3, respectively.

Table 4.1.

[Rb] **(cm^{-3})**	**A** **(mW^{-1})**	**B** **(mW^{-1})**
3×10^{12}	0.19 ± 0.04	0.020 ± 0.005
1×10^{12}	0.16 ± 0.05	0.020 ± 0.007

4.4 Effects of different quenching gases on the electron polarization

In this experiment, we investigated how the choice of buffer gas affected the performance of the system. The buffer gas plays many crucial roles in optically-pumped polarized electron sources [29]. For instance, it slows the diffusion of rubidium atoms out of the pump beam's path. This allows the alkali atoms to undergo the number of cycles of photon absorption and emission needed to become polarized. Additionally, oriented rubidium atoms can spend more time along the electron beam's path before they are replaced by unpolarized ones. The buffer gas also mitigates the effects of radiation trapping. It quenches excited alkali atoms, causing them to decay non-radiatively. It is thus essential to polarize the rubidium vapor. For example figure 4.15, which represents data gathered by Norrgard *et al.* [64] in their study on the dependence of P_{Rb} on pump light wavelength, shows that for approximately the same [Rb], a peak polarization of ~80% is obtained with 1Torr of buffer gas (nitrogen) compared to 50% with 0.1Torr.

In addition to facilitating the polarization of rubidium atoms, the buffer gas increases the likelihood that free electrons will undergo spin-exchange collisions. By scattering multiple times against particles comprising the gas, electrons experience a longer effective path length through the cell [29]. They may also lose energy in the process. Since the spin-exchange cross section is largest for thermal electrons [57], both the slowing down of the particles and the increase in effective path length contribute to higher probabilities that spin-exchange collisions between rubidium atoms and electrons can occur. We thus wish to find a buffer gas that provides an optimal combination of these properties to maximize the polarization of the free electron beam.

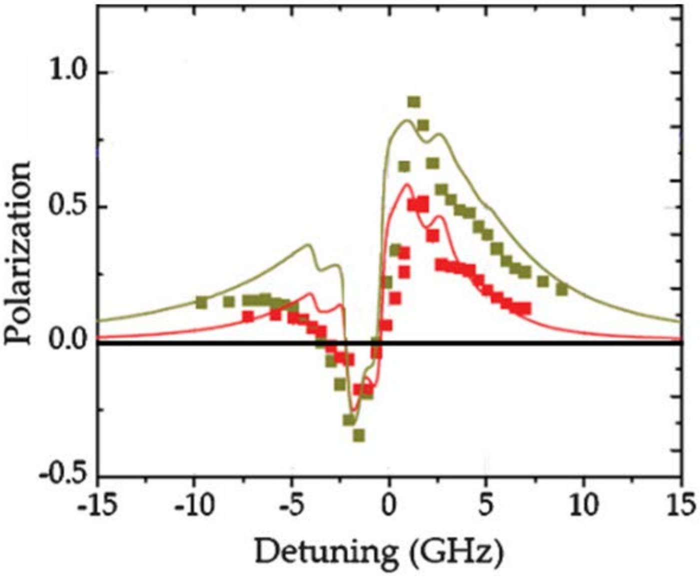

Figure 4.15: Measured (data points) and calculated (curves) polarization of a natural-abundance rubidium vapor as a function of the pump laser frequency. Red data: 0.1Torr nitrogen, 8.4×10^{12} cm^{-3} rubidium density; red curve: 0.1Torr nitrogen, 99.5% σ^+ light polarization. Green data: 1.0Torr nitrogen, 8.8×10^{12} cm^{-3} rubidium density; green curve: 1.0Torr nitrogen, 99.5% σ^+ light polarization. (Adapted from [64].)

In this study, we tried four different gases. Following Batelaan *et al.* [29], we operated the system with nitrogen and helium. Unlike the former, we used approximately the same pressure for both. Thus, we could roughly compare their performance as buffer gases. Hydrogen gas was chosen at the suggestion of W. Happer, whose group has worked on the production of spin-polarized atomic hydrogen by spin-exchange optical pumping for many years [110]. The final gas investigated was ethylene (C_2H_4). Optical pumping studies involving this gas are scarce. Hrycyshyn *et al.* [58] found that its quenching cross section is largest compared to the other gases under consideration (see Table 4.2). Thus it should be best at mitigating radiation trapping, and at orienting rubidium atoms.

Table 4.2: Characteristics of the different buffer gases studied. Here, σ_Q represents the quenching cross-section [58, 55], Q the probability that an excited rubidium atom decays to the ground state by spontaneous emission rather than quenching when the buffer gas pressure is ~200mTorr [106], and λ_{mfp} [103] the mean free path of electrons in the different gases under the current experimental conditions (see text for more details). Also shown are the threshold energy for ionizing the gases, and the peak electron-impact ionization cross-section [131, 103, 134]. (See text for details)

Gas	σ_Q ($\times10^{-16}$ cm^2)	Mass (Kg)	Q	Rubidium diffusion coefficient (cm^2/s)	λ_{mfp} (mm)	Ionization threshold (eV)	Peak electron-impact σ_{ion} ($\times10^{-16}$ cm^2)
helium	<< 1	6.65×10^{-27}	-	0.54	3	24.59	0.37
nitrogen	58	4.65×10^{-26}	0.95	0.33	0.5	15.58	1.85
hydrogen	6	3.35×10^{-27}	0.99	1.34	1	15.43	1.06
ethylene	139	4.66×10^{-26}	0.89	0.24	0.7	10.51	5.79

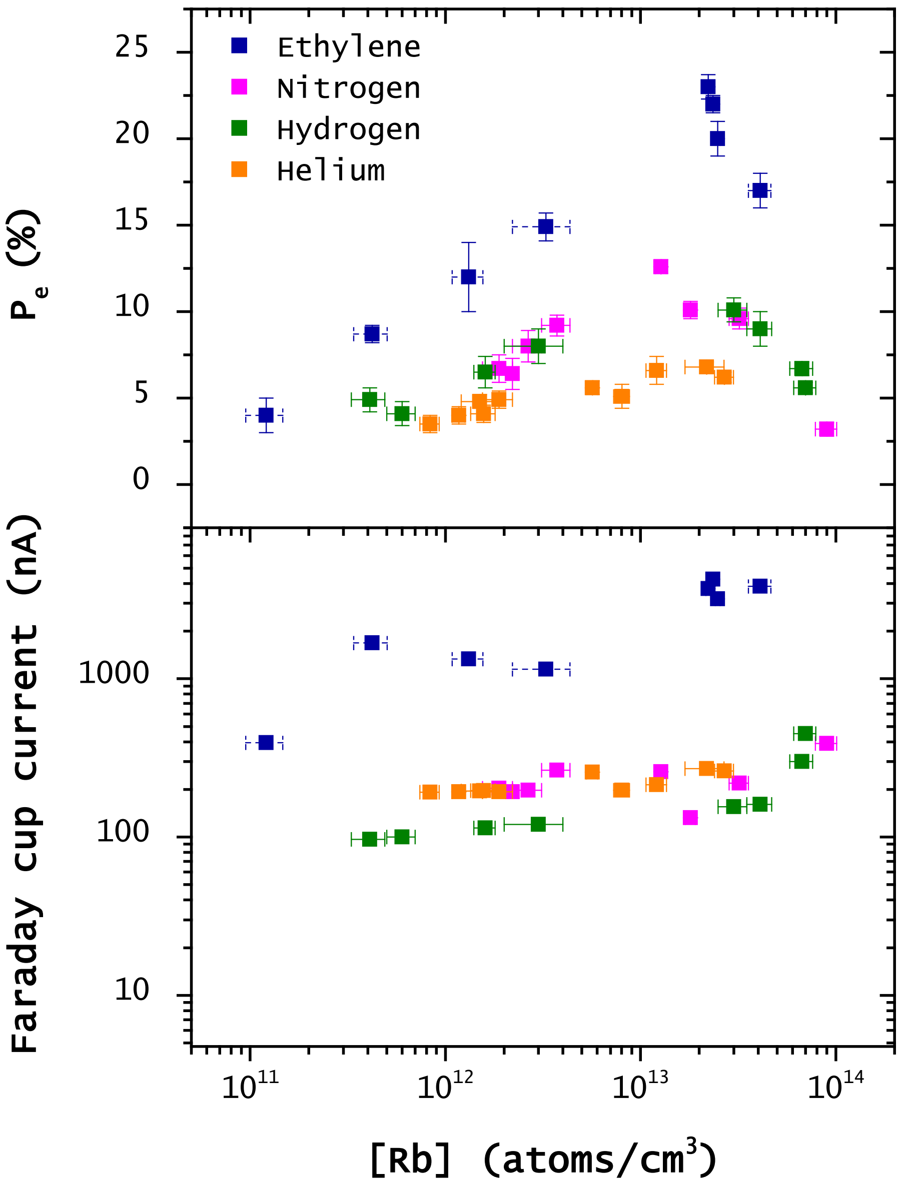

Figure 4.16: Performance of the system with the different buffer gases. Top panel shows electron polarization P_e as a function of rubidium density $[Rb]$. The bottom panel indicates the average current recorded on the Faraday cup at each $[Rb]$ at which P_e was measured (see text for details).

In this study, the optical configuration shown in figure 2.4 was used; only the polarization P_e of the electron beam could be monitored. For each buffer gas, I varied the rubidium density and measured the electron polarization. The results are shown in figure

4.16. The pump laser's wavelength was 794.9762nm, its bandwidth ~2GHz, and its power ~650mW (measured after the quarter wave-plate "QWP" in figure 2.9). The gas pressure in each run was ~200mTorr. This value corresponds to the corrected Convectron gauge reading. The incident electron energies for the nitrogen, helium and hydrogen cases were ~2eV. It was higher for the run with ethylene because the latter poses problems to the electron gun. The hydrocarbon molecules break down on contact with the hot tungsten filament and leave an apparently electrically-conductive layer of carbon on the electrodes. This carbon deposit causes the electrodes to short out with each other, making the electron gun unstable to operate at low energies. I had to use electrons with incident energies of ~4eV in the experiment with ethylene. However, this thermal decomposition of ethylene and the resulting carbon residue prove to be beneficial to the filament emission current. Indeed, the emission current was about 300µA with helium, hydrogen or nitrogen in the system while it rose to 3mA with ethylene. Previous investigations [75] have shown that carburized tungsten filaments can have a lower work function and hence, a higher emission current than pure tungsten. A direct effect of this increase in emission current can be seen in the bottom panel of figure 4.16 which shows the current $I_{Faraday}$ recorded on the Faraday cup during the experiments with the four buffer gases. As the electron polarization was being measured at each rubidium density of interest, 120 samples of $I_{Faraday}$ were being collected as discussed in chapter 3. Every data point on the plot in the bottom panel of figure 4.16 represents the average of these 120 samples. The graph essentially describes the behavior of the mean Faraday cup current over time because the rubidium metal was heated slowly, its vapor density allowed to increase gradually, and P_e measurements made at particular values of [Rb] along the way. During this whole process, the tungsten filament was on and was interacting with the buffer gas. The time interval between the first and the last P_e measurements correspond to approximately 7 hours for each run with the different buffer gases. We can thus see from the bottom panel of figure 4.16 that the average Faraday cup current was relatively low (~200nA) and fairly consistent over the time period of the run with helium, hydrogen or nitrogen in the system. With ethylene as buffer gas, $I_{Faraday}$ started at ~400nA and rose to reach a value of about 4μA. We also observe that the system worked best with that same buffer gas. A maximum electron polarization of ~24% was obtained, which also represents the best performance attained to date with this system. Figure 4.16 also shows that under almost identical experimental conditions, nitrogen fares better than helium in the operation of the current system, which suggests that the higher electron polarization recorded by Batelaan *et al.* [29] with the latter gas (see figure 1.11) is potentially due to the different pressures used (0.4 Torr with nitrogen compared to 2 Torr with helium).

Several properties unique to ethylene may have contributed to its better performance as a buffer gas. For instance, compared to the other gases in this study, ethylene has the largest quenching cross-section (see Table 4.2). This means that excited rubidium atoms are most likely to decay non-radiatively in ethylene. Indeed, the probability Q for an alkali atom in the excited state to decay to the ground state by spontaneous emission rather than quenching is given by [106, 81, 59]

$$Q = \frac{1}{1 + R_Q \tau}, \tag{4.18}$$

where $R_Q\left(=n_Q\sigma_Q\bar{v}\right)$ is the rate of quenching collisions, n_Q the density of the buffer gas, σ_Q the quenching cross-section, $\bar{v}$ the mean relative velocity between an alkali atom and a quenching particle, and τ the lifetime of the rubidium $5^2P_{1/2}$ excited states. Such probabilities, obtained under the current experimental conditions, are tabulated in Table 4.2, and they show that excited rubidium atoms are least likely to decay by spontaneous emission in ethylene, and thus emit depolarizing photons.

From Table 4.2, we also see that the mean free paths of electrons in the different buffer gases are less than the length of the collision cell. Therefore, electrons, on average, make multiple collisions with the buffer particles. However, Warman *et al.* [111] have calculated that electrons without enough energy to excite molecular electronic states (≤ 1eV) thermalize fastest in ethylene; the thermalization time in ethylene is 100 times shorter than that in nitrogen. The hydrocarbon molecules, being polyatomic, have more vibrational modes which relatively low-energy free electrons can excite [112]. If free electrons do lose more energy in ethylene, they will be more likely to undergo spin-exchange collisions with rubidium atoms because they will experience larger spin-exchange cross-sections (see figure 1.12).

In the data sets, the electron polarization rises rapidly, reaches a maximum, and eventually decreases with higher rubidium density. To understand this behavior qualitatively, we refer back to the solution of the rate equation for the electron polarization from section 4.1:

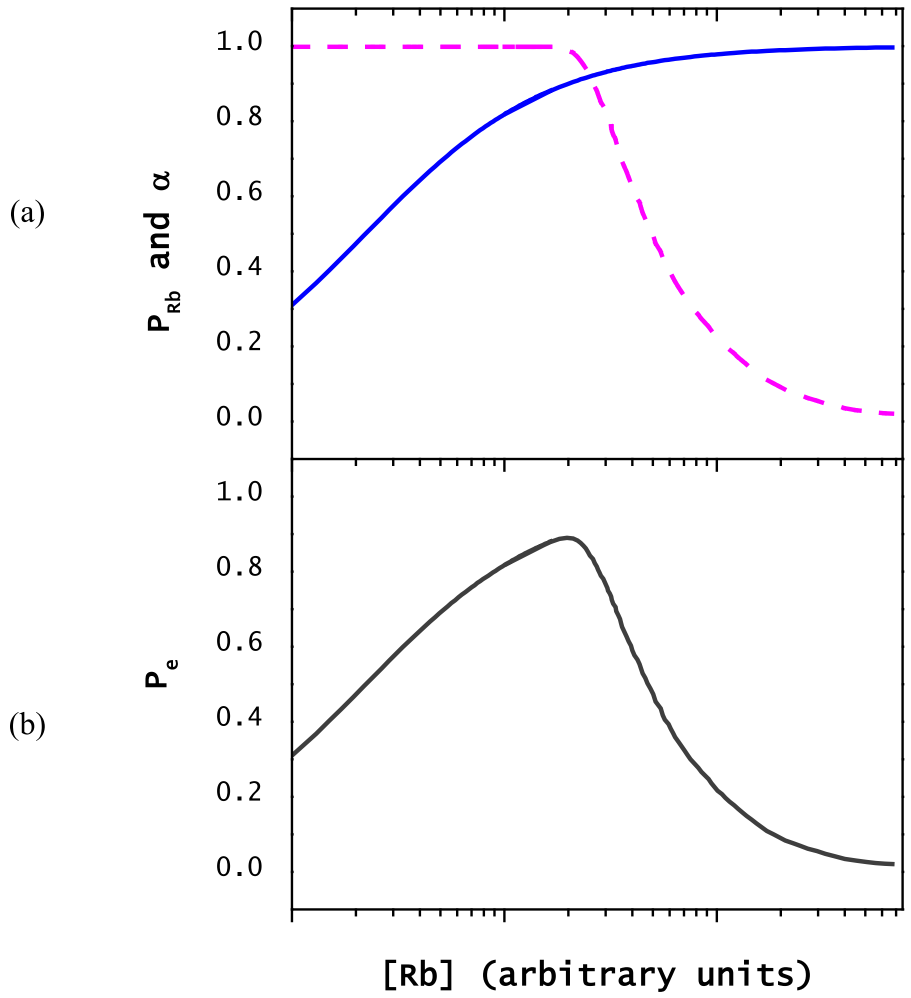

Figure 4.17: (a) An example of how the polarization transfer efficiency α (blue solid curve) behaves as a function of rubidium density [Rb]. It tends to 1 as the density rises. Also shown is a typical behavior of the rubidium polarization P_{Rb} (magenta dashed curve) as [Rb] increases (adapted from [113, 114]). (b) Electron polarization $P_e (= \alpha \cdot P_{Rb})$ which would be obtained from the representative polarization transfer efficiencies and P_{Rb} depicted in (a). (See text for details.)

$$\begin{aligned} P_e\left(t_c\right) &= \frac{k_{SE}\left[Rb\right]}{k_{SE}\left[Rb\right]+\Gamma_e}\left\{1-\exp\left[-\left(k_{SE}\left[Rb\right]+\Gamma_e\right)t_c\right]\right\}\cdot P_{Rb} \\ &= \alpha \cdot P_{Rb}. \end{aligned} \tag{4.19}$$

Here, t_c is the average time free electrons spend in the collision cell interacting with the rubidium vapor, k_{SE} the spin-exchange rate coefficient, $[Rb]$ the rubidium density, Γ_e

the relaxation rate of the electron polarization through processes other than spin-exchange collisions, and P_{Rb} the rubidium polarization. The expression for α in equation 4.18 can be used to see a representative behavior of the polarization transfer efficiency as a function of rubidium density. The blue curve in figure 4.17a is an example of the behavior of α as a function of [Rb] for an arbitrary set of k_{SE}, Γ_e and t_c. This curve does not correspond to actual experimental data. It was generated from the expression for the polarization transfer efficiency to get a feel for how it changes as the rubidium density is varied. It is noted that the x-axis of figure 4.17 represents [Rb] much greater than zero. The polarization transfer efficiency would actually be zero for $[Rb]=0$ because no electron-rubidium spin-exchange collisions could occur in the absence of alkali atoms. It is also seen that the blue curve representing the behavior of the polarization transfer efficiency in figure 4.17a rises slowly, eventually approaching 1, as [Rb] increases. Indeed, as more and more rubidium atoms become available, a growing number of free electrons can effectively undergo spin-exchange collisions with them. Figure 4.17a also shows a typical behavior of P_{Rb} as a function of [Rb] (magenta dashed curve), which was calculated by Tupa *et al.* [113] for the case of optical pumping of an arbitrary alkali vapor in a weak magnetic field such that $F=I+J$ and $m_F=m_I+m_J$ are good quantum numbers. For low rubidium densities, P_{Rb} is large and constant. The alkali atoms decay primarily non-radiatively, so radiation trapping is not an issue. As the vapor thickens, more and more rubidium atoms can be excited and can thus decay by spontaneous emission. This situation leads to the production of many depolarizing photons which are absorbed by polarized rubidium atoms. Radiation trapping ensues, and it causes P_{Rb} to fall rapidly.

The electron polarization P_e is the product of the polarization transfer efficiency and the rubidium polarization. The curve in figure 4.17b denotes the electron polarization which would be obtained from the representative α and P_{Rb} shown in figure 4.17a. The behavior of P_e depends on those of both the polarization transfer efficiency and the rubidium polarization. Even though P_{Rb} is high in the beginning, P_e is low because it is limited by the availability of rubidium atoms. Absence of alkali atoms would mean that no spin-exchange collisions could occur, and the polarization transfer efficiency as well as the electron polarization would be zero (note: the x-axis of figure 4.17 shows rubidium densities much greater than zero; the point where [Rb] is zero is not shown). As the rubidium vapor density increases, more free electrons can undergo spin-exchange collisions with oriented alkali atoms and be polarized. The electron polarization would rise rapidly. Eventually, addition of rubidium atoms does not affect the polarization transfer efficiency as much, and the behavior of P_e is dominated by that of P_{Rb}.

Performing simultaneous measurements of P_e and P_{Rb} will help us know how the rubidium polarization and the polarization transfer efficiency vary with rubidium density. Such information will enable us to better understand the trends observed in this study with the different buffer gases. Such measurements may also help us answer whether the high electron polarization recorded with ethylene is due to better orientation of the rubidium atoms and/or to higher polarization transfer efficiency.

4.5 Dependence of electron polarization on the axial electric field

The longitudinal electric field applied across the collision cell is crucial to the operation of the optically-pumped polarized electron source. In both the system developed by Batelaan *et al.* [29] and the current one, an axial electric field drives the free electrons through the mixture of buffer gas and rubidium vapor towards the exit aperture of the collision cell (part h in figure 2.28). In the former, the electric field strength could be controlled by setting the voltage on an electrically-isolated field plate containing the exit aperture (part 4 in figure 1.10). In our system, changes to the potentials of the collision cell and the exit electrode (parts j and k in figure 3.1) vary the axial electric field. Until now, no study of how electron polarization varies with electric field strength inside the interaction region has been undertaken. This would have been difficult to do in the apparatus of reference 28 because the exit electrode's potential had significant influence on the characteristics of the DC discharge responsible for producing the free electrons.

One may anticipate a link between the polarization of the electron beam and the electric field strength across the collision cell because a stronger field will result in increased electron drift velocities. Larger drift velocities cause electrons to experience lower spin-exchange cross-sections. Hence, the electron-rubidium spin-exchange mean free path is longer, and free electrons are less likely to be polarized.

In this experiment, I varied the potential on the exit electrode (part k in figure 3.1) while keeping those of the other elements constant. In effect, this increased the electric field strength across the collision cell. I measured the electron polarization for several exit electrode potentials. The incident electron energy, the rubidium density, the buffer gas (in this case, nitrogen) pressure and the pump light parameters were not changed in this experiment. During the investigation, the nitrogen pressure was ~200mTorr while the rubidium density was close to 10^{13} atoms/cm^3. The electrons had a kinetic energy of ~4eV at the entrance electrode (part i in figure 3.1). This element of the electron gun was at a potential of -35V while that of the collision cell was at -34V; both potentials are with respect to ground, and they were constant during the experiment. All the voltages quoted were read directly from the front panels of the relevant power supplies, and did not account for contact potentials. The pump light was tuned to 794.9762nm. Its bandwidth was ~2GHz, and its power was ~600mW.

Figure 4.18 summarizes the results obtained from this experiment. The current I_F recorded on the Faraday cup and the electron polarization P_e are shown as functions of the exit electrode potential V_{exit}. The last panel of figure 4.18 describes how the figure-of-merit $P_e^2 I_F$, which is a measure of the quality of a source of polarized electrons as discussed in section 1.3 [1], changed as V_{exit} was varied. We note that the electric field becomes stronger as the voltage applied to the exit electrode becomes less negative. The system was modeled using the SIMION® software (version 8.1) to obtain electric field strengths across the collision cell for the different experimental conditions employed. These are plotted in figure 4.19.

Figure 4.18 reveals that the exit electrode's potential V_{exit}, and hence the longitudinal electric field strength $\overrightarrow{E}$, affects both the current emerging from the collision

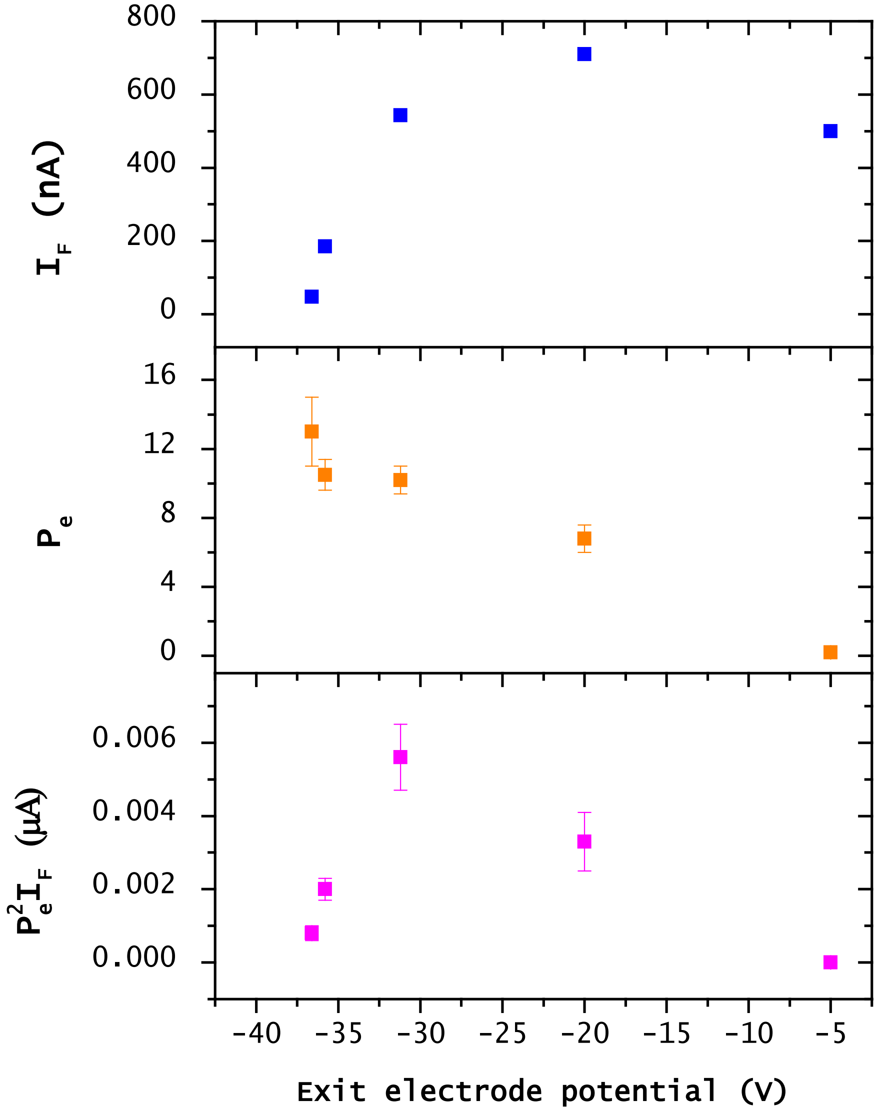

Figure 4.18: Effects of the longitudinal electric field along the collision cell on the Faraday cup current I_F, the electron polarization P_e and the figure-of-merit of the system. The field (see figure 4.19) gets stronger as the potential on the exit electrode becomes less negative.

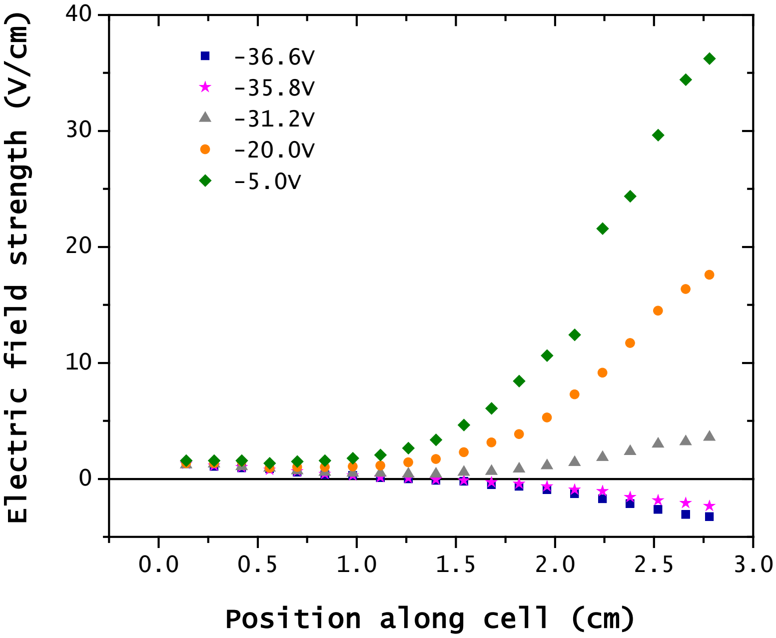

Figure 4.19: Electric field strengths across the collision cell for the different exit electrode potentials used in this study. These were obtained by modeling the system using the SIMION® software. Electrons experience retarding fields as they approach the exit electrode when electric field strengths are negative. Length of the collision cell is 2.8cm. The position marked 0.0cm corresponds to the entrance of the interaction region. (See text for details.)

cell and the electron polarization. Therefore, it directly impacts the figure-of-merit of the system. For the most negative exit electrode potential (-36.6V), and hence the lowest electric field strength across the collision cell, the Faraday cup current I_F recorded is smallest (~48nA). As V_{exit} becomes less negative, and $\vec{E}$ rises, I_F increases; more and more electrons emerge from the collision cell. Eventually, a plateau is reached where the current recorded on the Faraday cup stays fairly constant. The electron polarization, on the other hand, is largest for the most negative exit electrode potential (-36.6V) and lowest electric field strength. It stays somewhat steady as V_{exit} becomes less negative and

$\vec{E}$ increases. Ultimately, it decreases as $\vec{E}$ rises further, even reaching zero for the largest electric field strength investigated.

Two additional observations are not apparent from figures 4.18 and 4.19. First, when the entrance electrode, the collision cell and the exit electrode are electrically connected together, and thus, no electric field exists across the collision cell, less than a nanoampere of current is recorded on the Faraday cup. This is not surprising considering that the collision number NQL (where N is the density of nitrogen molecules, Q the electron-nitrogen total scattering cross-section, and L the length of interaction region) is ~26 under the present experimental conditions, and collisional processes become important when $NQL \sim 1$. The electrons collide multiple times with the nitrogen gas. Without a longitudinal magnetic field to limit their lateral diffusion [115], the electrons would scatter rapidly out of the primary beam and onto the walls of the collision cell. Second, both with and without gas in the collision cell, the same exit electrode potential of -37V is needed to "kill" the beam and prevent electrons from emerging from the interaction region. This indicates that some component of the electron beam did not lose energy as it traveled through the gas.

The observations discussed in the previous paragraph together with those represented in figure 4.18 suggest that the electric field strengths obtained from the SIMION simulation (figure 4.19) do not correspond to what actually happens in the collision cell. For example, with no field $(\vec{E} = 0)$ across the interaction region, we recorded less than a nanoampere of current on the Faraday cup. Let this current corresponding to $\vec{E} = 0$ be denoted by I_0. If electrons now experienced a retarding field as they approached the exit electrode, we would expect the current emerging from the cell and collected on the Faraday cup I_F would be lower than that with no electric field, I_0. Figure 4.19, which describes results of the SIMION simulation, shows that electrons supposedly experience retarding fields when the exit electrode potentials V_{exit} are -36.6V and -35.8V. However, as can be seen from figure 4.18, the Faraday cup current observed were 48nA and 185nA in those two cases. These currents are clearly greater than the one observed with no electric field across the collision cell, I_0. This implies that electrons do not experience retarding fields but attractive ones as they approach the exit electrode for all V_{exit}, even for -36.6V and -35.8V. Such attractive electric fields would cause the current emerging from the collision cell to be greater than that with no electric field, I_0, agreeing with our observations. Since the voltages entered in the software during the modeling process were read directly from the front panel of the relevant power supplies and did not account for contact potential differences, it may prove problematic to simulate the system accurately. Perhaps, the free electrons do experience more attractive electric fields than the SIMION® simulation is suggesting.

With no electric field across the interaction region, the majority of electrons scatter laterally or backwards after colliding with the buffer gas molecules multiple times. Hence, very low I_F (less than a nanoampere) is recorded in this case. It takes a relatively weak electric field of about 2V/cm, corresponding to $V_{exit} \sim -30V$, to extract the majority of scattered electrons from the collision cell; for stronger fields, I_F stays fairly constant. This may suggest that most of the incident electrons scatter in the half of the collision cell closer to the exit electrode. Since most scattered electrons are extracted with an electric field corresponding to $V_{exit} \sim -30V$, the main effect of stronger fields is to increase the drift velocity of the particles as they travel through the interaction region. Consequently, free electrons experience long spin-exchange mean free paths, and are less likely to be polarized. The electron polarization starts to decrease. For the strongest electric field investigated, which corresponds to $V_{exit} = -5V$, the drift velocity is likely too large for free electrons to undergo significant spin-exchange collisions with polarized rubidium atoms, and P_e approaches zero.

These results show that if the electric field is weak, the electron polarization is high, but the current emerging from the collision cell is low. If, on the other hand, the field is too strong, the polarization is low whereas the current is high. A compromise has to be found on the electric field strength used during the operation of the system. Under the current experimental conditions, average electric field strengths of about 2V/cm maximize the figure-of-merit of the polarized electron source.

4.6 Dependence of electron polarization on incident energy

In the experiments discussed so far, I have used free, unpolarized electrons of relatively low incident energy (between 2 and 4 eV) because the electron-rubidium spin exchange cross-section decreases rapidly as energy rises. For instance, the spin-exchange cross-section at 30meV is $\sim 10^{-13}$ cm^2 compared to $\sim 10^{-15}$ cm^2 at 1eV [57]. However, at low incident energies, the electron beam transmitted through the quenching gases is severely reduced owing to the larger total scattering cross-sections. The electrons collide more frequently with the gas, and diffuse rapidly out of the primary beam. The current recorded on the Faraday cup is relatively small compared to the GaAs photocathodes; in experiments done in our lab, GaAs photocurrents are typically $\geq 20\mu A$ [24]. Thus, one major improvement to our system would be to increase the electron beam intensity without significantly compromising the electron polarization.

In this section, I discuss the dependence of the electron polarization on the incident electron energy. I varied the energy of the electrons incident on the collision cell while keeping the buffer gas pressure (nitrogen, in this case), the rubidium density, and kept the relevant parameters of the pump light constant. An effect, especially at energies where N_2 can be ionized, has been observed that may help increase the intensity of the polarized electron beam. This effect is closely related to the energy loss of the incident electrons through inelastic collisions with the nitrogen buffer gas. Before presenting the results of the dependence of P_e on the incident electron energy, I will show and discuss curves obtained from performing retarding field analysis on the electron beam after it emerges from the collision cell. Such analyses were performed for several incident electron energies.

4.6.1 Retarding field analysis of incident electron beams

Retarding field analyzers are often used to obtain information about the energy distribution of an electron beam [116]. For the basic retarding field analyzer depicted in figure 4.20a, electrons with kinetic energy $E = eV_o$ are assumed to be heading towards the collector in a beam of infinitesimal extent and perfect collimation. On their way to the collector plate, they go through an electrode A with a tiny aperture. They are retarded by the axially directed electrostatic field of this electrode. If the retarding potential V_A is less than V_o, the electrons will reach the collector. If $V_A > V_o$, the particles will be repelled. Only electrons with kinetic energies greater than the analyzing voltage V_A can traverse this potential barrier and be collected. Thus, the retarding field analyzer acts, in effect, as a high pass filter. By sweeping the potential of the analyzer and making it more negative, only higher and higher energy components of the electron beam are collected. We can thus obtain the energy distribution of the electron beam.

If the electrons are mono-energetic, the curve shown in figure 4.20b is obtained for the current I of the collector as a function of the retarding potential. The current stays constant until the repulsive potential barrier becomes V_o. At this point, the particles do not have enough energy to overcome the barrier. The current on the collector therefore drops to zero. However, this curve represents an idealized situation where the

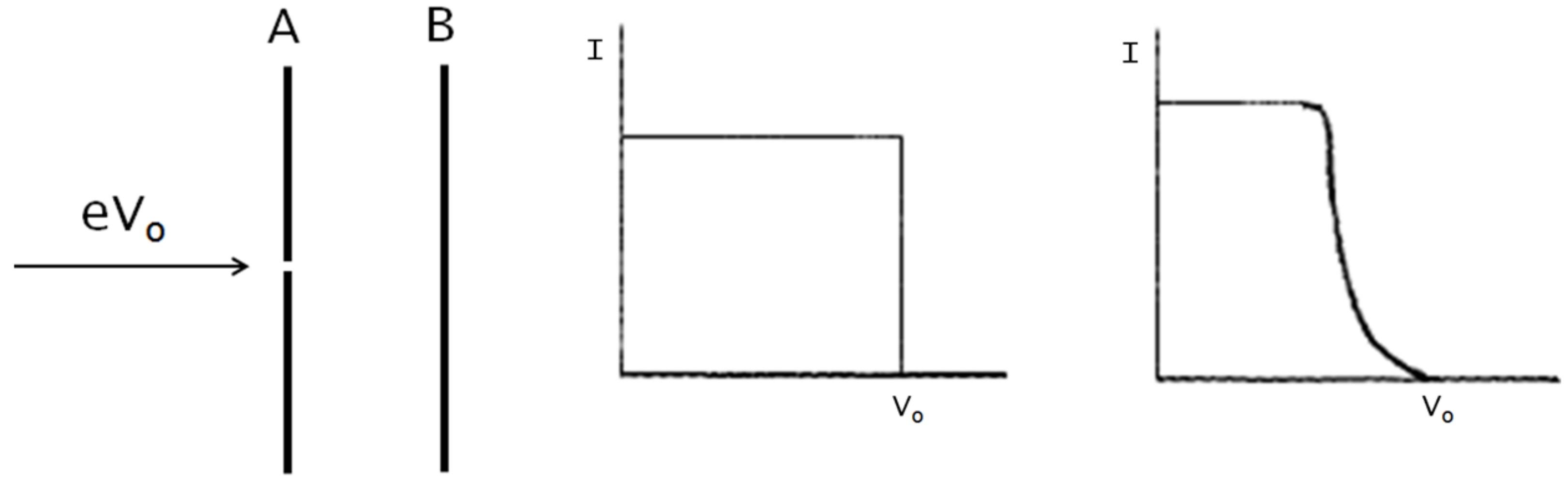

(a) (b) (c)

Figure 4.20: (a) Basic retarding field analyzer. Here, A is the electrode on which the retarding potential is applied. Electrons with kinetic energy eV_o are heading towards the collector B. (b) An ideal retarding field cutoff curve for mono-energetic particles. (c) A more typical retarding field cutoff curve. (Adapted from [116])

electron beam is perfectly collimated and its diameter is negligible. In reality, the curve will behave more like the one in figure 4.20c, even for a perfectly mono-energetic beam. The current on the collector will decrease gradually over a range of retarding potentials instead of exhibiting a sharp drop at V_o as in figure 4.20b. Such situations result from the geometry of the retarding field analyzer. The aperture in the device not only produces lens effects which forces incident electron beams to diverge [116], but it also causes the retarding field to be non-uniform. Thus, the resolution of the device is limited by the diameter of the aperture; the former worsens as the size of the latter increases [116]. Finally, we can obtain information about the energy distribution of electrons in the beam by determining $-dI/dV$, which is proportional to the number of particles per unit energy in the beam [117].

I now present the results of applying a retarding field analysis technique to electron beams in our system. I used the target cylinder (part labeled H in figure 2.31) in the electron polarimeter chamber as the retarding electrode. The opening of the target cylinder is 6mm in diameter. This is relatively large compared to conventional retarding field analyzers, which typically have apertures of 1mm or less [118, 119]. The target cylinder therefore represents a non-ideal, low resolution analyzer. However, it was the only component with which we could obtain information about the energy distribution of the electron beam. Other electrodes in the system were either crucial for electron transport or were being used to collect the beam. The electrons overcoming the potential barrier of the target cylinder were collected at the Faraday cup. It is noted that the electrode at the entrance of the collision cell ("i" in figure 3.1) was biased at about -33V, the collision cell at -32.5V, and the electrode at the exit ("k" in figure 3.1) at -29.5V. Thus, electrons can only overcome the barrier at the entrance of the collision cell and head to the polarimeter chamber if the potential at the tip of the tungsten filament (the electron emitter), which is controlled by the power supply "a" (also known as the filament bias) in figure 3.1, is more negative than that of the entrance electrode.

I performed retarding field analysis on electron beams going through both an empty spin-exchange collision cell, and one with ~110mTorr of nitrogen. The analysis was undertaken for several energies of electrons incident on the interaction region, namely 2, 8, 10, 14, 20, 30, 60 and 80 eV with an empty collision cell, and 3, 9, 19, 28, 59 and 108 eV for the case with 110mTorr of nitrogen gas. Figures 4.21 and 4.22 show the currents I recorded on the Faraday cup as functions of the retarding potentials for the situations discussed. In each case, the data were normalized to the maximum current recorded on the Faraday cup. Since the maximum I is observed when the target cylinder is grounded, the normalized Faraday cup current is 1 at a retarding potential of 0V. Using the data gathered from the retarding field analyses, energy distributions of the electron beam $(-dI/dV)$ were determined. These are plotted in the bottom panel of figure 4.21, and in 4.23. In the legend of the figures mentioned above, the numbers in parentheses correspond to the approximate kinetic energy of the incident electrons at the entrance of the collision cell while those outside the parentheses denote the total initial energy (potential plus kinetic) of the particles.

Figure 4.21 describes the behavior of the electron beam current recorded on the Faraday cup for several incident energies as the potential barrier of the polarimeter's

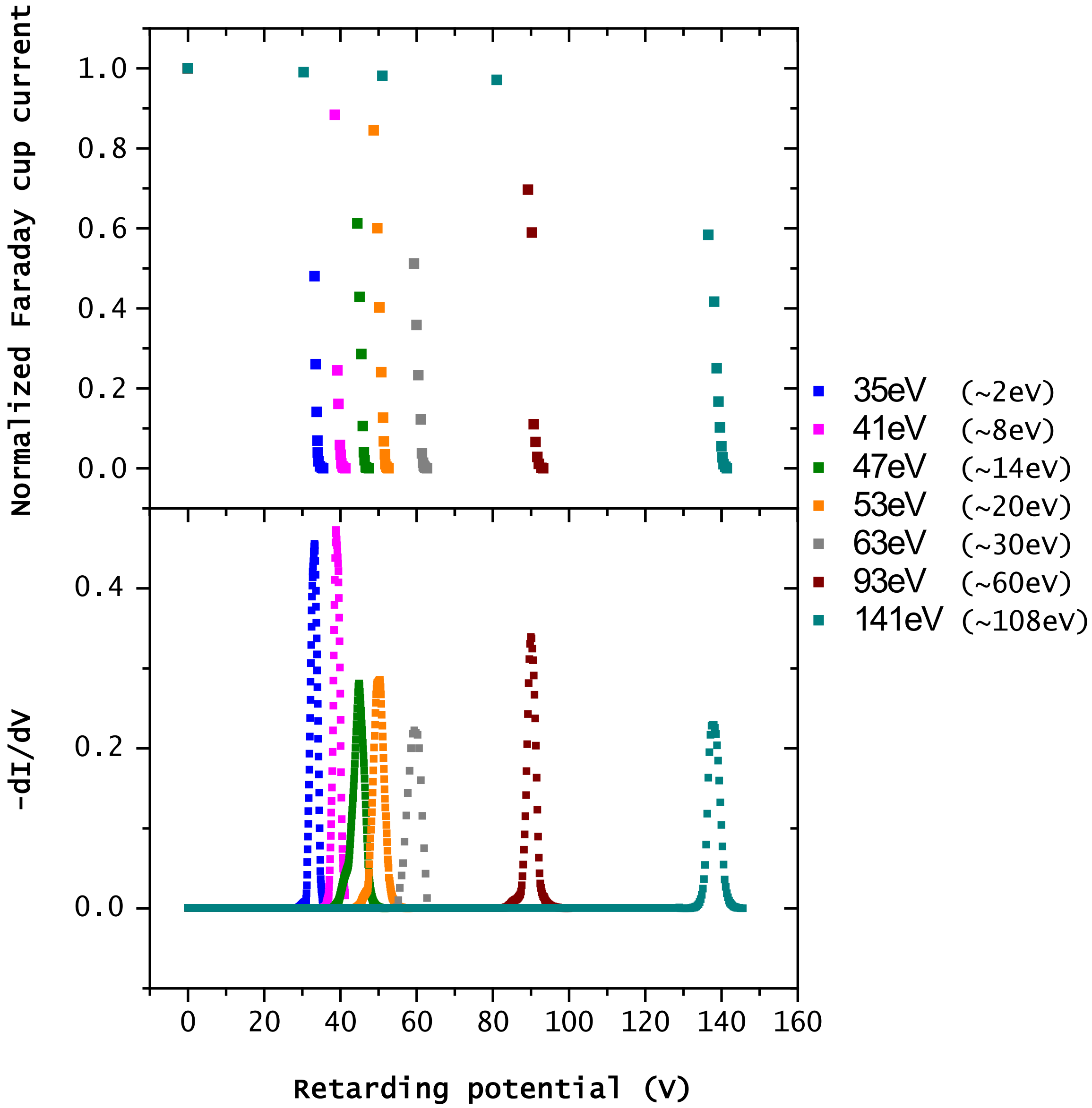

Figure 4.21: Retarding field analyses of electron beams with different energies incident on an empty collision cell. Numbers in parentheses in the legend correspond to the approximate kinetic energy of the electrons at the entrance electrode. Top panel shows how current collected on the Faraday cup varied as the potential on the target cylinder was gradually made more negative. The bottom panel describes the energy distributions obtained by interpolating the points in the top panel, and taking the derivative with respect to the retarding potential. With no gas, the beam has an average apparent energy width (FWHM) of about 2eV.

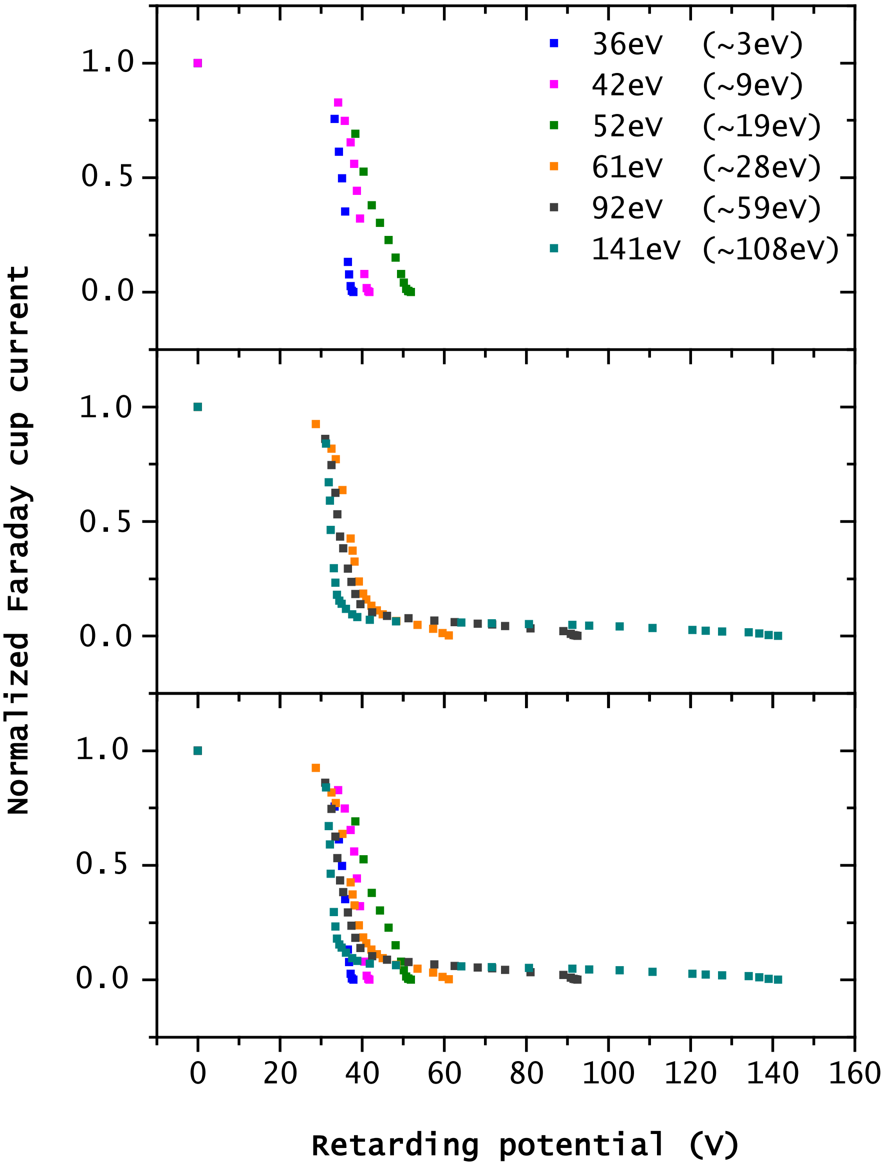

Figure 4.22: Retarding field analyses of electron beams with different energies incident on the collision cell with 110 mTorr of N_2. In the legend, the numbers in parentheses denote the approximate kinetic energy of the electrons at the entrance electrode. Top panel shows retarding field curves for the three slowest incident energies investigated while data in the middle panel correspond to the highest incident energies studied. Results for all incident energies have been combined in the bottom panel.

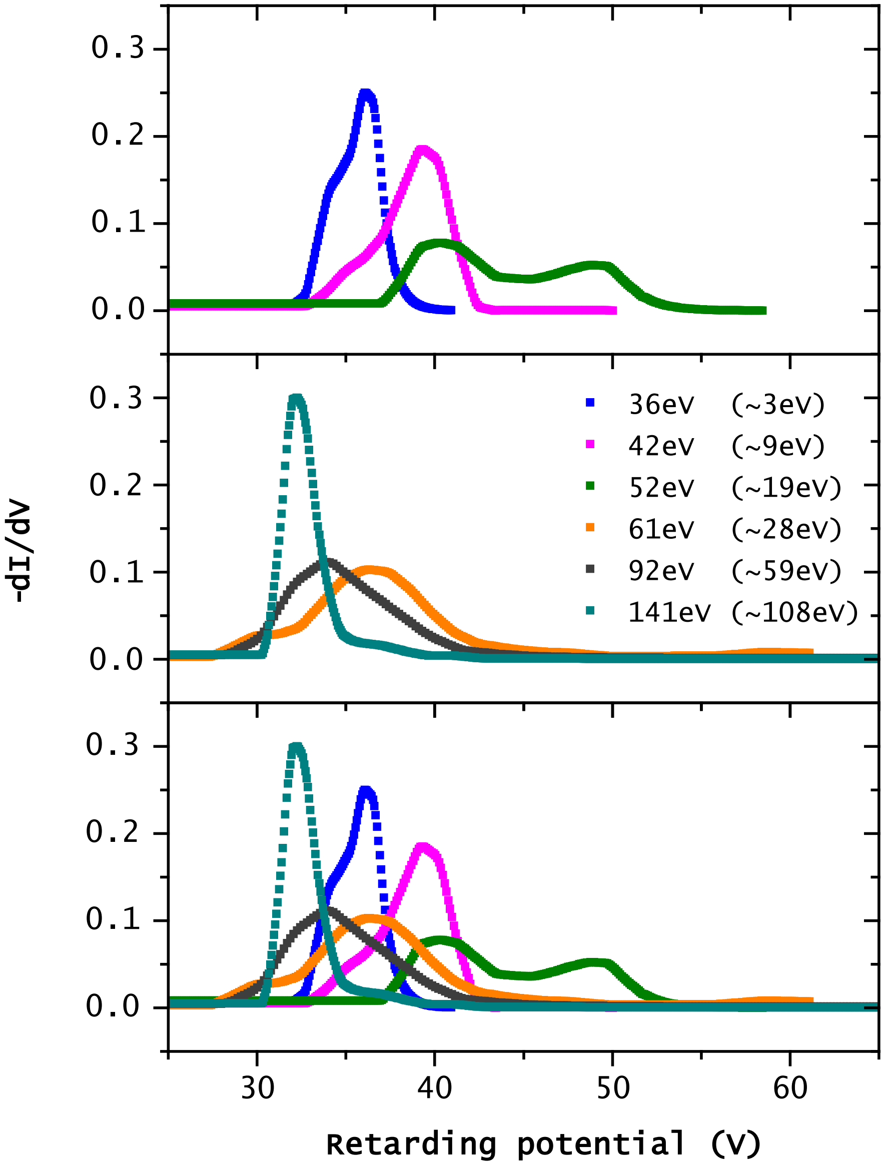

Figure 4.23: Energy distributions obtained from the retarding field analyses of electron beams with different energies incident on the collision cell with 110 mTorr of N_2 (see figure 4.24). In the legend, the numbers in parentheses denote the approximate kinetic energy of the electrons at the entrance electrode. The top panel shows energy distributions for the three slowest incident energies investigated while data in the middle panel correspond to the highest incident energies studied. Results for all incident energies have been combined in the bottom panel.

target cylinder is made more repulsive with no gas in the collision cell. Looking at the data corresponding to an electron beam with total initial energy of ~141eV, for example, we see that the current registered on the collector is fairly constant until the retarding potential reaches about 138eV. Then, it drops sharply, and the retarding field analysis data follow a somewhat similar behavior to the plot in figure 4.20c. The corresponding energy distributions are plotted in the bottom panel of figure 4.21. These were obtained by interpolating the data from the retarding field analyses (top panel of figure 4.21), and then, carrying out the derivative with respect to retarding voltage. The energy distributions indicate that with no gas in the collision cell, the average energy width (FWHM) of the electron beam is approximately 2eV. However, it is important to keep in mind that this value may not represent the actual energy width of the electron beam emerging from the collision cell. As discussed previously, the target cylinder in the polarimeter chamber is a very crude, low-resolution retarding field analyzer. Obtaining the real energy width is further complicated by the “flaring out” of the magnetic field lines at the end of the apparatus (see figure 2.22), which will cause the beam to diverge, and the electrons to have a wider distribution of longitudinal velocities.

Figure 4.22 shows the retarding field analyses with 110mTorr of nitrogen in the collision cell. They behave differently from those with no gas in the system, especially at the higher incident energies. The curves do not have slopes as steep as those taken with no gas in the collision cell, indicating a wider distribution of electron energies in the final beam. This is indeed obvious from figure 4.23, which describes the energy distributions obtained from the retarding field analyses.

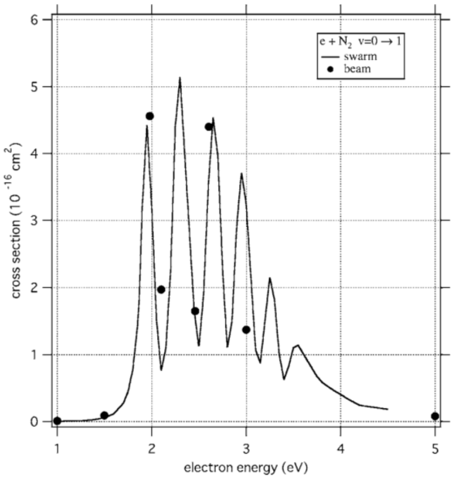

Figure 4.24: Cross-sections for the vibrational excitation $\upsilon = 0 \rightarrow 1$ of N_2 by electron impact. The results obtained from a swarm analysis are compared with the recommented values based on a beam measurement. (After Itikawa [120].)

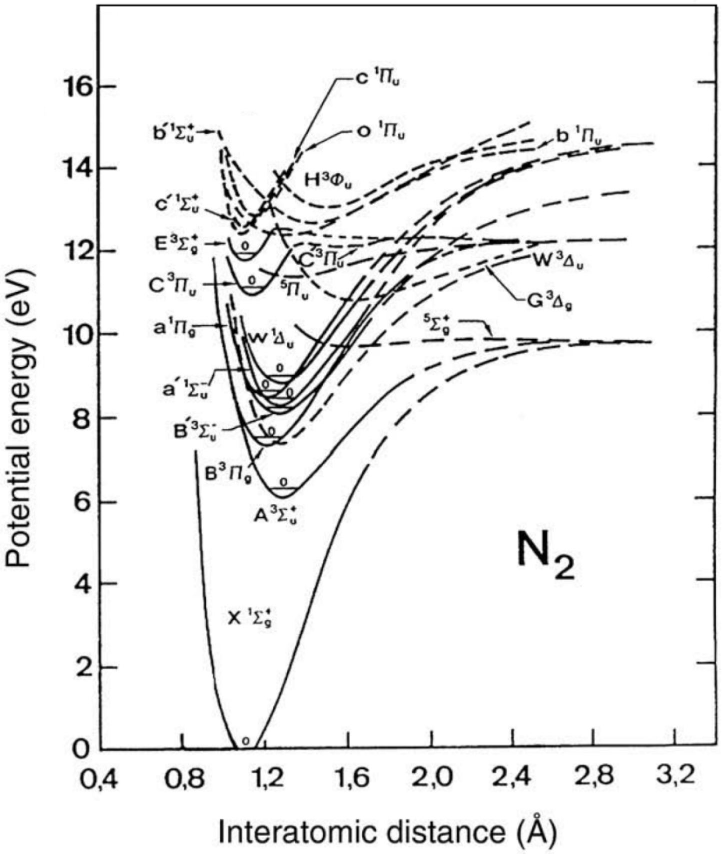

Figure 4.25: Potential energy curves of molecular nitrogen. (After Bogaerts [121].)

For electrons with ~2eV of incident energy, the total collision number *NQL* is ~21 [120]; the particles collide multiple times with the nitrogen molecules. These collisions can be elastic in nature or can result in the vibrational excitation of the nitrogen molecules [120]. Electrons can lose significant energy in the latter process as will be discussed shortly. Figure 4.24 shows the cross-sections for the vibrational excitation $\upsilon = 0 \rightarrow 1$ of molecular nitrogen by electron impact. Electrons are likely to undergo such a process if their incident kinetic energies fall between ~1.8eV and ~3.5eV. Electrons ~6eV of incident kinetic energy and above can excite electronic states of the N_2 molecules. Figure 4.25 shows the potential energy curves for the different electronic states of molecular nitrogen which can be excited by incoming electrons. A single such collision can cause them to lose a significant fraction of their energy. Under the current experimental conditions, the probability for electrons to excite any particular electronic state of N_2 as they travel along the length of the cell is less than 1 because the cross-sections for such processes are ~10 times smaller than those for electron-impact vibration excitations. However, for electrons with incident kinetic energy above 15.6eV (corresponding to the ionization energy of N_2), excitation and ionization of nitrogen molecules are the predominant energy loss mechanisms [122, 123]. Using available electron impact ionization cross-sections σ_{ion} [120], we find that the probability of an electron ionizing a nitrogen molecule as it travels the length of the collision cell containing ~110mTorr of gas increases from 0.5 for an incident kinetic energy of 19eV to 1 for 100eV electrons, which corresponds to the energy where σ_{ion} peaks for such a process. As the kinetic energy of the electrons increases from 26eV to 106eV, they are more and more likely to ionize nitrogen molecules. In the process, they will lose energy (each ionizing collision will cause the primary electron to dissipate at least 15.6eV, the ionization threshold energy), but they will also produce secondary electrons. These secondary electrons can become part of the final beam emerging from the gas. It is thus important to determine where their energy contribution would appear in the retarding field analyses data.

For several energies of electrons incident on N_2, Opal *et al.* [124] have measured the energy and angular distributions of secondary electrons emerging from the ionization of nitrogen molecules. When an electron ionizes an N_2 molecule, two or more free electrons are obtained after the collision. In general, one cannot distinguish the secondary from the primary electrons. By convention [122], the fast one is called the primary electron, and the slow one the secondary electron. Opal *et al.* [124] have tabulated $\sigma(E_{p,}E_s,\theta)$, the doubly differential cross-section in square centimeters/electron volt⋆steradian, where E_p is the energy of the incident (primary) electron, E_s is that of an electron observed leaving the collision, and θ is the angle between the directions of the incident and departing electrons. Their measurements allowed them to determine the cross-section integrated over angle:

$$\sigma(E_p,E_s)=\int_0^{\pi}\sigma(E_p,E_s,\theta)\cdot 2\pi\sin\theta\,\mathrm{d}\theta. \tag{4.20}$$

We thus have the singly-differential cross-section [120] with respect to energy of the electrons emerging from the ionization process. The measurements of Opal *et al.* [124]

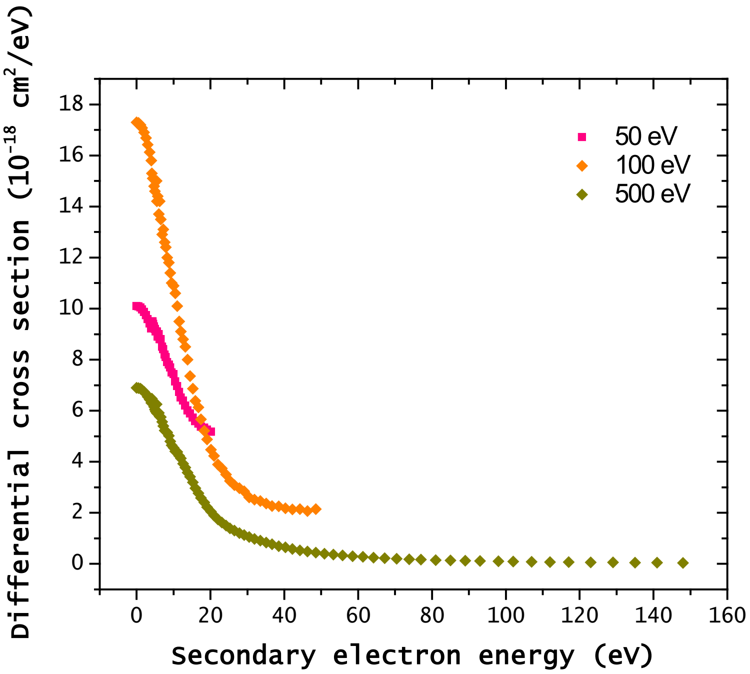

Figure 4.26: Singly differential cross-section (SDCS) for the ionization of N_2. The incident electron energies are 50 eV, 100 eV and 500 eV. For electrons emerging from the ionization process with energies below 4.13 eV, data have been extrapolated using the analytic form of the SDCS (see text).

are limited to electrons leaving with 4.13eV of energy and above. They have nonetheless found that these singly differential cross-sections can be fitted to an analytic function of the form [125]

$$\sigma = \frac{C(\mathrm{E}_p)}{1+\left(E_s/D\right)^{\alpha}}. \tag{4.21}$$

The fitting parameters include α and D, which are independent of incident energy, whereas C is a normalization constant that does depend on the incident energy. The fitting is good for electrons of energies below 30eV. I have fitted their data to this equation for primary electrons of 50eV, 100eV and 500eV to obtain singly differential cross-sections for electrons emerging from the ionization process with energies lower than 4.13eV. For primary electrons of 100 eV,

$$\sigma(E_p = 100\,\mathrm{eV}, E_s) = \frac{17.3}{1+\left(\dfrac{E_s}{13}\right)^2} \times 10^{-18}\, cm^2 eV^{-1}, \tag{4.22}$$

which agrees with the parameters obtained by Itikawa [122] for the same incident energy while for primary electrons of 50eV and 500eV, the constants (C, D, α) are found to be $(10.1 \pm 0.8, 16 \pm 4, 2)$ and $(6.9 \pm 0.9, 12 \pm 2, 2)$ respectively.

Figure 4.26 shows how $\sigma(E_p, E_s)$ varies with electron energy for the three primary energies mentioned above. The data obtained by Opal *et al.* [124] suggests that electrons emerging from the ionization of nitrogen molecules are predominantly very slow. If the beam emerging from the collision cell was composed of any secondary electrons, one would therefore expect that most of their energy contribution would appear at the lower repulsive potentials in the retarding field analyses. The energy distributions in figure 4.23 do show that for incident kinetic energies of 28, 59 and 108 eV, the beams emerge from the collision cell consisting mostly of slow electrons in marked contrast to those in figure 4.21.

Finally, figures 4.27a and 4.27b describe the actual current recorded on the Faraday cup for the different electron energies used in the retarding field analyses when the target cylinder was grounded. The x-axis represents the total initial energy of the electrons. The values in parentheses denote the approximate kinetic energy of the electrons at the entrance electrode. For example, a total initial electron energy of 40eV corresponds to a kinetic energy of ~7eV at the entrance electrode. It is important to note that the filament emission current used with nitrogen in the collision cell was ~3 times that without the buffer gas. More electrons were being emitted per unit time in the former case. This fact may account for the higher current recorded on the Faraday cup with electrons of ~100eV incident kinetic energy when nitrogen was introduced in the collision cell (8.6μA with nitrogen compared to 4.8μA without).

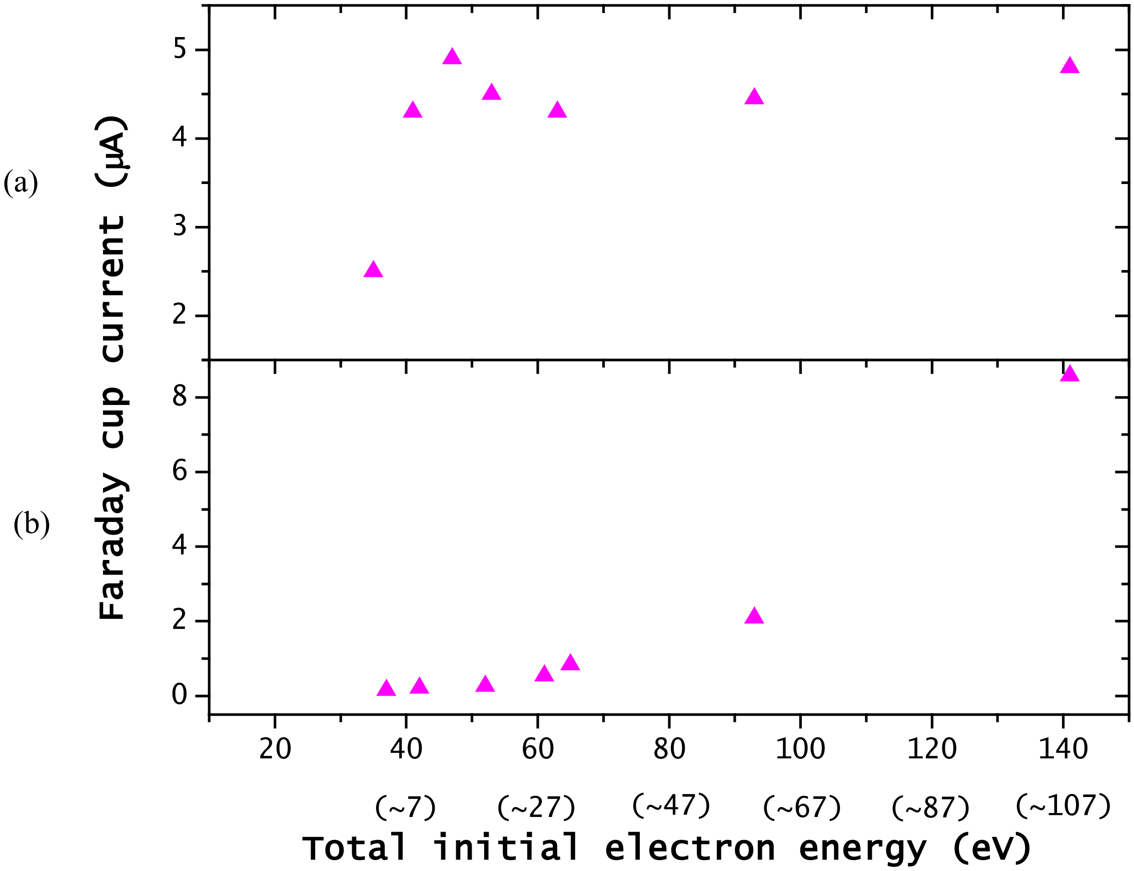

Figure 4.27: Current observed on the Faraday cup with (a) no gas and (b) 110mTorr of N_2 in the collision cell when the target cylinder retarding potential is 0V. The numbers in parentheses correspond to the approximate kinetic energy of the electrons at the entrance electrode.

Figure 4.27a (for no nitrogen in the collision cell) shows the electron beam "turning on" when the total initial energy is around 35eV. At this point, the particles have enough kinetic energy to overcome the potential of the entrance electrode. The current on the Faraday cup stays fairly constant for the higher electron energies. The current recorded on the Faraday cup when nitrogen is introduced in the collision cell (figure 4.27b) exhibits a different behavior. It is fairly constant at the lower incident energies. For electrons with kinetic energies of ~27eV and above at the entrance electrode, the Faraday cup current rises significantly. Better transmission of the electron beam through the nitrogen gas at the higher energies may have contributed to this increase. For example, the electron-nitrogen total scattering cross section is $11.5\times10^{-16}\,\text{cm}^2$ at 8eV compared to $8.94\times10^{-16}\,\text{cm}^2$ at 100eV [120]. According to Beer's law [103], the transmitted current I_t through the gas is equal to $I_o e^{-NQL}$ where I_o is the initial current, N the number density of nitrogen molecules, Q the electron-nitrogen total scattering cross section, and L the length of the collision cell. An estimate of the ratio of $\left(I_t/I_o\right)$ through 110mTorr of nitrogen gas in the ~3cm long collision cell at 100eV to that at 8eV yields

$$\frac{\left(\dfrac{I_t}{I_o}\right)_{100eV}}{\left(\dfrac{I_t}{I_o}\right)_{8eV}}=\frac{\left(e^{-NQL}\right)_{100eV}}{\left(e^{-NQL}\right)_{8eV}}\sim 20. \tag{4.23}$$

Since the electrons at lower energies collide more frequently with nitrogen molecules owing to their larger total scattering cross-section, they diffuse rapidly out of the beam and onto the walls of the collision cell. Therefore, electron beams at the lower energies are attenuated to a greater extent than those at the higher energies.

The ratio in Faraday cup current recorded with these two particular incident electron energies is actually closer to 40. Several facts may have contributed to this increase. First, simulations in SIMION® reveal that the electron optics of the system were optimized for electron transport at high energies. More electrons are therefore expected to emerge from the collision cell at such incident energies. Moreover, electrons incident on the collision cell with kinetic energies of 15.6eV and above can ionize nitrogen molecules [120]. The ionization cross-section starts to increase at ~16eV and peaks at about 100eV. Therefore, as the kinetic energy of the incident electrons rises above 16eV, their probability of ionizing nitrogen molecules and producing secondary electrons becomes larger. The presence of a magnetic field along the collision cell would reduce the diffusion of these secondary electrons to the walls while the longitudinal electric field would help in their extraction by causing them to drift through the gaseous mixture and out of the interaction region [126]. Instead of undergoing rapid, lateral diffusion due to collisions with nitrogen molecules, electrons experience the effects of the Lorentz force acting on them, and they gyrate around the magnetic field lines. Given that the gyro-radius of slow secondary electrons (~1eV) is about 0.2mm under the current experimental conditions, the particles do not stray far from the primary beam, and they are likely to emerge out of the 2mm exit aperture of the collision cell. Thus, they would contribute to enhancing the primary electron beam.

4.6.2 Effect of incident energy on electron polarization

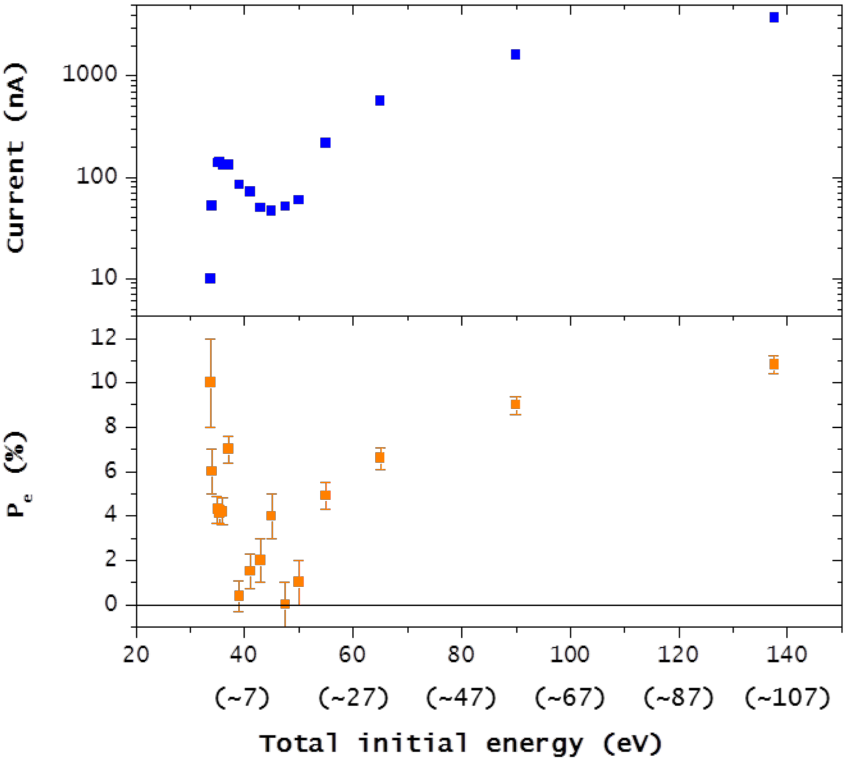

Figure 4.28: Dependence of the Faraday cup current and the electron polarization on the total initial energy of the electrons. The numbers in parentheses correspond to the kinetic energy of the electrons in eV at the entrance electrode.

The retarding field analyses data motivated the study of how the P_e depends on the energy of the incident electrons, especially in the range where ionization of the nitrogen gas and production of very slow particles can occur. For this investigation, I used a nitrogen pressure of 130mTorr, and a rubidium density close to 10^{13} atoms/cm^3. The pump power was 650mW, its wavelength 794.9762nm, and its bandwidth ~2GHz. The results of this investigation are shown in figure 4.28. The current recorded on the Faraday cup as a function of the primary electron beam's total initial energy and its approximate kinetic energy at the entrance electrode (the numbers in parentheses) is shown in the top panel while the behavior of the electron polarization is given at the bottom.

Electrons with the lowest incident energies yield very high electron polarization. This is not surprising considering that the electron-rubidium spin-exchange cross-section is largest for such particles. As the energy increases, the electron polarization decreases as would be expected from the behavior of the spin-exchange cross-section. However, there is a short plateau in P_e around ~2.5eV of incident kinetic energy, and the electron polarization appears to rise again, peaks and then drops to zero near 6eV. This rise is likely due to the presence of shape resonances in nitrogen in the range between 2eV and 4eV [127]. At such energies, vibrational excitation of nitrogen by the electrons can occur via the formation of a temporary negative ion state (see figure 4.29). After ~10^{-13} s, the state decays, often leaving the neutral molecule in a vibrational state other than $\nu = 0$. Electrons can lose energy by undergoing such a process.

Table 4.3. Vibrational excitations of N_2. [128]

Transition	**Energy (eV)**	**Cross-section (cm^2)**
$0 \to 1$	1.95	5.6×10^{-16}
$0 \to 2$	2.00	3.7×10^{-16}
$0 \to 3$	2.15	3.1×10^{-16}
$0 \to 4$	2.22	2.1×10^{-16}
$0 \to 5$	2.39	1.3×10^{-16}
$0 \to 6$	2.48	7.1×10^{-17}
$0 \to 7$	2.64	3.8×10^{-17}

Table 4.3 lists the major vibrational energy loss channels. These manifest themselves as the pronounced bumps in the electron-nitrogen scattering cross-section between approximately 1.8eV and 3.5eV (see for example figure 4.24 and 4.30). Under the current experimental conditions, the collision number corresponding to, for instance, the vibrational excitation $\upsilon = 0 \rightarrow 1$ of nitrogen by electrons, $NQ_{vib}L$, is equal to $\left(3.4\times10^{16}\times0.13\times5.6\times10^{-16}\times2.8\right)\approx 7$. Electrons would lose 1 quanta of vibrational energy in this process. If each quantum of energy is ~0.3eV, electrons will, in this case, dissipate, on average, ~2.1eV of energy after traveling through the collision cell. The formation of temporary negative ion states and the subsequent vibrational excitation of nitrogen molecules are an efficient way of causing electrons to lose energy, thus increasing their likelihood of undergoing spin-exchange collisions with oriented rubidium atoms. For simplicity, the above analysis has assumed that the cross-section for vibrational excitation of nitrogen molecules stays constant as the electrons lose energy.

The polarization drops close to zero for electrons with 6eV of incident kinetic energy (see figure 4.28). Given a total scattering cross-section of $11.4\times10^{-16}\,\text{cm}^2$ at this energy [120], the collision number under the present experimental conditions is ~10. From figure 4.30, it can be seen that these electrons undergo mainly elastic collisions. They lose only $\sim10^{-4}\,\text{eV}$ per collision in such processes [103]. Therefore, the electron-rubidium spin-exchange cross-section stays fairly small. It is unlikely that these electrons can undergo spin-exchange collisions with oriented rubidium atoms.

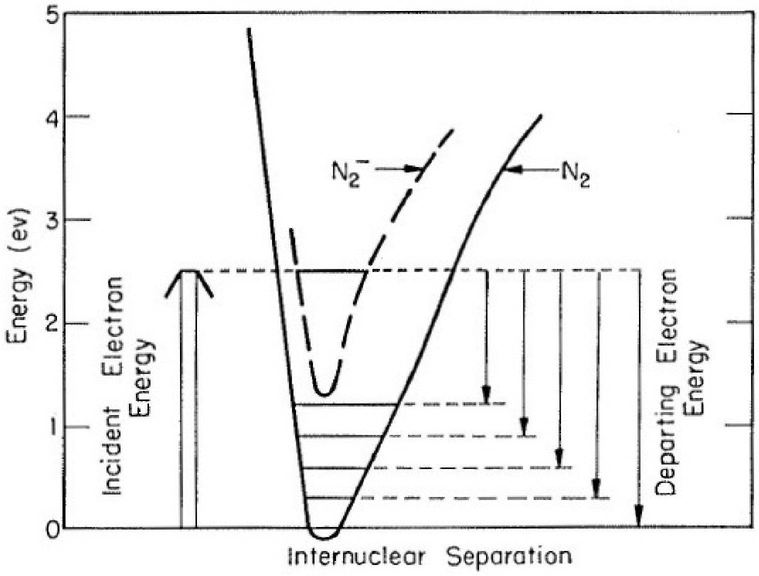

Figure 4.29: Schematic representation of inelastic scattering of electrons via formation of a temporary negative ion state. This process leads to vibrational excitation of the neutral N_2 molecule. [129]

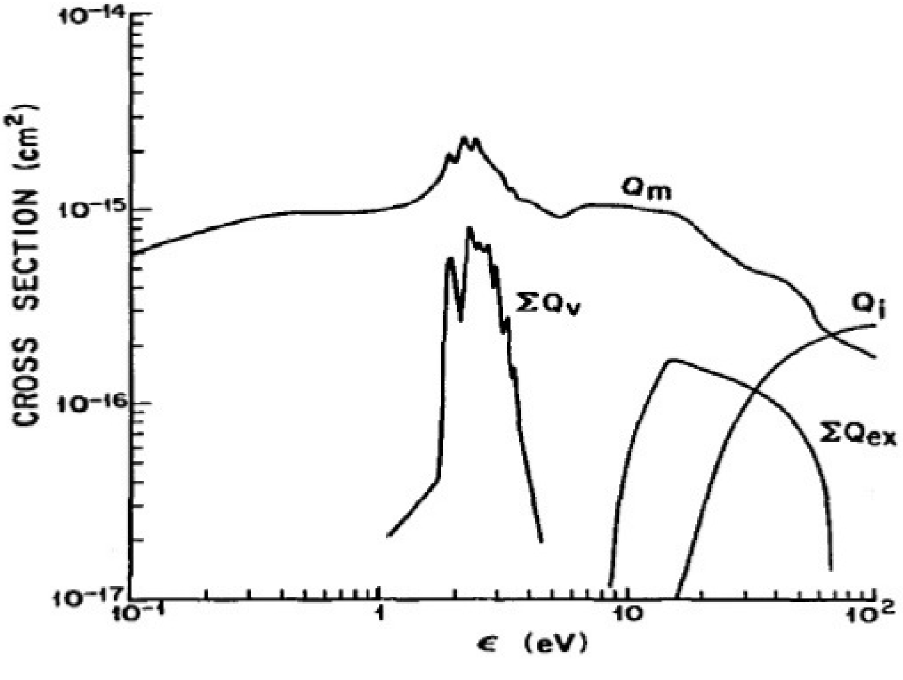

Figure 4.30: Cross-sections as a function of electron energy in N_2. Shown are the momentum transfer cross-section Q_m, the sum of vibrational cross-sections $\sum Q_v$, the sum of excitation cross-sections $\sum Q_{ex}$, and the ionization cross-section Q_i. (Adapted from [130])

For electrons with incident kinetic energies of 8eV and above, the electron polarization rises again. It peaks around 12eV before falling to zero at 15eV. In this energy range, electrons can excite the electronic states of N_2 (see figures 4.25 and 4.30), and will dissipate a large portion of their energy in this process. Table 4.4 lists the main electronic states (based on the magnitude of cross-sections) which electrons with the incident energies under consideration can excite. Also shown are the corresponding cross-sections, the onset energies for the excitation processes (or the approximate energy lost in the excitation process), and the approximate amount of energy the electron has after a single excitation. The collision number $NQ_{ex}L$ has been determined for the current experimental conditions, corresponding to 130mTorr of nitrogen, and a cell length of 3cm.

Under the present experimental conditions, the collision number $NQ_{ex}L$ for the excitation of an electronic state of N_2 is less than 1; only a fraction of the beam incident on the collision cell can excite any particular electronic state. Moreover, between 6eV and 15eV, electrons cannot rely on any other process involving molecular nitrogen to lose significant energy; the cross-sections for the vibrational excitation $\upsilon = 0 \to 1$ of N_2 by electron impact are negligible in this energy range. But once they excite an electronic state of N_2, some electrons may end up with energies where they experience large cross-sections σ_υ for forming temporary negative ions with nitrogen [127]. They can then excite vibrational states of N_2, dissipating more energy in the process. Or electrons with energies between 6eV and 15eV may excite an electronic state of N_2, and end up with less than 1eV after a single inelastic collision. Both collisional pathways just discussed would cause electrons to slow down, experience large spin-exchange cross-sections, and be more likely to be polarized by colliding with oriented rubidium atoms.

Table 4.4. Main electronic states of N_2 which incident electrons can excite. [120]

Incident kinetic energy (eV)	**Main electronic excitations**	**Cross-section Q_{ex} ($\times 10^{-16}$ cm^2)**	**$NQ_{ex}L$**	**Onset energy for excitation (eV)**	**Approximate energy remaining after a single excitation (eV)**
7-9	$A^3\Sigma_u^+$	0.090 - 0.140	0.2 - 0.3	6.2	1.8 - 2.8
	$a^1\Pi_g$	0.038	0.1	8.5	0.5
9-11	$A^3\Sigma_u^+$	0.140 - 0.155	0.3	6.2	2.8 - 3.5
	$B^3\Pi_g$	0.141 - 0.300	0.3 - 0.6	7.4	1.8 - 3.5
	$a^1\Pi_g$	0.100 - 0.174	0.2 - 0.4	8.4	1.8 - 3.5
	$W^3\Delta_u$	0.020 - 0.120	0.04 - 0.25	7.4	1.8 - 3.5
11-13	$a'^1\Sigma_u^-$	0.051 - 0.069	0.1 - 0.2	8.4	2.6 - 3.5
	$a^1\Pi_g$	0.174 - 0.254	0.4 - 0.5	8.5	2.5 - 3.5
	$w^1\Delta_u$	0.080 - 0.100	0.2	8.9	2.1 - 3.5
	$E^3\Sigma_g^+$	0.030 - 0.148	0.06 - 0.3	11.9	0.0 - 1.0
	$C^3\Pi_u$	0.074 - 0.147	0.2 - 0.3	11.0	0.5 - 1.0
		0.230 - 0.335	0.5 - 0.7	11.0	1.8 - 2.0
14-16	$A^3\Sigma_u^+$	0.150 - 0.180	0.3 - 0.4	6.2	7.8 - 9.8
	$B^3\Pi_g$	0.224 - 0.308	0.5 - 0.7	7.4	6.6 - 8.6
	$W^3\Delta_u$	0.216 - 0.238	0.5	7.4	6.6 - 8.6
	$B'^3\Sigma_u^-$	0.143 - 0.162	0.3	8.2	5.8 - 7.8
	$a'^1\Sigma_u^-$	0.095 - 0.110	0.2	8.4	5.6 - 7.6
	$a^1\Pi_g$	0.394 - 0.469	0.8 - 1.0	8.5	5.5 - 7.5
	$w^1\Delta_u$	0.078 - 0.103	0.2	8.9	5.1 - 7.1
	$C^3\Pi_u$	0.447 - 0.551	0.9 - 1.0	11.0	3.0 - 5.0

As an example, take an 8eV beam with an energy width of ~2eV, which corresponds to the experimental conditions in this study. Table 4.4 shows that electrons with energy between 8eV and 9eV can excite the $A^3\Sigma_u^+$ electronic state of N_2, and end up with 1.8eV to 2.8eV. These electrons can subsequently excite the vibrational states of nitrogen molecules via the formation of temporary negative ions, thus losing more energy. Particles with ~9eV of energy in the incident beam under consideration can also excite the $a^1\Pi_g$ electronic state of molecular nitrogen, which will cause them to have less than 1eV after a single inelastic collision. These processes increase the chance that such an electron beam undergoes spin-exchange collisions with oriented rubidium atoms. A 12eV incident beam with the same energy width as above has more electronic excitation channels of N_2 open to it. Electrons can excite the $a'\,^1\Sigma_u^-$, $a^1\Pi_g$, $w^1\Delta_u$ and $C^3\Pi_u$ states, and fall in an energy band where they are likely to produce vibrational excitations of nitrogen molecules. They can also lose a significant amount of energy, and have less than 1eV left by exciting the $E^3\Sigma_g^+$ and $C^3\Pi_u$ electronic states of N_2. Electrons incident with energies ranging between 14eV and 16eV have large impact excitation cross-sections of molecular nitrogen (see Table 4.4). However, they have a significant amount of energy left, between ~3eV and ~10eV, after exciting any particular electronic state. The particles do not dissipate enough energy to enhance their likelihood of undergoing spin-exchange collisions with oriented rubidium atoms, and be polarized. Energy distributions obtained from retarding field analyses (see figure 4.31) seem to

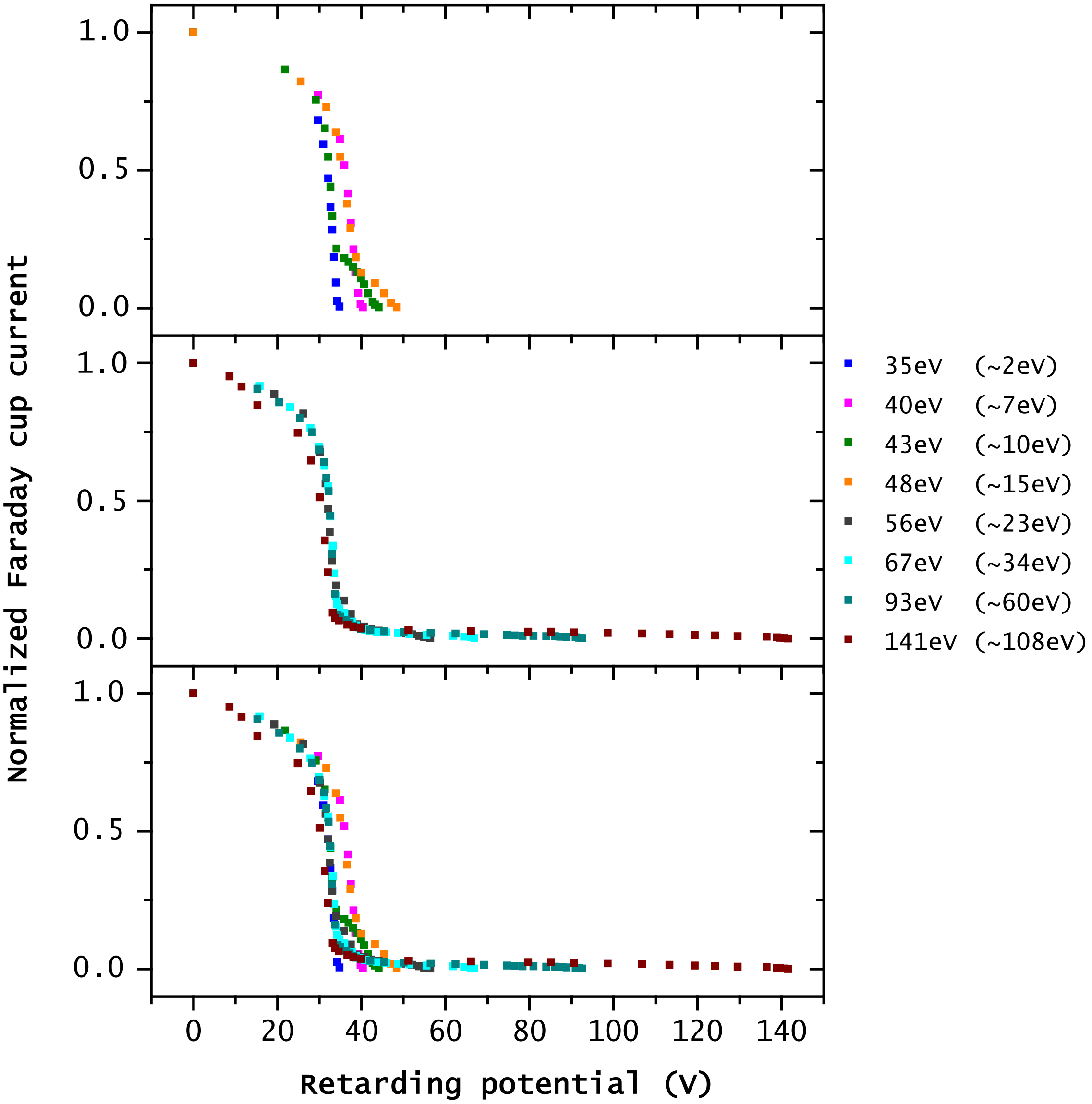

Figure 4.31: Retarding field analyses of electron beams with different energies incident on the collision cell with 130mTorr of N_2 and a rubidium vapor of ~10^{13} atoms/cm^3 in density. In the legend, the numbers in parentheses denote the approximate kinetic energy of the electrons at the entrance electrode. The top panel shows retarding field curves for the four slowest incident energies investigated while data in the middle panel correspond to the highest incident energies studied. Results for all incident energies have been combined in the bottom panel.

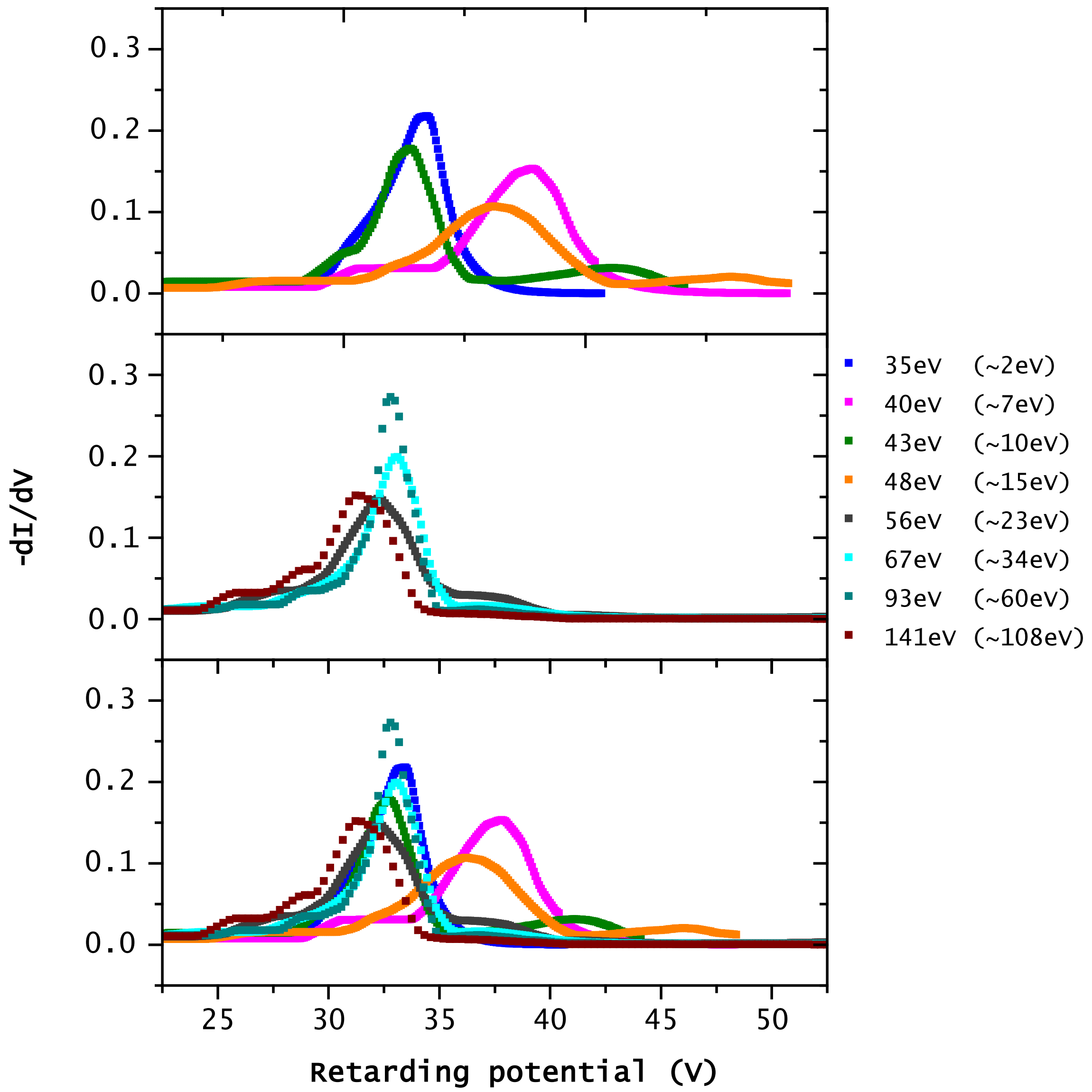

Figure 4.32: Energy distributions obtained from the retarding field analyses of electron beams with different energies incident on the collision cell with 130mTorr of N_2 and a rubidium vapor of ~10^{13} atoms/cm^3 in density (see figure 4.31). In the legend, the numbers in parentheses denote the approximate kinetic energy of the electrons at the entrance electrode. The top panel shows energy distributions for the fours lowest incident energies investigated while data in the middle panel correspond to the highest incident energies studied. Results for all incident energies have been combined in the bottom panel.

support this hypothesis for electrons incident with kinetic energies of 15eV (see figure 4.32). It shows that the majority of electrons introduced into the cell with 10eV emerge slower than those injected with either 7eV or 15eV (see top panel of figure 4.32). Electrons with incident kinetic energies of 7eV and 15eV are less likely to undergo spin-exchange collisions with oriented rubidium atoms, and the polarization of the beam is close to zero.

Above energies corresponding to the threshold for the ionization of nitrogen molecules (15.6eV), the electron polarization rises as the incident kinetic energy increases. At 105eV, which is close to the maximum ionization cross-section [120], it matches the peak electron polarization observed at the lowest energies. As was discussed previously, excitation and ionization of nitrogen molecules by primary electrons result in significant energy loss and the production of slow particles. This phenomenon can be observed again in figure 4.32. For incident energies above the ionization of molecular nitrogen, the energy distribution of beams emerging from the collision cell consists mainly of low energy electrons. These slow particles have high probabilities of undergoing spin exchange collisions with oriented rubidium atoms.

The experimental data in this section suggests that the ionization process may be a key factor in enhancing the current obtained from the optically-pumped electron spin filter. By ionizing the buffer gas, the primary electrons lose energy, and also produce slow secondary electrons. So, in addition to having a large cross-section for quenching excited rubidium atoms, an ideal buffer gas will possess large electron-impact ionization cross-sections. Ethylene has a maximum electron-impact ionization cross-section twice that of nitrogen [120, 131]. From figure 4.33, we see that its cross-section peaks at about the same energy as nitrogen. Future experiments should therefore include repeating the present study with ethylene.

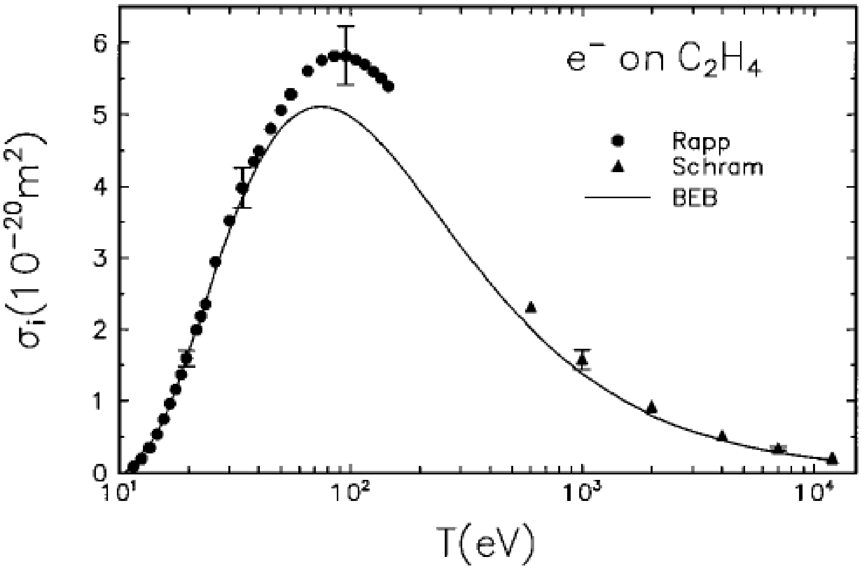

Figure 4.33: Electron impact ionization cross-section of ethylene. Comparison of the binary-encounter Bethe model (BEB) cross-section to experiment. (After Hwang *et al.* [131])

Chapter 5. Summary

In this study, we have built a more robust, easy to use source of polarized electrons than that of Batelaan *et al.* [29]. We have particularly addressed issues raised by work following the efforts of Batelaan *et al.* [29], namely the instability of the cold cathode discharge as the source of free, unpolarized electrons, and our later inability to produce beams of polarizations greater than 2% [30]. In the present setup, thermionic emission from a pure tungsten filament produces the beam of free, unpolarized electrons, and a turn-key diode laser is used to orient the rubidium vapor. These modifications simplify the operation of the system, and take us a step closer towards the realization of a "black-box" source of polarized electrons with less stringent vacuum requirements. Compared to standard GaAs sources, our new source would be much better for experiments in a university research laboratory setting.

Chapters 2 and 3 contain extensive descriptions of the system and how it is operated, especially with regard to transport of electron beams, manipulation of rubidium and its vapor, and measurements of electron polarization P_e. Measurements of P_e were carried out with a new, compact optical electron polarimeter [91]. This instrument offers several attractive features for electron spin analysis. Unlike earlier helium optical electron polarimeters which were designed for transversely polarized particles, this model can measure the polarization of longitudinally polarized electron beams. It is also relatively simple and compact in its construction. By relying on a magnetic field to guide the longitudinally spin-polarized electron beam, the present instrument employs fewer electrodes. It also uses a commercially-available integrated photon counting module. These features allow it to occupy a smaller volume and make it easier to operate. Moreover, this optical electron polarimeter offers a maximum fluorescence detection efficiency of ~20 Hz/nA, which is an order of magnitude higher than earlier versions reported by us.

The results in chapter 4 demonstrate that the present system can produce polarized electron beams with sufficient reliability to allow us to undertake systematic studies to find the factors affecting P_e. It was thus observed that the pump light parameters, the choice of buffer gas, the electric field across the collision region, and the energy of the incident electrons have an impact on the resulting polarization of the electron beam. Measurement of P_e as a function of pump light wavelengths, for instance, shows that the electron polarization tracks that of the rubidium closely, which is to be expected given the results of Batelaan *et al.* [29]. Norrgard *et al.* [64] have demonstrated that the electron spin polarization of rubidium vapors can reverse direction for a range of wavelengths if the pump light is not purely circularly-polarized but contaminated with some linear component, and is spectrally-narrow so that only a few of the hyperfine transitions are being pumped. The polarization of our electron beam exhibits a similar reversal when the pump laser's wavelength is varied. This spin-reversal phenomenon can, in effect, be used to provide an independent means of flipping the spin-polarization of the electrons in addition to reversing the pump light's helicity. Users of polarized sources based on the spin-exchange collisions of slow electrons with optically-pumped alkali vapors could potentially have two ways of reversing P_e for the study and elimination of systematic instrumental asymmetries. Above all, this experiment highlights the inefficiency of our present optical pumping scheme which involves a single pump laser. As suggested by Norrgard *et al.* [64], the polarization of the alkali vapor may increase significantly by employing two pump lasers: one tuned to the $F_g = 2 \rightarrow F_e = 2,3$ transitions of rubidium-85 and the $F_g = 1 \rightarrow F_e = 1,2$ transitions of rubidium-87, and another to the $F_g = 3 \rightarrow F_e = 2,3$ transitions of rubidium-85 and $F_g = 2 \rightarrow F_e = 1,2$ transitions of rubidium-85 (see figure 5.1). Under such conditions, the population of all sublevels can absorb photons, and can be transferred to the target state to be polarized. The rubidium atoms will not be stuck in any particular state even if the pump light is not perfectly circularly-polarized. This scheme has the potential to increase the rubidium polarization, and hence that of the electron beam without the need to add tens of Torr of buffer gas as suggested by the work of Rosenberry *et al.* [59]. It would thus relax the vacuum requirements for this kind of polarized electron source.

Unlike the system developed by Batelaan *et al.* [29], the source of free, unpolarized electrons in the present setup is separate from the buffer gas. In other words, electron beams can be produced with or without buffer gas in the collision cell. This feature allowed us to see how the gas affects the energy of the incident electrons. It was, for example, observed that inelastic processes such as excitation and ionization of the buffer gas can cause electrons to dissipate large amounts of energy. The ionization process also produces slow secondary electrons which may increase the electron current exiting the collision cell. Electrons resulting from such inelastic processes experience

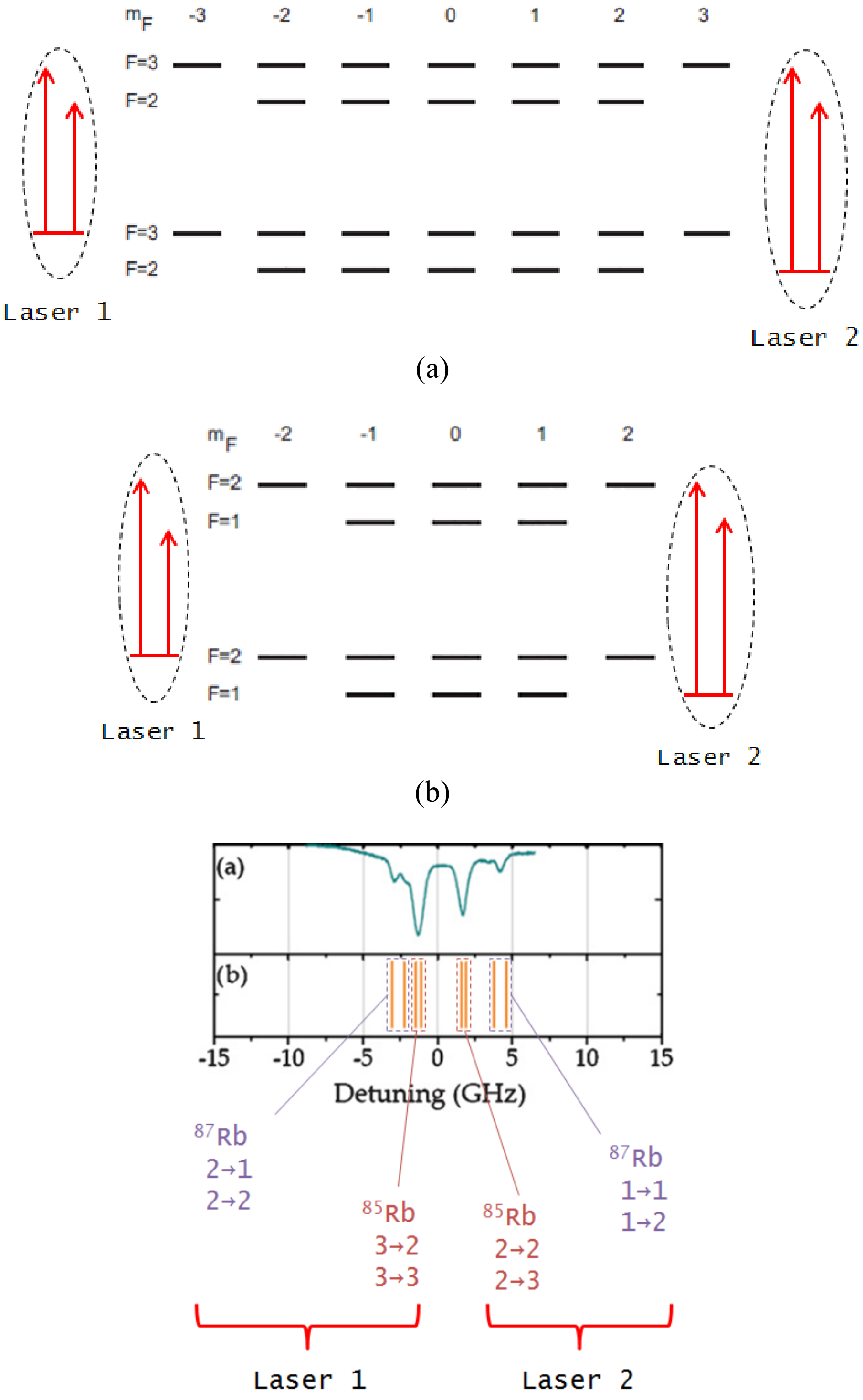

(a)

(b)

(c)

Figure 5.1: Using two lasers to pump on all D1 hyperfine transitions of (a) rubidium-85 and (b) rubidium-87 may lead to higher alkali vapor polarization according to Norrgard *et al.* [64]. (See text for details.)

large spin-exchange cross-sections, and are likely to be polarized. It was indeed observed that P_e for electrons with relatively high incident energies (~100eV) matched that of slow incoming particles while at the same time offering a 40-fold increase in the current collected on the Faraday cup. This experiment suggests that another criterion should be added to the list of desirable characteristics an ideal buffer gas would possess, namely large ionization cross-sections.

So far the present source has yielded its maximum figure-of-merit (FOM) with ethylene as buffer gas. An electron polarization of ~24% with 4μA of current has been recorded, corresponding to a figure-of-merit of 0.23μA. This value is comparable to that of Batelaan *et al.* [29], 0.26μA, but is much smaller than FOMs typically obtained with GaAs sources in our lab, which can be about 1.8μA.

It is however not known whether the high P_e achieved with ethylene is due to its large quenching cross-section or to its ability to slow down electrons, both of which would improve the polarization of the beam. The former would allow thick rubidium vapors to achieve high degrees of orientation while the latter would cause free electrons to experience large spin-exchange cross-sections, thus increasing their likelihood of being polarized. Modifying the electron gun/collision cell assembly by either offsetting the tungsten filament or by using a spirally-shaped one to let the probe beam through the collision cell consistently would help us study how different buffer gases affect the rubidium polarization. Such a change would allow us to investigate whether ethylene is indeed better at orienting rubidium atoms. The addition of a high resolution retarding field analyzer, maybe in place of the electron collector on the rotary feedthrough in the differentially-pumped chamber, would help us obtain more accurate information on the effects of the buffer gases on the energy of incident electrons.

Future experiments should extend this study to include benzene as buffer gas. Norrish *et al.* [132] have determined that it has a quenching cross-section about twice that of ethylene while Warman *et al.* [111] have estimated that electrons with ~1eV of energy will thermalize slightly faster in benzene. Given these characteristics, we can expect to see even higher electron polarizations with benzene compared to ethylene.

The pressure of buffer gas the system can handle is currently limited to ~200mTorr. By decreasing the exit aperture diameter from 2mm to 1mm, it is estimated that ~600mTorr of gas may be introduced in the collision cell before the pressure above the diffusion pump reaches the mTorr regime where significant backstreaming of diffusion pump oil into the source chamber would occur. Higher buffer gas pressures would prove beneficial to both the polarization of the rubidium vapor and the slowing down of incident electrons.

Finally, the present source could also benefit from a temperature control system. Currently, the heater power supplies have to be adjusted constantly to keep the temperature of the collision cell and hence, the rubidium density steady. By maintaining a vapor with a constant thickness, a temperature control system would allow us to study whether the electron polarization and the current recorded on the Faraday cup of the source are stable over time periods typically used in experiments involving polarized electrons, which can extend to several hours in a university lab setting. Moreover, the temperature control system could be interfaced with Labview, and could be programmed to start heating the source and allow the rubidium vapor to stabilize, say, an hour before the user arrives. It would cut down on the waiting time, and allow the experimenter to use the source immediately.

Appendix A. Labview VI

This section contains the Labview “codes” used in the data-taking process during this study. The main Labview VI employed was built from three fundamental subroutines: one to acquire a reading of the Convectron gauge attached to the optical electron polarimeter chamber, another to gather multiple samples of the current read by the picoammeter connected to the Faraday cup, and a final one to obtain the total photon counts from the photomultiplier tube in a user-defined time interval. The front panel and the block diagram of these Labview subroutines are shown below.

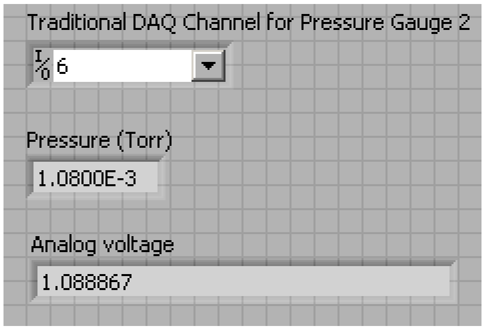

Traditional DAQ Channel for Pressure Gauge 2: 6

Pressure (Torr): 1.0800E-3

Analog voltage: 1.088867

Figure A.1: Front panel of the “pressure gauge” Labview VI. The user must first find the channel on the National Instruments card to which the Convectron gauge has been connected, and then, put that number is the box at the top. The Labview VI will read the analog voltage being sent out by the pressure gauge, which will be shown at the bottom of the front panel. This analog voltage is converted into the corresponding chamber pressure reading using the appropriate functional relationship given in the pressure gauge owner’s manual.

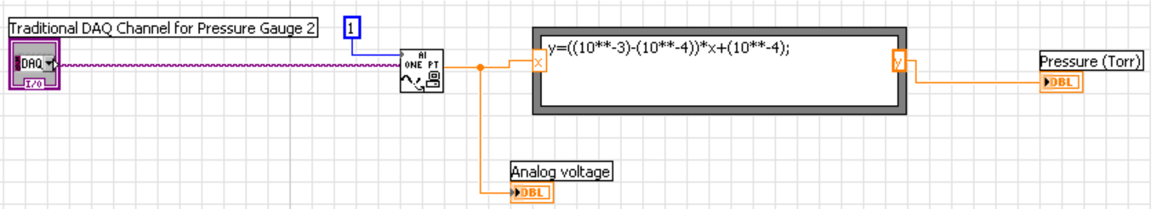

```
y=((10**-3)-(10**-4))*x+(10**-4);
```

Figure A.2: Block diagram of the Labview VI used to acquire a sample of the pressure gauge reading. The equation to convert the analog voltage output by the pressure gauge into its corresponding pressure value is shown in the box. It can be found in the owner's manual for the pressure gauge.

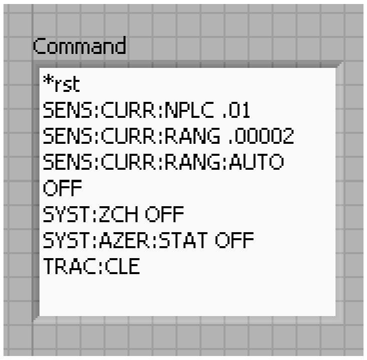

```
*rst
SENS:CURR:NPLC .01
SENS:CURR:RANG .00002
SENS:CURR:RANG:AUTO
OFF
SYST:ZCH OFF
SYST:AZER:STAT OFF
TRAC:CLE
```

Figure A.3: Front panel of the "GPIB read" VI (written by M. Fabrikant). These commands must be sent to the picoammeter before any reading can be acquired with Labview.

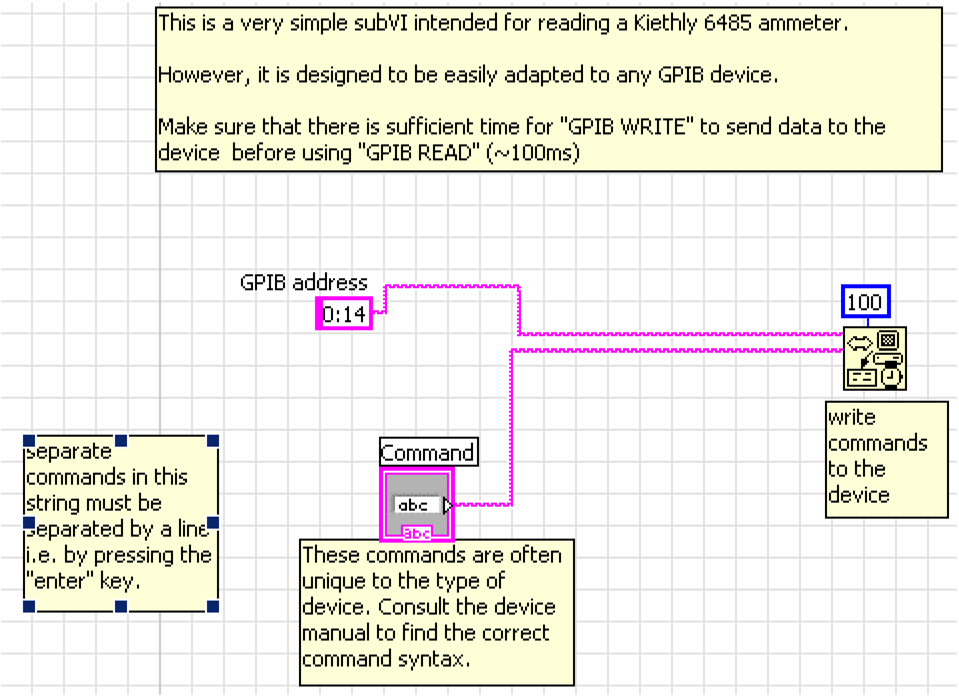

This is a very simple subVI intended for reading a Kiethly 6485 ammeter.

However, it is designed to be easily adapted to any GPIB device.

Make sure that there is sufficient time for "GPIB WRITE" to send data to the device before using "GPIB READ" (~100ms)

GPIB address: 0:14

separate commands in this string must be separated by a line i.e. by pressing the "enter" key.

These commands are often unique to the type of device. Consult the device manual to find the correct command syntax.

write commands to the device

Figure A.4: Block diagram of the “GPIB read” Labview VI.

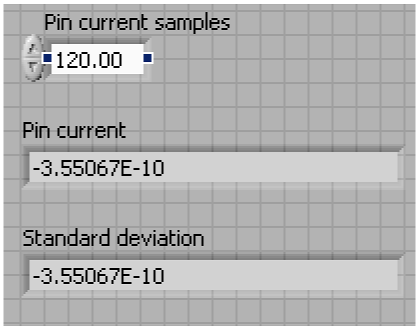

Pin current samples: 120.00

Pin current: -3.55067E-10

Standard deviation: -3.55067E-10

Figure A.5: Once the “GPIB read” VI has been run, the “Keithley” VI can be used to gather multiple samples of the picoammeter reading. The user can define the number of samples to be gathered in the top box. After acquiring the desired number of current readings, the VI will calculate its average and standard deviation, and output it.

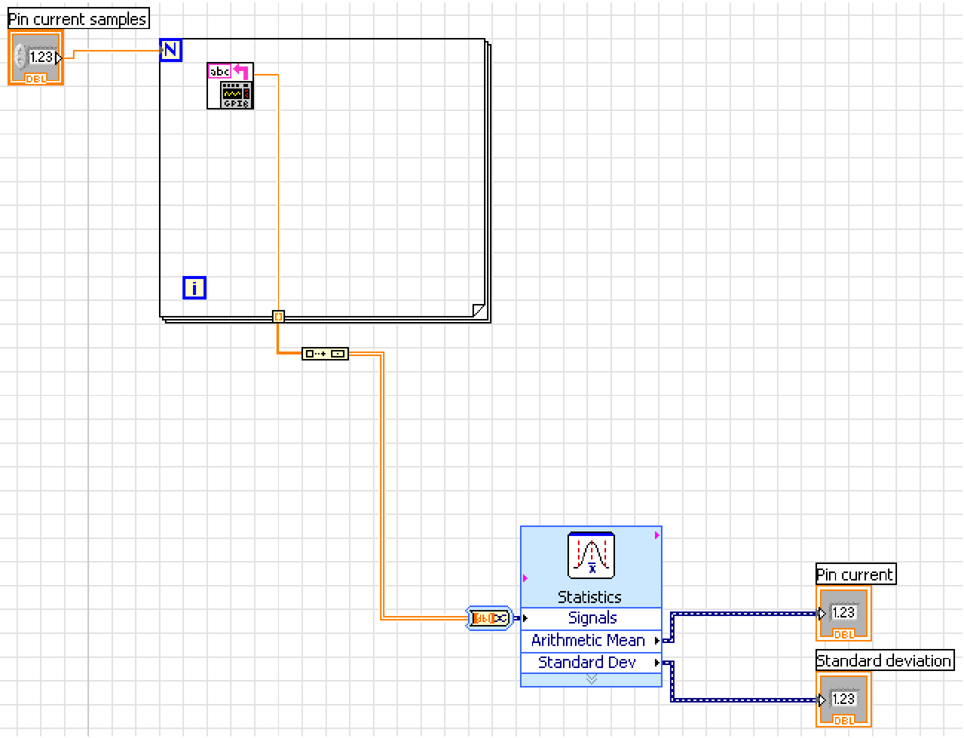

Figure A.6: Front panel of the "Keithley" VI.

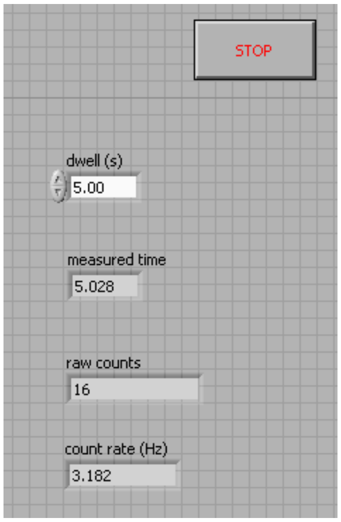

dwell (s)
5.00

measured time
5.028

raw counts
16

count rate (Hz)
3.182

Figure A.7: The "counter" VI (written by J. Maseberg) acquires the total number of counts from the photomultiplier tube in a user-defined time interval. This interval is specified in the box labeled "dwell." At the end, the software will output the actual time period over which photon counts were gathered in the second box. The VI will output the total number counts and the corresponding count rate in the last two boxes.

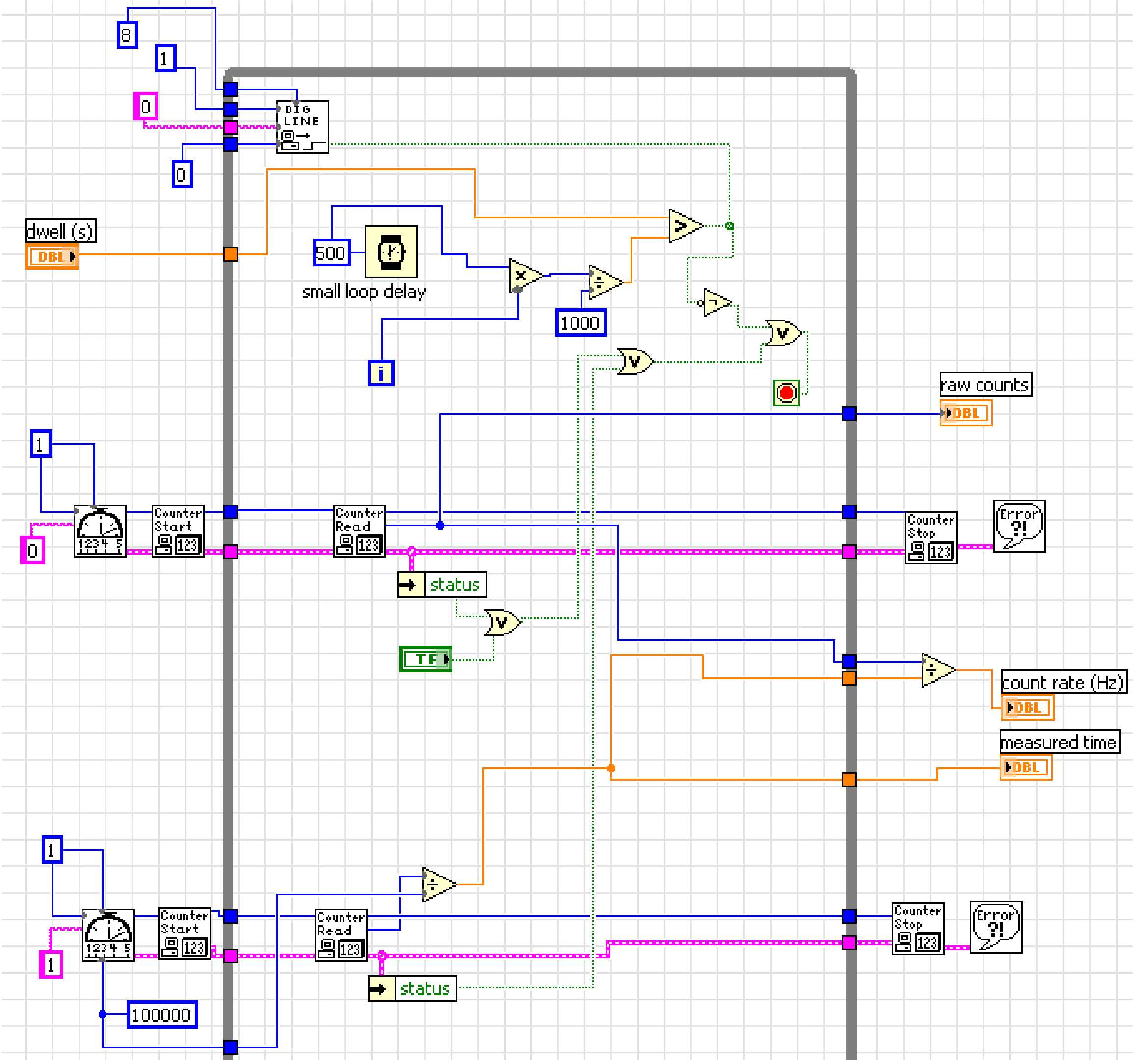

Figure A.8: Block diagram of the “counter” VI.

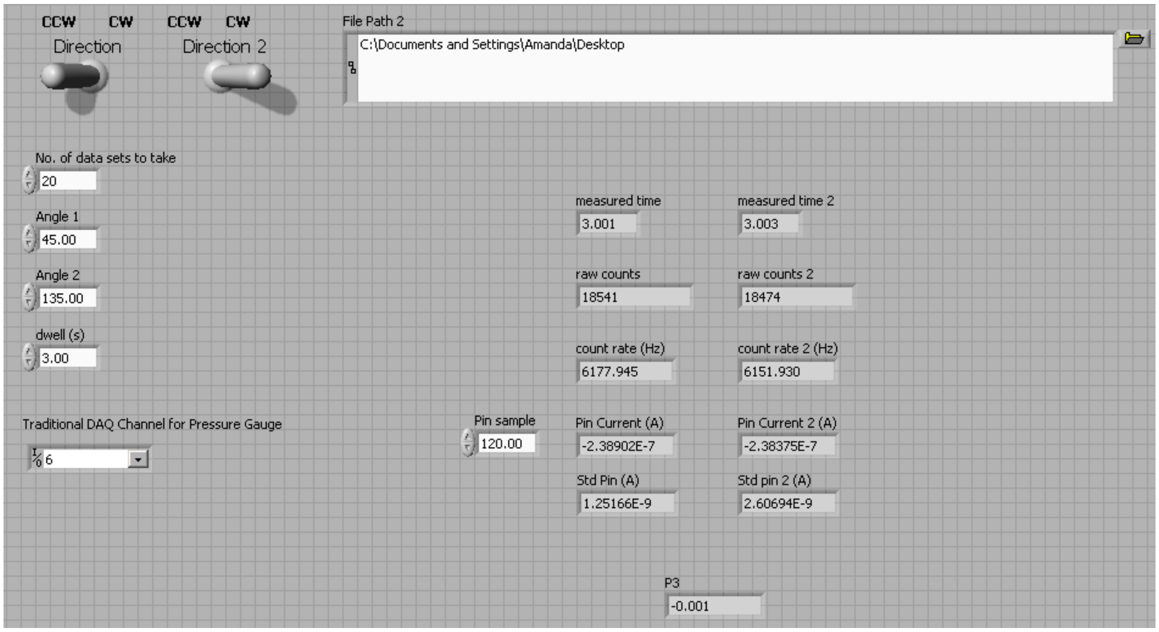

File Path 2: C:\Documents and Settings\Amanda\Desktop

No. of data sets to take: 20

Angle 1: 45.00

Angle 2: 135.00

dwell (s): 3.00

Traditional DAQ Channel for Pressure Gauge: 6

Pin sample: 120.00

measured time: 3.001

measured time 2: 3.003

raw counts: 18541

raw counts 2: 18474

count rate (Hz): 6177.945

count rate 2 (Hz): 6151.930

Pin Current (A): -2.38902E-7

Pin Current 2 (A): -2.38375E-7

Std Pin (A): 1.25166E-9

Std pin 2 (A): 2.60694E-9

P3: -0.001

Figure A.9: Shown is the front panel of the “polarimeter” VI used during the experiments in this study. To determine the magnitude of the relative Stokes parameter P_3, the retarder’s fast/slow axis is set at an angle of 45° and 135°, and data corresponding to the Faraday cup current, pressure in the polarimeter chamber, and photon count rate are acquired. Before using the VI, the user has to undertake the steps described in chapter 3 to locate the retarder’s fast/slow axis, and set it at 45° to the linear polarizer’s transmission axis. Once this step has been completed, the user can proceed to input 45° and 135° in the boxes labeled “Angle 1” and “Angle 2.” The number of times the user wants the relative Stokes parameter P_3 to be determined in any given experimental run must be specified in the box labeled “No. of data sets to take.” Every time a set of data (measured times, raw counts, count rates, Faraday cup currents) corresponding to the two positions of interest of the retarder’s fast/slow axis (45° and 135°) is acquired, the VI will output an un-normalized value of P_3. The user will have to analyze the data more thoroughly later according to the procedure described in chapter 3. In the box labeled “File path 2” the user can specify the file path (usually a .txt file) to which data being gathered by the VI will be saved.

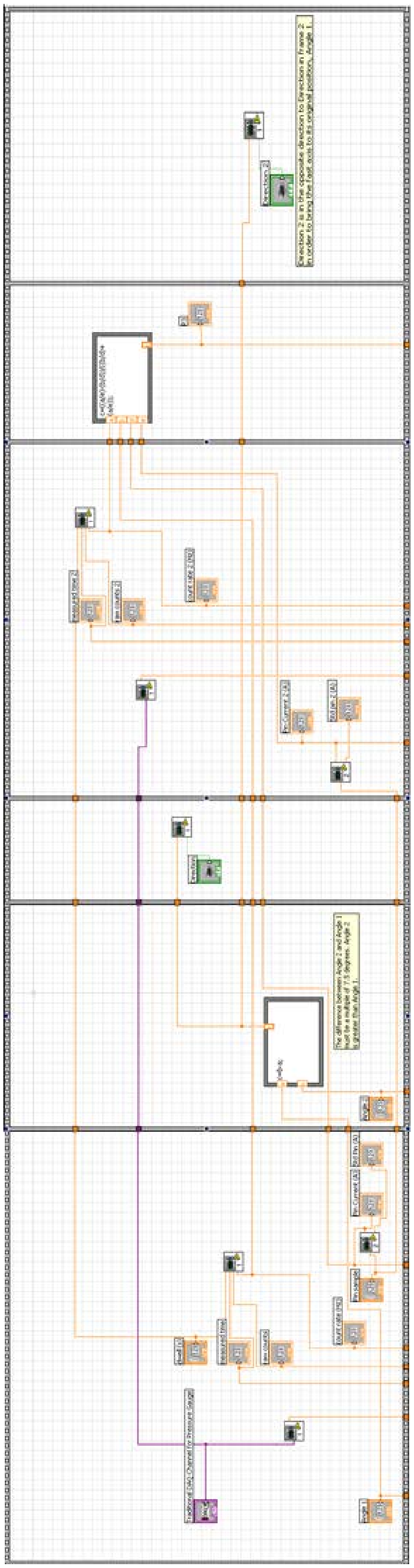

Figure A.10: Block diagram of the “polarimter” VI.

References

[1] J. Kessler, Polarized electrons, Berlin Heidelberg New York: Springer-Verlag, 1985.

[2] D. Bohm, Quantum theory, New York: Dover Publications, 1989.

[3] M. Auzinsh, D. Budker and S. Rochester, Optically Polarized Atoms, New York: Oxford University Press, 2010.

[4] L. Bergmann and C. Schaefer, Constituents of matter, Berlin New York: de Gruyter, 1997.

[5] O. Berger and J. Kessler, *J. Phys. B,* vol. 19, p. 3539, 1986.

[6] K. W. Trantham, M. E. Johnston and T. J. Gay, *J. Phys. B,* vol. 28, p. L543, 1995.

[7] R. A. Rosenberg, *Top Curr Chem,* vol. 298, p. 279, 2011.

[8] W. A. Bonner, M. A. van Dort and M. R. Yearian, *Nature,* vol. 258, p. 419, 1975.

[9] L. A. Hodge, F. B. Dunning, G. K. Walters, R. H. White and G. J. Schroepfer, *Nature,* vol. 280, p. 250, 1979.

[10] M. J. Alguard et al., *Phys. Rev. Lett. ,* vol. 37, p. 1261, 1976.

[11] C. Y. Prescott et al., *Phys. Letters B,* vol. 77, p. 347, 1978.

[12] C. Y. Prescott et al., *Phys. Letters B,* vol. 84, p. 524, 1979.

[13] D. T. Pierce, *Physica Scripta.,* vol. 38, p. 291, 1988.

[14] R. Feder, Polarized electrons in surface physics, Singapore: World Scientific, 1985.

[15] I. Zutic, J. Fabian and S. Das Sharma, *Rev. Mod. Phys.,* vol. 76, p. 323, 2004.

[16] D. Johnson, N. B. Brookes, S. L. Hulbert, R. W. Klaffky, N. V. Smith, R. J. Celotta, M. H. Kelly, D. T. Pierce, B. J. Waclawski and M. R. Howells, *Rev. Sci. Instrum,* vol. 63, p. 1902, 1992.

[17] J. B. Pendry, *Phys. Rev. Lett.,* vol. 45, p. 1356, 1980.

[18] J. Unguris, A. Seiler, J. Celotta, D. T. Pierce, P. D. Johnson and N. V. Smith, *Phys. Rev. Lett. ,* vol. 49, p. 1047, 1982.

[19] J. Kirschner, D. Rebenstorff and H. Ibach, *Phys. Rev. Lett.,* vol. 53, p. 698, 1984.

[20] E. Bauer, *Rep. Prog. Phys.,* vol. 57, p. 895, 1994.

[21] P. Dey and W. Weber, *J. Phys.: Condens. Matter,* vol. 23, p. 473201, 2011.

[22] Y. Lassailly, H. J. Drouhin, A. J. van der Sluijs, L. G and C. Marliere, *Phys. Rev. B,* vol. 50, p. 13054, 1994.

[23] M. Plihal, D. L. Mills and J. Kirschner, *Phys. Rev. Lett.,* vol. 82, p. 2579, 1999.

[24] R. J. Celotta and D. T. Pierce, *Adv. At. Mol. Phys.,* vol. 16, p. 101, 1980.

[25] T. J. Gay, *Adv. At. Mol. Phys.,* vol. 57, p. 157, 2009.

[26] D. T. Pierce, F. Meier and P. Zurcher, *Appl. Phys. Lett.,* vol. 26, p. 670, 1975.

[27] D. T. Pierce and F. Meier, *Phys. Rev. B,* vol. 13, p. 5484, 1976.

[28] H. M. Al-Khateeb, B. G. Birdsey, T. C. Bowen, A. S. Green and M. E. Johnston, *Rev. Sci. Instrum.,* vol. 70, p. 3882, 1999.

[29] H. Batelaan, A. S. Green, H. A. Hitt and T. J. Gay, *Phys. Rev. Lett.,* vol. 82, p. 4216, 1999.

[30] M. A. Rosenberry, H. Batelaan, J. P. Reyes and T. J. Gay, "Progress with optically pumped sources of polarized electrons," *AIP Conf. Proc. ,* vol. 604, p. 264, 2002.

[31] F. C. Tang, M. S. Lubell, K. Rubin, A. Vasilakis, M. Eminyan and J. Slevina, *Rev. Sci. Instrum.,* vol. 57, p. 3004, 1986.

[32] J. W. Maseberg and T. J. Gay, *J. Phys. B.,* vol. 39, p. 4861, 2006.

[33] M. J. Alguard, J. E. Clendenin, R. D. Ehrlich, V. W. Hughes, J. S. Ladish, M. S. Lubell, K. P. Schüler, G. Baum, W. Raith, R. H. Miller and W. Lysenko, *Nucl. Instrum. Methods,* vol. 163, p. 29, 1979.

[34] U. Fano, *Phys. Rev.,* vol. 131, p. 178, 1969.

[35] W. von Drachenfels, U. T. Koch, T. M. Müller, W. Paul and S. H. R, *Nucl. Instrum. Methods,* vol. 140, p. 47, 1977.

[36] P. F. Wainwright, M. J. Alguard, G. Baum and M. S. Lubell, *Rev. Sci. Instrum. ,* vol. 49, p. 571, 1978.

[37] N. Muller, W. Eckstein and W. Heiland, *Phys. Rev. Lett.,* vol. 29, p. 1651, 1972.

[38] E. Kisker, G. Baum, A. H. Mahan, W. Raith and B. Reihl, *Phys. Rev. B,* vol. 18, p. 2256, 1978.

[39] M. V. McCusker, L. L. Hatfield and G. K. Walters, *Phys. Rev. Lett. ,* vol. 21, p. 817, 1969.

[40] P. J. Keliher, R. E. Gleason and G. K. Walters, *Phys. Rev. A,* vol. 11, p. 1279, 1975.

[41] G. Rutherford, J. M. Ratliff, J. G. Lynn, F. B. Dunning and G. K. Walters, *Rev. Sci. Instrum.,* vol. 61, p. 1460, 1990.

[42] T. J. Gay, private communication.

[43] M. V. McCusker, L. L. Hatfield and G. K. Walters, *Physical Review A,* vol. 5, p. 177, 1972.

[44] P. G. Burke and H. M. Shey, *Phys. Rev. ,* vol. 126, p. 163, 1962.

[45] G. F. Drukarev and V. D. Ob'edkov, *Sov. Phys. Usp.,* vol. 22, p. 236, 1979.

[46] P. S. Farago and H. Siegmann, *Phys. Lett.,* vol. 20, p. 279, 1966.

[47] D. M. Campbell, H. M. Brash and P. S. Farago, *Proc. R. Soc. Edinb. A,* vol. 70, p. 15, 1971.

[48] R. J. Krisciokaitis and Wu-Yang Tsai, *Nucl. Instrum. Methods,* vol. 83, p. 45, 1970.

[49] R. Krisciokaitis-Krisst and W. K. Peterson, *Nucl. Instrum. Methods,* vol. 118, p. 157, 1974.

[50] K. Aulenbacher et al., *Nucl. Instrum. Methods. Phys. Res. Sect. A,* vol. 391, p. 498, 1997.

[51] A. Kastler, *J. Phys. Radium,* vol. 11, p. 255, 1950.

[52] G. Breit and I. I. Rabi, *Phys. Rev.,* vol. 38, p. 2082, 1931.

[53] L. W. Anderson and T. Walker, *Nucl. Instrum. Meth. A,* vol. 316, p. 123, 1992.

[54] M. Tanaka, Y. Takahashi, T. Shimoda, M. Yosoi, K. Takahisa and Y. A. Plis, *Rev. Sci. Instrum.,* vol. 79, p. 02B308, 2008.

[55] W. Happer, *Rev. Mod. Phys.,* vol. 44, p. 169, 1972.

[56] T. G. Walker and W. Happer, *Rev. Mod. Phys.,* vol. 69, p. 629, 1997.

[57] I. I. Fabrikant, private communication, 2011.

[58] E. S. Hrycyshyn and L. Krause, *Can. J. Phys.,* vol. 48, p. 2761, 1970.

[59] M. A. Rosenberry, J. P. Reyes, D. Tupa and T. J. Gay, *Phys. Rev. A,* vol. 75, p. 023401, 2007.

[60] Z. Wu, M. Kitano, W. Happer, M. Hou and J. Daniels, *Phys. Rev. A,* vol. 49, p. 3854, 1994.

[61] J. P. Reyes, Master's thesis, University of Nebraska-Lincoln, 2005.

[62] T. J. Walker, *J Phys Conf Ser. ,* vol. 294, p. 012001, 2011.

[63] B. Bederson and L. J. Kieffer, *Rev. Mord. Phys.,* vol. 43, p. 601, 1971.

[64] E. B. Norrgard, D. Tupa, J. M. Dreiling and T. J. Gay, *Phys. Rev. A ,* vol. 82, p. 033408, 2010.

[65] E. Dennison, "Magnet Formulas," 2005. [Online]. Available: http://www.netdenizen.com/emagnet/solenoids/thinsolenoid.htm. [Accessed 19 April 2013].

[66] D. J. Griffiths, Introduction to Electrodynamics, Boston: Addison-Wesley, 2012.

[67] Granville-Phillips, Series 307 Vacuum Gauge Controller Instruction Manual, Boulder: Granville-Phillips, 1994.

[68] T. G. Anderson, B. G. Birdsey, S. M. Woeher, M. A. Rosenberry and T. J. Gay,

Rev. Sci. Instrum. , vol. 72, p. 2923, 2001.

[69] K. W. Trantham, T. J. Gay and R. J. Vandiver, *Rev. Sci. Instrum.,* vol. 67, p. 4103, 1996.

[70] T. Fischer and J. Kessler, *Rev. Sci. Instrum.,* vol. 66, p. 4885, 1995.

[71] E. T. Litaker, J. R. Machacek and T. J. Gay, *Eur. J. Phys.,* vol. 32, p. 1107, 2011.

[72] J. H. Moore, C. C. Davis, M. A. Coplan and S. C. Greer, Building Scientific Apparatus, Cambridge: Cambridge University Press, 2009.

[73] O. W. Richardson, Thermionic Emission from Hot Bodies, Palm Springs: Wexford College Press, 2003.

[74] P. D. Burrow, private communication, 2013.

[75] J. B. Baker and G. B. Gaines, "Evaluation of electron-emission behavior for detecting carbon in tungsten and rhenium," Battelle Memorial Institute, Columbus, 1963.

[76] K. Aflatooni, private communication, 2010.

[77] "WebElements," 1993-2012. [Online]. Available: http://www.webelements.com/compounds/rubidium/dirubidium_oxide.html. [Accessed 13 8 2013].

[78] Science Lab Chemicals and Laboratory Equipment, "ScienceLab.com," 2012. [Online]. Available: http://www.sciencelab.com/msds.php?msdsId=9927187. [Accessed 2013].

[79] T. J. Gay, M. C. Fritts, J. E. Furst, M. A. Khakoo and E. R. Mell, *J. Vac. Sci.*

Technol. A, vol. 12, p. 2903, 1994.

[80] J. H. Moore, C. C. Davis, M. A. Coplan and S. C. Greer, Building Scientific Apparatus, Cambridge: Cambridge University Press, 2009.

[81] S. J. Seltzer, Ph.D. thesis, Princeton University , 2008.

[82] W. Happer, in *Advances in Atomic and Molecular Physics*, Academic Press, 1988.

[83] E. B. Norrgard, Honor's thesis, 2010.

[84] A. Ueno, K. Takasaki, K. Ogura, Y. Wakuta, I. Kumabe, K. O-Ohata, Y. Mori and S. Fukumoto, *Nucl. Instrum. Meth. A,* vol. 262, no. 2-3, pp. 170-178, 1987.

[85] P. Siddons, "Absorption and dispersion profile simulation for Rb D1 Line," 2008. [Online]. Available: http://massey.dur.ac.uk/resources/psiddons/absdisD1.nb. [Accessed 2013].

[86] P. Siddons, Ph.D. thesis, Durham, UK: University of Durham, 2011.

[87] C. B. Alcock, V. P. Itkin and M. K. Horrigan, *Can. Metall. Quart.,* vol. 23, p. 309, 1984.

[88] T. J. Gay, *J. Phys. B,* vol. 16, p. L553, 1983.

[89] H. G. Berry, G. Gabrielse and W. E. Livingston, *Appl. Opt. ,* vol. 16, p. 3200, 1977.

[90] K. Bartschat, B. K, G. F. Hanne and J. Kessler, *J. Phys. B,* vol. 14, p. 3761, 1981.

[91] M. Pirbhai, D. M. Ryan, G. Richards and T. J. Gay, *Rev. Sci. Instrum. ,* vol. 84, p. 053113, 2013.

[92] A. B. Wedding, A. G. Mikosza and J. F. Williams, *JOSA A,* vol. 8, p. 1729, 1991.

[93] J. E. Furst, W. M. K. P. Wijayaratna, D. H. Madiosn and T. J. Gay, *Phys. Rev. A,* vol. 47, p. 3775, 1993.

[94] J. W. Maseberg, Ph.D. thesis, University of Nebraska - Lincoln, 2009.

[95] P. A. Hayes, D. H. Yu, J. Furst, M. Donath and J. F. Williams, *J. Phys. B,* vol. 29, p. 3989, 1996.

[96] I. C. Ruset, Ph.D. thesis, University of New Hampshire, 2005.

[97] N. C. M. Bartlett, J. Jankunas, R. N. Zare and J. A. Harrison, *Phys. Chem. Chem. Phys.,* vol. 12, p. 15689, 2010.

[98] V. I. Balykin, *Opt. Commun.,* vol. 33, p. 31, 1979.

[99] "Meadowlark Optics," 2006. [Online]. Available: http://www.meadowlark.com/retarders.php?pg=ret. [Accessed 30 9 2013].

[100] E. Collett, Polarized Light: Fundamentals and Applications, Worldwide: CRC Press, 1992.

[101] "Optical pumping of the polarized H- ion source at LAMPF," in *Accelerator Science and Technology Conference Record* , San Francisco, IEEE, 1991, p. 1931.

[102] H. G. Dehmelt, *Phys. Rev.,* vol. 109, no. 2, p. 381, 1958.

[103] G. G. Raju, Gaseous Electronics, Boca Raton: CRC Press, 2006.

[104] S. Appelt, A. Ben-Amar Baranga, C. J. Erickson, M. V. Romalis, A. R. Young and W. Happer, *Phys. Rev. A,* vol. 58, p. 1412, 1998.

[105] A. Corney, Atomic & Laser Spectroscopy, Oxford: Oxford University Press, 1978.

[106] S. J. Seltzer and M. V. Romalis, *J. Appl. Phys.,* vol. 106, p. 114905, 2009.

[107] D. A. Steck, "http://george.ph.utexas.edu/~dsteck/alkalidata/rubidium87numbers.pdf," 2 5 2008. [Online]. Available: http://george.ph.utexas.edu/~dsteck/alkalidata/rubidium87numbers.pdf. [Accessed 24 8 2013].

[108] O. Svelto, Principles of lasers, New York: Springer, 2010.

[109] S. Liu, Y. Zhang, D. Fan, H. Wu and P. Yuan, *Applied Optics,* vol. 50, p. 1620, 2011.

[110] S. G. Redsun, R. J. Knize, G. D. Cates and W. Happer, *Phys. Rev. A,* vol. 42, p. 1293, 1990.

[111] J. M. Warman and M. C. Sauer, *J. Chem. Phys.,* vol. 62, p. 1971, 1975.

[112] R. E. Johnson, Introduction to atomic and molecular collisions, New York: Plenum Press, 1982.

[113] D. Tupa and L. W. Anderson, *Phys. Rev. A,* vol. 36, p. 2142, 1987.

[114] B. Chann, E. Babcock, L. W. Anderson, T. G. Walker, W. C. Chen, T. B. Smith, A. K. Thompson and T. R. Gentile, *J. Appl. Phys. ,* vol. 94, p. 6908, 2003.

[115] W. Blum, W. Riegler and L. Rolandi, Particle detection with drift chambers, New York City: Springer, 2008.

[116] J. A. Simpson, *Rev. Sci. Instr.,* vol. 29, p. 701, 1958.

[117] G. F. Derbenwick, D. T. Pierce and W. E. Spicer, in *Methods of experimental*

physics, V.11, New York, Academic Press , 1974, p. 67.

[118] Y. Cui, Y. Zou, A. Valfells, M. Reiser, M. Walter, I. Haber, R. A. Kishek, S. Bernal and P. G. O'Shea, *Rev. Sci. Instrum. ,* vol. 75, p. 2736, 2004.

[119] "Kas'yanenko, D; Louksha, O; Sominski, G; Piosczyk, B; Thumm, M," in *Proceedings of displays and vacuum electronics*, Berlin, VDE Verlag GMBH, 2004, p. 81.

[120] Y. Itikawa, *J. Phys. Chem. Ref. Data,* vol. 35, p. 32, 2006.

[121] A. Bogaerts, *Spectrochim. Acta, Part B,* vol. 64, p. 126, 2009.

[122] Y. Itikawa, Molecular processes in plasmas, Berlin Heidelberg New York: Springer-Verlag, 2007.

[123] A. Mozumber, Fundamentals of radiation chemistry, San Diego: Academic Press, 1999.

[124] C. B. Opal, E. C. Beaty and W. K. Peterson, *At. Data. Nucl. Data Tables,* vol. 4, p. 209, 1972.

[125] C. B. Opal, W. K. Peterson and E. C. Beaty, *J. Chem. Phys.,* vol. 55, p. 4100, 1971.

[126] W. Blum and L. Rolandi, Particle detection with drift chambers, Berlin Heidelberg: Springer-Verlag, 1993.

[127] G. J. Schultz, *Phys. Rev,* vol. 125, p. 229, 1962.

[128] M. Allan, *J. Phys. B,* vol. 18, p. 4511, 1985.

[129] M. A. Biondi, *Adv. Electron. El. Phys.,* vol. 18, p. 67, 1963.

[130] "Liu, J; Raju, R G," *JFI,* vol. 329, p. 181, 1992.

[131] W. Hwang, Y. K. Kim and M. E. Rudd, *J. Chem. Phys.,* vol. 104, p. 2956, 1996.

[132] R. G. W. Norrish and W. MacF.Smith, *Proc.Roy.Soc.London,* vol. A176, p. 295, 1940.

[133] D. A. Steck, 19 9 2012. [Online]. Available: http://steck.us/alkalidata/rubidium85numbers.pdf. [Accessed 2 6 2013].

[134] Y. Kim, W. R. Johnson and M. E. Rudd, *Phys. Rev. A,* vol. 61, pp. 034702-1, 2000.